JOURNAL OF BIOLOGICAL REGULATORS & HOMEOSTATIC AGENTS
Volume 36, No. 2, March-April, 2022

CONTENTS

CASE REPORT

Successful treatment of a patient with apnea caused by traumatic large posterior fossa epidural hematoma: a case report

H-X. Guo[1#], S-B. Wang[1#], L. Wang[1], N. Feng[1], D-F. Wang[2] and Z-F. She[3*]

[1]Department of Neurosurgery, Ordos Central Hospital, Kangbashi, China; [2]Department of Imaging, Ordos Central Hospital, Kangbashi, China; [3]Department of General Surgery, Ordos Central Hospital, Kangbashi, China

[#]These authors contributed equally to this work

Posterior fossa extradural hematoma (PFEDH) is unusual among head injuries and represents about 4%-7% of all epidural hematomas (EDH) cases. PFEDH has no specific clinical findings, and they most commonly occur with silent presentations. Understanding the cerebellum anatomy and posterior fossa malformations benefits neurosurgeons, which help proper EDH management (1). Classification of posterior fossa disorders is generally based on biological developmental, neuroimaging, and developmental anatomy. Based on the developmental anatomy, it is either disorder correlated with large posterior fossa including mega cisterna magna, classic Dandy-Walker malformation, Blake's pouch cyst, and posterior fossa arachnoid cyst or malformations with small posterior fossa, which include the neocerebellar hypoplasias, Dandy-Walker variant, tecto cerebellar dysgraphia, Joubert's syndrome, rhombencephalosynapsis, and cerebellar atrophy (2, 3).

The paper describes a case of traumatic PFEDH that was surgically treated and had an excellent postoperative clinical outcome.

CASE REPORT

The patient, a 37-year-old female, was admitted to the hospital in November 2018 after falling from a high altitude and becoming unconscious for 3 hours. Physical examination on admission: The patient was in a deep coma, and a 4cm irregular wound could be seen in the right parieto-occipital area, which had been sutured. The Glasgow score GCS=3 points, bilaterally dilated pupils, 5mm in diameter, weak spontaneous respiration, decreased blood pressure, and endotracheal intubation was given. Emergency CT examination revealed an epidural hematoma in the right posterior fossa, with a volume of about 170ml. The hematoma stretched across the transverse sinus and sigmoid sinus, and the brain stem was compressed (Fig. 1). CT bone window of the head showed a linear fracture of the right paroccipital region, extending from the top to the level of the foramen magnum (Fig. 2).

A hole was drilled in the right occipital region beside the bed, and 150ml of viscous and blood fluid was sucked out, with active bleeding. After drilling, breathing was restored, and the pupil was narrowed. Emergency surgery was performed with PFEDH removal and decompression of bone flap. A midline incision near the posterior cranial fossa was used during the operation, and local infiltration of lidocaine was used. After the scalp was cut and subcutaneous tissue and muscle were separated, it was found that

Keywords: traumatic posterior fossa epidural hematoma, local anaesthesia, bedside drilling, apnea

[*]*Corresponding Author:*
Zhan-Fei She
Department of General Surgery,
Ordos Central Hospital,
Kangbashi, China
e-mail: zhanfeishe@protonmail.com

0393-974X (2022)

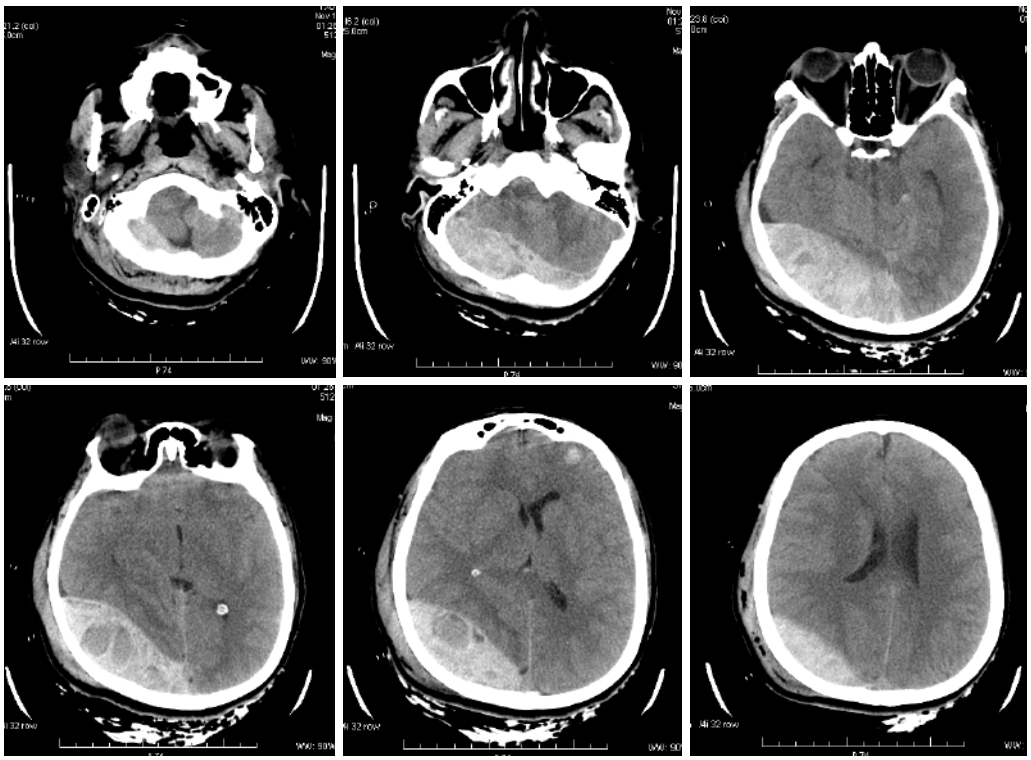

Fig. 1. *Emergency head CT showed an epidural hematoma in the right posterior fossa, with a volume of about 170ml. The hematoma stretched across the transverse sinus and sigmoid sinus, with obvious brain stem compression. The lowest level of the hematoma was at the level of the foramen magnum, and the highest level was at the level of the lateral ventricle.*

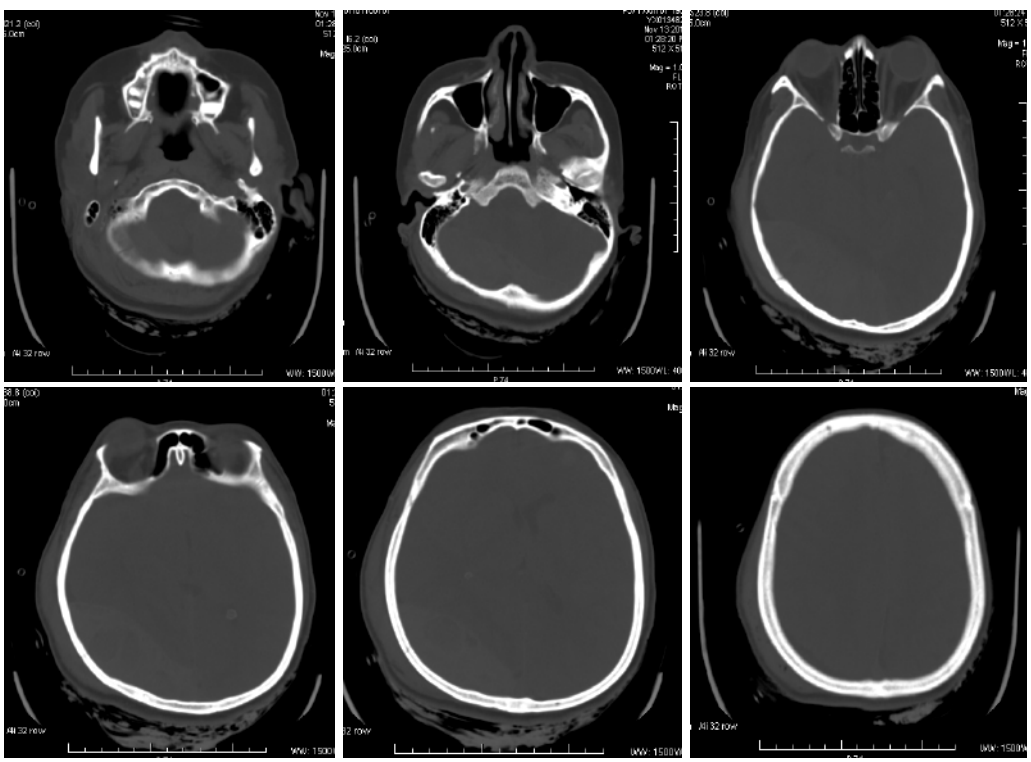

Fig. 2. *CT bone window of the head demonstrates a linear fracture of the right occipital region extending from the foramen magnum to the lateral ventricle*

the fracture line of the right occipital and parietal bone was formed and extended to the skull base. The bone window with a diameter of about 5cm was milled at the original borehole to remove the blood clot. The bone window was expanded, and the dura oozed blood in multiple places. The hemostasis was given by electrocoagulation, and the dura was sutured with tension reduction. The drainage tube was indwelling, and the incision was closed layer by layer.

On November 14, the patient regained consciousness, GCS=10 points. The patient was conscious on November 27, GCS=15 points, and the head was in good condition on head CT (Fig. 3). She was discharged on January 22, 2019; physical examination on discharge: the patient was conscious, GCS=15 minutes, bilateral pupils of equal size and equal circle, about 2mm in diameter, sensitive to light reflection. Bilateral limb muscle strength and muscle tension were normal, pathological signs were negative, co-aid examination and cooperation. On April 15, 2019, the patient came to our hospital for a head CT review (Fig. 4). The cranial repair was performed on April 23, 2019 (Fig. 5). The operation was successful, and the patient recovered. Informed consent was signed to participate in the study.

DISCUSSION

Epidural hematomas account for 1% of patients with craniocerebral trauma, while PFEDH only accounts for 0.1-0.3% of patients with craniocerebral trauma, and most of PFEDH are associated with skull fractures. In contrast to supratentorial epidural hematomas, 85% of the bleeding in patients with PFEDH is due to transverse sinus or sigmoid sinus injury due to fracture (4). The epidural hematomas in the temporal-parietal area are usually from the middle meningeal artery, and the epidural hematomas in the frontal area are generally from the pre-ethmoidal artery. At present, the popularity of CT makes the diagnosis of PFEDH easier (5, 6). The fatality rate of PFEDH is high, and the most important influencing factors include delayed diagnosis, patient consciousness level at the time of operation, degree

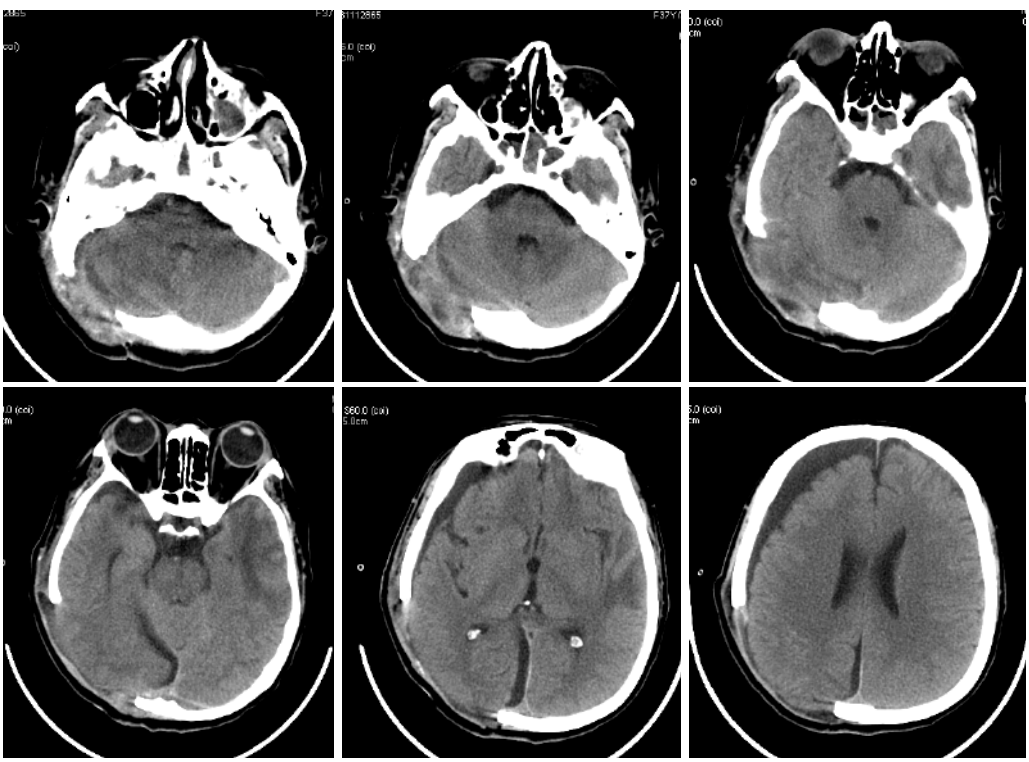

Fig. 3. *Postoperative head CT reexamination showed cerebral contusion in the left temporal lobe and right occipital lobe, subdural effusion in the right frontotemporal lobe, and skull absence in the right occipital region*

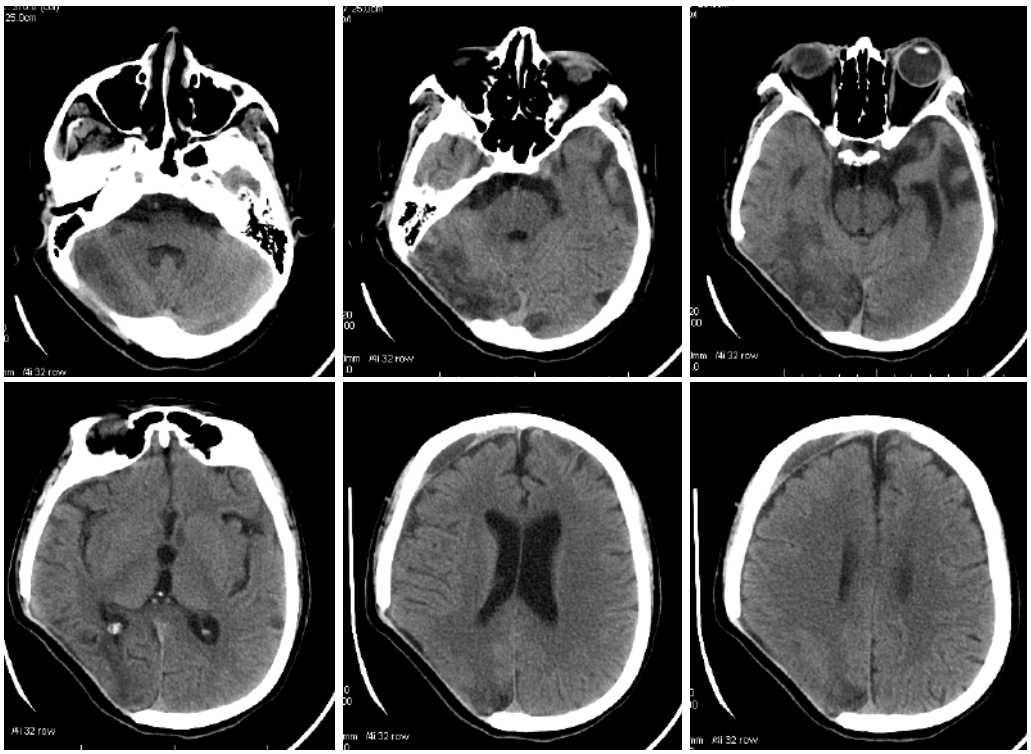

Fig. 4. *Head CT reexamination 6 months after surgery revealed softening foci in the right occipital lobe and left temporal lobe, absorption of subdural effusion, and absence of right occipital skull*

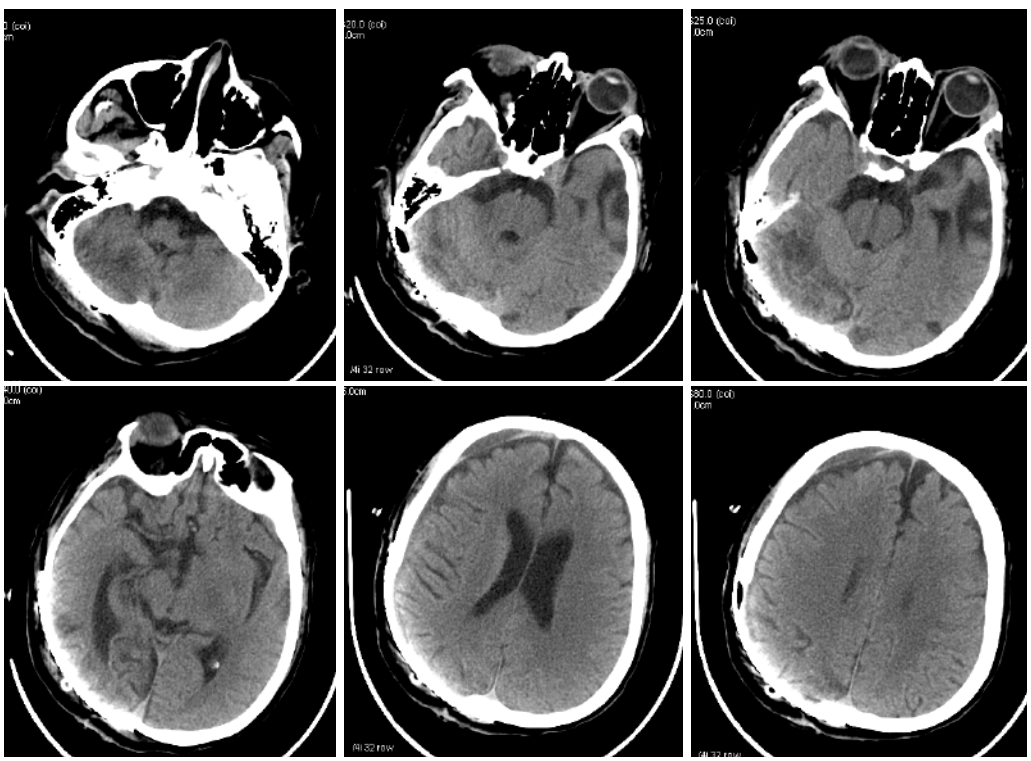

Fig. 5. *Changes after cranial repair*

of brainstem compression, respiratory and circulation stability (7).

Generally speaking, the bleeding of PFEDH comes from veins, so the progress is relatively slow. However, in this case, the patient suffered a severe injury, long fracture line, large and rapid bleeding, and the treatment was difficult. The successful treatment of this patient is due to the quick treatment. First, in the case of the dilated pupillary pupil, a bedside drilling was performed, and a large amount of hematoma was sucked out with a negative pressure device to buy more time for craniotomy (8). Second, the operation under local anesthesia avoids the risk of anesthesia and buys time for the operation. Thirdly, posterior fossa hematomas often involve venous sinuses, and the risk of surgery is high. Preoperative blood preparation or blood recovery machine preparation can reduce the risk of surgery and improve the survival rate (9, 10).

The overall prognosis is mostly determined by the symptoms' speed and the first GCS. Acute hematomas have a significant mortality rate, ranging from 12% to 70%. According to several studies, aggressive surgical therapy is required in all patients with PFEDH to avoid morbidity and death (11).

In the posterior fossa, epidural hematomas are quite rare. While clinical development is slow, deterioration may occur rapidly. It might be fatal if you do not seek immediate assistance. There can be no doubt about the value of early detection. Due to the small size of the affected region and vital structures, surgical removal of an epidural hematoma in the posterior fossa should be performed as soon as feasible.

Conflict of Interest:

The authors declare no conflict of interest.

REFERENCES

1. Kiessling JW, Hertzler DA, Drucker DEM, Spader HS. Traumatic Frontal Epidural Hematoma Caused by Multiple Arterial Injuries in the Anterior Fossa. World Neurosurg 2017;97:757.e19-.e23.
2. Sencer A, Aras Y, Akcakaya MO, Goker B, Kiris T, Canbolat AT. Posterior fossa epidural hematomas in children: clinical experience with 40 cases. J Neurosurg Pediatr 2012; 9(2):139-43.
3. Sheng HS, You CG, Yang L, Zhang N, Lin J, Lin FC, et al. Trephination mini-craniectomy for traumatic posterior fossa epidural hematomas in selected pediatric patients. Chin J Traumatol 2017; 20(4):212-15.
4. Xu Q, Chen J, Liu J, Sun C, Lu J, Wang D. Unusual, Acute, and Delayed Traumatic Torcular Herophili Epidural Hematoma Causing Malignant Encephalocele During Surgery: A Case Report. Am J Case Rep 2018; 19:1030-34.
5. Abe S, Furukawa K, Endo S, Hoshi S, Kanaya H. [Acute epidural hematoma of the posterior fossa caused by forehead impact]. [Article in Japanese] No shinkei geka 1988;16(3):321-5.
6. Han K, Li Z, Yin H, Yao W, Lan X, Bo Y. Liquid Posterior Fossa Epidural Hematoma in Pediatric Trauma: A Single-Center Case Series. J Neurol Surg A Cent Eur Neurosurg 2018; 79(5):380-5.
7. Jamous MA, Samara QA, Jbarah OF, Ahmed YB. Management of traumatic posterior fossa epidural hematomas in pediatrics: our experience and review of the literature. Childs Nerv Syst 2021; 37(9):2839-46.
8. Kırcelli A, Özel Ö, Can H, Sarı R, Cansever T, Elmacı İ. Is the presence of linear fracture a predictor of delayed posterior fossa epidural hematoma? Ulus Travma Acil Cerrahi Derg 2016; 22(4):355-60.
9. Lee S, Park SK, Joo BE, Lee JA, Kong DS, Park K. The pathogenesis of delayed epidural hematoma after posterior fossa surgery. J Clin Neurosci 2018; 47:223-7.
10. Ortiz-Ordonez A, Jiménez-Deleg G Sr, Salman S. Fatal Distant Venous Epidural Hematoma Following Posterior Cranial Fossa Surgery in a Twelve-Year old Child. Cureus 2021; 13(1):e12686.
11. Winter RC. Posterior Fossa Epidural Hematoma. Pediatr Emerg Care 2015; 31(11):808-9.

CASE REPORT

A case of unexplained amaurosis fugax: the teamwork between clinic and laboratory physicians

L. Pistelli[1], E. Micaglio[2] and M. M. Corsi-Romanelli[3,4,#]

[1]Residency program in Clinical Pathology and Clinical Biochemistry, University of Milan, Milan, Italy; [2]Arrhythmia and Electrophysiology Department, IRCCS Policlinico San Donato, San Donato Milanese, Milan, Italy; [3]Department of Biomedical Science for Health, University of Milan, Milan, Italy; [4]Department of Pathology and Laboratory Medicine, Unit of Clinical Pathology, IRCCS Policlinico San Donato, San Donato Milanese, Milan, Italy

Amaurosis fugax (AF) is a transient monocular visual loss caused by a temporary closure of the central retinal artery or its branches, resulting in retinal ischemia (1). A multitude of causes exists, including acquired and genetic factors. Frequent causes include micro embolism, atherosclerotic plaques (1), atrial fibrillation or endocarditis (2). However, the presence of a thrombophilic state represents an important underlying cause that has to be considered. Here we are presenting a case of amaurosis fugax in a young woman, where the presence of a genetic prothrombotic condition – the MTHFR gene mutation - was exacerbated by environmental factors triggering the ischemic episode; this is a rare presentation of a subclinical condition of hypercoagulability that needs the presence of additional factors to be revealed.

Case presentation

We are presenting a 49-year-old woman born from non-consanguineous parents with an episode of amaurosis fugax.

She was driving when suddenly she noticed a transient visual loss in the left eye associated with paresthesia in the left arm. During this attack, she also recused left-sided chest pain with subsequent dyspnea that resolved spontaneously in a couple of minutes. She presented at the emergency department, undergoing a comprehensive clinical workup.

The patient's medical record was unremarkable except for occasional cigarette smoking, iron deficiency (ferritin 12 ng/mL [reference interval (RI), 13–150]) – already on integrative treatment and the use of combined oral contraceptives during the last few weeks for menometrorrhagia. In addition, her family history was positive for coronary artery disease (CAD), with her father developing CAD at sixty years old.

The patient's physical examination was unrevealing: heart rate was 84 beats/min; blood pressure was 154/84 mmHg; the temperature was 37.1°C; oxygen saturation was 98% in environmental air by pulse oximetry, and Glasgow Coma Scale (GCS) was 15.

On the patient's presentation, a neurological examination showed no remarkable signs. Neuroimaging confirmed these findings: carotid and vertebral artery Doppler sonography revealed no unstable atherosclerotic plaques, and computerized brain tomography (CT) scan without contrast recorded neither acute ischemic nor hemorrhagic lesions. Moreover, cardiologic evaluation, including electrocardiogram (ECG), was normal. She subsequently underwent transthoracic

Keywords: amaurosis fugax, thrombophilia, hyperhomocysteinemia, MTHFR variant

**Corresponding author:*
Prof. Massimiliano M. Corsi Romanelli, MD PhD,
Department of Biomedical Sciences for Health,
Medical Faculty, University of Milan,
Via Luigi Mangiagalli 31,
20133 Milan, Italy
e-mail: mmcorsi@unimi.it

0393-974X (2022)

echocardiography (TTE), which did not detect any pathological features.

A few hours later, the patient was transferred to the General Medicine Department for further examinations. Laboratory test results are listed in Table I. All biochemical tests were between reference values for sex and age except vitamin B12 and homocysteine, which decreased (157 pg/mL – RI, 200–1000) and slightly increased (17.6 µmol/L – RI, 5–15), respectively. Thrombophilia biochemical testing, including protein C, protein S and antithrombin III, resulted negative. During hospitalization, the patient was treated with low-dose aspirin, folic acid, and vitamin B6 and vitamin B12 supplements. Neurological symptoms gradually recovered with only a partial visual field defect in her left eye.

The patient was discharged from the hospital without a defined diagnosis, and further investigations were planned in the outpatient clinic. Therefore, she consulted an ophthalmologist, who confirmed a persistent visual field defect. The hematologist decided to discontinue both vitamin B6 and B12 supplementation six months later, maintaining only the aspirin assumption. However, symptoms persisted with a left-sided impairment in the visual field. Remarkably, a diagnosis was still lacking.

Finally, she was referred to our hospital for genetic counselling: a possible predisposition to thrombosis has been suspected due to paternal history. So genetic tests for thrombophilia were performed: factor V Leiden G1691A variant, factor II (prothrombin) G20210A variant, both methylenetetrahydrofolate reductase (*MTHFR*) C677T and A1298C variants. These tests have been performed from peripheral-blood extracted DNA with Polymerase Chain Reaction (PCR) and automatic sequencing with fluorescent technology. Genetic tests revealed the homozygous C677T *MTHFR* gene variant, whereas the other variants as mentioned above presented a wild-type allele.

DISCUSSION

Amaurosis fugax (AF) is defined as a transient (<24 h) monocular visual loss, mostly caused by micro embolism from the ipsilateral internal carotid

Table I. *Laboratory test results.*

Test name	Result	Reference interval/ Units
Sodium	135	135-146 mmol/L
Potassium	3.6	3.6-5 mmol/L
Calcium	8.91	8.1-10.4 mg/dL
Creatinine	0.57	0.6-1 mg/dL
Alkaline phosphatase	44	30-120 U/L
Uric acid	3.9	2.4-5.7 mg/dL
Ferritin	44	12-120 ng/mL
Vitamin B12	**157**	200-1000 pg/mL
Folic acid	2.4	2-16 ng/mL
Homocysteine	**17.6**	5-15 µmol/L
CRP	0.26	0-0.5 mg/dL
TSH	4.14	0.25-5 µU/mL
Antithrombin III	84	80-120 %
Protein C	124	70-140 %
Free protein S	101	54-124 %

artery, atherosclerotic plaques (1) and by congenital or acquired (atrial fibrillation and endocarditis) heart diseases (2). These conditions can temporarily clog the central retinal artery or its branches, resulting in retinal ischemia and visual symptoms (1).

Other less common causes of AmF include vasculitis and thrombotic predisposition, commonly related to genetic factors (3).

Environmental risk factors such as arterial hypertension, dyslipidemia and type 2 diabetes can also play a role in the occurrence of AmF regardless of genetic status (3).

The most common thrombotic predisposition is related to three specific genetic variants: G1691A in the factor V gene (also called "Leiden variant"), the C677T variant in the MTHFR gene and the G20210A prothrombin gene variant. The antithrombin, protein C and protein S are less common causes of such predisposition, and they are rarely confirmed at genetic testing due to the lack of a clear genotype-phenotype correlation (4).

A huge variety of different mechanisms generates acquired conditions responsible for AmF. We can mention antiphospholipid antibody syndrome, major surgery, cancer, trauma, prolonged hospital stay, pregnancy and drugs. However, the most important therapies associated with thrombotic predisposition are hormones, used for either contraceptive or replacement use (4).

Some mechanisms mentioned above recognize hyperhomocysteinemia as a final common pathway for onset of thrombosis (5).

Homocysteine (Hcy), a sulfhydryl amino acid, is an intermediate in the methionine-cysteine metabolic pathway. It is derived from the demethylation of methionine and metabolized to cysteine through the trans-sulfuration pathway by the vitamin B6-dependent enzyme cystathionine β-synthase (CBS) (6, 7).

Homocysteine can also be converted to methionine via the folate cycle-dependent remethylation pathway in a reaction catalyzed by methionine synthase (MS) and requiring vitamin B12 as a cofactor (6, 7). The methyl group is donated by 5-methyl-tetrahydrofolate (CH_3-THF), which is synthesized from the intermediary

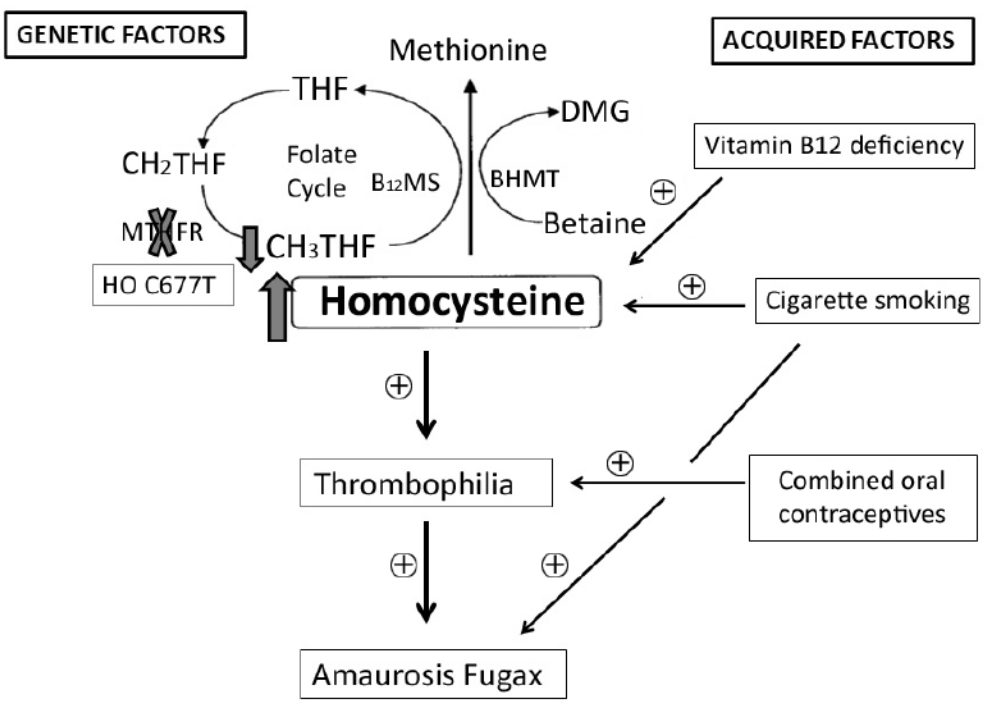

Fig. 1. *Pathological pathway in the patient. Modified from (7).*

5,10-methylenetetrahydrofolate (CH_2-THF) by the enzyme methylene-tetrahydrofolate reductase (MTHFR) (6). Consequently, an impairment of the trans-sulfuration or remethylation pathway can increase plasma homocysteine levels.

Hyperhomocysteinemia can be due to both genetic and acquired factors (7). Genetic factors mainly include the C677T and A1298C MTHFR variants because the encoded enzyme is dysfunctional. On the other hand, CBS gene homozygous mutations can be less commonly responsible for thrombotic predisposition (6).

Common acquired thrombogenic factors are folic acid, vitamin B6 and vitamin B12 deficiencies, elderly, cigarette smoking, chronic renal failure, hypothyroidism, malignancies and medications. Among those, methotrexate, phenytoin, carbamazepine and theophylline are the most important (6, 7). In our case, the patient was homozygous for the C677T *MTHFR* genetic variant. This single nucleotide substitution of cytosine for thymine at position 677 leads to an alanine-to-valine replacement at amino acid position 222. In the homozygous state, so when the variant is present in both alleles of the MTHFR gene, the enzymatic activity is decreased by about 50%, as reported by Ma et al. (8).

The decreased enzymatic activity resulted in a lower level of CH_3-THF that compromised the remethylation of homocysteine into methionine with consequent hyperhomocysteinemia (8) (Fig. 1).

The various pathogenic mechanisms of hyperhomocysteinemia leading to the prothrombotic state have not been completely understood (9). However, there is increasing evidence that hyperhomocysteinemia exerts a direct toxic effect on endothelial cells. In addition, it shows a mitogenic effect on vascular smooth muscle cells (9) promotes membrane lipid peroxidation and the oxidation of low-density lipoproteins (6). Other effects of hyperhomocysteinemia are a higher grade of both platelet adhesion and aggregation (9) a reduction in protein C activation and antithrombin III binding activity. According to recent research, this might be due to inhibiting endothelial thrombomodulin and heparan sulfate, respectively (6, 9).

In our patient, genetically caused hyperhomocysteinemia was emphasized by the concurrent vitamin B12 deficiency (Fig. 1). Vitamin B12 acts as a cofactor for methionine synthase in the remethylation of homocysteine to methionine (6, 7). Thus, its deficiency further reduced the possibility to revert the excess of homocysteine. However, in this case, physicians did not consider the abnormality of homocysteine metabolism: the neurologist treated the patient with nonspecific neuroprotective therapy. Subsequently, the hematologist discontinued therapy without considering that appropriate vitamin supplementation could prevent hyperhomocysteinemia. Therefore, we recommend treating hyperhomocysteinemic patients with folic acid, vitamin B12 and vitamin B6 to normalize plasma homocysteine levels and protect against the associated thrombophilia.

In conclusion, thrombotic predisposition is a multifactorial condition resulting from the dynamic interaction between genetic and acquired factors (4). Genetic factors are insufficient to cause thrombosis, but they are associated with an increased risk exacerbated by additional acquired factors. Therefore, the confluence of these factors, namely the homozygous C677T MTHFR gene variant and the use of combined oral contraceptives, could have triggered an amaurosis fugax episode in our patient, as shown in Fig. 1.

In this context, thrombophilic screening represents a useful tool to identify patients at risk of thrombotic episodes like AmF. Genetic testing for the aforementioned common variants should be performed in patients with recurrent thrombosis regardless of site, thrombotic episodes before 50 years-of-age and thrombosis in atypical locations such as cerebral and splanchnic veins. For the patients in pregnancy, puerperium, oral contraceptives or hormone-replacement therapy (HRT), the indication for genetic testing is still a source of debate (10). Consequently, the development of thrombotic events should suggest an underlying genetic predisposition, especially in young people without other possible environmental causes.

If a Factor V Leiden and/or an MTHFR gene variant are detected, it is mandatory to remove triggers and administer vitamin supplements to prevent thrombosis.

CONCLUSION

In conclusion, the laboratory plays a pivotal role in the diagnostic process. However, genetic testing may be not appropriate in patients with only hyperhomocysteinemia, especially considering the uncertain frequency of the C677T MTHFR gene variant in the Caucasian population (that varies from 8 to 18% in heterozygous state). Therefore, teamwork between clinicians and laboratory physicians is the best way to assess the cost/benefit ratio.

ACKNOWLEDGEMENTS

This study received funding from the Italian Ministry of Health to IRCCS Policlinico San Donato.

Informed Consent

The study was conducted at the IRCCS Policlinico San Donato, San Donato Milanese, Milan, Italy. This study was performed following the International Conference on Harmonization of Good Clinical Practice guidelines, the Declaration of Helsinki (2008) and the European Directive 2001/20/EC. The patient gave informed consent for a medical procedure and data publication.

Author contributions

All authors confirmed they have contributed to the intellectual content of this paper and have met the following 4 requirements: (a) significant contributions to the conception and design, acquisition of data, or analysis and interpretation of data; (b) drafting or revising the article for intellectual content; (c) final approval of the published article; and (d) agreement to be accountable for all aspects of the article thus ensuring that questions related to the accuracy or integrity of any part of the article are appropriately investigated and resolved.

List of abbreviations

Reference interval (RI)
Coronary artery disease (CAD)
Glasgow Coma Scale (GCS)
Computerized tomography (CT)
Electrocardiogram (ECG)
Transthoracic echocardiography (TTE)
Methylenetetrahydrofolate reductase (MTHFR)
Polymerase Chain Reaction (PCR)
Amaurosis fugax (AmF)
Homocysteine (Hcy)
Cystathionine β-synthase (CBS)
Methionine synthase (MS)
5-methyl-tetrahydrofolate (CH3-THF)
5,10-methylene-tetrahydrofolate (CH_2-THF)

List of human genes

F5, Coagulation factor V, Factor V Leiden
MTHFR, Methylenetetrahydrofolate reductase
F2, Coagulation factor II, Thrombin

Conflicts of interest

The authors declare no conflict of interest.

REFERENCES

1. Barnett HJ, Peerless SJ, Kaufmann JC. "Stump" on internal carotid artery — A source for further cerebral embolic ischemia. Stroke 1978; 9:448-456.
2. Petty GW, Khandheria BK, Whisnant JP, Sicks JD, O'Fallon WM, Wiebers DO. Outcomes among valvular heart disease patients experiencing ischemic stroke or transient ischemic attack in Olmsted County, Minnesota. Mayo Clin Proc 2005; 80:1001-8.
3. Glueck CJ, Goldenberg N, Bell H, Golnik K, Wang P. Amaurosis fugax: associations with heritable thrombophilia. Clin Appl Thromb Hemost 2005; 11:235-41.
4. Seligsohn U, Lubetsky A. Genetic susceptibility to venous thrombosis. N Engl J Med 2001; 344:1222-31.
5. Humphrey P. Stroke and transient ischaemic attacks. J Neurol Neurosurg Psychiatry 1994; 57::534-43.
6. Welch GN, Loscalzo J. Homocysteine and atherothrombosis. N Engl J Med 1998; 338:1042-50.
7. Jacobsen DW. Homocysteine and vitamins in cardiovascular disease. Clin Chem 1998; 44:1833-43.
8. Ma J, Stampfer MJ, Hennekens CH,

Frosst P, Selhub J, Horsford J, et al. Methylenetetrahydrofolate reductase polymorphism, plasma folate, homocysteine, and risk of myocardial infarction in US physicians. Circulation 1996; 94:2410-6.
9. D'Angelo A, Selhub J. Homocysteine and thrombotic disease. Blood 1997; 90:1-11.
10. Liew SC, Gupta ED. Methylenetetrahydrofolate reductase (*MTHFR*) C677T polymorphism: epidemiology, metabolism and the associated diseases. Eur J Med Genet 2015; 58:1-10.

Simultaneous L5-S1 anterior lumbar interbody fusion and total hip arthroplasty through minimally invasive anterior approaches in hip-spine syndrome

R. Bassani[1], P. Sirtori[1], C. Morselli[1], A. Cirullo[1], R. Ciliberto[1], L. Mangiavini[1,2], and G.M. Peretti[1,2]

[1]IRCCS Istituto Ortopedico Galeazzi, Milan, Italy; [2]Department of Biomedical Sciences for Health, University of Milan, Milan, Italy

The coexistence of degenerative spine disease and hip osteoarthritis (OA) is one of the most common scenarios of Hip Spine Syndrome (HSS). Usually, when a patient with an HSS is referred to surgery, two separate treatments are considered for the hip and spine in two different hospitalization steps. We present a novel strategy of HSS treated simultaneously with an anterior lumbar interbody fusion (ALIF) and a total hip arthroplasty (THA) through an anterior minimally invasive surgery (AMIS). A simultaneous minimally invasive L5-S1 ALIF and an anterior minimally invasive total hip arthroplasty. (AMIS-THA) was performed on a 48-year-old man with left hip OA, and previous failed L5-S1 posterior instrumented surgery resulted in non-union and residual spinopelvic mismatch. A specific blended analgesic protocol (epidural injection plus deep sedation) was applied. Radiological evaluation showed improvement of L5-S1 lordosis from 10° preop to 22° postop. Intraoperative total blood loss was 250 ml, and total surgical time was 120 minutes. Four hours after surgery, the patient showed full ability to walk without crutches. He was discharged on post-operative day three. As far as we know, this is the first described case in which HSS has been treated with simultaneous single surgical step by two anterior minimal invasive approaches. It was planned to avoid a delay in one of the surgical procedures and to set the hip appropriately for the new lordosis, restoring the ideal spino-pelvic alignment and the hip's full range of motion.

The most common hip degenerative disease, hip osteoarthritis (OA), can ensure degenerative spine disease (DSD) and vice versa, as often as 60% of all cases (1). The hip-spine syndrome (HSS) is a combined degenerative pathologic process affecting the lower lumbar spine, the pelvis and the hip joints and could represent an emerging problem in daily practice. The HSS was firstly described by Offierski and MacNab (2); since then, the correlation between hip and spine have, and the biomechanical assessment of the lumbar-pelvic complex (LPC) have been deeply investigated to understand their behaviour when pelvic retroversion compensates a spinal malalignment (1-3).

We describe a simultaneous single-stage combined L5-S1 anterior interbody fusion (ALIF) with anterior minimally invasive total hip arthroplasty (THA) in a patient suffering from HSS to reduce the overall length of stay, thus lowering the risk of the complications. To the best of our knowledge, it represents the first report of this

Keywords: anterior lumbar interbody fusion, anterior minimally invasive total hip arthroplasty, hip spine syndrome

Corresponding author:
Carlotta Morselli MD
2° Spinal Surgery, Department of Human Neuroscience,
"Sapienza" University, Rome, Italy
IRCCS Istituto Ortopedico Galeazzi, Milan, Italy
Tel.: +393319380540
e-mail: cmorselli822@gmail.com

0393-974X (2022)

novel surgical strategy that could be a favourable solution for a special group of patients.

Case description

A 48-year-old man presented with chronic low back pain in the setting of a history of failed L5-S1 stabilization surgery without fusion performed three years earlier. The pain was radiated to the posterior left lower extremity and the ipsilateral groin and the medial area of the left thigh. On clinical examination, antalgic

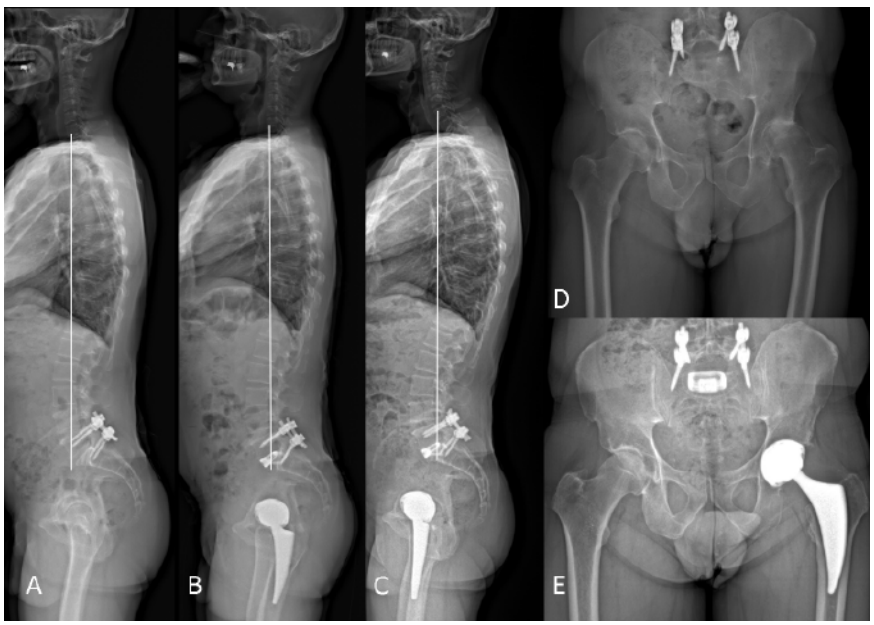

Fig. 1. ***A-D****: Pre-operative (**A, C**) and Post-operative (**B, D**) frontal and lateral full spine-Xray performed by X-Rays EOS™ and Hip X-Rays. Pre-operative full spine X-Rays (**A**) showed a type 4 spine shape according to Roussouly classification in previous L5-S1 screws fixation without segmental lordosis restoration or fusion. Post-operative full spine X-Rays control (**B**) showed correct cage position in L5-S1 ALIF- and segmental lordosis restoration in presence of left AMIS. **C**: Pre-operative frontal Hip X-Rays revealed 12mm sub-leveling of the right iliac crest. **D**: Post-operative control revealed the correct position of the left THA with restoration of iliac crest alignment.*

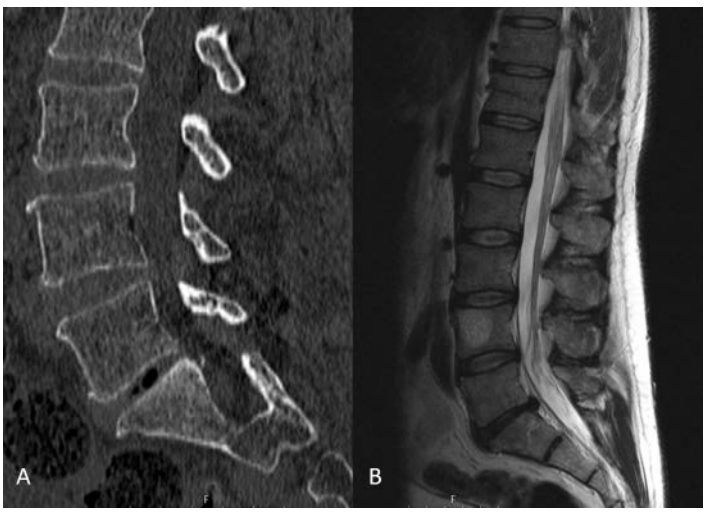

Fig. 2. ***A-B****: M, 48. **A**: sagittal CT scan showing evidence of collapsed disc height, L5-S1 non-union in previous L5-S1 screws fixation without fusion, with intradiscal vacuum phenomenon. **B**: T2 sagittal plane MRI showing degeneration of L5-S1 disc.*

gait was present with a fixed-flexed positioning of the hip and a 1.8 cm shortening of the left lower limb.

Neurological examination did not show any strength or sensory impairment: Lasegue and Wassermann tests were negative, and osteo-tendinous-reflexes were unremarkable bilaterally. The patient was able to walk bearing toes and heels. The hip range of motion (ROM) was 10-60° of flexion, 0-10° of internal rotation, and 0-25° of external rotation. Abduction and adduction were also limited; FADIR (flexion, adduction, internal rotation) and Thomas's test were positive. Preoperative Harris's Hip Score (HHS) was 32,1.

A full radiological workup was done, and MRI and CT demonstrated L5-S1 non-union with intradiscal vacuum phenomenon, local kyphosis, and severe hip OA secondary to CAM-type femoral-acetabular impingement (Fig. 1, 2). Also, X-Rays EOS™ revealed a 12 mm sub-levelling of the right iliac crest and a type 4 spinal shape according to Roussouly classification (4) (Fig. 1).

A radiological pre-operative digital planning (Sectra IDS7. Stockholm, Sweden) for the hip and spine was made, considering the LPC's theoretical modifications after the surgical spinal correction. Pre-operative spinopelvic and hip parameters were compared with ideal values (5) (Table I, II). Based on the coexistence of DSD in failed spinal surgery and hip OA, the diagnosis of HSS was made.

A simultaneous single-stage L5-S1 ALIF with minimally invasive technique and left AMIS-

Table I. *Preoperative and postoperative spinopelvic parameters compared with ideal values.*

SPINO-PEVIC PARAMETERS	PRE-OPERATIVE VALUES	IDEAL VALUES	POST-OPERATIVE VALUES
PI	54°	-	54°
SS	46°	42°	45°
PT	8°	12°	10°
LL (L1-S1)	58°	57°	59°
L4-S1	31°	38°	39°
L5-S1	10°	NA	22°
SVA	24mm	<50 mm	25 mm

PI: *Pelvic Incidence;* ***SS:*** *Sacral Slope;* ***PT:*** *Pelvic Tilt;* ***LL:*** *Lumbar Lordosis in L1-S1, L4-S1, L5-S1;* ***SVA:*** *Sagittal Vertical axis.* ***NA:*** *not applicable.*

Table II. *Preoperative and postoperative acetabular and femoral parameters.*

HIP PARAMETERS	PRE-OPERATIVE VALUES	POST-OPERATIVE VALUES
Acetabular inclination	52.8	51.5°
Acetabular anteversion*	N/A	14.3°
CCD	130°	129.2
Femoral Offset	58 mm	59 mm
LLD	6 mm (shortening)	1 mm (shortening)

CCD: *Cervicodiaphyseal angle;* ***LLD:*** *Leg Length Discrepancy;* ***NA:*** *not applicable. *Calculated using Lewinnek's method.*

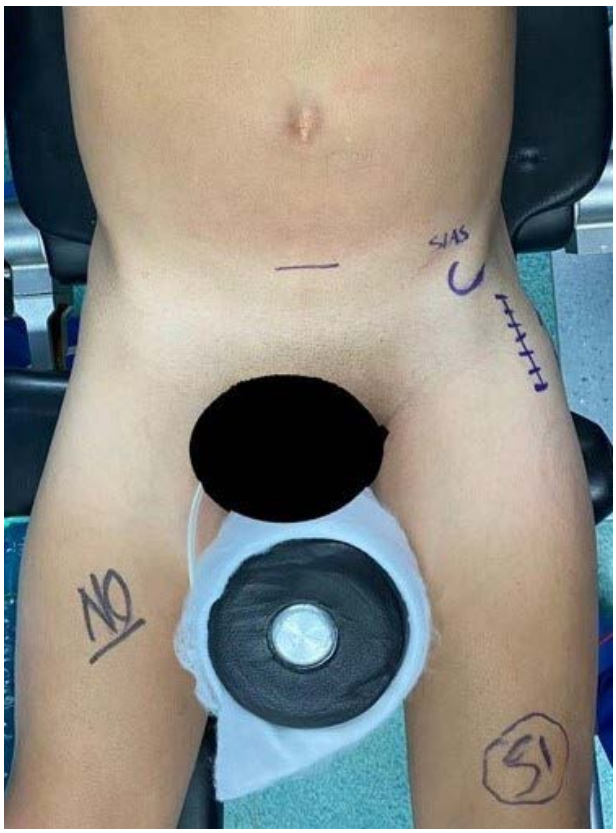

Fig. 3. *Intraoperative patient supine positioning. A single surgical field was prepared to include both the abdominal area for a modified 5 cm Pfannestiel skin incision for a minimally invasive retroperitoneal approach to the spine and the anterolateral surface of the left thigh for an AMIS approach to the hip.*

THA was proposed to correct the underlying HSS' pathological biomechanical dynamics. Fully informed written consent was obtained regarding the risks and benefits of the procedure. The patient was placed supine with the left lower limb on specific leg support (mobile leg positioner, Medacta, Castel San Pietro Switzerland) (Fig. 3, 4). A single surgical field was prepared for both procedures. The operation started addressing the spine anteriorly to achieve the final proper version of the pelvis.

As previously described by Bassani et al. (6), a 5 cm transverse modified Pfannenstiel incision was performed (Fig. 3). Blunt dissection and a short incision in the far lateral tract of the arcuate line allowed visualization of the retroperitoneal space. Through Karl Storz ® High Definition endoscopic assistance (30°), the intervertebral disc's anterior surface was prepared with subsequent complete resection of the anterior longitudinal ligament (ALL), taking care of the inferior hypogastric plexus between the iliac vessels. Then, the vertebral bodies were mobilized, despite posterior screws, with a spreader, providing posterior indirect decompression. Finally, a lordotic 15° titanium cage filled with heterologous bone substitute was implanted, overpowering posterior instrumentation, successfully restoring segmental lordosis (7) (Fig. 5).

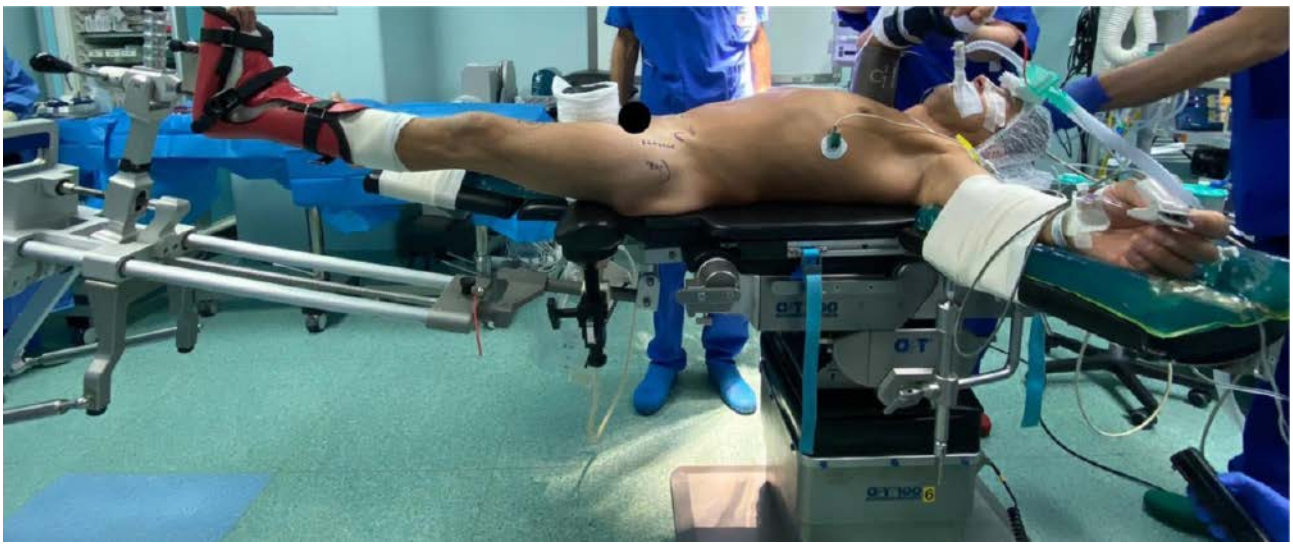

Fig. 4. *Patient supine positioning on flat traction bed.*

Immediately after the closure of the surgical approach to the spine, the THA was performed through a minimally invasive anterior approach (AMIS) (8). First, the skin incision was made between the tensor fascia lata and the Sartorius muscle; successively, blunt dissection of the innominate fascia, the anterolateral circumflex artery, and the vein identified and sectioned, and an inverted U-shape anterior capsulotomy was performed. The femoral head confirmed the severe degenerative changes. Following the anterior pelvic plane and the transverse acetabular ligament (TAL) as an anatomical landmark for the acetabular orientation, a 54-mm trabecular metal cup with a ceramic liner was placed. Then, a short double-wedged cementless femoral stem was positioned, and, subsequently, the hip's ROM and stability were evaluated without signs of subluxation or impingement.

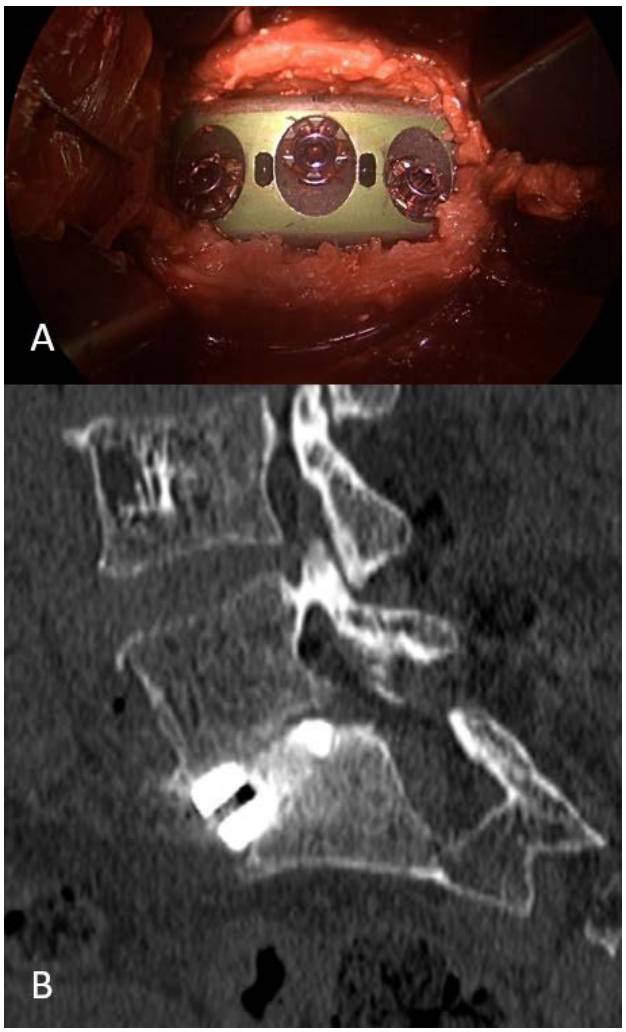

Fig. 5. **A**: *Endoscopic view and magnification showing lordotic shape (15°) titanium cage filled by heterologous bone substitute implanted after endplates preparation and mobilization of the two vertebral bodies. The posterior wall of the disc space has been decompressed.* ***B****: Post-operative CT scan sagittal view, showing restoring of disc space after lordotic cage implant.*

Afterwards, a 20 ml solution of local infiltration analgesia (LIA) was performed with Ropivacaine 10 mg/ml, Ketorolac 30 mg/ml, and tranexamic acid 100 mg/dl, as indicated by our local institutional protocol. Then, the capsular reconstruction was made. Total intra-operative blood loss was 250 ml. No perioperative complications were noted, and post-operative radiological examinations through X-rays, CT and EOS documented the correct positioning of the anterior lumbar cage (without spinopelvic mismatch) and hip prosthesis (Fig. 1). Four hours after surgery, the patient began physical therapy showing full ability to bear weight, and was discharged three days postoperatively.

DISCUSSION

Arthritic degeneration of the hip and spine can significantly alter body kinematics and spinopelvic alignment (3, 9). Rivière et al. (3, 10) defined two categories of patients based on the more involved district concerning the compensation mechanism: patients with stiff (degenerated or fused) lumbar spines demanding higher hip mobility (Hip User) and patients with flexible lumbar spines protecting the hip joint (Spine User). In addition, patients with sagittal malalignment after failed lumbar spine fixation usually develop compensatory mechanisms to preserve horizontal gaze.

In the presence of hip OA, the joint is usually fixed in flexion, reducing the activation of the main compensatory mechanism and patients with lumbar spinal fusion have less adaptability to the lumbosacral junction. In our case, the choice to attempt simultaneous surgeries was guided by the feasibility of performing a double minimally invasive approach, focusing on the two techniques' strengths, which we currently use in our institution to treat DSD and hip OA. The video-assisted ALIF technique is a

minimally invasive surgical procedure that provides a retroperitoneal pathway to the spine (6).

Unlike other surgical approaches, ALIF offers direct access to reconstruct the anterior aspect of the spine (11). This approach allows a significant disc distraction and a remarkable grade of lordosis (7, 11). Although the main indications of ALIF are represented by discogenic back pain and spondylolisthesis correction (both isthmic and degenerative types), it can also be used in revision surgery for failed posterior fusion and intervertebral foraminal stenosis secondary to loss of disc height (7,11). This technique is increasingly being used because it allows sparing paraspinal muscle trauma and denervation, it is highly reproducible, and it significantly decreases post-operative pain and blood loss, thus, fastening patient recovery (6, 12). Notably, potential complications in ALIF surgery can be almost always avoided with proper visualization and identification of the anatomical structures (6, 12).

The anterior approach to the hip represents true intermuscular access between the sartorius muscle and tensor of the fascia lata. It allows for excellent exposure of the joint while also sparing soft tissue damage, especially the posterior joint capsule and the short external rotators of the hip. Notably, it properly visualises the acetabulum and the transverse acetabular ligament (TAL) (13). Recent studies demonstrated that this technique does not affect the acetabular component's orientation compared with other surgical approaches. Moreover, the pelvic position is more stable and does not change significantly during surgery, leading to a more accurate implant orientation positioning (14-15). Furthermore, this technique has proven to reduce intra- and post-operative blood loss, risk of dislocation, and post-operative pain, thus being superior in early functional outcomes to other approaches (10, 15).

Since the spinal correction was performed first, the pre-operative hip planning was no more reliable. Therefore, considering the latter pelvic parameters, we decided to use the anterior pelvic plane and the TAL to orientate the acetabular cup within a safe zone without the risk of impingement. In addition, sparing the short external rotators, preserving the posterior joint capsule, and reconstructing the anterior capsule would give further joint stability. Postoperatively, the spinopelvic and hip parameters obtained satisfactory corrections (Table I, II).

CONCLUSION

The difficulties of getting the correct diagnosis are still present, and the treatment of HSS requires a meticulous analysis of both districts and related compensation mechanisms. The

sequential order and surgical techniques for treating this intricate pathology are still controversial; therefore, close cooperation and relationship between spinal and hip surgeons is mandatory. The synergistic use of these two minimally invasive anterior techniques made it possible to obtain a series of advantages that would not have been possible if the patient had undergone two different surgical interventions: short hospital stays, minimal blood loss, very early mobilization, proper segmental lordosis restoration and better acetabular component positioning.

Abbreviation list:

hip osteoarthritis (OA), degenerative spine disease (DSD), hip-spine-syndrome (HSS), lumbar-pelvic complex (LPC), anterior interbody fusion (ALIF), total hip arthroplasty (THA), local infiltration analgesia (LIA), transverse acetabular ligament (TAL), Pelvic Tilt (PT).

REFERENCES

1. Yeganeh A, Moghtadaei M, Motalebi M. A challenge on Orthopedic Sciences: The Influence of Spinal Disease and Deformities on Total Hip Arthroplasty: A Review on Literature. Arch Bone Jt Surg. 2018; Sep; 6 (5):346-352.
2. Offierski CM, MacNab I. Hip-spine syndrome. Spine (Phila Pa 1976). 1983; Apr;8(3):316-21.
3. Rivière C, Lazic S, Dagneaux L, et al. Spine-hip relations in patients with hip osteoarthritis. EFORT Open Rev. (2018) Feb 21;3(2):39-44.
4. Roussouly P, Gollogly S, Berthonnaud E, et al. Classification of the normal variation in the sagittal alignment of the human lumbar spine and pelvis in the standing position. Spine (Phila Pa 1976). 2005; Feb

1;30(3):346-53

5. Le Huec JC, Thompson W, Mohsinaly Yet al. Sagittal balance of the spine. Eur Spine J. 2019; Sep; 28(9):1889-1905.
6. Bassani R, Morselli C, Querenghi AM, et al. Video-assisted anterior retroperitoneal approach to the lumbar spine. A minimally invasive technique improved by the use of an endoscopic camera to treat lumbar spinal diseases. Consideration over 269 patients. J Biol Regul Homeost Agents. 2020; 34(4 Suppl. 3):7-14.
7. Bassani R, Gregori F, Morselli C, et al. Use of lordotic cages in L5-S1 Anterior Lumbar Interbody Fusion (ALIF) procedures. J Biol Regul Homeost Agents. 2020; 34(4 Suppl. 3):23-28.
8. Sirtori P, Peretti GM, Ulivi M, et al. Comparison of early functional outcomes between two different surgical approaches for total hip arthroplasty. J Biol Regul Homeost Agents. 2018; Nov-Dec;32(6 Suppl. 1):89-96.
9. Bassani R, Querenghi AM, Giacalone A, et al. Modifications of spinopelvic parameters and acetabular orientation after spinal surgery for adult deformity in patient who underwent bilateral total hip arthroplasty. J Biol Regul Homeost Agents.2020; 34(4 Suppl. 3):15-21.
10. Rivière C, Lazennec JY, Van Der Straeten C, et al. The influence of spine-hip relations on total hip replacement: A systematic review. Orthop Traumatol Surg Res. Jun; 2017; 103(4):559-568.
11. Bassani R, Morselli C, Querenghi AM, et al. Functional and radiological outcome of anterior retroperitoneal versus posterior transforaminal interbody fusion in the management of single level lumbar degenerative disease. Neurosurg Focus. 2020; 49(3):E2.
12. Bassani R, Gregori F, Peretti G. Evolution of the Anterior Approach in Lumbar Spine Fusion. World Neurosurg. 2019; Nov 131:391-398.
13. Kamal D, Anjan P, Diwakar M, et al. Orientation of Transverse Acetabular Ligament With Reference to Anterior Pelvic Plane, Arthroplasty Today, 2021; Volume 7, Pages 1-6.
14. Grammatopoulos G, Gofton W, Cochran MJ. et al. Pelvic positioning in the supine position leads to more consistent orientation of the acetabular component after total hip arthroplasty. The Bone & Joint Journal. 2018; 100-B:10, 1280-1288.
15. Lombardo MDM, Maffulli N, Bassani R, et al. Bilateral THA in the same sitting for avascular necrosis of the head of the femur in sickle cell patient: our African experience. J Biol Regul Homeost Agents. 2020; Jul-Aug;34(4 Suppl. 3):111-114.

Early application value of pulmonary ultrasound combined with arterial blood gas analysis in emergency patients with multiple severe injuries complicated by respiratory failure

J. Diao[1#], X. Yuan[2#], Z. Xu[1] and Z. Wang[1*]

[1]Emergency Trauma Department, Shanghai Pudong Hospital, Fudan University Pudong Medical Center, Shanghai, China; [2]Department of Endocrinology, Shanghai Pudong Hospital, Fudan University Pudong Medical Center, Shanghai, China

[#]These authors contributed equally to this study

OBJECTIVE: To study the early application value of pulmonary ultrasound combined with arterial blood gas analysis in emergency patients with multiple severe injuries complicated by respiratory failure.

METHODS: Eighty-one patients with multiple severe injuries complicated by respiratory failure treated in the intensive care unit of the emergency department of our hospital between January 2020 and January 2021 were retrospectively analyzed. According to the different examination methods, the patients were divided into three groups (n = 21), diagnosed only using pulmonary ultrasound (group A), diagnosed only using arterial blood gas analysis (group B), and diagnosed using pulmonary ultrasound combined with arterial blood gas analysis (group C). The initial diagnosis time, diagnosis time, and correct treatment time for patients in each group were recorded. The diagnostic rates of bedside pulmonary ultrasound, blood gas analysis, and bedside pulmonary ultrasound combined with blood gas analysis were compared. Patients were divided into a survival group (n = 65) and a death group (n = 16), and the predictive effect of pulmonary ultrasound on the long-term prognosis of patients was analyzed.

RESULTS: The initial diagnosis, diagnosis, and initial correct treatment times in groups B and C were significantly shorter than those in group A, and the initial diagnosis time, diagnosis time, and initial correct treatment time in group C were significantly shorter than those in group B ($P < 0.05$). The diagnosis rate of the examination method in group A was significantly lower than that in groups B and C ($P < 0.05$). The lung ultrasound (LUS) score in the survival group was significantly lower than that in the death group, while the right diaphragm displacement, left diaphragm displacement, and average diaphragm displacement in the survival group was significantly higher than those in the control group ($P < 0.05$). The LUS score in the survival group was significantly lower than that in the death group, while the right diaphragm displacement, left diaphragm displacement, and average diaphragm displacement in the survival group was significantly higher than those in the control group ($P < 0.05$). The receiver operating characteristic curve results showed that right diaphragm displacement, left diaphragm displacement, and average diaphragm displacement had good predictive value.

CONCLUSION: Pulmonary ultrasound combined with arterial blood gas analysis is of significant value in the early assessment of patients with multiple severe injuries complicated by respiratory failure and has important clinical significance in the timely treatment and prediction of patient prognosis.

Keywords: pulmonary ultrasound; arterial blood gas analysis; severe multiple injuries; respiratory failure

**Corresponding Author:*
Dr Zhihua Wang,
Emergency Trauma Department, Shanghai Pudong Hospital,
Fudan University Pudong Medical Center,
2800 Gongwei Road, Pudong,
Shanghai 201399, China
e-mail: wxdq3w@163.com

0393-974X (2022)

Multiple severe multiple injuries mostly refer to chest and chest injury complications caused by trauma, with a rapid onset and progressive disease course (1). The application of imaging examinations in emergencies can help diagnose and provide timely and effective treatment, which is important for patient outcomes. As the gold standard for diagnosing chest injury in patients with multiple injuries, chest computed tomography (CT) examination has a high detection rate, but its application is limited by the need to transfer the patient, slow detection, and radiation exposure (2). In contrast, bedside ultrasound is gradually being widely used in diagnosing and treating multiple injuries in the emergency department due to its portability and ability to detect injury rapidly (3). In addition, severe multiple injuries are often accompanied by respiratory failure, which leads to critical conditions in patients. Blood gas analysis is an effective tool for diagnosing respiratory failure, can determine the type of respiratory failure and is widely used in emergency medicine (4). Some studies have shown that bedside ultrasound shows some diagnostic performance for severe multiple injuries complicated by respiratory failure (5).

Monitoring diaphragmatic motion in patients using ultrasound has clinical value in predicting the prognosis of patients with respiratory failure (6). However, there are few clinical studies on the application of pulmonary ultrasound together with arterial blood gas in patients with multiple severe injuries complicated by respiratory failure. Therefore, we compared and analyzed the value of pulmonary ultrasound combined with arterial blood gas analysis in the early management stage of patients with multiple severe injuries complicated by respiratory failure and investigated the clinical diagnosis and prognostic significance of each test method in this study.

MATERIALS AND METHODS

General information

Eighty-one patients with severe multiple injuries complicated by respiratory failure who were admitted to the intensive care unit of the emergency department of our hospital between January 2020 and January 2021 were retrospectively selected. Among them, 57 were male, and 24 were female, ranging from 18 to 82 years, with a mean age of 46 years. The causes of injury were traffic accidents in 41 cases, falls from a height in 18 cases, crush injury in 12 cases, and falls in 10 cases. The ethics committee approved the study of the hospital, and the patients signed an informed consent form. The patients were divided into three groups: diagnosed using pulmonary ultrasonography only (group A), diagnosed using arterial blood gas analysis only (group B), and diagnosed using pulmonary ultrasonography and arterial blood gas analysis (group C). Table I shows a comparison of the baseline information between the three groups. At the year follow-up, the patients were divided into a survival group (n=65) and a death group (n=16) according to their outcome, and baseline information is compared in Table II.

The inclusion criteria were as follows: (i) all cases had multiple severe injuries and met the diagnostic criteria for acute respiratory failure in "Respiratory Medicine" (7), and clinical manifestations, laboratory tests confirmed the diagnosis, and chest CT; and (ii) intubation and ventilator use for assisted breathing.

The exclusion criteria were as follows: (i) history

Table I. *Comparison of baseline information among the three groups [n (%)]*

Group	n	Age ($\bar{x}$ ±s, years)	BMI ($\bar{x}$ ±s, kg/m2)	Mean arterial pressure ($\bar{x}$ ±s, mmHg)	Length of hospitalization ($\bar{x}$ ±s, d)	Respiratory rate ($\bar{x}$ ±s, times/min)
Group A	21	45.03±5.89	22.12±1.12	51.78±1.84	31.09±4.35	29.01±4.36
Group B	21	44.29±5.14	22.34±1.28	51.16±1.57	31.14±4.72	28.23±4.83
Group C	21	46.67±5.35	22.31±1.21	51.50±1.64	31.25±4.53	29.49±4.52
t/P value		0.826/>0.05	0.257/>0.05	0.368/>0.05	3.872/>0.05	0.925/>0.05

of chronic respiratory disease; (ii) congenital sternal malformation; (iii) recent history of severe pneumonia or other infectious diseases; (iv) respiratory distress due to haematological disease or other systemic diseases; and (v) patients with impaired communication or inability to cooperate.

Methodology

Pulmonary ultrasound: All pulmonary ultrasound examinations were performed using a Philips IE33 portable ultrasound machine, with the patient in a supine position and the heart as the marker; changes in the width of the inferior vena cava with breathing were observed; changes in the width of the transhepatic inferior vena cava in the mid-axillary line of the right abdomen with breathing was examined. The examination included the upper blue point, lower blue point, diaphragmatic point, transverse line of the right little finger, posterior blue point, and bilateral images were compared. Evaluation markers: (i) Bilateral chest and lungs were observed for the presence of pneumothorax

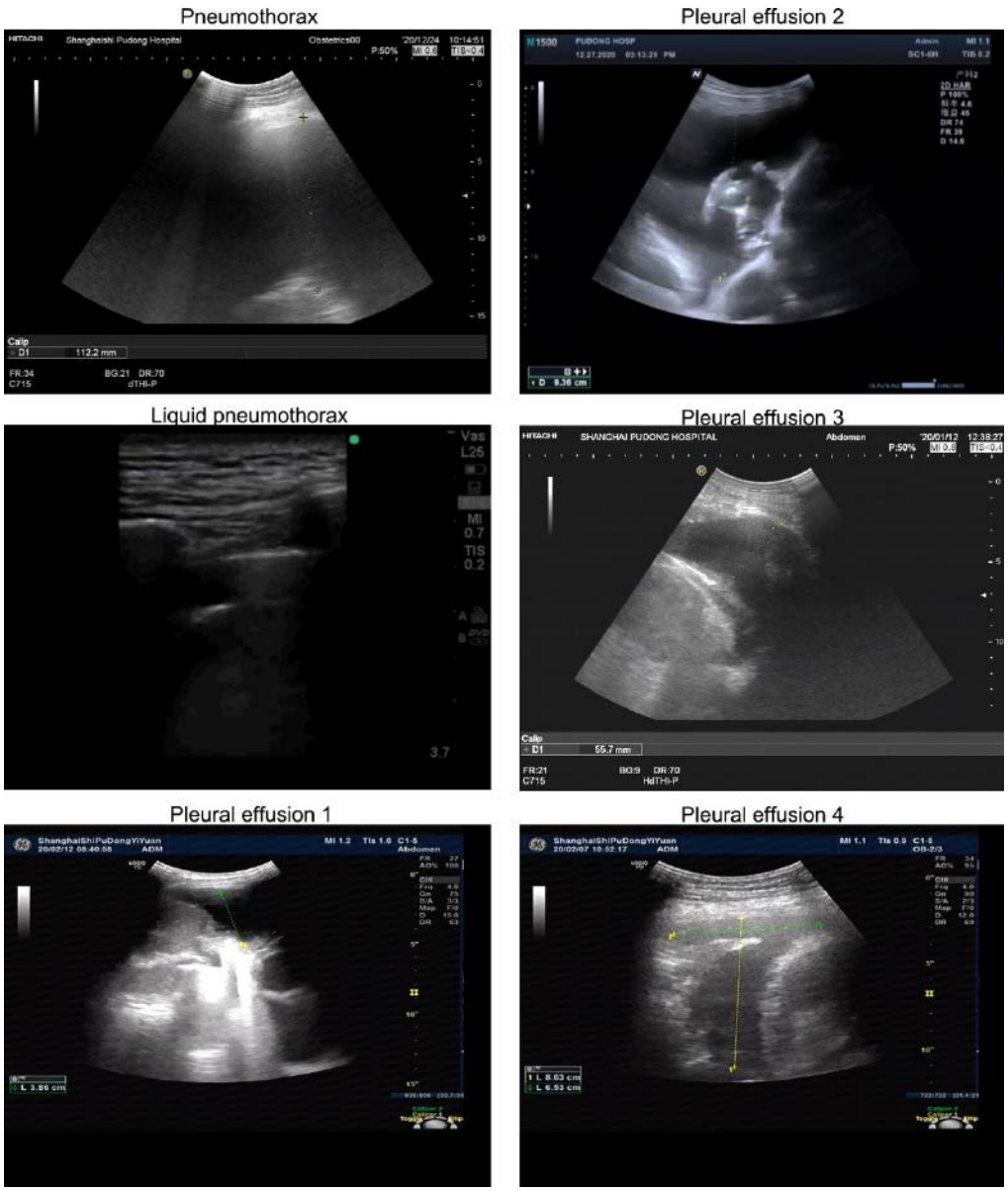

Fig. 1. *Bedside ultrasound*

and pleural effusion, A-line sign, or B-line sign; (ii) lung ultrasound score (LUS), performed by two physicians who were qualified in critical care ultrasound, based on scoring the LUS score of images on a 4-point scale: 1, smooth A-line or less than two isolated B-lines; 2: the presence of a large number of well-defined B-lines spaced more than 7 mm apart; (iii) diaphragmatic displacement measurement method: after examining the patient's diaphragm, the probe was placed in the right anterior axillary line and left mid-axillary line, with the probe facing the apex of the diaphragm to focus on the diaphragm position. The maximum amplitude of diaphragmatic movement in the inspiratory phase was measured, and diaphragmatic displacement and movement time were recorded. The mean diaphragmatic displacement was calculated as the average of multiple measurements.

Ultrasound images of the lungs of some patients are shown in Fig. 1. Pneumothorax: the images show the disappearance of lung movement, visible lung spots, and stratosphere signs; liquid pneumothorax: ultrasound shows a large amount of fluid accumulated in the pleural cavity, and the surface of the effusion can be seen in the gas-liquid mirror; and pleural effusion: the images show the separation of pleural cavity walls, and the gap is filled with a fluid sonolucent area, a hypoechoic lung "suspension" could be observed in the sonolucent zone, and the amount of fluid can be estimated approximately based on the sonolucent zone.

Blood gas analysis: All blood gas analysis examinations were performed using a Siemens fully automated blood gas analyzer (RAPIDLab 1265) to measure the arterial partial pressure of oxygen (PaO_2) and arterial partial pressure of carbon dioxide ($PaCO_2$), and blood pH.

Observation markers

1) The time to initial diagnosis, time to diagnosis confirmation, and time to initial correct treatment in the patients in each group were observed. 2) The diagnosis confirmation rates for each examination method were compared. 3) All images used for lung ultrasound (LUS) were scored by two imaging physicians qualified in critical care ultrasound to assess their prognostic value.

Statistical processing

All data were analyzed using the IBM SPSS 22.0 statistical software; quantitative data are expressed as (±s) and were compared using a t-test. Qualitative data are expressed as n (%) and were compared using the χ^2 test. The predictive power of pulmonary ultrasound and blood gas analysis for severe multiple injuries complicated by respiratory failure was explored by analyzing the area under the receiver operating characteristic (ROC) curve, optimal threshold, sensitivity, and specificity. The difference was considered statistically significant at $P < 0.05$.

RESULTS

Comparison of diagnosis and treatment times for patients in each group

The time to initial diagnosis, time to diagnosis, and time to initial correct treatment was significantly shorter in groups B and C than in group A. The time to initial diagnosis, time to diagnosis, and time to initial correct treatment was significantly shorter in group C than in group B ($P < 0.05$). The results are presented in Table III.

Table II. *Comparison of baseline information between the two groups [n (%)]*

Group	n	Age ($\bar{x}$ ±s, years)	BMI ($\bar{x}$ ±s, kg/m2)	Mean arterial pressure ($\bar{x}$ ±s, mmHg)	Length of hospitalization ($\bar{x}$ ±s, d)	Respiratory rate ($\bar{x}$ ±s, times/min)
Survival group	65	45.45±5.73	22.42±1.25	51.52±1.59	31.21±4.25	29.18±4.54
Death group	16	44.36±5.66	22.37±1.38	51.63±1.51	31.17±4.47	28.37±4.71
t/P value		0.683/>0.05	0.140/>0.05	0.250/>0.05	3.339/>0.05	0.635/>0.05

Comparison of the diagnostic rates of patients in various groups

The examination method used in Group A had a significantly lower diagnostic confirmation rate than that in groups B and C ($P < 0.05$). The results are presented in Table IV.

Comparison of LUS scores and diaphragm displacement between the two groups

The LUS score was significantly lower in the survival group than in the death group, and right diaphragmatic displacement, left diaphragmatic displacement, and mean diaphragmatic displacement were significantly higher than those in the control group ($P < 0.05$). The results are presented in Table V.

Evaluation value of LUS score and diaphragmatic displacement on lung ultrasonography for prognostic assessment of patients with multiple severe injuries complicated by respiratory failure

Plotting the ROC curves showed that the predictive values of right diaphragm displacement, left diaphragm displacement, and mean diaphragm displacement were better (Table VI, Fig. 2).

DISCUSSION

Multiple serious injuries are often seen with chest injuries and cause impaired pulmonary ventilation or

Table III. *Time to diagnosis and treatment in the three groups of patients (x±s, min)*

Group	n	Time to initial diagnosis	Time to diagnosis	Time to initial correct treatment
Group A	21	32±12	62±19	43±12
Group B	21	24±8a	44±15a	31±8a
Group C	21	16±4ab	36±10ab	24±6ab

Table IV. *Diagnostic rate of patients in each examination method group*

Group	n	Number of diagnosed cases	Diagnosis confirmation rate (%)
Group A	21	13*	61.90
Group B	21	19	90.47
Group C	21	20	95.24
Gold standard	21	21	100.00

*Note: *P < 0.05 Compared to gold standard*

Table V. *Comparison of LUS scores and diaphragmatic displacement between the two groups*

Group	n	LUS score (points)	Right diaphragmatic displacement (min)	Left diaphragmatic displacement (ml)	Mean diaphragmatic displacement (d)
Survival Gr	65	14.03±4.89	18.12±6.12	14.78±5.84	14.09±6.35
Death Gr	16	19.29±5.14	11.34±6.28	9.16±4.57	8.14±5.72
t-value		3.817	3.950	3.583	3.419
P-value		<0.05	<0.05	<0.05	<0.05

pulmonary exchange, leading to multiple severe injuries complicated by respiratory failure and increased patient morbidity and mortality (8). Some studies have shown that bedside ultrasound allows physicians to make rapid diagnostic findings, improving diagnostic accuracy and shortening the time for diagnosis confirmation (9). This

Table VI. *Prognostic assessment of the LUS score and diaphragm displacement in lung ultrasonography in patients with severe multiple injuries complicated with respiratory failure*

Marker	AUC	95% CI	Optimal cut-off value	Specificity	Sensitivity
LUS score	0.647	0.542~0.719	21.567	0.678	0.887
Right diaphragmatic displacement	0.754	0.683~0.839	14.378	0.935	0.656
Left diaphragmatic displacement	0.768	0.682~0.818	12.467	0.957	0.682
Mean diaphragmatic displacement	0.779	0.712~0.842	10.379	0.982	0.729

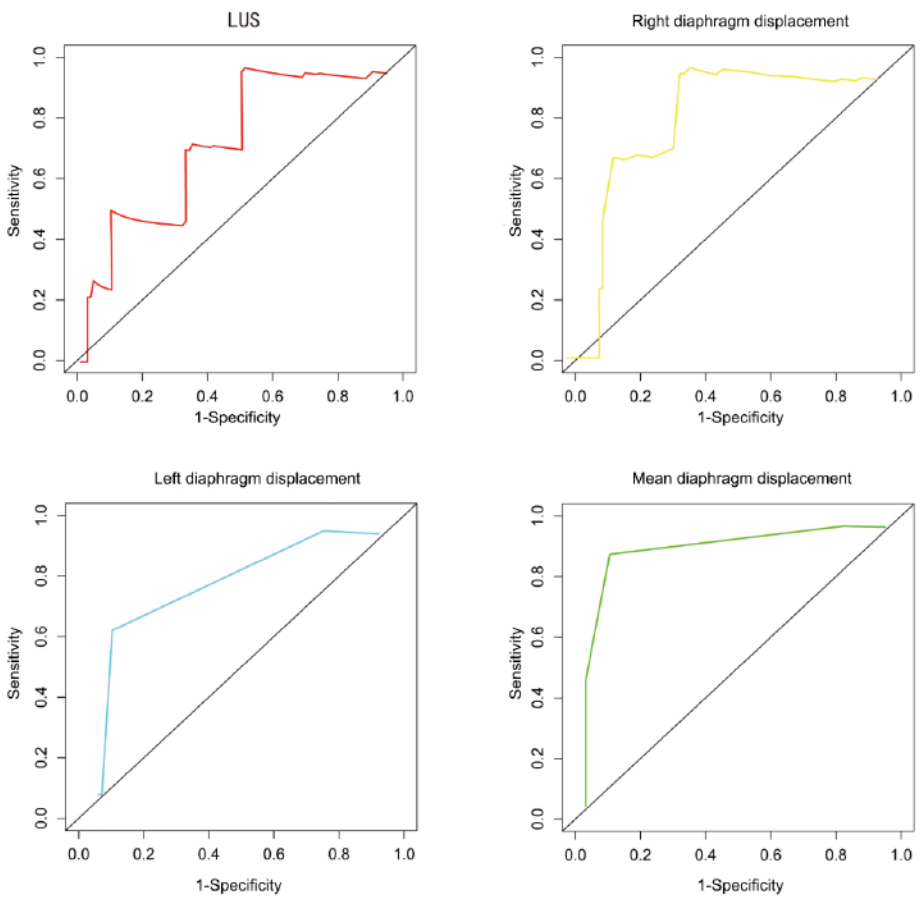

Fig. 2. *ROC curve showing prediction results for various markers*

study compared the diagnostic performance of different examination methods in patients with severe multiple injuries complicated by respiratory failure. The results showed that the time to initial diagnosis, time to confirmation of diagnosis, and time to initial correct treatment were significantly shorter in patients who underwent combined pulmonary ultrasound and blood gas analysis examinations than in the other groups, suggesting that combined examinations were more efficient and enabled patients to receive prompt and effective treatment. The diagnostic performance results showed no significant difference between the blood gas analysis and combined examination. This is due to the high diagnostic value of the blood gas analysis itself (10), but the relatively convenient and rapid application of bedside ultrasound in emergency department work also has a corresponding clinical value (11).

This study aimed to investigate the value of bedside ultrasound in emergency medicine. A study showed that pulmonary ultrasound is valuable in determining the prognosis of patients with respiratory failure (12). Therefore, patients were stratified according to their prognosis in this study, and pulmonary ultrasound imaging was used for analysis. The results showed significant differences between the images of patients in the survival and death groups. LUS is a strong manifestation of altered pulmonary ventilation and can assess the severity of respiratory failure in patients (13). However, only right diaphragmatic displacement left diaphragmatic displacement, and mean diaphragmatic displacement had a good predictive value in this study, while LUS did not have a high predictive prognostic value; this may be due to the small sample size. An imbalance in respiratory load and respiratory muscle strength can lead to poor prognosis in patients with respiratory failure. The major respiratory muscle in the human body is the diaphragm, especially during spontaneous breathing, and observation of the diaphragm is a potential method for determining the prognosis of patients (14). More information about diaphragmatic function can be obtained using bedside ultrasound, such as clear anatomical images and diaphragm activity patterns. In addition, right diaphragmatic displacement left diaphragmatic displacement, and mean diaphragmatic displacement have predictive value for clinical weaning of ventilators (15). Therefore, applying pulmonary ultrasound in patients with severe multiple injuries complicated by respiratory failure is clinically important.

This study has some limitations. First, this was a retrospective study, and there may be bias in the clinical information. Second, the sample in this study was small. Larger sample size could be used in future studies.

This study was conducted to investigate the diagnostic performance of pulmonary ultrasound and arterial blood gas analysis methods in patients with multiple severe injuries complicated by respiratory failure and determine the prognostic, predictive ability of pulmonary ultrasound in patients. Although pulmonary ultrasound has a limited role in the early diagnosis of severe combined respiratory failure in contrast to blood gas analysis, it has a better predictive power for the long-term prognosis of patients. In conclusion, pulmonary ultrasound combined with arterial blood gas analysis has clinical significance in the early stages of patients with severe multiple injuries complicated by respiratory failure in the emergency department.

ACKNOWLEDGEMENTS

1. This work was supported by the Project of Key Medical Specialty and Treatment Center of Pudong Hospital of Fudan University (Grant No: Zdzk2020-15)

2. The Special Fund for Scientific Research Projects of Shanghai Pudong New Area Health Committee (Grant No: PW2021A-70).

REFERENCES

1. Ming T, Yuan M, Kong Q, Huang Q, Xia Z, Wu X. Dexmedetomidine alleviates blunt chest trauma and hemorrhagic shock resuscitation induced acute lung injury through inhibiting the NLRP3 inflammasome. Mol Med Rep 2020; 22:2507-15.
2. Kelleher MS Jr, Gao G, Rolen MF, Bokhari SA. Completion CT of Chest, Abdomen, and Pelvis after Acute Head and Cervical Spine Trauma: Incidence of Acute Traumatic Findings in the Setting of Low-

Velocity Trauma. Radiology 2016; 279:395-99.
3. Talbot BS, Gange CP Jr, Chaturvedi A, Klionsky N, Hobbs SK, Chaturvedi A. Traumatic Rib Injury: Patterns, Imaging Pitfalls, Complications, and Treatment. Radiographics 2017; 37:628-51.
4. Golub J, Gorenjak M, Pilinger EZ, Lesnik A, Markota A. Comparison between arterial and peripheral-venous blood gases analysis in patients with dyspnoea and/or suspected acute respiratory failure. Eur J Intern Med 2020; 75:112-13.
5. Dureau P, Bougle A, Melac AT, et al. Colour Doppler ultrasound after major cardiac surgery improves diagnostic accuracy of the pulmonary infection score in acute respiratory failure: A prospective observational study. Eur J Anaesthesiol 2019; 36:676-82.
6. Kelley RC, Ferreira LF. Diaphragm abnormalities in heart failure and aging: mechanisms and integration of cardiovascular and respiratory pathophysiology. Heart Fail Rev 2017; 22:191-207.
7. Wang C, Xiao F, Qiao R, Shen YH. Respiratory medicine in China: progress, challenges, and opportunities. Chest 2013; 143:1766-73.
8. Chiumello D, Brioni M. Severe hypoxemia: which strategy to choose. Crit Care 2016; 20:132.
9. Stevenson JG. The Development of Color Doppler Echocardiography: Innovation and Collaboration. J Am Soc Echocardiogr 2018; 31:1344-52.
10. Gattinoni L, Pesenti A, Matthay M. Understanding blood gas analysis. Intensive Care Med 2018; 44:91-93.
11. Mitchell DG, Needleman L, Bezzi M, et al. Femoral artery pseudoaneurysm: diagnosis with conventional duplex and color Doppler US. Radiology 1987; 165:687-90.
12. Lichtenstein D. Lung ultrasound in the critically ill. Curr Opin Crit Care 2014; 20:315-22.
13. Loi B, Vigo G, Baraldi E, et al. Lung Ultrasound to Monitor Extremely Preterm Infants and Predict Bronchopulmonary Dysplasia. A Multicenter Longitudinal Cohort Study. Am J Respir Crit Care Med 2021; 203:1398-1409.
14. Matamis D, Soilemezi E, Tsagourias M, et al. Sonographic evaluation of the diaphragm in critically ill patients. Technique and clinical applications. Intensive Care Med 2013; 39:801-10.
15. Lesser TG, Schubert H, Gullmar D, Reichenbach JR, Wolfram F. One-lung flooding reduces the ipsilateral diaphragm motion during mechanical ventilation. Eur J Med Res 2016; 21:9.

Comprehensive analysis of m6A regulator signature for prediction of prognosis and immune cell infiltration in lung adenocarcinoma

J-Z. Zhang, S-H. Bai, Y-L. Yan, H-J. Kang, G-Z. Li, Z-D. Feng, W. Ma, X. Wang and J. Ren*

Department of Oncology Radiotherapy, First Affiliated Hospital of Xi'an Jiaotong University, Xi'an, Shaanxi Province, China

Received November 29, 2021 – Accepted April 20, 2022

OBJECTIVE: This study aimed to elucidate the molecular mechanism of N6-methyladenosine (m6A) regulation in lung adenocarcinoma (LUAD) development.

METHODS: Gene expression profiles were derived from the TCGA and GEO databases. The expression levels of m6A regulators in LUAD and normal tissues were assessed. Consensus clustering was conducted for differential tumor subtypes. m6A regulators related to prognosis were screened using the LASSO algorithm. A score (RS) system was constructed and verified. The correlation between the risk score signature, prognosis, and immune cell infiltration was further analysed.

RESULTS: We identified the modification features of m6A regulators in LUAD and found that 16 m6A genes were aberrantly expressed in tumor tissue compared with normal tissue. Six optimised m6A regulators, including FTO, RBM15B, and RBMX, were obtained to construct a risk score system. More importantly, the AUC values of the ROC curve were 0.790, 0.729, 0.776, and 0.765 for the four datasets, indicating high predictive ability. Patients in the high-risk group had worse prognoses than those in the low-risk group ($P < 0.05$). Three clinical factors (RS status, pathological stage, and tumor recurrence) correlated independently with survival outcomes. The proportions of the four immune cell types showed abnormal changes in the two risk groups. The m6A regulatory signature was significantly related to infiltration by immune cells, such as B cells, CD4+ and CD8+ T cells, and neutrophils ($P < 0.05$).

CONCLUSION: We demonstrated the potential roles of six m6A regulators in LUAD progression and immune cell infiltration. The risk score signature may serve as a reliable tool for prognosis prediction and may provide effective guidance in LUAD therapy.

Adenocarcinoma is a common histological type of lung cancer, accounting for approximately 40% of all lung cancer cases. In 2021, an estimated more than 235,000 new lung or bronchus cancer cases will be diagnosed, and 131,000 deaths will occur in the USA (1). Tobacco smoking and outdoor air pollution are major risk factors for lung cancer. Targeted therapies have improved therapeutic effects for some genetic mutations in *EGFR*, *KRAS*, *MET*, *BRAF*, and *ALK*, but the disease will inevitably progress due to primary and acquired resistance (2-5). Immune checkpoint blockade (ICB) has demonstrated encouraging outcomes in many cancer types. Nevertheless, only

Keywords: lung adenocarcinoma, m6A modification, prognosis, tumor microenvironment, immune cell infiltration

*Corresponding author:
Dr Juan Ren,
Department of Oncology Radiotherapy,
First Affiliated Hospital of Xi'an Jiaotong University,
Xi'an 710061,
Shaanxi Province, China
e-mail: 869491533@qq.com

0393-974X (2022)

a minority of patients achieve a durable response (6). Thus, understanding molecular mechanisms and identifying effective therapeutic targets may facilitate novel drug therapies for lung cancer.

The m6A modification is the most common regulatory mechanism in eukaryotic species. It modulates target RNA processing, splicing and stability via three types of enzymes: methyltransferases are the "writers" (METTL3, METTL14), demethylases are "erasers" (FTO and ALKBH5), and binding proteins are "readers" (YTHDF1, YTHDF2, and YTHDC1) (7-9). Aberrant m6A modifications have been observed in many types of cancer, including lung cancer. The demethylase FTO was first reported as an m6A eraser, and it modulated leukaemia cell transformation by regulating target gene expression, such as ASB2 and RARA (10). FTO overexpression induces lung cancer cell progression via m6A demethylation (11). The methyltransferase METTL3 is also upregulated in non-small cell lung cancer (NSCLC) tissues, and a study has confirmed that METTL3-m6A modification promotes Bcl-2 translation, resulting in enhanced cell proliferation and migration in NSCLC (12). Furthermore, METTL3 upregulates precursor miR-143-3p splicing to induce miRNA genesis; activating the miR-143-3p/VASH1 pathway facilitates cancer progression and brain metastasis, leading to poor prognosis in lung cancers (13). These findings suggest that m6A methylation regulators may affect cancer prognosis and serve as potential prognostic biomarkers for lung adenocarcinomas (LUADs).

Emerging evidence demonstrates the crucial role of m6A modification in tumor microenvironment (TME) formation. The TME consists of cancer cells, stromal cells, infiltrating immune cells, and various cytokines. m6A modification affects transcriptional and protein expression and induces diverse biological processes of immune cells in the TME, resulting in modulated tumor metastasis, ICB therapy response, and drug resistance (14). One study analysed RNA sequencing (RNA-seq) transcriptomic data, finding that m6A modification patterns play a key role in immune infiltration and prognosis in hepatocarcinoma, while high expression of binding protein YTHDF1 was correlated with decreased CD4+ and CD8+ T cell infiltration (15). Similarly, by analysing public transcriptomic files, a recent study showed that high expression of six m6A regulators was linked with PDL1 expression in oesophagal squamous cancer (ESCC), and alteration of these regulators dynamically affected the proportions of infiltrating immune cells, such as regulatory T cells, resting cells, and CD8 T cells (16). In addition, some studies have focused on the regulatory role of a single m6A regulator in the TME. The deficiency of the methyltransferase METTL14 in macrophages impairs CD8+ T cell functions and promotes CRC progression (17). The M6A demethylase ALKBH5 interacts with the 3′ UTR of PD-L1 mRNA and promotes its expression in tumour-associated macrophages, resulting in decreased immune cell infiltration, while patients with high expression of ALKBH5 exhibited more sensitivity to anti-PD1 immunotherapy (18). Nevertheless, the specific mechanism of m6A regulation in LUAD progression and prognosis requires further study.

In this study, we used public data mining to explore the expression changes of m6A-related genes in LUAD specimens and screened six optimal regulators associated with survival outcomes. The m6a regulator-based risk score (RS) system was established for prognosis prediction. The correlation between the RS signature, prognosis, and immune cell infiltration was also analysed. Our study provides novel insights into the mechanism of m6A genes in LUAD. The RS signature served as a reliable tool for prognosis prediction in LUAD, and these m6A regulators may be potential therapeutic targets for LUADs.

MATERIALS AND METHODS

Data resource

Gene expression profiles of LUAD (the expression level data were normalised by Log2 [FPKM+1]) and corresponding clinical information was obtained from TCGA (https://gdc-portal.nci.nih.gov/) and tested on the Illumina HiSeq 2000 RNA Sequencing platform. After matching with the corresponding clinical information, we finally obtained 559 lung tissue samples with survival outcomes, including 58 normal tissues and 501 LUAD specimens. This dataset was used as a training set.

Meanwhile, literature retrieval was performed

in the NCBI GEO database by using the keywords "lung adenocarcinoma" and "*Homo sapiens*." The selection thresholds were as follows: genomic profiles derived from solid tumor tissue of LUAD patients (haematological malignancy and cell line datasets were excluded), containing histology types, sample number >150, available samples >100, and containing clinical prognostic information. Finally, two datasets were obtained and used as the validation sets. GSE50081 (19) consisted of 181 samples and was tested on the GPL570 Affymetrix Human Genome U133 Plus 2.0 Array platform. Of 181 samples, 127 contained prognostic information. GSE37745 (20) included 196 samples and was tested on the GPL570 Affymetrix Human Genome U133 Plus 2.0 Array platform. Of 196 samples, 106 had clinical information. GSE31210 (21) contained 246 samples and was tested on the GPL570 Affymetrix Human Genome U133 Plus 2.0 Array platform, of which 226 contained prognostic information.

Selection of m6A-related genes

The alteration of m6A-related genes (including writers: *METTL3, METTL14, METTL15, WTAP, VIRMA, RBM15, RBM15B, KIAA1429,* and *ZC3H13*; erasers: *FTO* and *ALKBH5*; readers: *RBMX, YTHDC1, YTHDC2, IGF2BP1, IGF2BP2, IGF2BP3, YTHDF1, YTHDF2, YTHDF3, HNRNPA2B1,* and *HNRNPC*) was assessed in each TCGA sample.

The paired *t*-test in the R package (version 3.6.1, http://127.0.0.1:15190/library/stats/html/t.test.html) was used to detect the expression level of m6A regulatory genes in LUAD samples and normal tissues. The screening threshold was set at $P < 0.05$. The Pheatmap package (https://cran.r-project.org/web/packages/pheatmap/index.html) (22) was used to perform hierarchical clustering analysis for these differentially expressed genes.

Subtype analysis based on m6A regulators

Based on the dysregulated m6A genes, subtype analysis was conducted using the consensus cluster plus package (23) (Version 1.54.0, http://www.bioconductor.org/packages/release/bioc/html/ConsensusClusterPlus.html). Kaplan–Meier curves (24) (Version2.41-1, http://bioconductor.org/packages/survivalr/) and chi-square tests were employed to evaluate the correlations between different subtype samples and prognosis.

Correlation between subtypes and immune microenvironment

Immune cell infiltration in the TME is closely associated with clinical outcomes in cancer patients (25). Here, we used CIBERSORT (https://cibersort.stanford.edu/index.php) to analyse the proportions of immune cell types. CIBERSORT is a deconvolution method for analysing cell composition in tumor tissues (26). Changes in immune cell infiltration were detected in various subtypes using the *t*-test.

Immune scores were calculated using the estimate package (27) (http://127.0.0.1:29606/library/estimate/html/estimateScore.html). Subtypes with high immune scores are defined as the high tumor immune microenvironment (high TIME) group, while subtypes with low immune scores are referred to as the low TIME group. Gene set enrichment analysis (GSEA) (28) (http://software.broadinstitute.org/gsea/index.jsp) was used to screen the signalling pathways related to TIME. Adjusted $P < 0.05$ was set as the criterion.

Construction and verification of prognostic model

The Lasso algorithm in the "lars" package version 1.2 (29) (https://cran.r-project.org/web/packages/lars/index.html) was used to generate an optimal m6A gene signature. The parameter of min is the λ value of the simplest model in a varying range of lambda.

The formula was as follows:

$$\text{Risk score (RS)} = \sum \text{Coef}_{genes} \times \text{Exp}_{genes}$$

where Coef_{genes} represent the Lasso coefficient value of the target gene, and Exp_{genes} represent the expression level of the target gene in the TCGA set.

The performance of the RS model was verified using TCGA and GEO datasets (GSE50081, GSE37745, and GSE31210). The risk score of each LUAD sample was calculated, and all patients were divided into high-and low-risk groups according to the median RS value. Kaplan–Meier curves were generated to detect the actual survival outcomes and risk groups. Univariate and multivariate analyses were performed to identify the independent clinical parameters related to LUAD prognosis.

Correlation analysis of risk score signature and immune microenvironment

The online tool Tumor Immune Estimation Resource (TIMER) (30) was used (https://cistrome.shinyapps.io/timer/) to analyse the proportion of six immune cells (B cells, CD4+ and CD8+ T cells, neutrophils, macrophages,

and dendritic cells) based on the TCGA dataset. The immune cell proportion changes in the two risk groups were compared using an intergroup *t*-test. A correlation analysis was conducted between the RS signature and each immune cell type.

RESULTS

Screening differentially expressed m6A regulators in LUADs

The workflow of this study is shown in Fig. 1. We analysed the expression levels of 22 m6A-related genes in TCGA samples and found that 16 genes were significantly differentially expressed in LUAD samples compared with normal tissues. These regulators consisted of 4 downregulated genes (*FTO, ZC3H13, METTL14,* and *WTAP*) and 12 upregulated genes (*YTHDF3, RBM15B, YTHDF2, HNRNPA2B1, RBMX, METTL15, HNRNPC, YTHDF1, METTL3, RBM15, IGF2BP2,* and *IGF2BP3*). Clustering analysis of gene expression levels and tumor samples is shown in Fig 2.

Consensus clustering based on 16 m6A-related genes

Clustering analysis was conducted based on these gene combinations. The LUAD sample (k = 2) was classified into two subtypes, containing 323 and 178 tumor samples, respectively (Fig. 3). Survival analysis showed that patients with subtype 1 (n = 323) had a better prognosis than those with subtype 2 (n = 178, $P < 0.0001$). The distribution of clinical features in the two subtypes was statistically analysed and compared (Table I).

Analysis of immune cell type distribution between two subtypes

Immune cell infiltration in the two subtypes was calculated and analysed using the *t*-test. The proportions of eight immune cell types were dysregulated in both groups, including B lymphocytes, CD4+ T cells, M0 macrophages, and M1 macrophages (Fig.4).

The immune score represented the status of immune cell infiltration in the TME, and we obtained the immune score using the estimate package. Subtype 2, with a higher immune score, was defined

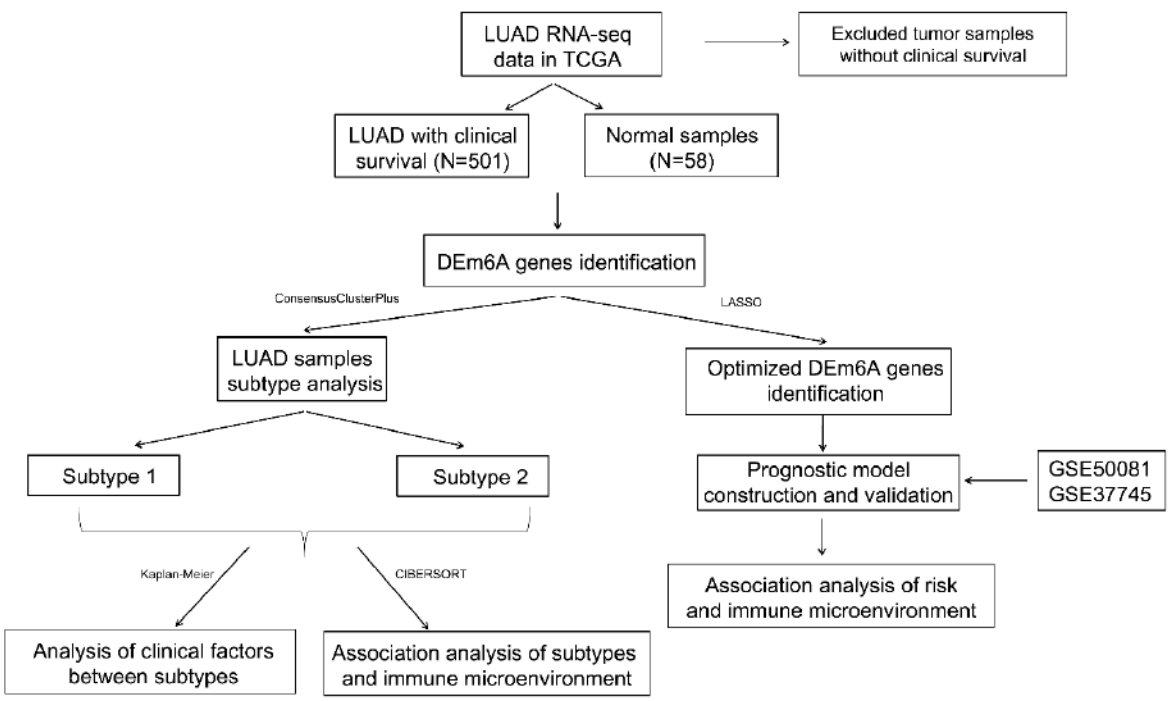

Fig. 1. *Schematic diagram of the analysis.*

as the high TIME group, whereas subtype 1, with a lower immune score, was defined as the low TIME group (Fig. 5A). Functional analysis showed that six pathways associated with TME were screened, including cell cycle, DNA replication, oocyte meiosis, progesterone-mediated oocyte maturation, basal transcription factor, and ubiquitin-mediated proteolysis (Fig. 5B).

Optimising m6A-related gene groups and constructing a risk prediction model

We screened the optimal gene groups from the above 16 m6A regulators using the Lasso algorithm. Using the defined screening criteria, we obtained six candidate genes associated with m6A methylation, including *FTO*, *RBM15B*, *RBMX*, *HNRNPC*, *METTL3*, and *IGF2BP3*. The LASSO regression coefficient of each gene was calculated to construct the risk score system using the following formula:

$$RS = (-0.000737507) * Exp_{FTO} + (0.000119939) * Exp_{RBM15B} + (-0.006157414) * Exp_{RBMX} + (0.086806793) * Exp_{HNRNPC} + (-0.058455046) * Exp_{METTL3} + (0.023552349) * Exp_{IGF2BP3}$$

Subsequently, the RS score of each sample was calculated using four datasets: TCGA, GSE50081, GSE37745, and GSE31210. The distribution of

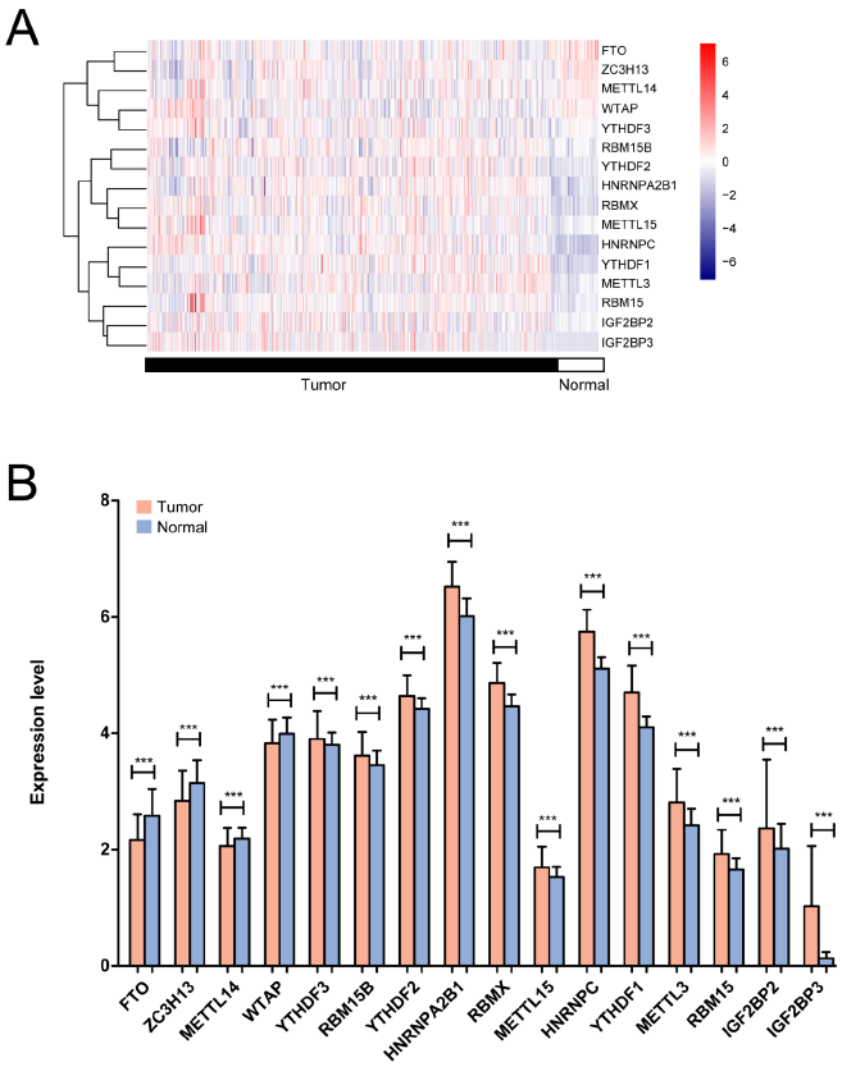

Fig. 2. *m6A-related genes are dysregulated in tumor tissues samples compared with normal samples **A**) Heatmap of tumor specimen and gene expression level; **B**) Dysregulation of m6A genes in lung adenocarcinoma tumors and control samples. *, $P < 0.05$; **, $P < 0.01$; ***, $P < 0.005$.*

Table I. *Clinical features distribution in two subtypes of LUAD patients*

Characteristics	N of case 501	Subtype		P value
		Subtype 1 (N=323)	Subtype 2 (N=178)	
Age(years)				
≤60	157	98	59	5.46E-01
>60	334	218	116	
Geneder				
Male	231	142	89	2.24E-01
Female	270	181	89	
Pathologic M				
M0	333	211	122	0.6642
M1	24	14	10	
Pathologic N				
N0	324	217	107	7.97E-02
N1	94	57	37	
N2	70	40	30	
N3	2	0	2	
Pathologic T				
T1	167	125	42	2.42E-03
T2	267	157	110	
T3	45	29	16	
T4	19	9	10	
Pathologic stage				
Stage I	268	185	83	4.69E-02
Stage II	119	70	49	
Stage III	81	45	36	
Stage IV	25	15	10	
Smoking history				
Never	28	16	12	3.96E-01
Reform	127	89	38	
Current	46	30	16	
Recurrence				
Yes	151	93	58	2.89E-01
No	275	184	91	

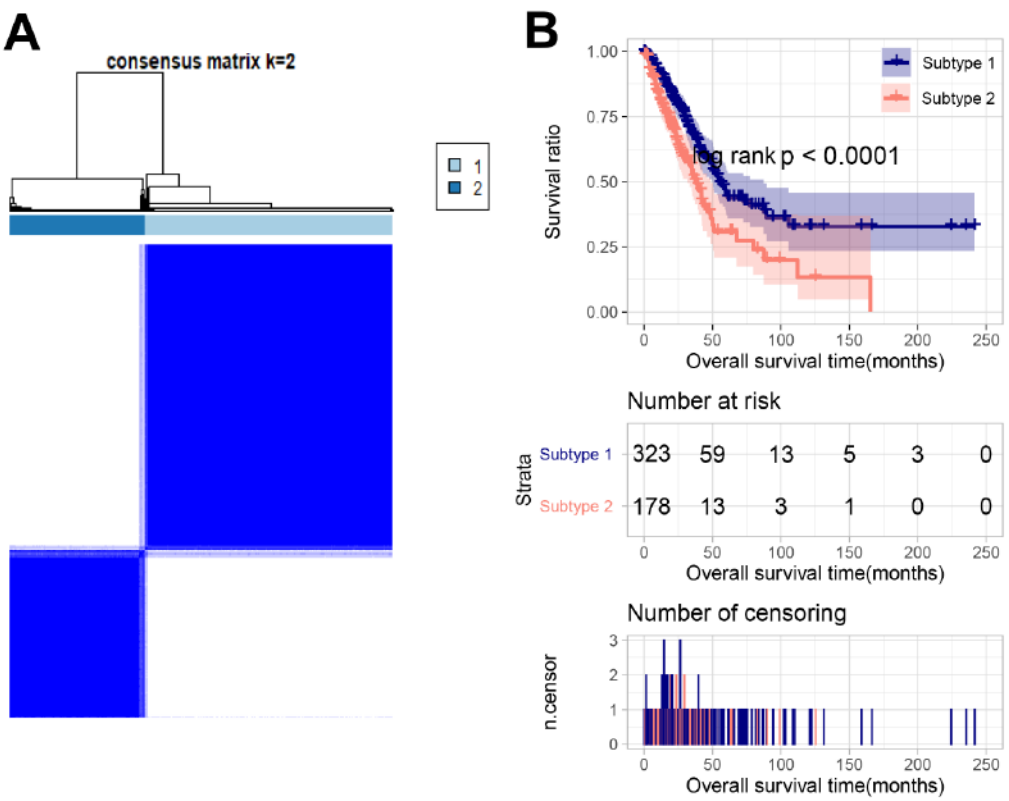

Fig. 3. *Heat map of consensus clustering analysis for lung adenocarcinoma samples (**A**) and Kaplan–Meier curve of different subtypes (**B**).*

samples in the two subtypes was visualised according to RS scores and clinical survival information. The properties of the RS score system for risk prediction were also validated in the four datasets, and the AUC values of the ROC curve were, respectively, 0.790, 0.729, 0.776, and 0.765 (Fig. 6).

Subsequently, the whole specimens in the three datasets were classified into high-and low-risk groups based on the median RS value. The survival curve revealed that patients in the low-risk group had a better prognosis than those in the high-risk group. The results were consistent in TCGA (log-rank p = 0.0029), GSE50081 (log-rank p = 0.022), GSE37745 (log-rank p = 0.001), and GSE31210 (log-rank p = 0.046) datasets, indicating a reliable predictive ability for the RS model (Fig.7A).

Moreover, pathological stage (P = 2.94E−14, P = 7.59E−03), RS status (P = 2.79E−03, P = 4.55E−03), and tumor recurrence (P = 2.44E−07, P = 1.84E−05) were identified as independent clinical factors according to univariate and multivariate analyses (Table II). The distribution of RS was visualized under different subtype groups, pathological stages, and according to tumor recurrence. The results showed that patients with subtype 2 (P < 0.0001), late pathologic stage (P = 0.0035), and tumor recurrence (P = 0.02) had a high risk score and poor prognosis (Fig.7B).

Correlation analysis of m6A genes signature and immune cell infiltrating

To explore the correlation between immune

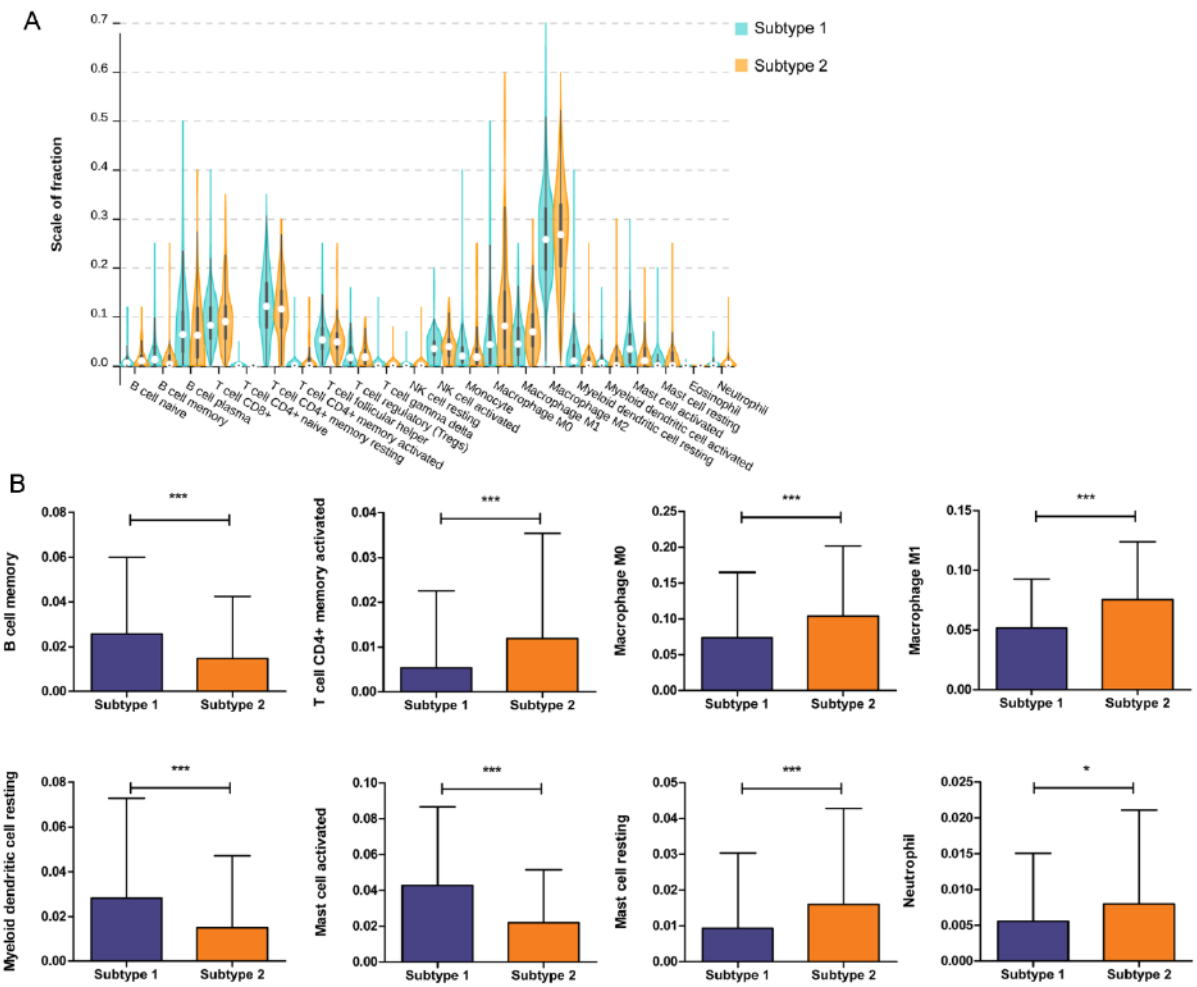

Fig. 4. *The proportions of 22 immune cell types in two subtypes (**A**) and eight immune cells with significant differential distribution (**B**). * P <0.05, ** P <0.01, *** P < 0.005.*

infiltrating cells and m6A gene signature, we analysed immune cell infiltration using the online tool TIMER. As shown in Fig. 8A, the proportion of B cells and CD4+ T cells was significantly decreased in the high-risk group samples compared to the low-risk groups (P = 7.6e-07 for B cells, and P = 4.6e-08), while CD8+ T cells and neutrophils exhibited the opposite results (P = 0.0081 for CD8+, and P = 0.045 for neutrophils). Meanwhile, B cell and CD4+ T cell infiltration were both negatively correlated with risk score status (P = 2.441e-09 for B cells, P = 3.447e-16 for CD4+). CD8 T cell and neutrophil infiltration were positively correlated with the RS signature (P = 1.498e-02 for CD8+ and P = 4.620e-02 for neutrophils) (Fig.8B).

DISCUSSION

In this study, we identified 16 significantly differentially expressed m6A regulators from LUAD samples compared with normal samples using public data mining. Functional analysis revealed that these m6A regulators mainly participate in several

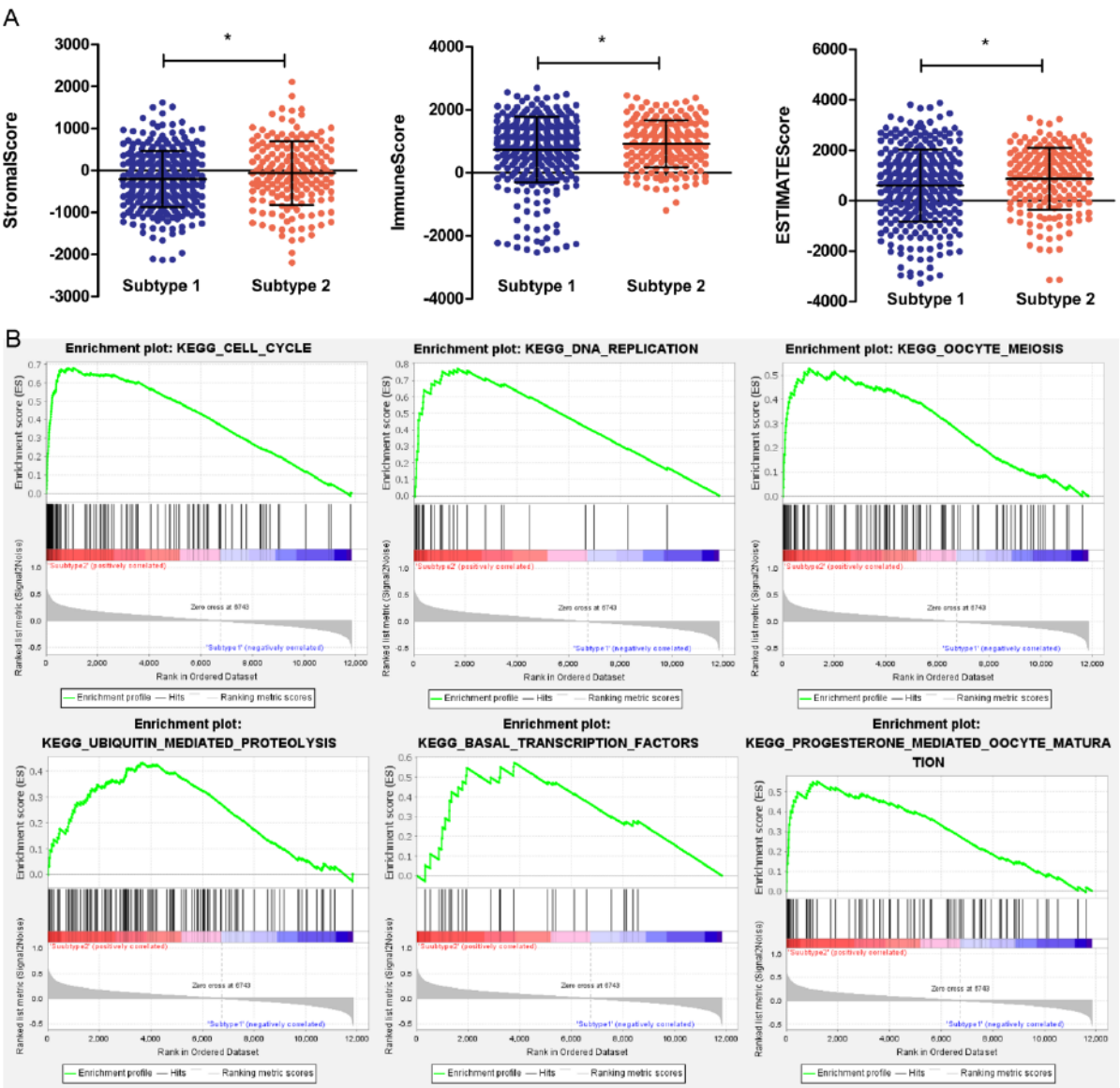

Fig. 5. *Estimated score in different subtype groups (A) and ES-plot of KEGG signaling pathways associated with the tumor immune microenvironment (B). * P < 0.05.*

pathways, such as the cell cycle, DNA replication, oocyte meiosis, and progesterone-mediated oocyte maturation. Six m6A genes (*FTO*, *RBM15B*, *RBMX*, *HNRNPC*, *METTL3*, and *IGF2BP3*) were screened as optimal molecules using the Lasso algorithm. Six m6A regulator-based risk scoring systems have been established to predict LUAD prognosis. In this model, individuals in the high-risk group exhibited poorer prognoses than those in the low-risk group. Property validation of the risk model showed a high AUC value for all three datasets. Subsequently, RS status, pathological stage, and tumor recurrence were independent clinical factors associated with the outcomes. Finally, the RS signature was significantly correlated with B cell, CD4+ and CD8+ T cell, and neutrophil infiltration ($P < 0.05$).

Among these genes, the eraser *FTO* and the writer *METTL3* have been extensively reported to be involved in cancer progression. A recent study showed that *FTO* upregulated *E2F1* expression, resulting in tumor growth, migration, and invasion in NSCLC (31). *HNRNPC*, *IGF2BP3*, and *RBMX* are

Table II. *Univariable and multivariable analysis for clinical factors related to prognosis*

Clinical characteristics	Uni-variable cox		Multi-variable cox	
	HR (95% CI)	P value	HR (95% CI)	P value
Age (years, mean±sd)	1.009[0.994-1.024]	2.64E-01	-	-
Gender (Male/Female)	1.060[0.792-1.418]	6.95E-01	-	-
Pathologic M (M0/M1)	2.111[1.232-3.616]	5.36E-03	1.226[0.494-2.036]	5.56E-02
Pathologic N (N0/N1/N2/N3)	1.710[1.443-2.027]	2.00E-10	0.860[0.519-1.426]	5.59E-01
Pathologic T (T1/T2/T3/T4)	1.550[1.289-1.863]	3.10E-06	1.187[0.879-1.602]	2.63E-01
Pathologic stage (I/II/III/IV)	1.679[1.463-1.928]	2.94E-14	2.177[1.230-3.853]	7.59E-03
Tumor recurrence (Yes/No/-)	2.392[1.700-3.367]	2.44E-07	2.464[1.631-3.723]	1.84E-05
Smoking history (Yes/No)	0.765[0.542-1.081]	1.29E-01	-	-
RS status (High/Low)	1.565[1.163-2.107]	2.79E-03	1.175[1.077-1.791]	4.55E-03

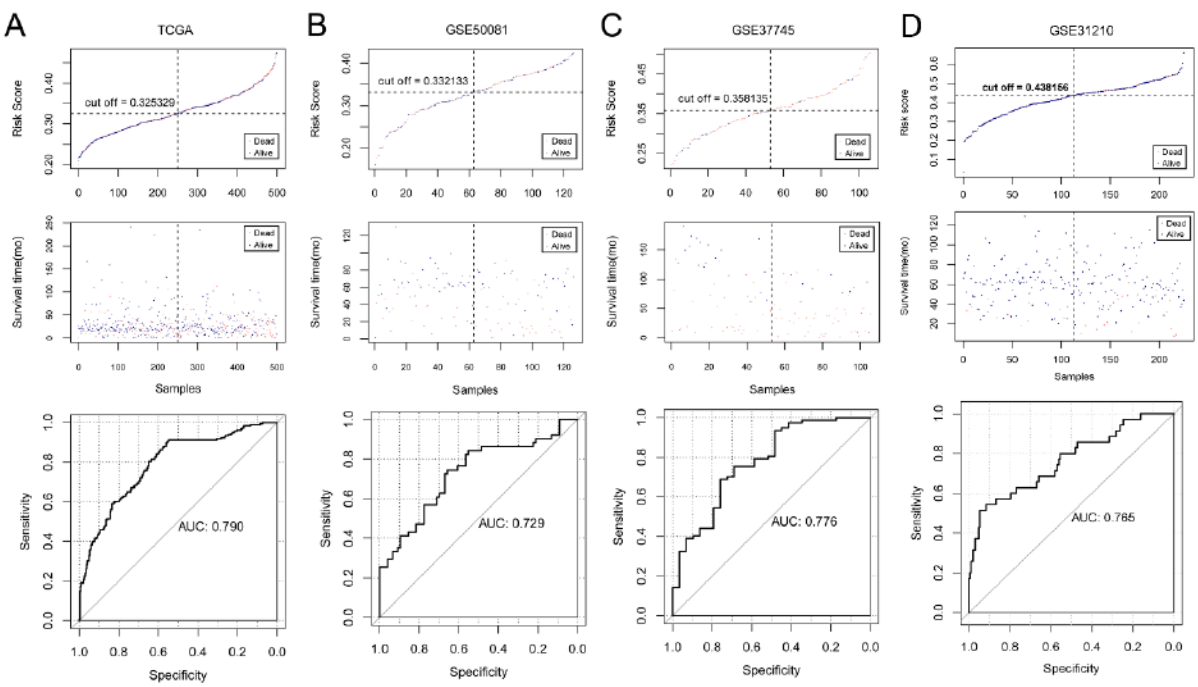

Fig. 6. *Validation of the risk score system in four datasets, TCGA (**A**), GSE50081 (**B**), GSE37745 (**C**), and GSE31210 (**D**), as well as specimen distribution, patient's survival time, and receiver operating characteristic curve.*

m6A readers. HNRNPC is a nuclear RNA-binding protein that regulates pre-mRNA processing, and its expression is substantially correlated with poor prognosis in lung cancer (32). IGF2BP3 or IMP3 is a member of IGF2BPs that contains highly conserved K-homology domains for RNA-binding, specifically recognising the m6A modification region of ABCB1 mRNA, promoting stability and expression of ABCB1, and thus affecting chemotherapy resistance in colorectal cancer (33). IGF2BP3 exhibits a stability-maintaining role in mRNA processing. However, it was also reported to be an RNA-destabilizing factor of eIF4E, induce translational activation of downstream signalling, and enhance lung cancer cell proliferation (34). Notably, IGF2BP3 could promote tumorigenesis by attenuating the deubiquitinating effect of USP10 on the tumor suppressor p53, and high expression of this gene implicated a poor prognosis for LUADs (35), suggesting that IGF2BP3 may be a crucial oncogene and potential prognostic biomarker in LUADs.

In addition, RBMX, also known as HNRNPG, is a heterogeneous nuclear ribonucleoprotein that exerts diverse biological functions such as RNA processing, DNA damage repair, and genomic stability maintenance (36, 37). HNRNPG binds to m6A-methylated RNAs via the low-complexity region of the RGG motifs (38). Co-transcription of HNRNPG and m6A-modified pre-mRNA regulates RNAPII occupancy and transcriptome-wide alternative splicing (39). During cancer development, RBMX facilitates the stable expression of BLACAT1 mRNA, which then promotes HCC progression and sorafenib resistance

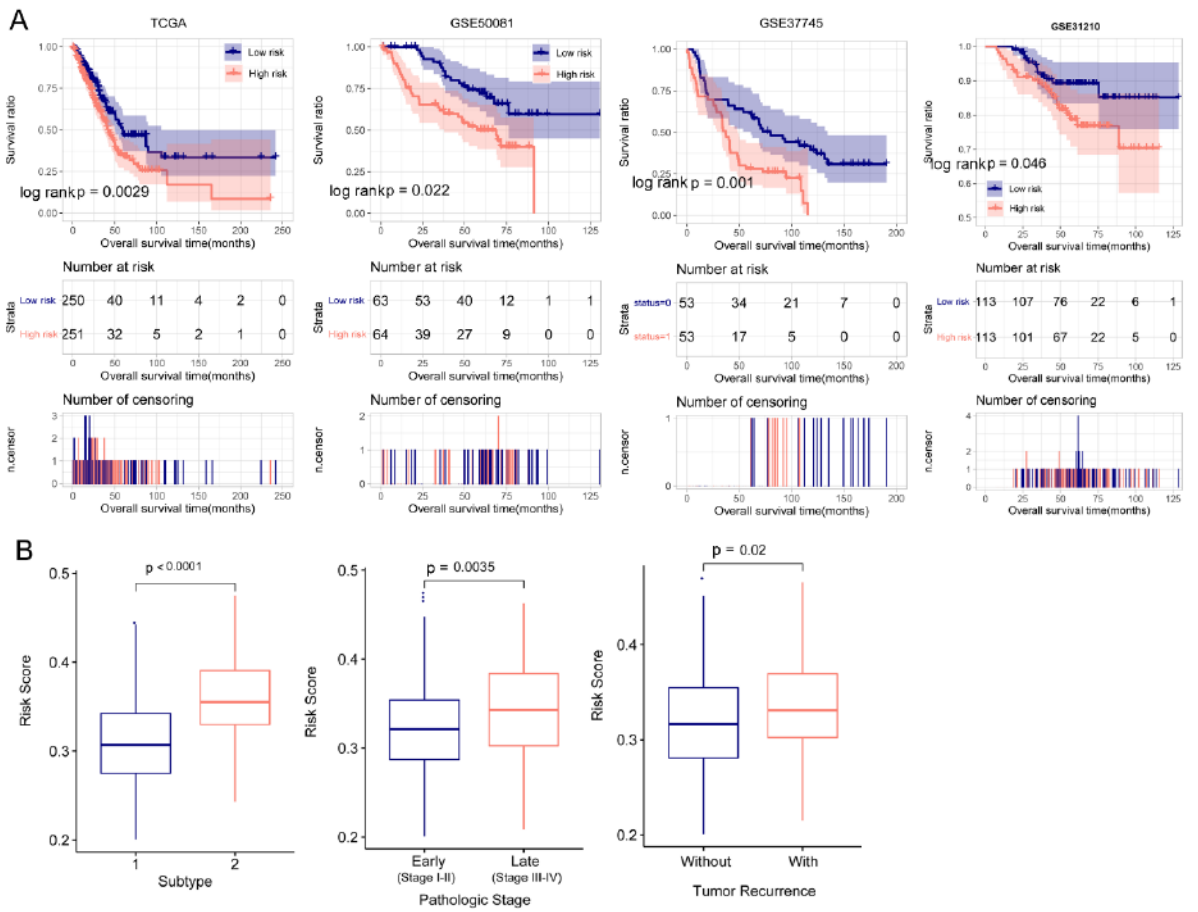

Fig. 7. *Kaplan–Meier curves of risk grouping in four datasets and risk score distribution in different clinical factor groups. A) Kaplan–Meier curves show overall survival times of high/low risk groups based on four datasets (TCGA, GSE50081, GSE37745 and GSE31210). B) The risk score status in differential subgroups (subtypes 1 and 2, pathologic stage, and tumor recurrence).*

(40). Tobacco smoking-induced RBMX mutations have been reported in lung squamous cell carcinoma, indicating that RBMX might be an oncogene in lung cancer (41). Conversely, in some cancer types, RBMX has a tumour-suppressive effect. For example, RBMX regulates the alternative splicing of PKM by interacting with hnRNPA1 protein, suppressing tumorigenesis and the progression of bladder cancer (42). RBM15B and OTT3 inhibit the formation of the spliceosome E complex by binding to serine-arginine proteins and regulating CDK11 mRNA splicing (43). RBM15B expression is positively correlated with the tumor suppressor gene BAP1 in uveal melanoma, breast, and colon cancer (44). However, the potential

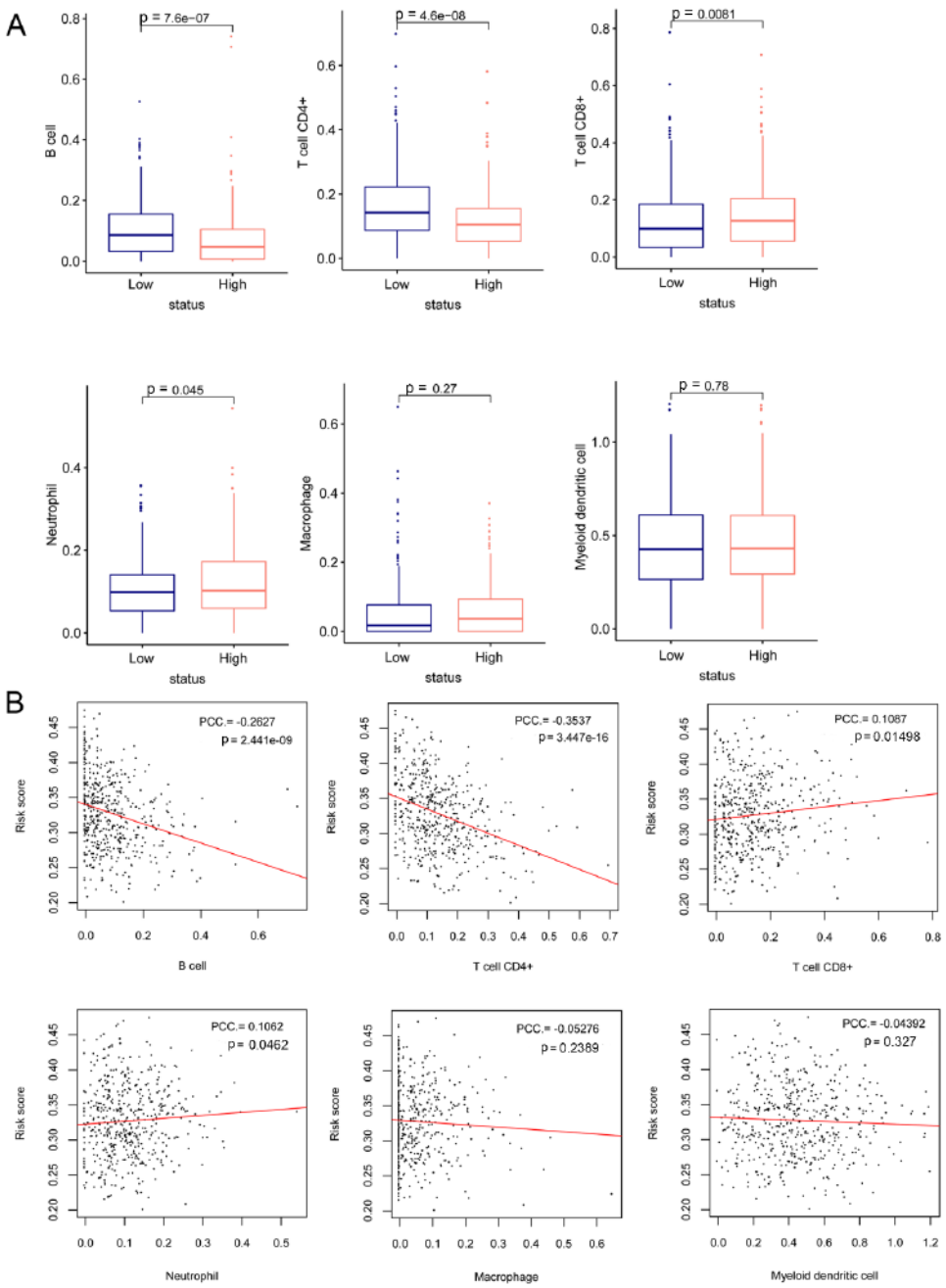

Fig. 8. *Correlation analysis of risk score signatures and infiltration by six immune cells (B cells, CD4+ and CD8+ T cells, neutrophils, macrophages, and myeloid dendritic cells).* ***A)*** *Proportions of six immune cells in high/low risk groups.* ***B)*** *Scatter plot of correlation analysis based on the TIMER database.*

role of RBM15B in LUAD has scarcely been reported.

Moreover, our results demonstrated a significant correlation between the m6A regulatory signature, prognosis, and immune cell infiltration. In the high-risk group, infiltration T cell CD8+ T cells and neutrophils were significantly increased and positively correlated with RS status ($P < 0.05$). The proportions of B lymphocytes and CD4 T cells decreased in the high-risk group and were negatively correlated with the risk score ($P < 0.05$). m6A modification is involved in the immune response in multiple cancer types, but the molecular mechanism of TIME formation remains unclear. METTL3 or METTL14 depletion increases CD8+ T cell infiltration and cytokine production in colon cancer, and the alteration of TME finally affects immune responses to anti-PD-1 therapy (45). Downregulation of METTL3 is related to tumor progression and poor prognosis of papillary thyroid carcinoma; disruption of METTL3 promotes interleukin-8 secretion and induces tumour-associated neutrophil recruitment (46).

However, our study had some limitations. First, the public profile-based analysis in our study lacks biological verification, especially experimental validation of the six m6A regulators. Further, more specimens and clinical factors, such as drug sensitivity, should be considered to verify the predictive ability of the risk score system. Moreover, the correlation of six m6A regulators with immune cell infiltration and potential regulatory mechanisms should be further studied to better understand LUAD progression.

In conclusion, our study explored the expression levels of m6A genes in LUAD samples and screened six optimal regulators to establish a risk score system. Immune cell infiltration in different disease subgroups was also determined, and six m6A regulator signatures were correlated with immune cell proportions, suggesting that the risk score system may be a promising tool for prognosis prediction in patients with LUAD.

Availability of data and materials

The datasets analysed during the current study are available in the TCGA repository (https://gdc-portal.nci.nih.gov/) and GEO database with the accession number of GSE50081 (https://www.ncbi.nlm.nih.gov/geo/query/acc.cgi?acc=GSE50081) and GSE37745 (https://www.ncbi.nlm.nih.gov/geo/query/acc.cgi?acc=GSE37745). Public access to the database is open.

Author contributions

JZ, SB and YY downloaded the data, and performed immune microenvironment analysis. HK, GL and ZF established and validated the prognosis model. WM and XW interpreted the results. JZ, WM and XW wrote the main manuscript text. JR conceived the study and revised the manuscript for important intellectual content. All authors reviewed the manuscript and approved the final version of the manuscript. The authors declare that they have no conflict of interest.

REFERENCES

1. Siegel RL, Miller KD, Fuchs HE, Jemal A. Cancer Statistics 2021. Cancer J Clin 2021; 71:7-33.
2. Planchard D, Besse B, Groen HJM, et al. Dabrafenib plus trametinib in patients with previously treated BRAF(V600E)-mutant metastatic non-small cell lung cancer: an open-label, multicentre phase 2 trial. Lancet Oncol 2016; 17:984-93.
3. Ramalingam SS, Vansteenkiste J, Planchard D, et al. Overall Survival with Osimertinib in Untreated, EGFR-Mutated Advanced NSCLC. N Engl J Med 2020; 382:41-50.
4. Shaw AT, Bauer TM, de Marinis F, et al. First-Line Lorlatinib or Crizotinib in Advanced ALK-Positive Lung Cancer. N Engl J Med 2020; 383:2018-29.
5. Awad MM, Liu S, Rybkin, II, et al. Acquired Resistance to KRAS(G12C) Inhibition in Cancer. N Engl J Med 2021; 384:2382-93.
6. Walsh RJ, Soo RA. Resistance to immune checkpoint inhibitors in non-small cell lung cancer: biomarkers and therapeutic strategies. Ther Adv Med Oncol 2020; 12:1758835920937902.
7. Yang Y, Hsu PJ, Chen YS, Yang YG. Dynamic transcriptomic m(6)A decoration: writers, erasers, readers and functions in RNA metabolism. Cell Res 2018; 28:616-24.
8. Roundtree IA, Evans ME, Pan T, He C. Dynamic RNA Modifications in Gene Expression Regulation. Cell

2017; 169:1187-200.
9. Zhao BS, Roundtree IA, He C. Post-transcriptional gene regulation by mRNA modifications. Nat Rev Mol Cell Biol 2017; 18:31-42.
10. Li Z, Weng H, Su R, et al. FTO Plays an Oncogenic Role in Acute Myeloid Leukemia as a N(6)-Methyladenosine RNA Demethylase. Cancer Cell 2017; 31:127-41.
11. Ding Y, Qi N, Wang K, et al. FTO Facilitates Lung Adenocarcinoma Cell Progression by Activating Cell Migration Through mRNA Demethylation. Onco Targets Ther 2020; 13:1461-70.
12. Zhang Y, Liu S, Zhao T, Dang C. METTL3-mediated m6A modification of Bcl-2 mRNA promotes non-small cell lung cancer progression. Oncol Rep 2021; 46:16.
13. Wang H, Deng Q, Lv Z, et al. N6-methyladenosine induced miR-143-3p promotes the brain metastasis of lung cancer via regulation of VASH1. Mol Cancer 2019; 18(1):181.
14. Gu Y, Wu X, Zhang J, et al. The evolving landscape of N(6)-methyladenosine modification in the tumor microenvironment. Mol Ther 2021; 29:1703-15.
15. Li J, Wang W, Zhou Y, et al. m6A Regulator-Associated Modification Patterns and Immune Infiltration of the Tumor Microenvironment in Hepatocarcinoma. Front Cell Dev Biol 2021; 9:687756.
16. Guo W, Tan F, Huai Q, et al. Comprehensive Analysis of PD-L1 Expression, Immune Infiltrates, and m6A RNA Methylation Regulators in Esophageal Squamous Cell Carcinoma. Front Immun 2021; 12:669750.
17. Dong L, Chen C, Zhang Y, et al. The loss of RNA N(6)-adenosine methyltransferase Mettl14 in tumor-associated macrophages promotes CD8(+) T cell dysfunction and tumor growth. Cancer Cell 2021; 39:945-57.
18. Li N, Kang Y, Wang L, et al. ALKBH5 regulates anti-PD-1 therapy response by modulating lactate and suppressive immune cell accumulation in tumor microenvironment. Proc Natl Acad Sci U S A 2020; 117:20159-70.
19. Der SD, Sykes J, Pintilie M, et al. Validation of a histology-independent prognostic gene signature for early-stage, non-small-cell lung cancer including stage IA patients. J Thorac Oncol 2014; 9:59-64.
20. Botling J, Edlund K, Lohr M, et al. Biomarker discovery in non-small cell lung cancer: integrating gene expression profiling, meta-analysis, and tissue microarray validation. Clin Cancer Res 2013; 19:194-204.
21. Okayama H, Kohno T, Ishii Y, et al. Identification of genes upregulated in ALK-positive and EGFR/KRAS/ALK-negative lung adenocarcinomas. Cancer Res 2012; 72:100-11.
22. Wang L, Cao C, Ma Q, et al. RNA-seq analyses of multiple meristems of soybean: novel and alternative transcripts, evolutionary and functional implications. BMC Plant Biol 2014; 14:1471-2229.
23. Zhang X, Ren L, Yan X, et al. Identification of immune-related lncRNAs in periodontitis reveals regulation network of gene-lncRNA-pathway-immunocyte. Int Immunopharmacol 2020; 84:14.
24. Wang P, Wang Y, Hang B, Zou X, Mao JH. A novel gene expression-based prognostic scoring system to predict survival in gastric cancer. Oncotarget 2016; 7:55343-51.
25. Giraldo NA, Sanchez-Salas R, Peske JD, et al. The clinical role of the TME in solid cancer. Br J Cancer 2019; 120:45-53.
26. Craven KE, Gökmen-Polar Y, Badve SS. CIBERSORT analysis of TCGA and METABRIC identifies subgroups with better outcomes in triple negative breast cancer. Sci Rep 2021; 11:021-83913.
27. Hu D, Zhou M, Zhu X. Deciphering Immune-Associated Genes to Predict Survival in Clear Cell Renal Cell Cancer. Biomed Res Int 2019; 2019:2506843.
28. Subramanian A, Tamayo P, Mootha VK, et al. Gene set enrichment analysis: a knowledge-based approach for interpreting genome-wide expression profiles. Proc Natl Acad Sci U S A 2005; 102:15545-50.
29. Goeman JJ. L1 penalised estimation in the Cox proportional hazards model. Biom J 2010; 52:70-84.
30. Li T, Fan J, Wang B, et al. TIMER: A Web Server for Comprehensive Analysis of Tumor-Infiltrating Immune Cells. Cancer Res 2017; 77:e108-e10.
31. Wang Y, Li M, Zhang L, Chen Y, Zhang S. m6A demethylase FTO induces NELL2 expression by inhibiting E2F1 m6A modification leading to metastasis of non-small cell lung cancer. Mol Ther Oncolytics 2021; 21:367-76.
32. Guo W, Huai Q, Zhang G, et al. Elevated Heterogeneous Nuclear Ribonucleoprotein C Expression Correlates With Poor Prognosis in Patients With Surgically

Resected Lung Adenocarcinoma. Front Oncol 2021; 10:598437.
33. Yang Z, Zhao F, Gu X, et al. Binding of RNA m6A by IGF2BP3 triggers chemoresistance of HCT8 cells via upregulation of ABCB1. Am J Cancer Res 2021; 11:1428-45.
34. Mizutani R, Imamachi N, Suzuki Y, Yoshida H, Tochigi N, Oonishi T, Akimitsu N. Oncofetal protein IGF2BP3 facilitates the activity of proto-oncogene protein eIF4E through the destabilisation of EIF4E-BP2 mRNA. Oncogene 2016; 35:3495-502.
35. Zhao W, Lu D, Liu L, et al. Insulin-like growth factor 2 mRNA binding protein 3 (IGF2BP3) promotes lung tumorigenesis via attenuating p53 stability. Oncotarget 2017; 8:93672-87.
36. Adamson B, Smogorzewska A, Sigoillot FD, King RW, Elledge SJ. A genome-wide homologous recombination screen identifies the RNA-binding protein RBMX as a component of the DNA-damage response. Nat Cell Biol 2012; 14:318-28.
37. Munschauer M, Nguyen CT, Sirokman K, et al. The NORAD lncRNA assembles a topoisomerase complex critical for genome stability. Nature 2018; 561:132-6.
38. Liu N, Zhou KI, Parisien M, Dai Q, Diatchenko L, Pan T. N6-methyladenosine alters RNA structure to regulate binding of a low-complexity protein. Nucleic Acids Res 2017; 45:6051-63.
39. Zhou KI, Shi H, Lyu R, et al. Regulation of Co-transcriptional Pre-mRNA Splicing by m(6)A through the Low-Complexity Protein hnRNPG. Mol Cell 2019; 76:70-81.
40. Song Y, He S, Ma X, et al. RBMX contributes to hepatocellular carcinoma progression and sorafenib resistance by specifically binding and stabilising BLACAT1. Am J Cancer Res 2020; 10:3644-65.
41. Zhang D, Qu L, Zhou B, Wang G, Zhou G. Genomic variations in the counterpart normal controls of lung squamous cell carcinomas. Front Med 2018; 12:280-8.
42. Yan Q, Zeng P, Zhou X, et al. RBMX suppresses tumorigenicity and progression of bladder cancer by interacting with the hnRNP A1 protein to regulate PKM alternative splicing. Oncogene 2021; 40:2635-50.
43. Loyer P, Busson A, Trembley JH, et al. The RNA binding motif protein 15B (RBM15B/OTT3) is a functional competitor of serine-arginine (SR) proteins and antagonises the positive effect of the CDK11p110-cyclin L2α complex on splicing. J Biol Chem 2011; 286:147-59.
44. Shahriyari L, Abdel-Rahman M, Cebulla C. BAP1 expression is prognostic in breast and uveal melanoma but not colon cancer and is highly positively correlated with RBM15B and USP19. PloS One 2019; 14:e0211507-e.
45. Wang L, Hui H, Agrawal K, et al. m(6) A RNA methyltransferases METTL3/14 regulate immune responses to anti-PD-1 therapy. EMBO J 2020; 39:e104514-e.
46. He J, Zhou M, Yin J, et al. METTL3 restrains papillary thyroid cancer progression via m(6)A/c-Rel/IL-8-mediated neutrophil infiltration. Mol Ther 2021; 29:1821-37.

Robot-assisted, laparoscopic and abdominal sacrocolpopexy for high-stage pelvic organ prolapse: a retrospective, multi-centre study

K. Niu[#], Q. Zhai[#], W. Fan, L. Li, W. Yang, M. Ye, Y. Lu[*] and Y. Meng[*]

Department of Gynecology and Obstetrics, Seventh Medical Center, Chinese PLA General Hospital, Beijing, China

Received November 26, 2021 – Accepted March 24, 2022

[#]These authors contributed equally to this work.

OBJECTIVE: To explore the efficacy of robotic-assisted, laparoscopic and abdominal sacrocolpopexy in treating high-stage pelvic organ prolapse.

METHODS: A retrospective multi-centre study was performed. From January 2013 to December 2020, female patients who underwent abdominal sacrocolpopexy (ASC), laparoscopic abdominal sacrocolpopexy (LASC) or robot-assisted abdominal sacrocolpopexy (RASC) in three medical centres of Chinese PLA General Hospital were included. Clinical data were collected, and all patients were followed up for more than 12 months. Anatomic POP-Q were recorded to evaluate the pelvic floor level. In addition, pelvic Floor Distress Inventory-20 (PFDI-20), Pelvic Floor Impact Questionaire-7 (PFIQ-7) and Patient Global Impression of Improvement (PGI-I) were used to evaluate the life quality after surgery.

RESULTS: Sixty-nine cases were enrolled in this study, including 35 undergoing ASC, 10 undergoing LASC and 24 undergoing RASC. Patients in ASC (56.3±7.2) were younger than those in LASC (62.2±8.0) and RASC (64.3±10.4). During surgery, the blood loss in ASC (244.9±216.6 ml) was significantly more than in LASC (126.3 ± 84.6 ml) and RASC (62.9 ± 77.5 ml). And RASC (149.0±43.6 min) had a significant advantage in operating time over ASC (188.9 ± 55.8 ml) and LASC (185.5 ± 44.4 ml). There was no intraoperative complication in three groups. In the POP-Q follow-up, postoperative Aa, Ba, Ap, Bp in all groups were significantly improved than the baseline (P<0.05). The objective and subjective cure rates were all 100%. PGI-I score was satisfying (1-2). Postoperative PFDI-20 and PFIQ-7 decreased dramatically after surgery in three groups (P<0.05). Mesh exposure occurred in 10 cases (5 in ASC, 1 in LASC, 4 in RASC, P>0.05) at 2-12 months and were less than 1cm in 8 cases (2A/T3/S1), 1-2cm in 2 cases (3B/T3/S1). The mesh exposures healed after estrogen local application without readmission for surgery.

CONCLUSION: RASC showed some advantages over LASC and ASC. It can be recommended in sacrocolpopexy with or without hysterectomy.

Due to its low recurrence rate, abdominal sacrocolpopexy (ASC) has been the gold standard for treating vaginal vault prolapse (1). However, compared to transvaginal procedures, it is associated with an increased hospital stay, analgesic requirement, and direct cost (2). The laparoscopic technique

Keywords: robotic-assisted; laparoscopic; sacrocolpopexy; pelvic organ prolapse

Corresponding author:
Dr Yuanguang Meng,
Department of Gynecology and Obstetrics,
Seventh Medical Center, Chinese PLA General Hospital,
5 Nancangmen, Dongsishitiao,
Dongcheng District, Beijing, China
e-mail: niuke304@163.com

0393-974X (2022)

DISCLOSURE: ALL AUTHORS REPORT NO CONFLICTS OF INTEREST RELEVANT TO THIS ARTICLE.

was introduced into sacrocolpopexy to minimize abdominal incision, potentially leading to less postoperative pain and shorter recovery time (3, 4). Unfortunately, the decreased degrees of freedom, two-dimensional vision, and the learning curve has increased operation time and limited its widespread use among surgeons (1). With the robotic surgical system in gynecologic surgery in 2005, researchers began to introduce this technology into POP surgery (5). Robotic technology can provide enhanced visualization wristed instrumentation, enabling surgeons to perform minimally invasive operations (6). So robotic-assisted sacrocolpopexy (RASC) has been regarded as a minimally invasive adaptation of sacrocolpopexy (7, 8). Some researchers reported fewer hospital stays and perioperative complications related to laparoscopic and robotic-assisted techniques (7-9). However, for the efficacy of the three methods, the relevant data remains demanding, especially for Chinese patients. Hence, we aimed to review and compare the outcomes and sequelae of ASC, LASC and RASC in advanced POP.

MATERIALS AND METHODS

From January 2013 to December 2020, patients undergoing ASC, LASC or RASC for symptomatic apical POP in Chinese PLA General Hospital were retrospectively analyzed. Inclusion criteria were symptomatic prolapse stage ≥ III, negative cervical cytology and no abnormal uterine bleeding. The concomitant presence of urinary incontinence was not considered an exclusion criterion. All patients received operation under general anaesthesia with a lithotomy position. Preoperative evaluation and operation were performed by 5 professional gynaecologists with more than 10 years of experience.

The intra-abdominal surgical procedures were the same in the three techniques. The anterior vaginal wall was dissected to the bladder neck, and the posterior was prepared down to the level of the levator ani. In patients with the previous hysterectomy, meshes were sutured to the anterior and posterior vaginal walls and then fixed to the sacral promontory with non-absorbable sutures. In patients with uterus preservation, the anterior mesh was Y-shaped and sutured to a sacral promontory with the posterior mesh.

In LASC, four trocars were placed. A 0-degree scope was placed through the umbilical 12mm trocar. A 10mm and a 5 mm trocar were bilateral to the superior anterior iliac spine. Another 5mm trocar was halfway between the symphysis and the umbilicus.

RASC was performed by gynaecological surgeons with Da Vinci Robotic surgical system (Intuitive Surgical Inc., Sunnyvale, CA, USA). An optical trocar was placed above the umbilicus. Two robotic arms were placed on the left side, and another robotic arm and the assistant's trocar were placed on the right side symmetrically.

The clinical data of the patients were collected, including age, body mass index, menopause, childbearing history, previous pelvic floor surgery history, operation time, intraoperative bleeding, postoperative complication and quality of life. Operation time for ASC was defined as the time from the skin incision to the last skin closure suture. Operation time for LASC and RASC included laparoscopic/robotic instruments placing and operating time. In addition, according to the technique protocol, we recorded all intra- and postoperative complications (bowel and bladder lesions, urinary tract infections, blood loss, fever) and the total postoperative hospital stay.

A pelvic organ prolapse quantification (POP-Q) system with eight points (points Aa, Ba, Ap, Bp, C, Gh, Pb, TVL) was used during the follow-up. The patients were followed up for more than 12 months by gynaecological checkups and postoperative prolapse evaluation in the outpatient department. The objective cure criteria were POP-Q≤I and Point C≤5cm. In addition, the Pelvic Floor Distress Inventory short form (PFDI-20) and Pelvic Floor Impact Questionnaire short form (PFIQ-7) surveys were used to evaluate the preoperative and postoperative life quality outcomes.

The clinical data of patients were collected with Microsoft Excel (Microsoft Corporation, Redmond, WA, USA) and statistically analyzed using SPSS 26.0 software.

RESULTS

Between January 2013 and December 2020, 69 consecutive women with symptomatic, stage III or IV POP were enrolled. Thirty-five patients received ASC, 10 patients underwent LASC, and 24 patients underwent RASC. The baseline demographic and clinical characteristics were presented in Table I. All patients suffered from vaginal protrusion without any

urinary and anorectal symptoms. The mean age of the enrolled patients in ASC was 56.3, significantly younger than that in LASC and RASC groups (P<0.05). There was no significant difference in pregnancy, delivery, baby weight or BMI (P>0.05). Fourteen of the 69 women had the previous hysterectomy for reasons not related to prolapse (Table I).

Perioperative Outcome

The mesh materials used for vaginal vault fixation were all Johnson & Johnson polypropylene mesh (Johnson, USA). Forty patients received hysterectomy during the surgical process. The mean operating time was 149 min for patients undergoing RASC, which was significantly shorter than those undergoing ASC (188 min, P<0.05) and those undergoing LASC (185 min, P<0.05). There was no significant difference between patients undergoing ASC and LASC (P>0.05). As for the bleeding, a significant difference was found among the three groups (P<0.05), indicating the RASC can reduce blood loss significantly. There were no complications in the three groups (Table I).

Postoperative follow-up

All the patients were followed up for more than 12 months (62.3 ± 22.0 months (15-103 months) (Table I). Twelve-month questionnaire and anatomic outcomes were listed in Table II and Table III. The standard of postoperative objective cure was POP-Q Stage I. In the outpatient follow-up, stage I was found

Table I. *Demographic information of enrolled patients*

	ASC (n=35)	LASC (n=10)	RASC (n=24)	P
Demographic data				
Age (Years)	56.3 ± 7.2 #	62.2 ± 8.0	64.3 ± 10.4	P=0.002
Pregnancy	3.5 ± 1.8	3.6 ± 1.3	3.0 ± 1.2	P=0.395
Delivery	1.8 ± 1.0	2.6 ± 1.4	1.9 ± 1.0	P=0.140
Baby weight (Max, Kg)	3.4 ± 0.5	3.9 ± 0.2	3.5 ± 0.4	P=0.057
BMI	23.6 ± 2.8	25.3 ± 3.7	24.3 ± 2.9	P=0.258
Menopause	29	9	21	P=0.803
Hysterectomy	10	2	2	P=0.165
Hypertension	7	1	8	P=0.278
Diabetes Mellitus	5	1	1	P=0.449
Surgery Parameters				
Blood loss	244.9 ± 216.6*#	126.3 ± 84.6#	62.9 ± 77.5	P=0.000
Operating time (min)	188.9 ± 55.8#	185.5 ± 44.4#	149.0 ± 43.6	P=0.012
Intra-operative complication	0	0	0	-
Hysterectomy	23	5	12	P=0.417
Postoperative data				
Postoperative fever	1	0	0	-
Hospital stay	9.1 ± 2.1	8.1 ± 3.0	8.5 ± 2.9	P=0.474
Urinary tract infection	0	0	0	-
Urinary catheter placement	5.7 ± 1.5#	5.3 ± 0.5#	3.0 ± 0.7	P=0.000
Wound infection	0	0	0	-
Follow-up	59.46±20.88	74.40±24.70	61.33±21.80	P=0.163
Mesh erosion	5 (14.3%)	1 (10%)	4 (16.7%)	P=0.085

**P<0.05 vs LASC; #P<0.05 vs RASC*

in all cases and no prolapse recurrence occurred. The objective cure rate for the apical compartment was 100% in all groups. Compared with the baseline, postoperative PFDI-12 and PFIQ-7 decreased dramatically in three groups (P<0.05), indicating that three surgical processes efficiently improved the prolapse symptoms. Also, no significant difference was found in postoperative PGI-I among the three groups (P>0.05).

Statistical improvements of POP-Q points are shown in Table III. There was no statistical difference in the baseline among the three groups. The postoperative Aa/Ba/Ap/Bp were all -3.0, indicating three surgical techniques can fix the uterus efficiently and cure rates for the anterior and posterior compartments were not significantly different among groups (P>0.05). Meanwhile, we found the Cx, Gh and TVL improved more in ASC (P<0.05). There were no cases of prolapse recurrence.

Without urodynamic examination, we performed the urination diary and urine pad test for all hospitalized patients. According to the patient's symptoms and examination results, we had full preoperative communication with the patients before the operation to fully understand the advantages and disadvantages of the operation and the possible impact on their postoperative life. As a result, all patients were willing to accept anti-incontinence surgery in SC.

Table II. *Life quality questionnaire before and after surgery*

Group	n	Time	PFDI-20	PFIQ-7	PGI-I
ASC	35	Preoperation	71.71±26.33	56.50±33.64	
		Postoperation	2.38±3.39	2.01±3.83	1.60±0.65
LASC	10	Preoperation	73.85±27.70	60.50±25.21	
		Postoperation	2.50±3.51	1.40±3.15	1.30±0.48
RASC	24	Preoperation	76.93±25.31	65.17±31.86	
		Postoperation	2.78±3.82	1.57±3.86	1.71±0.69
ASC vs. LASC vs. RASC		Preoperation	F=0.283 P=0.754	F=0.524 P=0.595	
		Postoperation	F=0.089 P=0.915	F=0.154 P=0.858	F=1.417 P=0.250

Table III. *Preoperative and postoperative POP-Q*

	(n=35)	(n=10)	(n=24)		(n=35)	(n=10)	(n=24)	
	Preoperation	Preoperation	Preoperation	P	Postoperation	Postoperation	Postoperation	P
Aa	1.41 ± 2.25	0.90 ± 2.64	0.90 ± 2.43	0.67	-3.00 ± 0.00	-3.00 ± 0.00	-3.00 ± 0.00	1.00
Ba	2.27 ± 2.57	2.00 ± 3.02	1.48 ± 2.54	0.53	-3.00 ± 0.00	-3.00 ± 0.00	-3.00 ± 0.00	1.00
Ap	-0.93 ± 1.86	-0.20 ± 1.99	-1.21 ± 2.08	0.40	-3.00 ± 0.00	-3.00 ± 0.00	-3.00 ± 0.00	1.00
Bp	-0.59 ± 2.22	-0.12 ± 2.11	-0.92 ± 2.39	0.64	-3.00 ± 0.00	-3.00 ± 0.00	-3.00 ± 0.00	1.00
Cx	1.54 ± 2.61	1.70 ± 2.00	1.52 ± 2.54	0.98	-8.09 ± 0.61	-7.30 ± 0.26	-7.40 ± 0.69	0.00
Gh	5.19 ± 1.15	4.75 ± 0.95	4.73 ± 0.44	0.14	3.65 ± 0.49	3.69 ± 0.21	4.06 ± 0.39	0.00
Pb	2.91 ± 0.46	3.05 ± 0.37	2.94 ± 0.37	0.67	3.68 ± 0.37	3.96 ± 0.27	3.68 ± 0.33	0.07
TVL	7.93 ± 0.56	7.85 ± 0.34	7.88 ± 0.45	0.85	8.21 ± 0.60	7.30 ± 0.26	7.67 ± 0.24	0.00

Nine patients received anti-incontinence surgery, 7 in the ASC group and 2 in LSC. For patients who did not show urinary incontinence before the operation, we also informed them and suggested they be followed up regularly. The patients expressed understanding and signed the informed consent.

However, mesh exposure occurred in 5 cases in the ASC group, 1 in the LASC group and 4 in the RASC group, with no significant difference (P>0.05). The exposure diameter was less than 1cm in 7 cases (2A/T3/S1), 1-2cm in 3 cases (3B/T3/S1), (IUGA/ICS Prosthesis/Graft Complication Classification System). Seven patients with less than 1 cm exposure did not show discomfort symptoms. Three patients with more than 1cm had increased vaginal secretions and bloody vaginal secretions, but it did not affect their daily life, nor did they did not feel local pain. The exposure position was located at the vaginal suture, and the exposure time was more than 12 months after the operation. All patients received the expected treatment. According to the guidelines proposed by the American Society of Obstetricians and Gynecologists (ACOG) and the Gynecological Urology Association (AUGS) in 2017 (10), estrogen ointment and metronidazole suppository was used locally in 7 cases (2B/T3/S1), and the exposed mesh was partially excised in 3 cases (3B/T3/S1). All patients healed in 3 months.

As for complications, there were no statistical differences between RASC and LASC (Table II). In addition, there were no intraoperative complications for either surgery. Finally, there was no statistical difference in VAS pain scores and PGI-I scores between RASC and LASC groups (Table II).

DISCUSSION

Chinese PLA General Hospital is one of the first hospitals that began POP surgery in China in 2000. Abdominal sacrocolpopexy has been used as the standard surgery for high-stage pelvic organ prolapse in the Fourth Medical Center. Laparoscopy

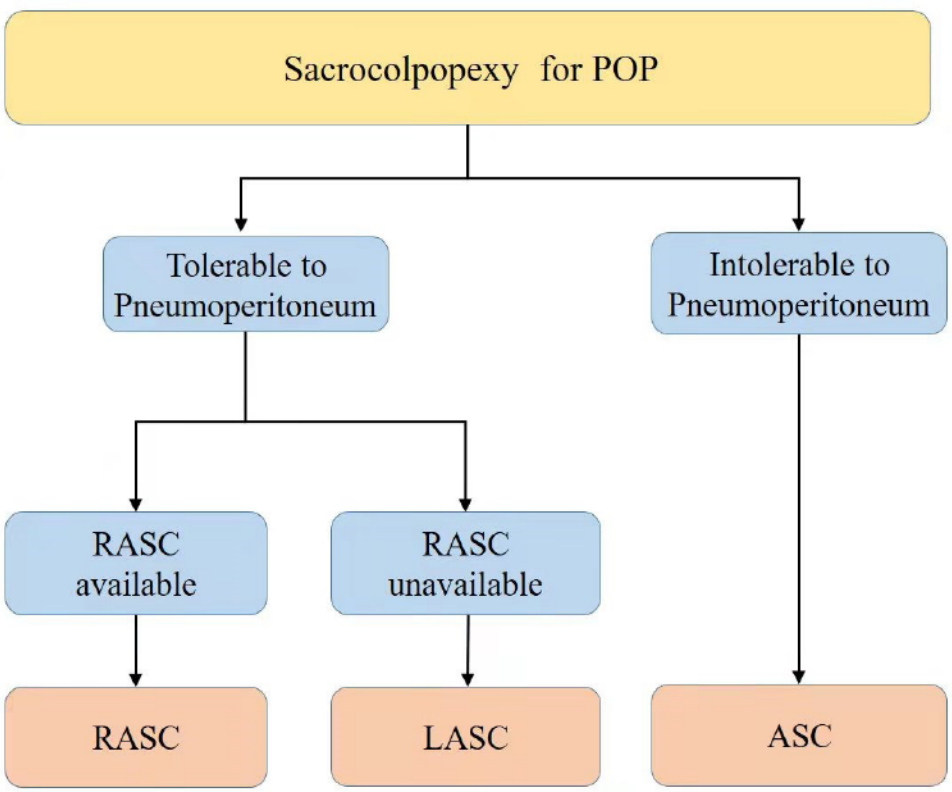

Fig. 1. *Flowchart for Choice of Sacrocolpopexy Surgery.*

sacrocolpopexy was performed in 2007, and robotic-assisted technology was introduced in gynecologic surgery in 2009 in the First Medical Center. The present study compared the outcomes of high-stage pelvic organ prolapse managed with ASC, LASC and RASC. Compared with ASC, LASC showed an advantage in intraoperative blood loss. However, RASC was superior in intraoperative blood loss, operating time and postoperative urinary catheter placement, compared with the other two groups. Significant improvements in postoperative POP-Q score and QOL were found in three groups with an overall objective cure rate of 100%. These results indicated that they were all safe and highly effective in treating advanced apical and anterior prolapse, and RASC has unique advantages over the other two methods.

In recent years, LASC and RASC became widely used in treating sacrocolpopexy due to their minimal invasiveness (11, 12). This trend has continued, with LASC and RASC accounting for the majority in the USA, more than 80% in 2016 (9). Recent studies showed that the minimally invasive approaches surpassed the abdominal approach for decreased hospital stay and wound infection (11-13). Our study confirmed these findings; this was attributed to the fact that ASC may be associated with potential morbidity. The naked-eyed dissection of the sacral promontory may cause vascular complications, particularly in obese women or those with vascular anatomical variations. For cases undergoing ASC in our study, sacral veniplex injury occurred in 2 patients, leading to 1000 ml blood loss.

Meanwhile, the laparoscopic and robotic assistance may provide a magnified view of the anatomy (14). Moreover, robotic assistance can simplify complex procedures such as suturing, knot tying and pre-sacral dissection (15). In addition, it may help the lateral suspension procedure in the dissection of the vesicovaginal space and the fixation of mesh. Though the exposure rate was 14.5% in our series, only 4% received secondary operation. Because our patients with mesh exposure had mild symptoms, it did not affect their daily life. According to the follow-up results in our study, we did not find an obvious relationship between hysterectomy and the occurrence of mesh exposure. The use of mesh and hysterectomy should be determined according to the severity of preoperative prolapse and subjective symptoms. Some researchers compared single anterior mesh only versus anterior and posterior mesh procedures in SC and found the single anterior mesh may reduce the risk of mesh extrusion, which is valuable in the mesh implantation in SC (16).

Although many outcomes favor RASC, the potential risk in LASC and RASC should be noticed. The steep downward Trendelenburg position may decrease lung compliance and cause brain oedema (17). Systemic vascular resistance and mean arterial pressure may increase (17,18). The pneumoperitoneum increases left ventricular filling pressure and decreases cardiac output (19). Subcutaneous emphysema may contribute to CO2 absorption. CO2 insufflation may cause pulmonary complications in the postoperative period (20). Hence, the preoperative evaluation is vital for patients with underlying lung and/or cardiac disease, which may be ineligible for LASC or RASC.

The cost of robotic surgery is an important issue in choosing therapeutic strategies. In 2011, Judd reported the cost of robotic surgery was $8,508, 47% more than commitment ASC ($5,792) and 15.7% more than laparoscopic surgery ($7,353) (21). In China, the average cost of robotic surgery is $8,400, about 8 times of ASC ($1,000) and about 7 times of laparoscopic surgery ($1,200). Meanwhile, robot-assisted surgery has not been covered by social insurance in China. The high cost hindered the wide application in China. Therefore, a cost-efficiency analysis is needed to confirm which patients benefit more from robotic surgery.

In conclusion, the indication to adopt minimally invasive prolapse surgery results from multiple factors. Firstly, if there are complex concomitant procedures, such as giant hysteromyoma / ovariocystectomy / hysterectomy, or there is risk of severe abdominal or pelvic adhesions, LASC or RASC may be ineligible. Secondly, patients who cannot tolerate pneumoperitoneum or the Trendelenburg position for extended periods are not ideal candidates for LASC or RASC (Fig. 1). Thirdly, the skill level of the surgeon is also important. Finally, the operator should be capable of the open procedure conversion from laparoscopic or robotic surgery to ASC.

As a retrospective, observational study, our study has some limitations. First, it contained both women who have undergone previous pelvic surgery and concomitant procedures at sacrocolpopexy, which may result in bias in operation time and bleeding volume. Fortunately, the matched-up demographics among the three groups may decrease the bias. Second, the sample size was small, and the study patients were not randomized. A large-sampled randomized clinical trial may be better in providing insight into a competitive evaluation of the three techniques.

Surgical correction of high-stage pelvic organ prolapses with ASC, LASC or RASC was safe and effective. In comparison, RASC showed priority despite high costs. However, future prospective randomized studies and cost-efficiency evaluations are needed to better determine these approaches' long-term efficacy, morbidity, and patient satisfaction.

Ethics approval and consent to participate

All procedures performed in the studies involving human participants were following the ethical standards of the institutional research committee and with the 1964 Helsinki Declaration and its later amendments or comparable ethical standards.

Consent for publication

Written informed consent for publication of this paper was obtained from the Chinese PLA General Hospital and all authors.

Authors' contributions

KN and QZ carried out the data collection, participated in the statistical analysis and drafted the manuscript. WF, WY and MY participated in the RASC and LASC, and YL dominated the ASC and revision of the manuscript. YM participated in its design and coordination and helped to draft the manuscript. All authors read and approved the final manuscript. The authors declare that they have no conflict of interest.

Availability of data and material

The datasets used and/or analyzed during the current study are available from the corresponding author.

Funding

This research received funding support from the National Key Research and Development Program (2021YFC2009105-1).

REFERENCES

1. Nygaard I, Brubaker L, Zyczynski HM, et al. Long-term outcomes following abdominal sacrocolpopexy for pelvic organ prolapse. JAMA 2013; 309(19):2016-24.
2. Murphy AM, Clark CB, Denisenko AA, D'Amico MJ, Vasavada SP. Surgical management of vaginal prolapse: current surgical concepts. Can J Urol 2021; 28(S2):22-26.
3. Nezhat CH, Nezhat F, Nezhat C. Laparoscopic sacral colpopexy for vaginal vault prolapse. Obstet Gynecol 1994; 84:885–888.
4. Cosson M, Rajabally R, Bogaert E, Querleu D, Crépin G. Laparoscopic sacrocolpopexy, hysterectomy, and Burch colposuspension: Feasibility and short-term complications of 77 procedures. JSLS 2002; 6:115–119.
5. Visco AG, Advincula AP. Robotic gynecologic surgery. Obstet Gynecol 2008; 112(6):1369-1384.
6. Maher C, Feiner B, Baessler K, Christmann-Schmid C, Haya N, Brown J. Surgery for women with apical vaginal prolapse. Cochrane Database Syst Rev 2016;10(10):CD012376.
7. Serati M, Bogani G, Sorice P, et al. Robot-assisted sacrocolpopexy for pelvic organ prolapse: a systematic review and meta-analysis of comparative studies. Eur Urol 2014; 66(2): 303-18.
8. Elliott DS, Frank I, Dimarco DS, Chow GK. Gynecologic use of robotically assisted laparoscopy: Sacrocolpopexy for the treatment of high-grade vaginal vault prolapse. Am J Surg 2004; 188(4A Suppl): 52S-56S.
9. Linder BJ, Occhino JA, Habermann EB, Glasgow AE, Bews KA, Gershman B. A National Contemporary Analysis of Perioperative Outcomes of Open versus Minimally Invasive Sacrocolpopexy. J Urol 2018; 200(4):862-867.
10. Committee on Practice Bulletins-Gynecology, American Urogynecologic Society. Practice Bulletin No. 185: Pelvic Organ Prolapse. Obstet Gynecol 2017; 130(5):e234-e250.

11. Salamon CG, Culligan PJ. Subjective and objective outcomes 1 year after robotic-assisted laparoscopic sacrocolpopexy. J Robot Surg 2013; 7(1):35-8.
12. Serati M, Bogani G, Sorice P, et al. Robot-assisted sacrocolpopexy for pelvic organ prolapse: a systematic review and meta-analysis of comparative studies. Eur Urol 2014; 66(2): 303-18.
13. Giannini A, Russo E, Malacarne E, Cecchi E, Mannella P, Simoncini T. Role of robotic surgery on pelvic floor reconstruction. Minerva Ginecol 2019; 71(1):4-17.
14. Illiano E, Giannitsas K, Zucchi A, Di Biase M, Del Zingaro M, Bini V, Costantini E. Sacrocolpopexy for posthysterectomy vaginal vault prolapse: long-term follow-up. Int Urogynecol J 2016; 27(10):1563-9.
15. Di Marco DS, Chow GK, Gettman MT, Elliott DS. Robotic-assisted laparoscopic sacrocolpopexy for treatment of vaginal vault prolapse. Urology 2004; 63(2):373-6.
16. d'Altilia N, Mancini V, Falagario U, et al. Are Two Meshes Better than One in Sacrocolpopexy for Pelvic Organ Prolapse? Comparison of Single Anterior versus Anterior and Posterior Vaginal Mesh Procedures. Urol Int 2021; 26:1-9.
17. Li J, Ma S, Chang X, Ju S, Zhang M, Yu D, Rong J. Effect of pressure-controlled ventilation-volume guaranteed mode combined with individualized positive end-expiratory pressure on respiratory mechanics, oxygenation and lung injury in patients undergoing laparoscopic surgery in Trendelenburg position. J Clin Monit Comput 2021.
18. Jin D, Yu H, Li H, et al. Hemodynamic changes of anesthesia, pneumoperitoneum, and head-down tilt during laparoscopic surgery in elderly patients. Ann Transl Med 2021; 9(14):1177.
19. Kim NY, Kim KJ, Kim TL, et al. Prediction of hypotension after postural change in robot-assisted laparoscopic prostatectomy using esophageal Doppler monitoring: a prospective observational trial. Sci Rep 2021; 11(1):14589.
20. Geller EJ, Parnell BA, Dunivan GC. Robotic vs abdominal sacrocolpopexy: 44-month pelvic floor outcomes. Urology 2012; 79(3):532-6.
21. Hoyte L, Rabbanifard R, Mezzich J, Bassaly R, Downes K. Cost analysis of open versus robotic-assisted sacrocolpopexy. Female Pelvic Med Reconstr Surg 2012; 18(6):335-9.

Role and mechanism of CD36/FAK/mTORC1 pathway in LPS-induced inflammatory cytokine expression in human mammary epithelial cells

Q. Fu[1#], D. Zhang[2#], Y. Zhang[2], X. Ren[2], C. Sun[2], X. Sun[2], Z. Yin[2], P. Zhao[2*] and L. Bao[2*]

[1]*Research Laboratory, Affiliated Hospital of Inner Mongolia Medical University, Hohhot, P.R. China;*
[2]*School of Basic Medicine, Inner Mongolia Medical University, Hohhot, P.R. China*

Received November 19, 2021 – Accepted April 1, 2022

[#]These Authors contributed equally

OBJECTIVE: To investigate the role and mechanism of the CD36/FAK/mTORC1 pathway in expressing inflammatory cytokines induced by lipopolysaccharide (LPS) in human mammary epithelial cells (MCF-10A).

METHODS: Cells were infected with *Escherichia coli* using LPS, and the expression of CD36, activation of the FAK/mTORC1 pathway and secretion of inflammatory cytokines were measured. The cell membrane receptors CD36 and TLR4 were subsequently blocked with anti-CD36 and anti-TLR4, and the activation of the CD36/mTORC1 pathway was assessed. The expression of inflammatory cytokines and the activation of the FAK/mTORC1 pathway in LPS-treated cells were evaluated after FAK signal inhibition using TAE226, a specific chemical inhibitor of FAK. The expression of inflammatory cytokines and the activation of the mTORC1 pathway in cells treated with or without LPS were also evaluated after mTORC1 signal inhibition using RNAi.

RESULTS: Western blot revealed that CD36 expression was significantly elevated at the mRNA and protein levels after treatment with LPS ($p<0.05$), and the activation of the FAK/mTORC1 pathway and related transcription factors was notably increased ($p<0.05$). ELISA showed an increase in the number of inflammatory cytokines TNF-α and IL-6 ($p<0.05$). The levels of phosphorylated FAK, S6 and 4EBP1 in LPS-stimulated cells were significantly attenuated ($p<0.05$) when CD36 was blocked compared to the levels in the control group. Further, the levels of phosphorylated FAK, S6, 4EBP1 and STAT1 decreased significantly when CD36 and TLR4 were blocked compared to the levels in the control group. TAE226 remarkably inhibited the activation of the FAK/mTORC1 pathway and the expression of inflammatory cytokines induced by LPS stimulation ($p<0.05$). The RNAi method was used to alter the expression of the key component of mTORC1, Raptor. The results were consistent with previous findings in Rapamycin-treated cells, in which the mTORC1 pathway was weakened, and the levels of TNF-α and IL-6 decreased.

CONCLUSION: CD36 is a co-receptor for LPS and binds to mTORC1 and FAK to form the CD36/FAK/mTORC1 pathway.

Mastitis is a highly prevalent and infectious disease primarily caused by bacteria (1, 2). As one of the most common bacteria responsible for mastitis, Gram-negative bacteria infection often leads to the development of clinical mastitis (1, 3). Lipopolysaccharide (LPS) is the main element in Gram-negative bacteria and can stimulate inflammatory cytokines, such as TNF-α and IL-6.

Keywords: CD36; FAK; mTORC1; lipopolysaccharide; inflammatory response

**Corresponding author:*
Dr. Pengwei Zhao and Dr. Lili Bao
School of Basic Medicine,
Inner Mongolia Medical University,
010110 Hohhot, P.R. China
e-mail[PZ]: pengwzhao@126.com
e-mail[LB]: 87151139@qq.com

0393-974X (2022)

Therefore, the LPS-induced mastitis model is widely used (2, 4, 5).

CD36 is a type B scavenger receptor that uses the extracellular ring portion of its transmembrane structure to recognise and bind specific ligands, triggering the inflammatory response and playing an anti-infection role (6, 7). CD36 interacts with toll-like receptors; binds with oxidised low-density lipoprotein, long-chain fatty acids and other ligands; activates downstream MyD88 and TRIF, and promotes the secretion and expression of inflammatory factors (8-10). CD36 mediates the interactions of the inflammatory signal pathway with bacterial chaperone 60 and LPS to induce an inflammatory response. It also plays an important role in the innate immune response and host defence (11). CD36 can bind to the Fyn inhibitor focal adhesion kinase (FAK), reducing the activity of the mammalian target of rapamycin complex 2 (mTORC2) (12, 13). Nuclear factor kappa-B (NFkB) is a pro-inflammatory gene that regulates the process of inflammation, cytokine generation, and cell survival.

mTORC1 can activate the phosphorylation of downstream eukaryotic initiation factor 4E binding protein 1 (4EBP1) and S6 kinase 1 (S6K1) and promote protein synthesis (14). FAK can associate with the downstream mTORC1 through at least three pathways to form the FAK/mTORC1 signalling pathway. mTOR regulates cell growth by interacting with Raptor, GβL, and PRAS40 to form mTORC1 (15). In addition, raptors can promote mTORC1 activation (16). The mTOR pathway is related to various inflammatory diseases such as malignant tumors, ulcerative colitis and myocarditis (14, 17). Therefore, we constructed a mastitis model *in vitro* using LPS to explore the mechanism underlying the role of CD36/ FAK/mTORC1 in mastitis.

MATERIALS AND METHODS

Cell culture

Human mammary epithelial cells (MCF-10A) were cultured under standard conditions (10% bovine serum(gibico),37°C, 5% CO_2), humidified air. And LPS (1 μg/mL) was used to effect the MCF-10A cells.

Delivery of the associated vectors

Gene-manipulating vectors, specifically pRNAT-Raptor-shRNA (siRaptor) vector, CD36-shRNA and TLR4-shRNA, were designed following Gene coding region sequence. And the scrambled sequence was used as the control group. The vectors were delivered into MCF-10A cells using the Lipofectamine 2000 reagent (Invitrogen, USA) following the manufacturer's protocol. The cells were used for further investigation at 48 h post-transfection when the vectors were successfully delivered into the cells.

Real-time quantitative polymerase chain reaction (RT-qPCR) analysis

The total RNA was extracted from MCF-10A cells using the commercial TRIzol reagent (Invitrogen, USA) following the manufacturer's instructions. The quality of the total RNA was determined by agarose electrophoresis, and the RNA was reverse transcribed into complementary DNA (cDNA) using the TIANScript RT kit (Tiangen Biotech, China). Afterwards, the SYBR Premix Ex Taq™ II Kit (Takara, Japan) was used to determine the relative gene expression and enrichment levels. The *Raptor* forward primer was 5¢-TGTGAGCGTCAATGGAGAT-3¢, and the reverse primer was 5¢-CATGAAGCCGTCGTAGTAC-3¢. The CD36 forward primer was 5'-TCGCTGGGGCTGTCATT G-3', and the reverse primer was 5'-GTTGCTGCTGTTCATCATC ACT-3'. The β-actin forward primer was 5'-TCACCAACT GGGACGACAT-3', and the reverse primer was 5'-GCACAGCCTGGATAGCAAC-3'.

Western blot analysis

Radio immunoprecipitation assay (RIPA) lysis buffer (Beyotime, Shanghai, China) was purchased to lyse the cells to extract the total protein, which was subsequently separated according to the molecular weight of the corresponding proteins using sodium dodecyl-sulfate polyacrylamide gel electrophoresis (SDS-PAGE). Afterwards, the target proteins were transferred to polyvinylidene fluoride (PVDF) membranes obtained from Millipore (USA), and the membranes were blocked with 5% non-fat milk for 40 min at room temperature. The primary antibodies (p-FAK 1:500 Santa Cruz Biotechnology, FAK 1:500 Santa Cruz Biotechnology, p-mTOR 1:2000 Abcam, mTOR 1:1000 Abcam, p-S6 1:5000 Cell Signal Technology, S6 1:2000 Cell Signal Technology, p-4EBP1 1:2000 Cell Signal Technology, 4EBP1 1:2000 Cell Signal Technology, TLR4 1:2000 Cell Signal Technology, Raptor 1:2000 Cell Signal Technology, p-STAT1 1:2000 Cell Signal

Technology, STAT1 1:2000 Cell Signal Technology, p-NF-κB-P65 1:1000 Cell Signal Technology, NF-κB-P65 1:1000 Cell Signal Technology, β-actin 1:5000 Cell Signal Technology) were incubated with the PVDF membranes at 4ºC overnight, then incubated with the secondary antibodies (1:3000, Cell Signaling Technology, USA) for 2 h. Finally, enhanced chemiluminescence (ECL) (Bio-Rad, USA) was used to visualise the protein bands, which were analysed using Image J software to obtain the grey values. The relative expression levels of the proteins were normalised based on the internal reference glyceraldehyde 3-phosphate dehydrogenase (β-actin).

Enzyme-linked immunosorbent assay (ELISA)

IL-6 and TNF-α levels were measured with ELISA (R&D Systems, USA) according to the manufacturer's instructions. Experiments were performed in triplicate.

Statistical analysis

The comparison between groups was performed using GraphPad Prism version 5 software (GraphPad Software, La Jolla, CA, USA). One-way analysis of variance (ANOVA) with Newman–Keuls post-hoc test was used to determine differences in the gene expression levels. Replicates were included in the statistical model. A 95% confidence level ($P < 0.05$) was deemed statistically significant. Data are shown as mean ± SD.

RESULTS

LPS promote the phosphorylation of NF-κB p65 and STAT1 in MCF-10A cells

In order to explore the optimum duration for the LPS (1 μg/mL) effect on NF-κB p65 and STAT1 in MCF-10A cells, p-STAT1, STAT1, p-NF-κB p65 and NF-κB p65 were detected by western blot. The results showed that the phosphorylation of STAT1 and NF-κB p65 gradually increased over 3 h, 6 h and 12 h. However, no significant differences were observed in the phosphorylation of STAT1 and NF-κB p65

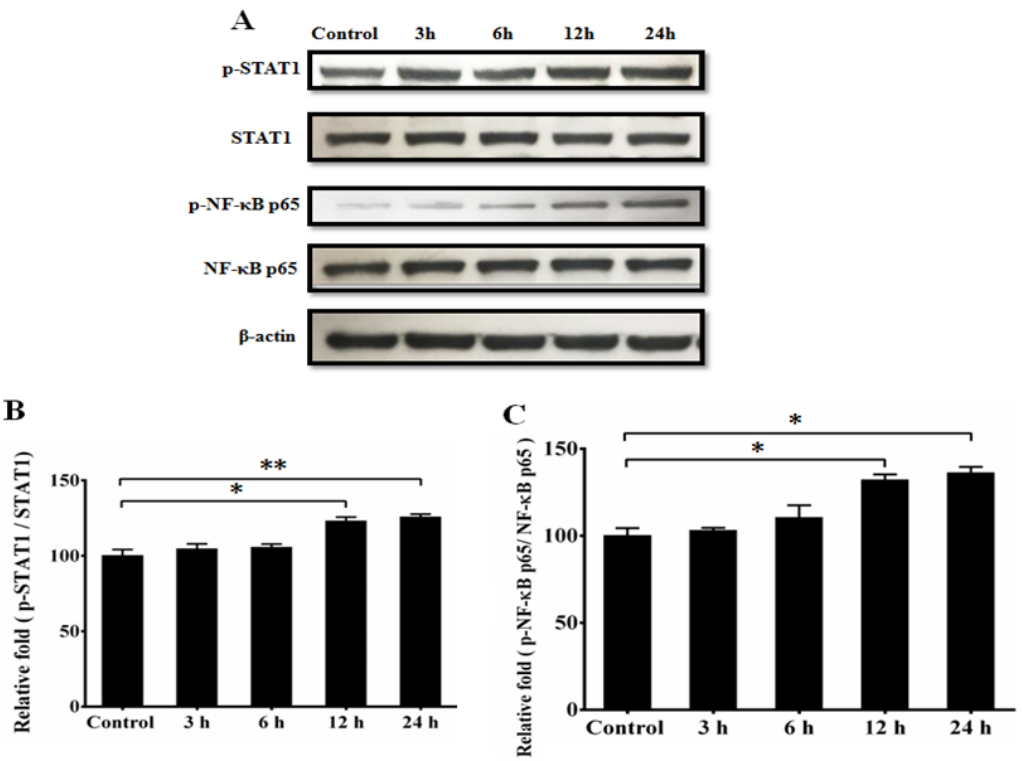

Fig. 1. *Effect of LPS treatment on NF-κB p65 and STAT1. A. Western blot analysis was conducted to examine the protein levels of NF-κB p65, p-NF-κB p65, STAT1 and p-STAT1 in MCF-10A cells. B-C. Relative expression of p-STAT1/STAT1 and p-NF-κB p65/NF-κB p65. Each experiment was performed in triplicate. * $P < 0.05$ and ** $P < 0.01$ were regarded as statistical significance.*

between 12 h and 24 h (Fig. 1A, B, C). hence, LPS could promote phosphorylation STAT1 and NF-κB p65 in MCF-10A cells.

LPS promote the expression of inflammatory factors and the activity of the FAK/mTORC1 pathway in MCF-10A cells

To detect the influence of LPS on the expression of inflammatory factors and the activity of the FAK/mTORC1 pathway in MCF-10A cells, the expression levels of inflammatory factors TNF-α and IL-6 were detected and the phosphorylation levels of FAK, mTOR, S6, 4EBP1, STAT1 and NF-κB p65 were showed. The expression levels of inflammatory factors TNF-α and IL-6 were higher in the LPS-treated cells than in the control group (Fig. 2A and B). In the LPS treated MCF-10A cells, the expression of CD36 at the mRNA and protein levels was higher than that in the control group (Fig. 2C-E). To explore the effects of LPS treatment on the FAK/mTORC1 signalling pathway and the activity of NF-κB p65 and STAT1. The results showed that in the LPS treatment group, the phosphorylation levels of FAK, mTOR, S6, 4EBP1, STAT1 and NF-κB p65 were higher than those in the control group (Fig. 2F-L). The expression levels of TNF-α and IL-6 and the phosphorylation levels of FAK, mTOR, S6, 4EBP1, STAT1 and NF-κB p65 were promoted by LPS.

CD36 and TLR4 regulate the effects on the expression of inflammatory factors and the activity of the FAK/mTORC1 pathway in MCF-10A cells induced by LPS

To explore the function of CD36 and TLR4, both inflammatory factors were blocked (Fig. 3A-C). After the MCF-10A cells were treated with LPS, the expression of CD36 and TLR4 was very low. The

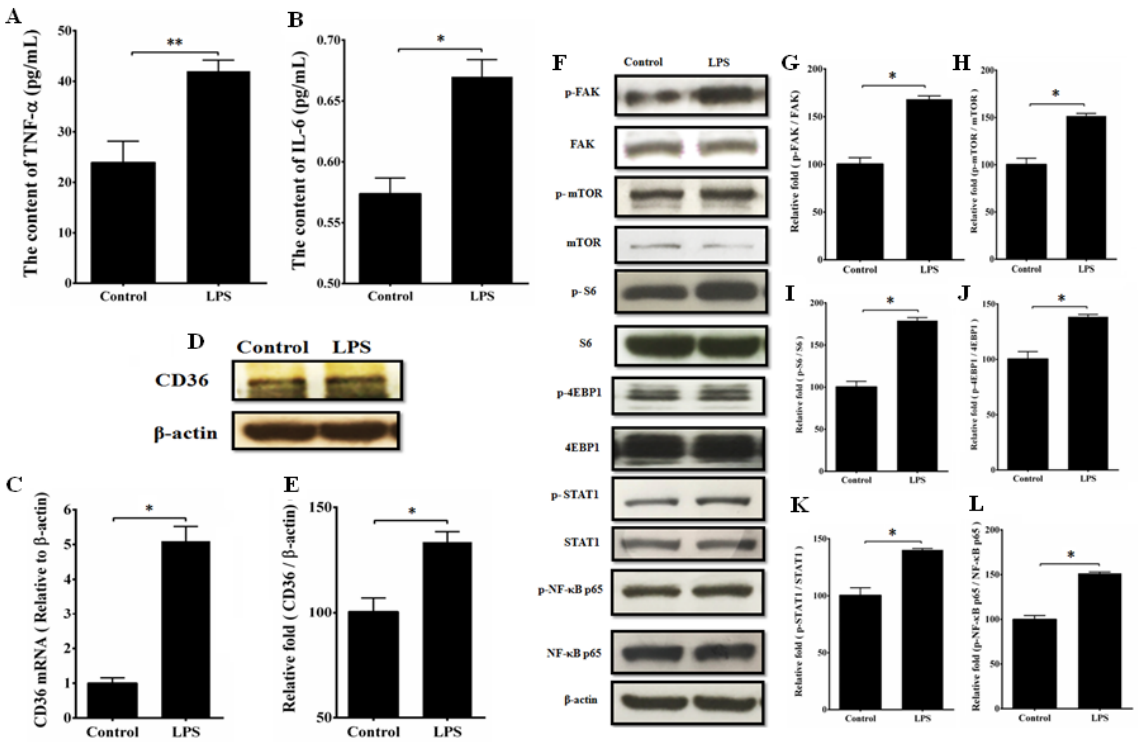

Fig. 2. *LPS induces the expression of inflammatory factors and the activity of the FAK/mTORC1 pathway in MCF-10A cells. A-B. The levels of TNF-α and IL-6 after LPS treatment in MCF-10A cells were detected using ELISA. C. The expression of CD36 at the mRNA level was assessed with RT-qPCR. D-E. Western blot analysis was conducted to examine the protein levels of CD36 in MCF-10A cells. F. Western blot analysis was conducted to examine the protein levels of the constituents of the FAK/mTORC1 pathway in MCF-10A cells. G-L. Relative expression of p-FAK/FAK, p-mTOR/mTOR, p-S6/S6, p-4EBP1/4EBP1, p-STAT1/STAT1 and p-NF-κB p65/NF-κB p65. Each experiment was performed in triplicate. * $P < 0.05$ and ** $P < 0.01$ were regarded as statistical significance.*

phosphorylation of FAK, mTOR, S6, 4EBP1, STAT1 and NF-κB p65 in CD36 and TLR4 blocked with LPS treatment was lower than with only LPS added (Fig. 3D-J). CD36 and TLR4 regulate the function of LPS, promoting the phosphorylation of FAK, mTOR, S6, 4EBP1, STAT1 and NF-κB p65.

The expression of inflammatory factors and the activity of FAK/mTORC1 pathway down-regulated induced by LPS in MCF-10A cells after FAK inhibition by TAE226

TAE226 was added to show the effects of FAK on the expression of inflammatory factors and the activity of the FAK/mTORC1 pathway induced by LPS in MCF-10A cells. Following FAK inhibition by TAE226, the expression of the inflammatory factors TNF-α and IL-6 in the group treated with LPS was lower than that in the control group and the group treated with only LPS without TAE226 (Fig. 4A-B). The phosphorylation of STAT1 and the expression of NF-κB p65 FAK, mTOR, s6 and 4EBP1 were lowest in the group treated with TAE226 (Fig. 4C-J). FAK could regulate the expression of TNF-α, IL-6 and the phosphorylation of STAT1 and the expression of NF-κB p65 FAK, mTOR, s6 and 4EBP1 induced by LPS.

The inhibited function on the expression of inflammatory factors and the activity of the FAK/mTORC1 pathway induced by LPS in MCF-10A cells after Raptor gene silencing by shRNA

The shRNA plasmid pRNAT-Raptor-shRNA was

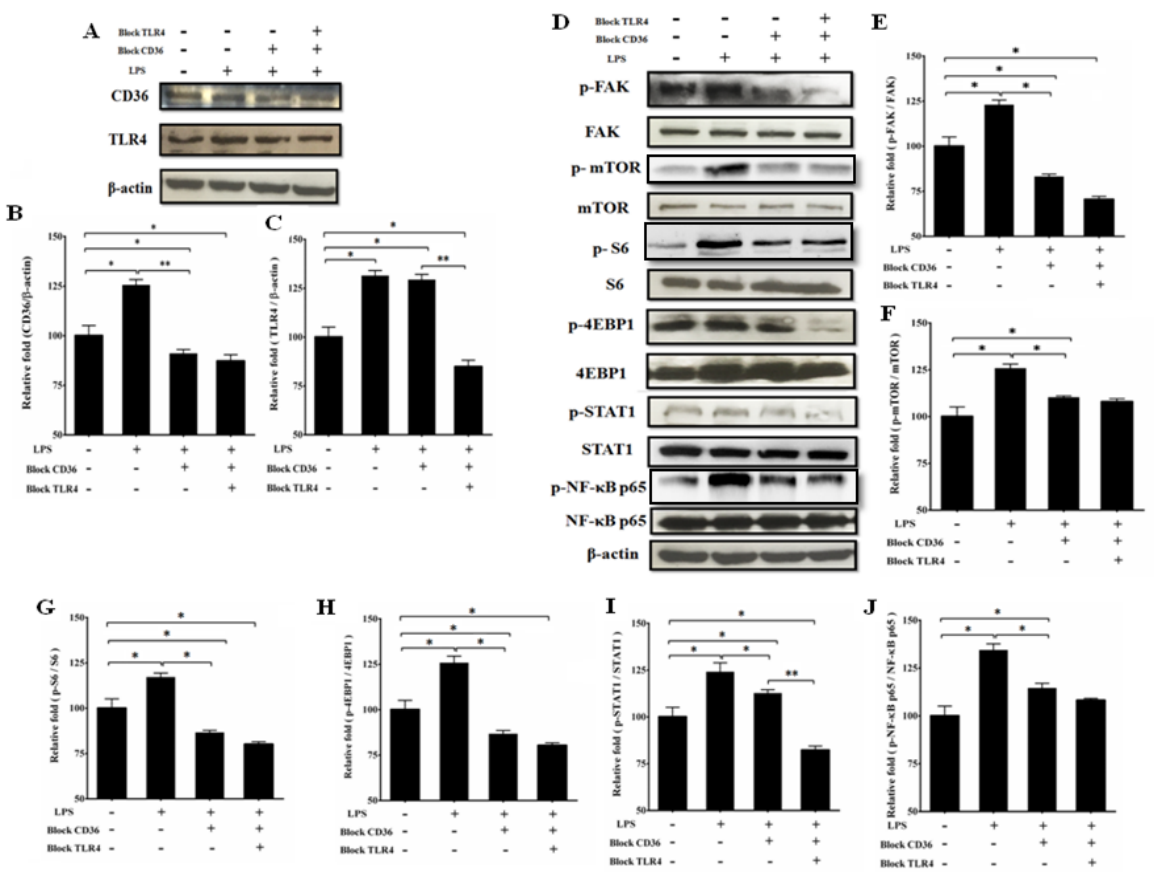

Fig. 3. *The expression of inflammatory factors and the activity of the FAK/mTORC1 pathway in MCF-10A was reduced by LPS treatment after blocking the membrane receptors CD36 and TLR4.* ***A)*** *Western blot analysis was conducted to examine the protein levels of CD36 and TLR4 in MCF-10A cells.* ***B-C)*** *Relative expression of CD36/β-actin and TLR4/β-actin.* ***D)*** *Western blot analysis was conducted to examine the protein levels of the constituents of the FAK/mTORC1 pathway in MCF-10A cells.* ***E-J)*** *Relative expression of p-FAK/FAK, p-mTOR/mTOR, p-S6/S6, p-4EBP1/4EBP1, p-STAT1/STAT1 and p-NF-κB p65/NF-κB p65. Each experiment was performed in triplicate. * $P < 0.05$ and ** $P < 0.01$ were regarded as statistical significance.*

constructed and successfully transfected into MCF-10A cells to inhibit the Raptor gene. The Raptor mRNA and protein levels decreased after transfection (Fig. 5A-D). The expression of TNF-α and IL-6 in pRNAT-Raptor-shRNA MCF-10A cells treated with LPS was lower than that in cells treated with LPS without pRNAT-Raptor-shRNA transfection (Fig. 5E-F). The phosphorylation levels of STAT1, NF-κB p65, FAK, mTOR, s6 and 4EBP1 were also lower than those in LPS-treated cells without pRNAT-Raptor-shRNA transfection (Fig. 5G-M). When the *Raptor* gene was silenced, the expression of TNF-α, IL-6 and the phosphorylation levels of STAT1, NF-κB p65, FAK, mTOR, s6, 4EBP1 were low.

DISCUSSION

Mastitis is a major disease in humans and other animals and is characterised by mammary gland inflammation (18, 19). LPS, as the main pathogenic factor of *Escherichia coli*, is often used to establish mastitis models (20, 21). The TLR4 receptor primarily mediates the effect of LPS. TLR4 activation leads to the activation of downstream NF-κB p65,

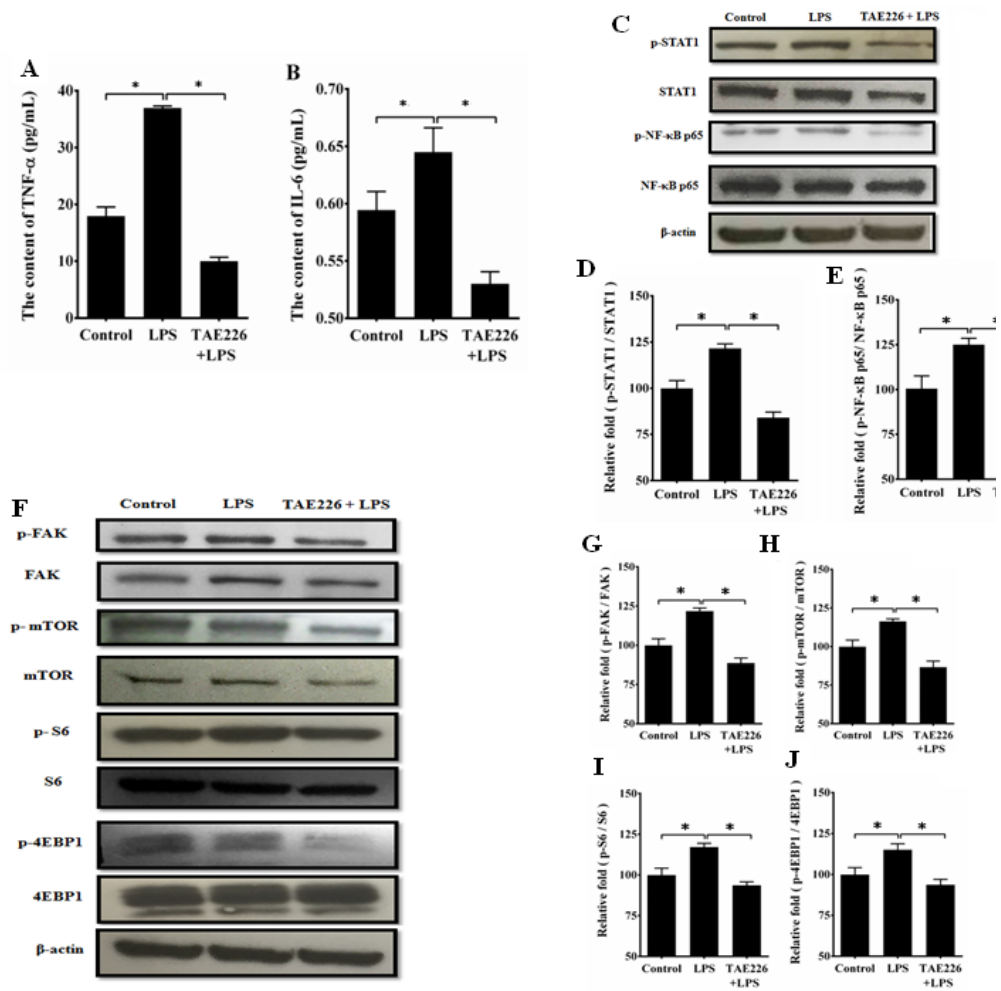

Fig. 4. *Effect of the expression of inflammatory factors and the activity of the FAK/mTORC1 pathway induced by LPS in MCF-10A cells after FAK inhibition by TAE226. A-B. The levels of TNF-α and IL-6 after LPS treatment in MCF-10A cells were detected with ELISA. C. Western blot analysis was conducted to examine the protein levels of NF-κB p65, p-NF-κB p65, STAT1 and p-STAT1 in MCF-10A cells. D-E. Relative expression of p-STAT1/STAT1 and p-NF-κB p65/NF-κB p65. F. Western blot analysis was conducted to examine the protein levels of FAK, mTOR and downstream effector proteins in MCF-10A cells. G-J. Relative expression of p-FAK/FAK, p-mTOR/mTOR, p-S6/S6 and p-4EBP1/4EBP1. Each experiment was performed in triplicate. * $P < 0.05$ was regarded as statistical significance.*

which eventually induces macrophages to produce proinflammatory cytokines, such as TNF-α, IL-1β and IL-6. In this study, LPS promoted the expression of TNF-α and IL-6 in MCF-10A cells (22-24). LPS could activate the inflammatory function in the MCF10A cells.

LPS can promote CD36 and TLR4 expression (11). After blocking CD36 and TLR4, the phosphorylation of FAK, mTOR, S6, 4EBP1, STAT1 and NF-κB p65 decreased. The results indicated that LPS regulated the phosphorylation of FAK, mTOR, S6, 4EBP1, STAT1 and NF-κB p65 via CD36 and TLR4 in MCF-10A cells. FAK plays a key role in focal adhesion dynamics and signals transduction. We found that when FAK was inhibited, the expression of TNF-α and IL-6 was downregulated. In addition, the phosphorylation of FAK, mTOR, S6, 4EBP1, STAT1 and NF-κB p65 was also downregulated.

Raptor, the key element in mTORC1, is the protein regulated upstream (15, 25). Hence, the *Raptor* gene was silenced using shRNA. As a result, the expression of TNF-α and IL-6 was lower in the group treated with LPS than in the group treated with LPS without pRNAT-Raptor-shRNA transfection. In addition, the phosphorylation of STAT1, NF-κB p65, FAK, mTOR, S6 and 4EBP1 was also lower than that in the group

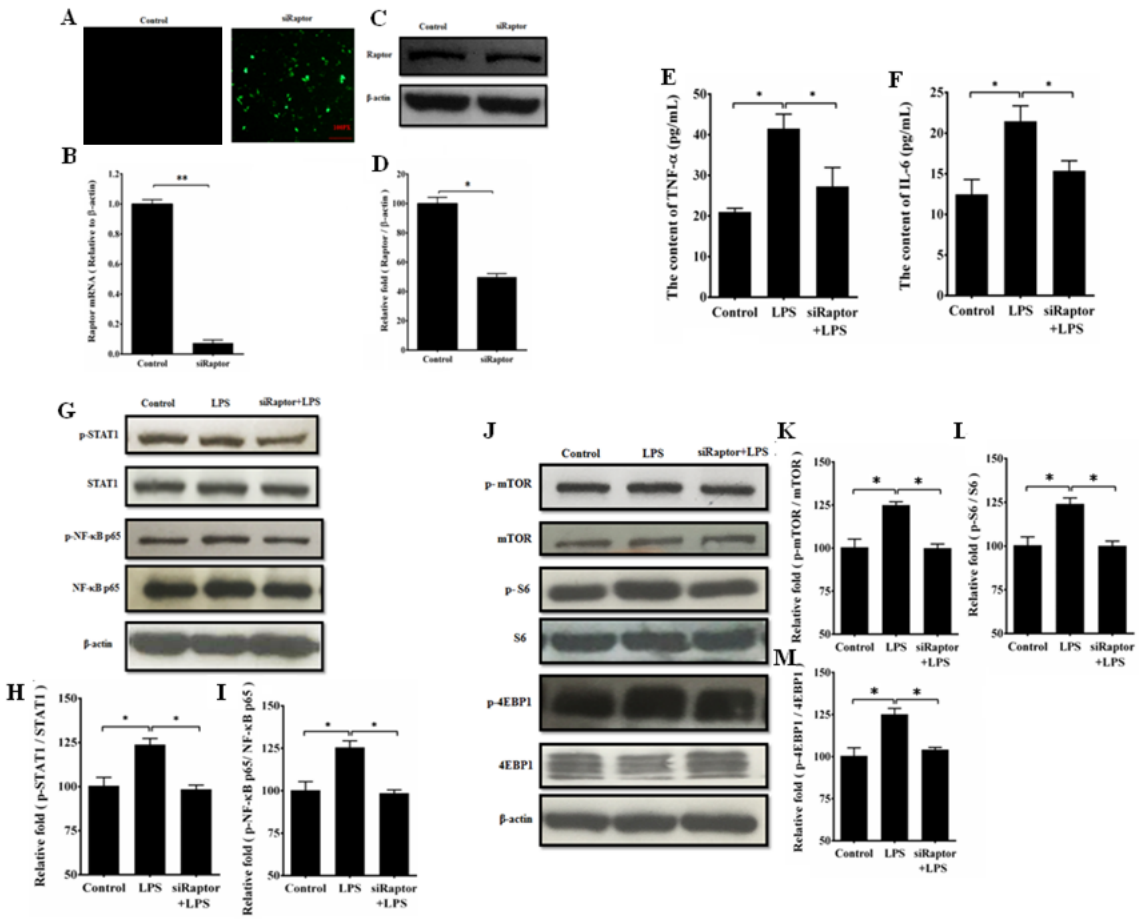

Fig. 5. *Effect of the expression of inflammatory factors and the activity of the FAK/mTORC1 pathway induced by LPS in MCF-10A cells after silencing the Raptor gene with shRNA. A. Fluorescence in MCF-10A cells after shRNA transfection. B. The expression of Raptor was assessed with RT-qPCR after shRNA transfection. C. Western blot analysis was conducted to examine the protein levels of Raptor after shRNA transfection. D. Relative expression of Raptor/β-actin. E-F. The levels of TNF-α and IL-6 after LPS treatment in MCF-10A cells were detected using ELISA. G. Western blot analysis was conducted to examine the protein levels of NF-κB p65, p-NF-κB p65, STAT1 and p-STAT1 in MCF-10A cells. H-I. Relative expression of p-STAT1/STAT1 and p-NF-κB p65/NF-κB p65. J. Western blot analysis was conducted to examine the protein levels of mTOR and downstream effector proteins in MCF-10A cells. K-M. Relative expression of p-mTOR/mTOR, p-S6/S6 and p-4EBP1/4EBP1. Each experiment was performed in triplicate. * $P < 0.05$ was regarded as statistical significance.*

treated with LPS without pRNAT-Raptor-shRNA transfection. These results indicated that FAK and mTORC1 play key roles in the promotion of TNF-α and IL-6 expression by LPS in MCF-10A cells.

In conclusion, as a co-receptor for LPS, CD36 mediates LPS signalling by regulating the activities of the inflammation-related transcription factors STAT1 and NF-κB p65, which induce the expression of inflammatory factors in MCF-10A cells. Furthermore, CD36-mediated LPS signalling can promote FAK expression, and LPS-induced FAK is involved in the mTORC1 pathway. Therefore, we propose that CD36 and FAK/mTORC1 combine to form a CD36/FAK/mTORC1 signalling pathway that regulates the activity of the transcription factors STAT1 and NF-κB p65, inducing an inflammatory response. However, this study did the cell test, and the animal test was not done. Therefore, the *in vitro* test needs to be carried out to further certify the conclusion.

ACKNOWLEDGEMENT

This work was supported by 1) the Natural Science Foundation of Inner Mongolia Autonomous Region (2019ms08113); 2) the Science and technology research project fund for colleges and universities of Inner Mongolia Autonomous Region (njzz20128); 3) the Project fund of Mongolian medicine collaborative innovation cultivation centre of Inner Mongolia Autonomous Region (myyxt201908); 4) the "Zhiyuan" talent plan project of Inner Mongolia Medical University (zy0201020); and 5) the "Big innovation plan" project of Inner Mongolia Medical University (202110132004).

Data availability statement

All data generated or analysed during this study are included in this published article.

REFERE CES

1. Wang X, Feng S, Ding N, et al. Anti-Inflammatory Effects of Berberine Hydrochloride in an LPS-Induced Murine Model of Mastitis. Evid Based Complement Alternat Med 2018; 2018:5164314.
2. Wang Y, He X, Hao D, et al. Low-level laser therapy attenuates LPS-induced rats mastitis by inhibiting polymorphonuclear neutrophil adhesion. J Vet Med Sci 2014; 76(11):1443-50.
3. Yu P, Shen L, Tang J, He S. Perioperative nursing study of the operating room for autologous stem cells in the treatment of necrosis of the femoral head. J Pak Med Assoc 2020; 70(9):145-8.
4. Chen X, Zheng X, Zhang M, et al. Nuciferine alleviates LPS-induced mastitis in mice via suppressing the TLR4-NF-kappaB signaling pathway. Inflamm Res 2018; 67(11-12):903-11.
5. Tong C, Chen T, Chen Z, et al. Forsythiaside a plays an anti-inflammatory role in LPS-induced mastitis in a mouse model by modulating the MAPK and NF-kappaB signaling pathways. Res Vet Sci 2021; 136:390-5.
6. Hrdinova T, Toman O, Dresler J, et al. Exosomes released by imatinibresistant K562 cells contain specific membrane markers, IFITM3, CD146 and CD36 and increase the survival of imatinibsensitive cells in the presence of imatinib. Int J Oncol 2021; 58(2):238-50.
7. Bai S, Wang W, Wang T, et al. CD36 deficiency affects depressive-like behaviors possibly by modifying gut microbiota and the inflammasome pathway in mice. Transl Psychiatry 2021; 11(1):16.
8. Bleriot C, Barreby E, Dunsmore G, et al. A subset of Kupffer cells regulates metabolism through the expression of CD36. Immunity 2021; 54(9):2101-16.
9. Trites MJ, Febbraio M, Clugston RD. Absence of CD36 alters systemic vitamin A homeostasis.
10. Sci Rep 2020; 10(1):20386.
11. Shu H, Peng Y, Hang W, et al. The role of CD36 in cardiovascular disease. Cardiovasc Res 2022; 118(1):115-129.
12. Hashemi-Monfared A, Firouzi M, Bahrami Z, et al. Minocycline decreases CD36 and increases CD44 in LPS-induced microglia. J Neuroimmunol 2018; 317:95-99.
13. Dobri AM, Dudau M, Enciu AM, Hinescu ME. CD36 in Alzheimer's Disease: An Overview of Molecular Mechanisms and Therapeutic Targeting. Neuroscience 2021; 453:301-11.
14. Banesh S, Trivedi V. CD36 Ectodomain Detects Apoptosis in Mammalian Cells. Mol Biotechnol 2021; 63(11):992-1003.

15. Deyama S, Ishikawa Y, Yoshikawa K, et al. Resolvin D1 and D2 Reverse Lipopolysaccharide-Induced Depression-Like Behaviors Through the mTORC1 Signaling Pathway. Int J Neuropsychopharmacol 2017; 20(7):575-84.
16. Jeoung NH, Jeong JY, Kang BS. Cryptotanshinone Prevents the Binding of S6K1 to mTOR/Raptor Leading to the Suppression of mTORC1-S6K1 Signaling Activity and Neoplastic Cell Transformation. J Cancer Prev 2021; 26(2):145-52.
17. Jewell JL, Fu V, Hong AW, et al. GPCR signaling inhibits mTORC1 via PKA phosphorylation of Raptor. Elife 2019; 8:e43038.
18. Li X, Jiang L, Lin S, et al. Inhibition of mTORC1 renders cardiac protection against lipopolysaccharide. Int J Clin Exp Pathol 2014; 7(12):8432-42.
19. Kan X, Liu J, Chen Y, et al. Protective effect of myricetin on LPS-induced mastitis in mice through ERK1/2 and p38 protein author. Naunyn Schmiedebergs Arch Pharmacol 2021; 394(8):1727-1735.
20. Tang X, Liu C, Li T, et al. Gambogic acid alleviates inflammation and apoptosis and protects the blood-milk barrier in mastitis induced by LPS. Int Immunopharmacol 2020; 86:106697.
21. Yu S, Liu X, Yu D, et al. Piperine protects LPS-induced mastitis by inhibiting inflammatory response. Int Immunopharmacol 2020; 87:106804.
22. Hu X, Fu Y, Tian Y, et al. The anti-inflammatory effect of TR6 on LPS-induced mastitis in mice. Int Immunopharmacol 2016; 30:150-56.
23. Kan X, Hu G, Fuang B, et al. Pedunculoside protects against LPS-induced mastitis in mice by inhibiting inflammation and maintaining the integrity of blood-milk barrier. Aging (Albany NY) 2021; 13(15):19460-74.
24. Gross JJ, van Dorland HA, Wellnitz O, Bruckmaier RM. Glucose transport and milk secretion during manipulated plasma insulin and glucose concentrations and during LPS-induced mastitis in dairy cows. J Anim Physiol Anim Nutr (Berl) 2015; 99(4):747-56.
25. Barham W, Sherrill T, Connelly L, et al. Intraductal injection of LPS as a mouse model of mastitis: signaling visualised via an NF-kappaB reporter transgenic. J Vis Exp 2012; 67:e4030.
26. Hou B, Liu S, Li E, Jiang X, et al. Different Role of Raptor and Rictor in Regulating Rasfonin-Induced Autophagy and Apoptosis in Renal Carcinoma Cells. Chem Biodivers 2020; 17(12):e2000743.

The correlation between apolipoprotein E gene polymorphism and the lipid-lowering effects of two statins

Q. Zhang* and Y-D. Wu

Department of Clinical Laboratory, Shunyi District Hospital of Beijing, Beijing, China

OBJECTIVES: This study aimed to investigate the correlation between apolipoprotein E (ApoE) gene polymorphism and the lipid-lowering effects of the statins rosuvastatin and atorvastatin to provide a laboratory basis for rational clinical drug use.

METHODS: A total of 146 patients using rosuvastatin calcium tablets (68 females and 78 males, with a mean age of 61.63 ± 7.32 years) and 114 patients using atorvastatin calcium tablets (51 females and 63 males, with a mean age of 64.15 ± 7.93 years) were selected for this study. A real-time fluorescent polymerase chain reaction was performed to detect ApoE genotypes in patients. In addition, the direct clearance method detected total serum cholesterol (TC) by enzyme colorimetry and serum low-density lipoprotein cholesterol (LDL-C).

RESULTS: After treatment with Rosuvastatin as lipid-lowering therapy, there was no significant difference ($P > 0.05$) in serum TC and LDL-C levels between patients with E2/E3 and E3/E3 genotypes, but levels were significantly lower ($P < 0.05$) in those patients than in those with the E3/E4 genotype. For the patients treated with atorvastatin as lipid-lowering therapy, there were significant differences ($P < 0.05$) in serum TC and LDL-C levels among the three genotypes, with levels lowest in patients with the E2/E3 genotype. For patients with the E2/E3 genotype, there were significant differences ($P < 0.05$) in serum TC and LDL-C levels between the rosuvastatin and atorvastatin groups. There was no significant difference ($P > 0.05$) in serum TC and LDL-C levels between the rosuvastatin and atorvastatin groups for patients with E3/E3 and E3/E4 genotypes.

CONCLUSION: The ApoE gene may be polymorphic, and this gene polymorphism is correlated with the lipid-lowering effects of statins. Rosuvastatin and atorvastatin have better lipid-lowering effects in E2/E3 patients and E3/E3 patients than in E3/E4 patients.

With the development of China's social economy and changes in people's dietary habits, concentrations of pro-atherogenic lipids in the country's population have gradually increased. As a result, dyslipidemia has also increased significantly, and the burden of dyslipidemia and related diseases in adults will continue to rise. Dyslipidemia is characterized by an increase in low-density lipoprotein cholesterol (LDL-C) or total cholesterol (TC) and is a significant risk factor for cardiovascular and cerebrovascular diseases. Reducing levels of TC and LDL-C can significantly reduce the incidence of atherosclerotic cardiovascular disease (ASCVD) and ASCVD mortality (1-3). Statins, the currently preferred

Keywords: Apolipoprotein E gene; Polymorphism; Rosuvastatin; Atorvastatin; Low-density lipoprotein cholesterol

*Corresponding author:
Dr Qiang Zhang
Department of Clinical Laboratory,
Shunyi District Hospital of Beijing,
No. 3 of Guangming South Street,
Shunyi District, Beijing 101300, China
e-mail: zhangqiang1225a@163.com

0393-974X (2022)

treatment drugs for regulating blood lipids, can significantly regulate blood lipid concentrations. However, their efficacy varies significantly between different populations (4). A previous study concluded that differences in therapeutic effect were related to apolipoprotein E (ApoE) gene polymorphism, race, and environment (5). The ApoE gene is a member of the soluble apolipoprotein family. ApoE plays a key role in lipid transport in the plasma and central nervous system by interacting with members of the low-density lipoprotein receptor family. It is also important in lipid regulation and the process of atherosclerosis (5).
Therefore, in the present study, the blood lipid concentrations of patients with different ApoE genotypes were reviewed, and the lipid-lowering effects of Rosuvastatin and atorvastatin were compared to provide a laboratory basis for rational clinical drug use.

MATERIALS AND METHODS

General information

A total of 146 patients using rosuvastatin calcium tablets (68 females and 78 males, with a mean age of 61.63 ± 7.32 years) and 114 patients using atorvastatin calcium tablets (51 females and 63 males, with a mean age of 64.15 ± 7.93 years) were selected for this study. Of the 146 patients treated with Rosuvastatin, 83% were residents in Shunyi District, Beijing City, in mainland China, and the remaining 17% were from other provinces in mainland China. Of the 114 patients treated with atorvastatin, 88% were from Shunyi District, and the remaining 12% were from other provinces in China. The Ethics Committee of our hospital approved this study, and all patients provided signed informed consent.

The inclusion criteria for patients were: (1) they had a diagnosis of hyperlipidemia; (2) were receiving oral administration of Rosuvastatin or atorvastatin; (3) were over 18 years of age; and (4) they gave informed consent. The exclusion criteria for patients were: (1) severe infections; (2) severe heart, liver, or kidney dysfunctions; and (3) incomplete medical data.

Sample collection

The patients received lipid-lowering therapy for 4 weeks: either Rosuvastatin at 5 mg per day or atorvastatin at 10 mg per day. After this period, their blood samples were collected, and 5 ml of serum sample was centrifuged for 15 minutes. The whole blood was then separated, and dipotassium ethylenediaminetetraacetic (EDTA-2K+) was added to the samples for anticoagulation, which was used to detect ApoE genotypes. Serum samples were used to detect the patients' blood lipid concentrations. Blood samples were placed in a refrigerator at −20°C for cryopreservation.

DNA extraction and genotyping

Whole blood genomic DNA extraction was performed using a blood genomic DNA extraction kit (centrifugal column type) purchased from Tiangen Biotech (Beijing, China). A LightCycler480 analyzer (Roche Diagnostics) and an ApoE gene polymorphism detection kit (Wuhan Youzhiyou Medical Technology Co., Ltd) were used for ApoE genotyping by fluorescent polymerase chain reaction (PCR). ApoE genotypes were determined by PCR fluorescent probe. The forward primer sequence was GGAGGAACAACTGACCCCGGT, and the reverse primer sequence was GTTCCA CCAGGGGCCCCA; ApoE genotyping was carried out by detecting the probe signal characteristics of different fluorescein markers in the process of real-time PCR (Fig. 1).

Laboratory measurements of serum TC and LDL-C

Serum TC was detected by enzyme colorimetry, and serum LDL-C was detected by the direct clearance method. A Beckman Coulter AU5800 automatic biochemical analyzer and commercial kits produced by Biosino Bio-Technology and Science Inc. (Beijing) were used to measure TC and LDL-C serum concentration.

Statistical analysis

Data were analyzed using the software SPSS Statistics 19.0. Measurement data were expressed as mean ± standard deviation (x ± SD), and count data were expressed as percentages (%). A normality test was conducted using the W-test, and homogeneity of variance was analyzed using the F-test. For multiple comparisons, each value was compared by a one-way ANOVA followed by Dunnett's test when the data conformed to the normal distribution, whereas the non-normally distributed continuous data were compared using non-parametric tests. Count data were compared using a Chi-square test. $P < 0.05$ was considered statistically significant.

RESULTS

Frequency distribution of ApoE alleles and genotypes

Testing in both populations revealed that the frequency of the ε3 allele in the ApoE gene was the highest, along with the frequency of the E3/E3 genotype. There was no statistically significant difference ($P > 0.05$) between the two treatment groups in terms of the frequency distribution of ApoE alleles and genotypes (Table I).

Comparison of serum TC and LDL-C concentrations between patients with different genotypes within each treatment group after lipid-lowering therapy

Before lipid-lowering therapy, there was no significant difference in the serum TC and LDL-C levels of patients with different genotypes within either group ($P > 0.05$). After the patients received Rosuvastatin or atorvastatin as lipid-lowering therapy, the serum TC and LDL-C levels were compared; the findings are as follows. In the group treated with Rosuvastatin, the difference in serum TC and LDL-C levels between patients with the E2/E3 genotype and those with the E3/E3 genotype was not statistically significant ($P > 0.05$); however, the differences in levels between patients with the E3/E3 genotype and those with the E3/E4 genotype and between patients with the E2/E3 genotype and those with the E3/E4 genotype were statistically significant ($P < 0.05$). In the group treated with atorvastatin, the differences in serum TC and LDL-C levels between patients with the E2/E3 genotype and those with the E3/E3 genotype, between patients with the E3/E3 genotype and those with the E3/E4 genotype, and between patients with the E2/E3 genotype and those with the E3/E4 genotype were all statistically significant ($P < 0.05$) (Table II).

Table I. *Distribution of the frequency of ApoE genotypes and alleles.*

Group	Genotypes					Alleles [n (%)]				
	E2/E3	E3/E3	E3/E4	χ^2	P	ε2	ε3	ε4	χ^2	P
Atorvastatin	10	79	25	2.374	0.305	10 (4.4)	193 (84.6)	25 (11.0)	2.372	0.305
Rosuvastatin	20	102	24			20 (6.8)	248 (84.9)	24 (8.2)		
Total	30	181	49			30 (5.7)	441 (84.8)	49 (9.4)		

Compared using Chi-square test. P<0.05 was considered statistically significant.

Table II. *Comparison of the serum TC and LDL-C concentrations in each treatment group(x±s,mmol/L)*

Index	genotype	n	TC(mmol/l)		LDL-C(mmol/l)	
			pre-therapy	post-treatment	pre-therapy	post-treatment
Rosuvastatin	E2/E3	20	5.43±0.82	3.95±0.93	2.78±0.65	1.91±0.60
	E3/E3	102	5.51±0.78	4.11±1.06	2.89±0.88	2.17±0.71
	E3/E4	24	5.57±0.85	4.58±0.88#*	2.83±0.84	2.52±0.75#*
Atorvastatin	E2/E3	10	5.42±0.68	3.25±0.65	2.75±0.81	1.78±0.59
	E3/E3	78	5.56±0.89	4.26±0.93#	2.86±0.76	2.28±0.73#
	E3/E4	25	5.46±0.96	4.52±0.85#*	2.76±0.82	2.70±0.62#*

**P<0.05 when compared with E3/E3 group; #P<0.05 when compared with E2/E3 group.*

Comparison of serum TC and LDL-C concentrations in patients with different genotypes between treatment groups

In order to better interpret the correlation between ApoE gene polymorphism and the lipid-lowering effects of the two statins, we compared serum TC and LDL-C concentrations in patients with different genotypes between the two treatment groups. We found that, for patients with the E2/E3 genotype, there were significant differences in serum TC and LDL-C levels between the rosuvastatin and atorvastatin groups, indicating that the lipid-lowering effect of atorvastatin may be better than that of Rosuvastatin. However, there was no significant difference between the rosuvastatin and atorvastatin groups regarding serum TC and LDL-C levels of patients with E3/E3 and E3/E4 genotypes (Table III).

Clinical goals achieved

After the administration of lipid-lowering treatment (either Rosuvastatin or atorvastatin), the $M_{0.5}$ (fifty per cent) of the serum TC level was lower than 4.1 mmol/L (the level recommended in the 2016 Guidelines for Prevention and Treatment of Dyslipidemia in Chinese Adults) in patients with E2/E3 and E3/E3 genotypes and more than 4.1 mmol/L in patients with the E3/E4 genotype. The serum LDL-C level was lower than 2.6 mmol/L (the recommended level) in 80% of patients with E2/E3 and E3/E3 genotypes but lower than 2.6 mmol/L in only 50% of patients with the E3/E4 genotype, i.e., the serum LDL-C level in 50% of patients with the E3/E4 genotype exceeded 2.6 mmol/L (Table IV).

Table III. *Comparison of serum TC and LDL-C concentrations between genotypes, comparing both treatment groups*

Genotype	Index	n	TC (mmol/L)	LDL-C (mmol/L)
E2/E3	Rosuvastatin	20	3.95±0.93	1.91±0.60
	Atorvastatin	10	3.25±0.65#	1.78±0.59#
E3/E3	Rosuvastatin	102	4.11±1.06	2.17±0.71
	Atorvastatin	78	4.26±0.93	2.28±0.73
E3/E4	Rosuvastatin	24	4.58±0.88	2.52±0.75
	Atorvastatin	25	4.52±0.85	2.70±0.62

#P<0.05 when compared with Rosuvastatin group

Table IV. *The quartile levels of TC and LDL-C in patients and with different genotypes after 4 weeks of lipid-lowering therapy with rosuvastatin and atorvastatin*

	Index	Rosuvastatin			Atorvastatin		
		E2/E3	E3/E3	E3/E4	E2/E3	E3/E3	E3/E4
TC	Q_1	3.50	3.24	3.83	2.90	3.38	3.94
	Q_2	3.70	4.08	4.31	3.36	3.93	4.48
	Q_3	4.51	4.76	4.96	4.01	4.61	5.15
LDL-C	Q_1	1.59	1.57	2.15	1.28	1.71	2.30
	Q_2	1.86	2.16	2.51	1.76	2.11	2.69
	Q_3	2.33	2.63	2.88	2.16	2.77	3.35

#P<0.05 when compared with Rosuvastatin group

DISCUSSION

The present study results reveal that the ApoE gene was polymorphic within the study population, with the ε3 allele having the highest frequency (85% of all alleles) and E3/E3 being the most common genotype (approximately 70% of all genotypes). The ε2 allele had the lowest frequency (approximately 5%), and the frequency of the ε4 allele was approximately 10%. The E2/E2 genotype was detected in only 2 patients, the E2/E4 genotype was detected in only 1 patient, and the E4/E4 genotype was not detected.

The finding that the ε3 allele was present in 85% of the study population is mainly consistent with the results of prior studies at home and abroad, which report a frequency range for ε3 of 50%–90%, with frequency ranges for ε2 and ε4 of approximately 1%–15% and approximately 5%–35%, respectively (6). Variations in frequency range are considered to be correlated to race and geography. The polymorphism of the ApoE gene manifests as subtypes with different levels of affinity to LDL-C, and the ε2 and ε4 isomers are considered to be related to the lipid-lowering effect of statins (7).

In patients treated with Rosuvastatin as lipid-lowering therapy, the differences in serum TC and LDL-C levels between patients with the E2/E3 genotype and those with the E3/E3 genotype were not statistically significant. In contrast, the differences in serum TC and LDL-C levels between patients with the above two genotypes and those with the E3/E4 genotype were statistically significant. In patients treated with atorvastatin as lipid-lowering therapy, the differences in serum TC and LDL-C levels among the three genotypes were statistically significant. In addition, in patients with the E2/E3 genotype, there was a significant difference in serum TC level between those treated with Rosuvastatin and those treated with atorvastatin. This result may indicate a correlation between ApoE gene polymorphism and the lipid-lowering effects of statins (8-10), and, in patients with the E2/E3 genotype, the lipid-lowering effect of atorvastatin may be better than that of Rosuvastatin.

In patients with the E3/E3 genotype, the difference between the effects of Rosuvastatin and those of atorvastatin as lipid-lowering therapy was not statistically significant. This result indicates that the lipid-lowering effect of statins in patients with the E3/E3 genotype is not related to the type of statin used and the baseline value of the blood lipid level. The serum TC and LDL-C levels after treatment of patients with the E3/E4 genotype were significantly different from those of patients with the other two genotypes, suggesting that treatment with Rosuvastatin or atorvastatin has fewer lipid-lowering benefits for people with the ε4 isomer. This result remains disputable.

The quartile levels of serum TC and LDL-C in the study patients indicate that most patients with E2/E3 and E3/E3 genotypes treated with Rosuvastatin or atorvastatin can reach the levels recommended in the 2016 Guidelines for the Prevention and Treatment of Dyslipidemia in Chinese Adults (TC: 4.1 mmol/L; LDL-C: 2.6 mmol/L). However, as fewer than 50% of study patients with the E3/E4 genotype reached the recommended TC and LDL-C levels after treatment with Rosuvastatin or atorvastatin, the indication is that Rosuvastatin and atorvastatin have poor lipid-lowering effects in patients with the E3/E4 genotype.

Although studies have found that ApoE gene polymorphism has an impact on the lipid-lowering effect of statins, its weight among the factors influencing the different effects of individual statins remains controversial (11-14). Similarly, guidance for clinical treatment based on the impact of ApoE gene polymorphism on the lipid-lowering effect of statins has not been generally agreed (15-20). Further in-depth studies on the role of the ApoE gene in the lipid-lowering effect of statins will help promote the accurate use of statins in the population with dyslipidemia in China.

A further recommendation for future study concerns the physiological mechanisms between ApoE gene polymorphism and lipid-lowering effects in patients treated with Rosuvastatin or atorvastatin, about which there was insufficient data in this study. Interest in the study of genes has grown recently (21-25), and we note that guidelines for dyslipidemia from different sources and other candidate gene association studies may influence and supplement the results of such research (26-29). Therefore, the need for further research into the correlation between ApoE gene

polymorphism and lipid-lowering effects in patients treated with Rosuvastatin or atorvastatin remains.

The ApoE gene may be polymorphic, and this gene polymorphism is correlated with the lipid-lowering effects of statins. For example, the medications rosuvastatin and atorvastatin have better lipid-lowering effects in E2/E3 patients and E3/E3 patients than in E3/E4 patients.

Competing interests

The authors declare that they have no competing interests.

REFERENCES

1. Egom EE. LDL-Cholesterol and Atherosclerotic Cardiovascular Disease: Innocent Bystander or Essential Ingredient. J Am Coll Cardiol 2018; 71:705-706.
2. Hoffmann MM. Towards a More Personalized Treatment of Dyslipidemias to Prevent Cardiovascular Disease. Curr Cardiol Rep 2018; 20:56.
3. Ravnskov U, de Lorgeril M, Diamond DM, et al. LDL-C does not cause cardiovascular disease: a comprehensive review of the current literature. Expert Rev Clin Pharmacol 2018; 11:959-970.
4. Hopewell JC, Reith C, Armitage J. Pharmacogenomics of statin therapy: any new insights in efficacy or safety? Curr Opin Lipidol 2014; 25:438-45.
5. Hatters DM, Peters-Libeu CA, Weisgraber KH. Apolipoprotein E structure: insights into function. Trends Biochem Sci 2006; 31:445-54.
6. Mahley RW, Rall SC Jr. Apolipoprotein E: far more than a lipid transport protein. Annu Rev Genomics Hum Genet 2000; 1:507-37.
7. Deshmukh HA, Colhoun HM, Johnson T, et al. CARDS, ASCOT, and PROSPER Investigators. Genome-wide association study of genetic determinants of LDL-c response to atorvastatin therapy: importance of Lp(a). J Lipid Res 2012; 53:1000-11.
8. White EJ, Gyulay G, Lhoták Š. Sialidase down-regulation reduces non-HDL cholesterol, inhibits leukocyte transmigration, and attenuates atherosclerosis in ApoE knockout mice. J Biol Chem 2018; 293:14689-706.
9. Zhang Z, Zhang R, Qin ZZ, Chen JP, Xu JY, Qin LQ. Effects of Chronic Whey Protein Supplementation on Atherosclerosis in ApoE-/- Mice. J Nutr Sci Vitaminol (Tokyo) 2018; 64:143-150.
10. Bedja D, Yan W, Lad V, et al. Inhibition of glycosphingolipid synthesis reverses skin inflammation and hair loss in ApoE-/- mice fed western diet. Sci Rep 2018; 8:11463.
11. Smit RA, Postmus I, Trompet S, et al. Rooted in risk: genetic predisposition for low-density lipoprotein cholesterol level associates with diminished low-density lipoprotein cholesterol response to statin treatment. Pharmacogenomics 2016; 17:1621-28.
12. Ciuculete DM, Bandstein M, Benedict C, et al. A genetic risk score is significantly associated with statin therapy response in the elderly population. Clin Genet 2017; 91:379-85.
13. Lefevre M, Ginsberg HN, Kris-Etherton PM, et al. ApoE genotype does not predict lipid response to changes in dietary saturated fatty acids in a heterogeneous normolipidemic population. The DELTA Research Group. Dietary Effects on Lipoproteins and Thrombogenic Activity. Arterioscler Thromb Vasc Biol 1997; 17:2914-23.
14. Minagawa H, Gong JS, Jung CG, et al. Mechanism underlying apolipoprotein E (ApoE) isoform-dependent lipid efflux from neural cells in culture. J Neurosci Res 2009; 87:2498-508.
15. Delsing DJ, Post SM, Groenendijk M, et al. Rosuvastatin reduces plasma lipids by inhibiting VLDL production and enhancing hepatobiliary lipid excretion in ApoE*3-leiden mice. J Cardiovasc Pharmacol 2005; 45:53-60.
16. Wei H, Hu C, Wang M, et al. Lipidomics reveals multiple pathway effects of a multi-components preparation on lipid biochemistry in ApoE*3Leiden. CETP mice. PLoS One. 2012; 7:e30332.
17. Gosselet F. [How ApoE regulates blood-brain barrier integrity]. Med Sci (Paris) 2012; 28:920-3. [Article in French]
18. Wu H, Zhang Y, Yang X, et al. Whole Body Vibration Retards Progression of Atherosclerosis via Insulin-Like Growth Factor 1 in Apolipoprotein E-Deficient Mice. Biomed Res Int 2018; 2018:4934861.
19. Zhang L, He S, Li Z, et al. Apolipoprotein E polymorphisms contribute to statin response in Chinese ASCVD patients with dyslipidemia. Lipids Health Dis 2019; 18:129.

20. Liu JE, Liu XY, Chen S, et al. SLCO1B1 521T > C polymorphism associated with rosuvastatin-induced myotoxicity in Chinese coronary artery disease patients: a nested case-control study. Eur J Clin Pharmacol 2017; 73:1409-16.
21. Zara-Lopes T, Galbiatti-Dias ALS, Castanhole-Nunes MMU, et al. Polymorphisms in MTHFR, MTR, RFC1 and CßS genes involved in folate metabolism and thyroid cancer: a case-control study. Arch Med Sci 2019; 15:522-530.
22. Gorący J, Kaczmarczyk M, Ciechanowicz A, et al. E-selectin gene haplotypes are associated with the risk of myocardial infarction. Arch Med Sci 2019; 15:1223-1231.
23. Shek AB, Alieva RB, Kurbanov RD, Hoshimov SU, Nizamov UI, Ziyaeva AV. Can metformin stabilize PCSK9 level in stable coronary artery disease patients treated with statins? Arch Med Sci Atheroscler Dis 2019; 4:e144-e150.
24. Socha M, Pietrzak A, Grywalska E, et al. The effect of statins on psoriasis severity: a meta-analysis of randomized clinical trials. Arch Med Sci 2019;16:1-7.
25. Nakhl S, Sleilaty G, Chouery E, Salem N, Chahine R, Farès N. FokI vitamin D receptor gene polymorphism and serum 25-hydroxyvitamin D in patients with cardiovascular risk. Arch Med Sci Atheroscler Dis 2019; 4:298-303.
26. Solnica B, Sygitowicz G, Sitkiewicz D, et al. 2020 Guidelines of the Polish Society of Laboratory Diagnostics (PSLD) and the Polish Lipid Association (PoLA) on laboratory diagnostics of lipid metabolism disorders. Arch Med Sci 2020; 16:237-252.
27. Soran H, Adam S, Mohammad JB, et al. Hypercholesterolaemia - practical information for non-specialists. Arch Med Sci 2018; 14:1-21.
28. Banach M, Jankowski P, Jóźwiak J, et al. PoLA/CFPiP/PCS Guidelines for the Management of Dyslipidaemias for Family Physicians 2016. Arch Med Sci 2017; 13:1-45.
29. Gluba A, Pietrucha T, Banach M, Piotrowski G, Rysz J. The role of polymorphisms within paraoxonases (192 Gln/Arg in PON1 and 311Ser/Cys in PON2) in the modulation of cardiovascular risk: a pilot study. Angiology 2010; 61:157-65.

Prostaglandin E receptor 3 promotes the dysfunction of vascular smooth muscle cells induced by platelet-derived growth factor via regulating PI3K/Akt pathway

R. Zhou[1#], X.S. Gu[2#], J.H. Xu[3] and J. Wan[1*]

[1]Department of Emergency and Intensive Care Unit, Pudong New Area People's Hospital, Shanghai, China; [2]Department of Cardiology, The Second Affiliated Hospital of Soochow University, China; [3]Department of Infectious Disease, Pudong New Area People's Hospital, Shanghai, China

[#]These authors contributed equally

BACKGROUND AND OBJECTIVE: The dysfunction of vascular smooth muscle cells (VSMCs) contributes to the pathogenesis of atherosclerosis, which is associated with coronary heart disease and acute myocardial infarction (AMI). This study is conducted to explain the biological function of prostaglandin E receptor 3 (EP3) in regulating the phenotypes of VSMCs.

MATERIALS AND METHODS: Platelet-derived growth factor-BB (PDGF-BB) was used to treat VSMCs to construct the cell model. qPCR was performed to examine the expression of EP3 in the VSMCs after PDGF-BB treatment. After EP3 was silenced, inhibited or overexpressed in VSMCs, CCK-8 assay, BrdU assay, flow cytometry and Transwell assay were performed to detect the viability, proliferation, cell cycle progression and migration of VSMCs. In addition, the expression levels of PI3K, p-p85, Akt, p-Akt in VSMCs was measured by Western blotting.

RESULTS: The expression of EP3 in VSMCs is promoted by PDGF-BB treatment in a time- and dose-dependent manner. EP3 overexpression facilitates the viability, proliferation and migration of VSMCs while silencing EP3 or pharmacological inhibition of EP3 represses the dysfunction of VSMCs induced by PDGF-BB. EP3 promoted phosphorylation of p85, Akt (Ser473) and Akt (Thr308) in VSMCs, and the promoting effects of EP3 on the viability, proliferation, migration and cell cycle progression of VSMCs were counteracted after PI3K signalling was inhibited.

CONCLUSION: EP3 participates in inducing the dysfunction of VSMCs induced by PDGF via regulating PI3K/Akt pathway, suggesting EP3 is a therapeutic target for atherosclerosis, AMI and other cardiovascular diseases.

Globally, coronary heart disease (CHD) is one of the leading killers of humans (1, 2). In addition, acute myocardial infarction (AMI) is the leading cause of death due to CHD (1, 2). Although significant progress has been made in diagnosing and treating AMI, the short-term and long-term mortality of patients with AMI is still high (2, 3).

AMI is caused by ischemic heart disease or coronary artery disease (2). In the pathogenesis of AMI, atherosclerotic plaque ruptures, and platelets form blood clots to entirely or partially block the coronary artery lumen (4). Phenotypic switch of the vascular smooth muscle cell (VSMC), from the contractile phenotype to synthetic phenotype, facilitating the proliferation and

Keywords: prostaglandin E receptor 3; vascular smooth muscle cells; platelet-derived growth factor; cardiovascular disease.

[*]*Corresponding Author:*
Dr Wan Jian,
Department of Emergency and Intensive Care Unit,
Pudong New Area People's Hospital,
Shanghai, China
e-mail: lrywkrza1061@163.com

0393-974X (2022)

migration of VSMCs, will promote the secretion of extracellular matrix and participate in the pathogenesis of atherosclerosis; importantly, excessive proliferation and migration of VSMCs induce the destabilization of atherosclerotic plaque, in turn, lead to unstable angina and AMI (5, 6). Platelets are important mediators in the initiation of thrombosis and the pathogenesis of AMI. Notably, there is an interplay between the phenotypes of VSMCs and platelets: on the one hand, platelet-derived growth factor (PDGF) secreted by platelets can promote the proliferation and migration of VSMCs (7); on the other hand, VSMCs-mediated vascular lesion induces the aggregation of platelets (8). However, the detailed mechanism of VSMC dysregulation has not been fully explained.

Prostaglandins (PGs) are associated with cardiovascular diseases and blood dynamic balance (9). PGs receptor family belongs to G protein-coupled receptors (10). Prostaglandin E receptor 3 (PTGER3, EP3) is a PGs receptor, which is widely and stably expressed in multiple tissues and organs (11). Accumulating evidence shows that EP3 plays an essential role in regulating platelet accumulation and thrombosis (12-13). EP3 inhibitors can not only effectively inhibit the aggregation of platelets but also not prolong the bleeding time (13). As a crucial regulator of platelet aggregation and pathogenesis of the cardiovascular disease, EP3 in the dysfunction of VSMCs has not been investigated by previous studies.

In the present work, we hypothesized that EP3 partly mediates PDGF-induced dysfunction of VSMCs. Our experiments were performed to validate this hypothesis, further clarifying the relationships between platelet accumulation, dysfunction of VSMCs, and the pathogenesis of AMI.

MATERIALS AND METHODS

Cell culture

Human VSMCs from the China Center for Type Culture Collection (CCTCC, Wuhan, China) were cultured in RPMI-1640 medium (Thermo Fisher Scientific, Waltham, MA, USA) supplemented with 100 U/ml penicillin, 100 μg/ml streptomycin (Thermo Fisher Scientific, Waltham, MA, USA), and 10% fetal bovine serum (FBS, Thermo Fisher Scientific, Waltham, MA, USA) in a humidified incubator containing 5% CO_2 at 37°C. To induce the phenotypic switch of VSMCs, the VSMCs were treated with PDGF-BB at different concentrations (0, 10, 20, and 40 ng/ml) for different times (0, 6, 12, and 24 h).

Cell transfection

EP3 overexpression plasmids (pcDNA-EP3) and control vector (pcDNA), siRNA targeting EP3 (si-EP3) and scramble siRNA (si-NC) were provided by GenePharma (Shanghai, China). First, according to the manufacturer's instructions, the plasmids or siRNA were transfected into VSMCs with Lipofectamine™ 3000 (Invitrogen, Carlsbad, CA, USA). Then, 36 h later, a quantitative polymerase chain reaction (qPCR) was used to detect the transfection efficiency.

qPCR

Total RNA of VSMCs was extracted with TRIzol reagent (Invitrogen, Carlsbad, CA, USA). According to the manufacturer's protocol, the synthesis of cDNA from 1 μg of total RNA was performed with a PrimeScript-RT Kit (Promega, Madison, WI, USA), and then qPCR was performed with an SYBR®Premix-Ex-Taq™ kit (Takara, Dalian, China) on ABI7300 system (Applied Biosystems, SanFrancisco, CA, USA). GAPDH was employed as the reference gene of EP3. The relative expression of EP3 was calculated with the $2^{-\Delta\Delta Ct}$ method. The primer sequences: EP3 forward, 5'-TCCTTCCTAATCGCCGTTC-3' and reverse, 5'-CTCCGCTTCAGGTTGTTCAT-3'; GAPDH forward, 5'- TGACTTCAACAGCGACACCCA-3'; reverse, 5'- CACCCTGTTGCTGTAGCCAAA-3'.

Cell counting kit-8 (CCK-8) assay

VSMCs were transferred to 96-well plates (1×10^3 cells/well) and cultured at different times. At each time point, each well was added with 10 μL of CCK-8 solution (Beyotime, Shanghai, China), and subsequently, the cells were incubated at 37°C for 2 h. Next, a microplate reader was employed to measure the optical density of the cells at 450 nm wavelength.

BrdU assay

BrdU assay was used to detect the proliferation of VSMCs. Briefly, the VSMCs were transferred into a 35 mm culture dish containing a coverslip and cultured with a serum-free medium for 12 h. Subsequently, the medium

was replaced by a complete medium, and then VSMCs were incubated with BrdU solution (Beyotime, Shanghai, China) for 4 h. Subsequently, the cells were fixed in 4% paraformaldehyde for 10 min. Next, an anti-BrdU antibody (Biocompare, South San Francisco, CA, USA) was used to incubate the cells at room temperature for 1 h, and the cells were stained with DAPI staining solution (Beyotime, Shanghai, China) to mark the nuclei. After the VSMCs were washed with phosphate buffer saline (PBS), five visual fields were randomly selected under a fluorescence microscope (Olympus, Tokyo, Japan), and the average number of BrdU positive-VSMCs was recorded.

Flow cytometry

Flow cytometry was used to analyze cell cycle progression. VSMCs were seeded at a density of 10^5 cells per well in 12-well plates. Then cells were stimulated with 40 ng/mL PDGF-BB for 16 h and transfected with si-EP3 and pcDNA-EP3. The VSMCs were fixed with 80% ethanol overnight and then stained with propidium iodide (PI) solution (50 μg/ml, BD Biosciences, Franklin Lakes, NJ, USA) for 20 min at room temperature. Next, the VSMCs were washed with PBS, and a flow cytometer (BD Biosciences, Franklin Lakes, NJ, USA) was used to analyze the cell cycle distribution of cells.

Transwell assay

The migration of VSMCs was assessed with the Transwell system (Millipore, Bedford, MA, USA). Briefly, 600 *μL of* RPMI-1640 medium containing 10% FBS was added to the Transwell system's lower compartment, and 100 *μL* of serum-free RPMI-1640 medium containing 1×10^5 VSMCs was added to the upper compartment. After the VSMCs were cultured at 37°C for 12 h, the remaining non-migrated cells in the upper surface of the membrane were wiped off with cotton swabs. The migrated cells attached to the below surface of the membrane were fixed with 4% paraformaldehyde for 10 min and then stained with 0.5% crystal violet solution. After the membrane was washed and dried, five visual fields of each membrane were randomly selected and observed under an inverted microscope, and the average number of migrated cells in each group was calculated and recorded.

Western blot

VSMCs in each group were harvested and lysed in RIPA lysis buffer (Beyotime, Shanghai, China) on ice. Then, the total protein was extracted, and the protein concentration was determined by the Bradford method. Successively, the protein samples were mixed with loading buffer and denatured in boiling water. Next, an equivalentent amount of protein samples in each group was separated by sodium dodecyl sulfate-polyacrylamide gel electrophoresis and subsequently transferred onto PVDF membrane (Millipore, Bedford, MA, USA). Then, the membrane was blocked in 5% defatted milk at room temperature for 1 h. Next, the membrane was incubated with the primary antibody overnight at 4°C. After the membranes were washed by tris buffered saline tween (TBST), a secondary antibody was added, and the membranes were incubated at room temperature for 1 h. The membranes were then washed again with TBST. Subsequently, electrochemiluminescence substrates A and B solutions (Millipore, Bedford, MA, USA) were mixed (1:1) and added onto the membranes, and Amersham Imager 600 (GE Healthcare, Chicago, IL, USA) was used to scan the signal of the protein bands. The antibodies used in this study included: anti-EP3 antibody (1:1000, Abcam, Cambridge, UK), anti-PI3K antibody (1 1000, Abcam, Cambridge, UK), anti-p-p85 antibody (1: 200, Abcam, Cambridge, UK), anti-Akt antibody (1:1000, Abcam, Cambridge, UK), anti-p-Akt antibody (Ser473) (1:200, Abcam, Cambridge, UK), anti-p-Akt antibody (Thr308) (1:200, Abcam, Cambridge, UK), anti-GAPDH antibody (1:3000, Proteintech, Wuhan, China), and the secondary antibody (1:2000, Proteintech, Wuhan, China).

Statistical analysis

All of the experiments were performed in triplicate. Statistical analysis was performed with SPSS (version 17.0) (SPSS Inc., Chicago, IL, USA). The data were expressed as "mean ± standard deviation" ($x \pm s$). The difference between the data of the two groups was analyzed with Student's t-test, and the difference between the data of more groups was analyzed with one-way ANOVA. $P < 0.05$ indicates the significant difference.

RESULTS

The expression of EP3 in VSMCs is up-regulated by PDGF-BB

First of all, we established a VSMCs dysfunction model induced by PDGF-BB. Then, after the treatment

of VSMCs with different concentrations (0, 10, 20, and 40 ng/ml) of PDGF-BB, it was observed that EP3 expression was increased in a time-dependent manner (Fig. 1A). In addition, after treating VSMCs with 40 ng/ml PDGF for 0, 6, 12, and 24 h, the expression of EP3 was up-regulated in a time-dependent manner, and the expression level reached the highest after 24 h (Fig. 1B). The condition that 40 ng/ml PDGF-BB was used to treat VSMC cells for 24 h was hence chosen for follow-up experiments.

EP3 knockdown represses the proliferation and migration of VSMCs induced by PDGF-BB

To investigate the function of EP3 in VSMCs, EP3 siRNA and overexpression plasmids were respectively transiently transfected into VSMCs, and the transfection efficiency was verified employing qRT-PCR (Fig. 2A). CCK-8 and BrdU assays suggested that PDGF-BB remarkably induced the proliferation of VSMCs, whereas EP3 knockdown inhibited the proliferation of VSMCs (Fig. 2B-C). Flow cytometry analysis indicated that PDGF-BB markedly promoted the cell cycle progression of VSMCs, but EP3 knockdown induced G2/M cell cycle arrest (Fig. 2D). In the Transwell experiment, PDGF-BB markedly increased the migration of VSMCs, while EP3 knockdown significantly impeded the migration of VSMCs (Fig. 2E). Meanwhile, EP3 overexpression exerted opposite biological effects (Fig. 2B-E).

Pharmacological inhibition of EP3 represses the proliferation and migration of VSMCs induced by PDGF-BB

Next, L-798106, the antagonist of EP3, was used to treat VSMCs. CCK-8 and BrdU assays suggested that L-798106 inhibited the viability, proliferation, cell cycle progression, and migration of VSMCs in both a dose-dependent and time-dependent manner (Fig. 3a-d).

As a control, the antagonist of EP4 L-161928 was also used to treat VSMCs. Interestingly, EP4 inhibition did not change the phenotypes of VSMCs (Fig. 4a-d).

The biological function of EP3 in VSMCs is dependent on PI3K/Akt pathway.

Next, we explored the downstream mechanism by which EP3 regulated the phenotypes of VSMCs. Some previous studies reported that EP3 could negatively regulate PI3K/Akt signal pathway in different human cells (14-16). In this work, we detected the expression levels of PI3K, p-p85, Akt, and p-Akt in the VSMCs of different groups. As shown, PDGF-BB treatment significantly promoted

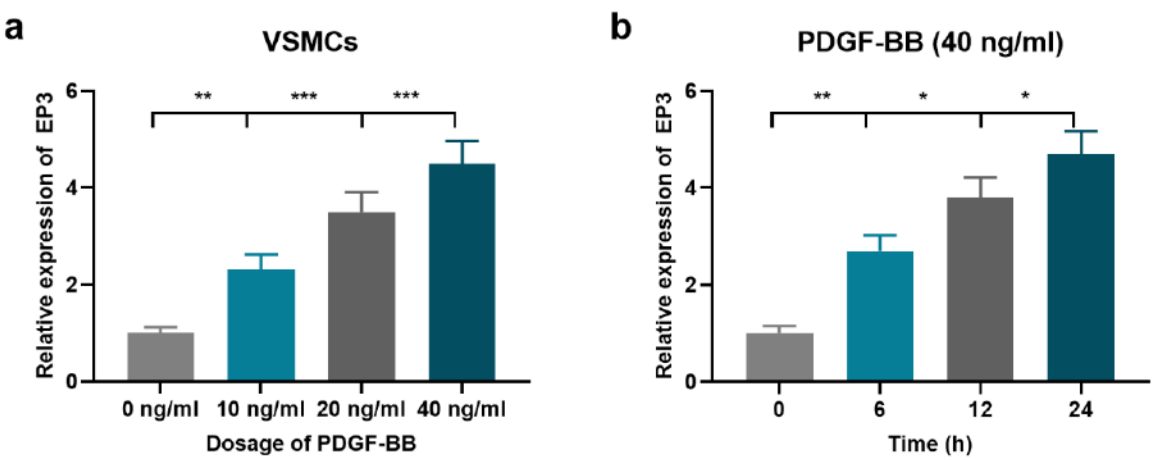

Fig. 1. *PDGF-BB treatment induces the expression of EP3 in VSMCs. **A**) VSMCs were treated with different doses of PDGF-BB (0 ng/mL, 10 ng/mL, 20 ng/mL and 40 ng/mL) for 24 h, then qPCR was performed to detect the expression of EP3 in VSMCs. **B**) VSMCs were treated with 40 ng/mL PDGF-BB for different times (0h, 6h, 12h and 24 h), then qPCR was performed to detect the expression of EP3 in VSMCs. *P<0.05, **P<0.01 and ***P<0.001.*

the phosphorylation of p85, Akt (Ser473) and Akt (Thr308) in VSMCs, and EP3 overexpression further promoted these effects; however, EP3 knockdown or L-798106 treatment reversed these effects induced by PDGF-BB (Fig. 5a). Consistently, after VSMCs were treated with LY294002, the inhibitor of PI3K, the promoting effects of EP3 on the viability, proliferation, migration and cell cycle progression of VSMCs were counteracted (Fig. 5b-e).

DISCUSSION

The pathogenesis of atherosclerosis is significantly associated with the dysfunction of VSMCs (17). VSMCs are the main component of the media of arteries; it not only has the physiological functions of maintaining vascular structure, maintaining vascular tension and regulating blood pressure but also show strong plasticity under the stimulation of the external

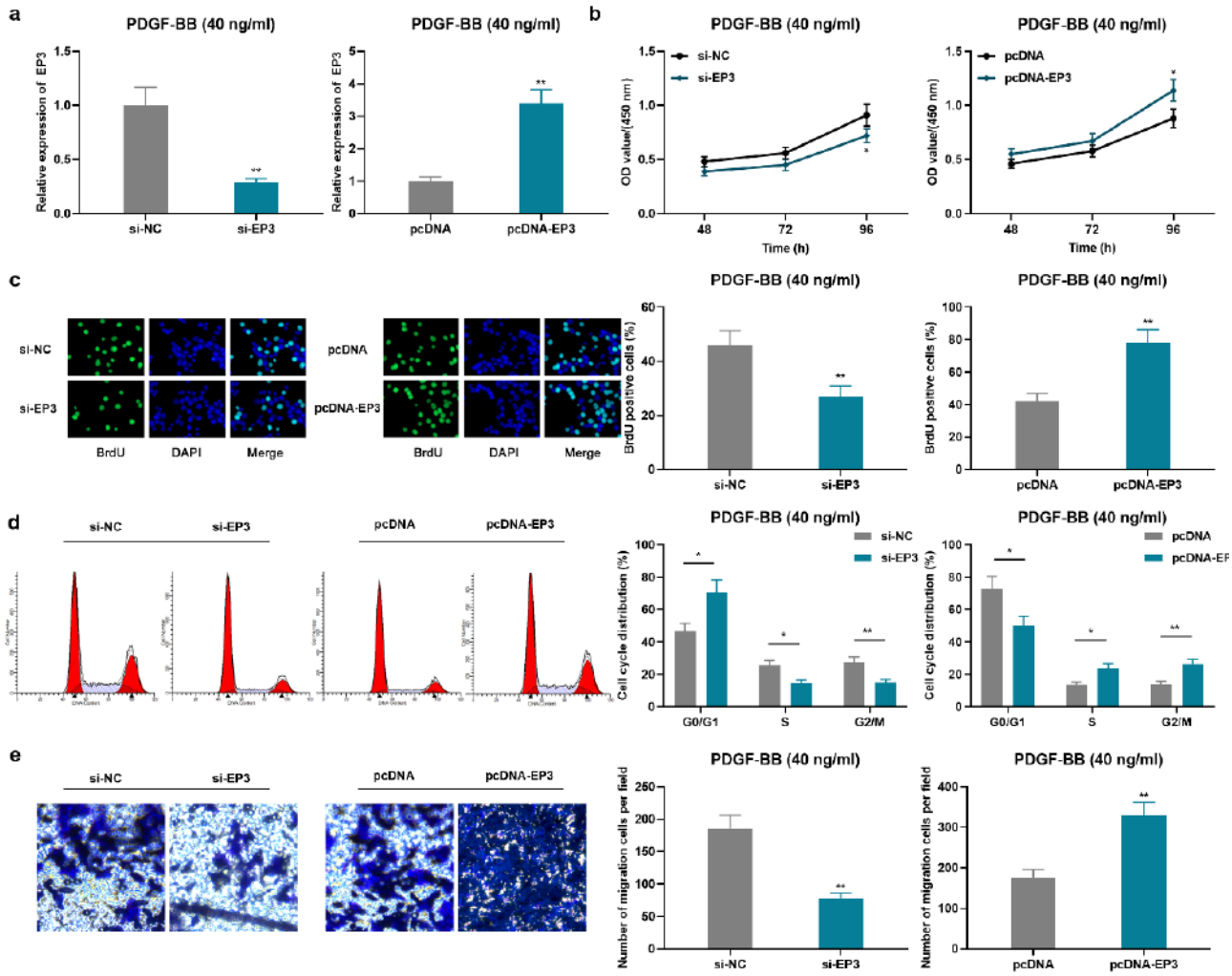

Fig. 2. *EP3 positively regulates the viability, proliferation, cell cycle progression and migration of VSMCs.* ***A****) EP3 siRNAs and overexpression plasmids were respectively transiently transfected into VSMCs, and the transfection efficiency was detected by qPCR;* ***B****) VSMCs were transfected with EP3 siRNAs or overexpression plasmids, and CCK-8 assay was performed to detect the viability of VSMCs;* ***C****) VSMCs were transfected with EP3 siRNAs or overexpression plasmids, and BrdU assay was performed to detect the proliferation of VSMCs;* ***D****) VSMCs were transfected with EP3 siRNAs or overexpression plasmids, and flow cytometry was conducted to evaluate the cell cycle progression of VSMCs;* ***E****) VSMCs were transfected with EP3 siRNAs or overexpression plasmids, and Transwell assay was performed to examine the migration of VSMCs. *P<0.05 and **P<0.01.*

environment, and it has the potential of proliferation, migration and secretion of inflammatory factors (17, 18). Under the condition of vascular injury, different stimulating factors will induce a phenotypic switch of VSMCs, from fully differentiated contractile type to dedifferentiated synthetic type, accompanied by the enhancement of proliferation, migration, synthesis and secretion (19). The phenotypic transformation of VSMCs can cause structural changes in blood vessels, changes in hemodynamics, participate in the formation of the narrow lumen and increase the risk of plaque rupture; additionally, VSMCs can secrete multiple inflammatory factors after phenotypic transformation, such as PDGF, monocyte chemoattractant protein-1 (MCP-1), interleukin 1 (IL-1), interleukin 6 (IL-6) and tumor necrosis factor α (TNF-α). These cytokines can not only recruit mononuclear cells to the lesion and promote the formation of foam cells but also increase inflammation and promote vascular injury (20-22). In the present study, we report that EP3 can promote the proliferation and migration of VSMCs, suggesting it is a regulator of the phenotypic switch of VSMCs, which is consistent with the findings in a previous study (23). Our data imply that EP3 is a promising target for treating atherosclerosis and AMI with obstructive coronary arteries. It is worth noting that, in the present work, we did not investigate the regulatory effects of EP3 on the inflammatory response of VSMCs, and this topic remains to be explored in the following studies, which will further clarify the relationship between EP3 and the dysfunction of VSMCs.

The relationship between EP3 and the

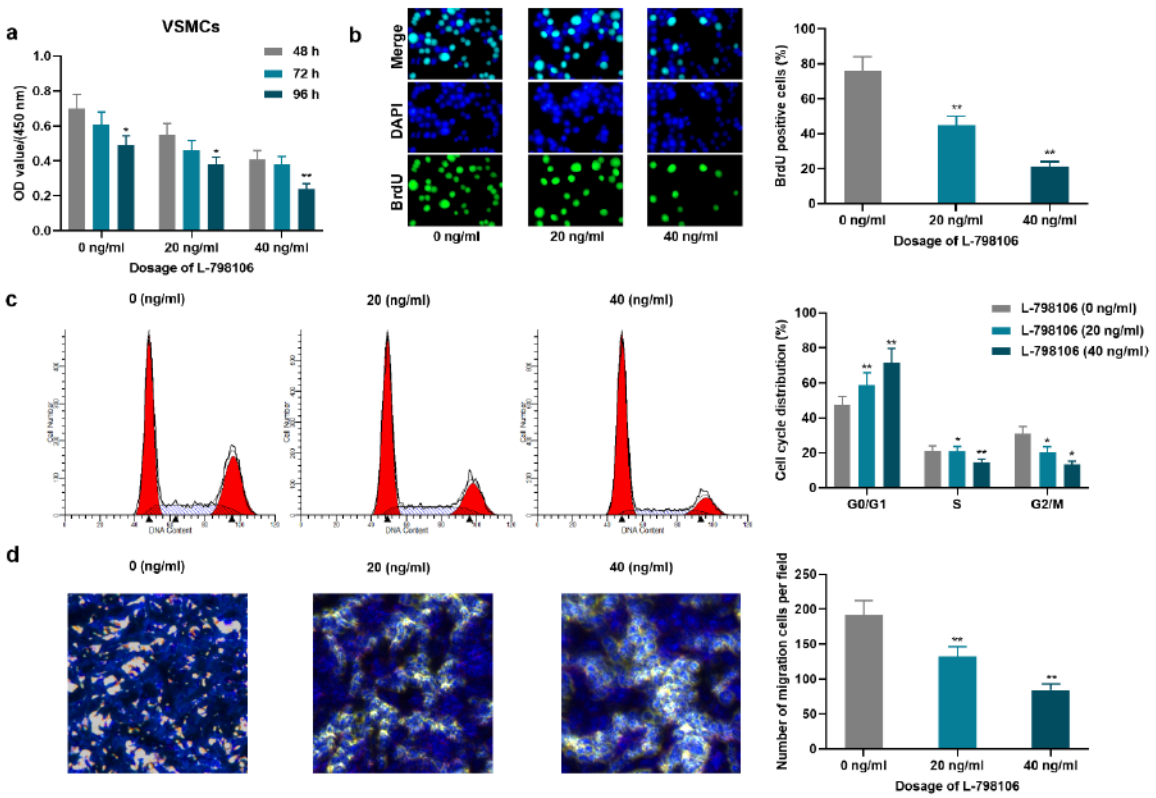

Fig. 3. *Inhibition of EP3 represses the viability, proliferation, cell cycle progression and migration of VSMCs.* ***A****) VSMCs were treated with L-798106 with different doses (0 ng/mL, 20 ng/mL or 40 ng/mL) for different times (48 h, 72 h or 96 h) and then CCK-8 assay was performed to detect the viability of VSMCs;* ***B****) After VSMCs were treated with L-798106 (0 ng/mL, 20 ng/mL or 40 ng/mL) for 48 h, BrdU assay was performed to detect the proliferation of VSMCs;* ***C****) After VSMCs were treated with L-798106 (0 ng/mL, 20 ng/mL or 40 ng/mL) for 48 h, Flow cytometry was conducted to evaluate the cell cycle progression of VSMCs.* ***D****) After VSMCs were treated with L-798106 (0 ng/mL, 20 ng/mL or 40 ng/mL) for 48 h, Transwell assay was performed to examine the migration of VSMCs. *P<0.05 and **P<0.01.*

physiological/pathological processes of vessels has been reported in several studies. It is reported that EP3 mediates prostaglandin E2 (PEG2)-induced constriction of porcine large cerebral arteries via modulating the phenotypes of VSMCs (24). In renal interlobular arteries, the vasoconstrictor effect of PEG2 is also mainly mediated via EP3 (25). Additionally, in a mice model, activation of the EP3 up-regulates baseline blood pressure and contributes to Ang II-dependent hypertension via modulating Ca^{2+} sensitivity and intracellular calcium concentration in VSMCs, and promotes the contractility of vessels (26). Another study reports that EP3 depletion may ameliorate pulmonary hypertension via repressing Rho/TGF-β1 pathway in pulmonary arterial smooth muscle cells (27). Based on the studies mentioned above, it can be easily concluded that EP3 positively modulates contractility and reduces the lumen diameter of arteries. Notably, coronary artery spasm (CAS) is one of the etiologies of AMI with non-obstructive coronary arteries. Our data suggest that activation of EP3 can probably aggravate CAS via promoting the dysfunction of VSMCs, which requires further investigation in the following work with animal models.

Platelets are crucial regulators in the pathogenesis of atherosclerosis and AMI (28). Platelets are activated at the injured intima of arteries, and they mediate the dedifferentiation and proliferation of VSMCs via releasing multiple factors, including PDGF (7). In the present work, we observed that PDGF-BB could up-regulate the expression of EP3 in VSMCs.

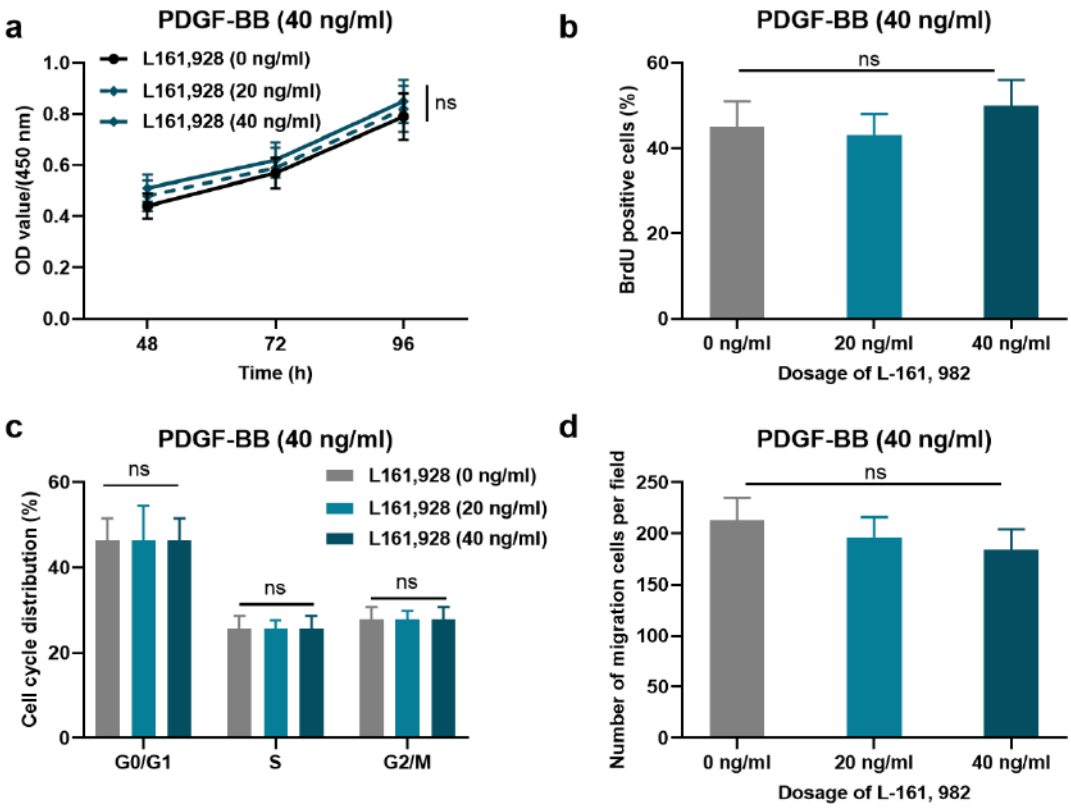

Fig. 4. *Inhibition of EP4 does not change the viability, proliferation, cell cycle progression and migration of VSMCs.* ***A****) VSMCs were treated with L-161928 with different doses (0 ng/mL, 20 ng/mL or 40 ng/mL) for different times (48 h, 72 h or 96 h) and then CCK-8 assay was performed to detect the viability of VSMCs.* ***B****) After VSMCs were treated with L-161928 (0 ng/mL, 20 ng/mL or 40 ng/mL) for 48 h, BrdU assay was performed to detect the proliferation of VSMCs.* ***C****) After VSMCs were treated with L-161928 (0 ng/mL, 20 ng/mL or 40 ng/mL) for 48 h, flow cytometry was conducted to evaluate the cell cycle progression of VSMCs.* ***D****) After VSMCs were treated with L-161928 (0 ng/mL, 20 ng/mL or 40 ng/mL) for 48 h, Transwell assay was performed to examine the migration of VSMCs.*
ns, no significance.

Interestingly, it is reported that EP3 activation in tissues/cells recruits platelets to accumulate. These findings suggest positive feedback among platelets accumulation, EP3 activation and VSMCs' dysfunction.

Interestingly, we observed that the promoting effects of PDGF-BB on the proliferation and migration of VSMCs were not dependent on EP4. This finding further supports the specific and important role of EP3 in the PDGF-mediated dysfunction of VSMCs. To our best knowledge, this is the first study to report the regulatory effects of PDGF on EP3 expression, partly explaining the mechanism of platelets promoting the dysfunction of VSMCs. Notably, a previous study reports that prostaglandin E_2 (PGE2) promotes the proliferation and migration of VSMCs via activating the EP3 signal pathway (23), suggesting that, besides PDGF, the other potential contributors are promoting the dysregulation and dysfunction of EP3 in VSMCs, which remain to be screened and validated in the future.

Some studies report that the activation of EP3 can promote the proliferation, migration and inflammatory responses of human cells via PI3K/Akt pathways. Specifically, PGE2 activates EP3/Src/EGFR/PI3K/AKT/GSK-3β pathway to promote proliferation, migration and invasion of cholangiocarcinoma cells (14); EP3 also activates PI3K/Akt signalling to promote the production of IL-6 in mast cells (15); additionally, in HEK cell line, PGE2 stimulation induces PI3K signalling activation partly via EP3-III isoform (16). In the present work, we observed that EP3 overexpression activates PI3K/Akt signalling in VSMCs, and inhibition of PI3K signalling partly

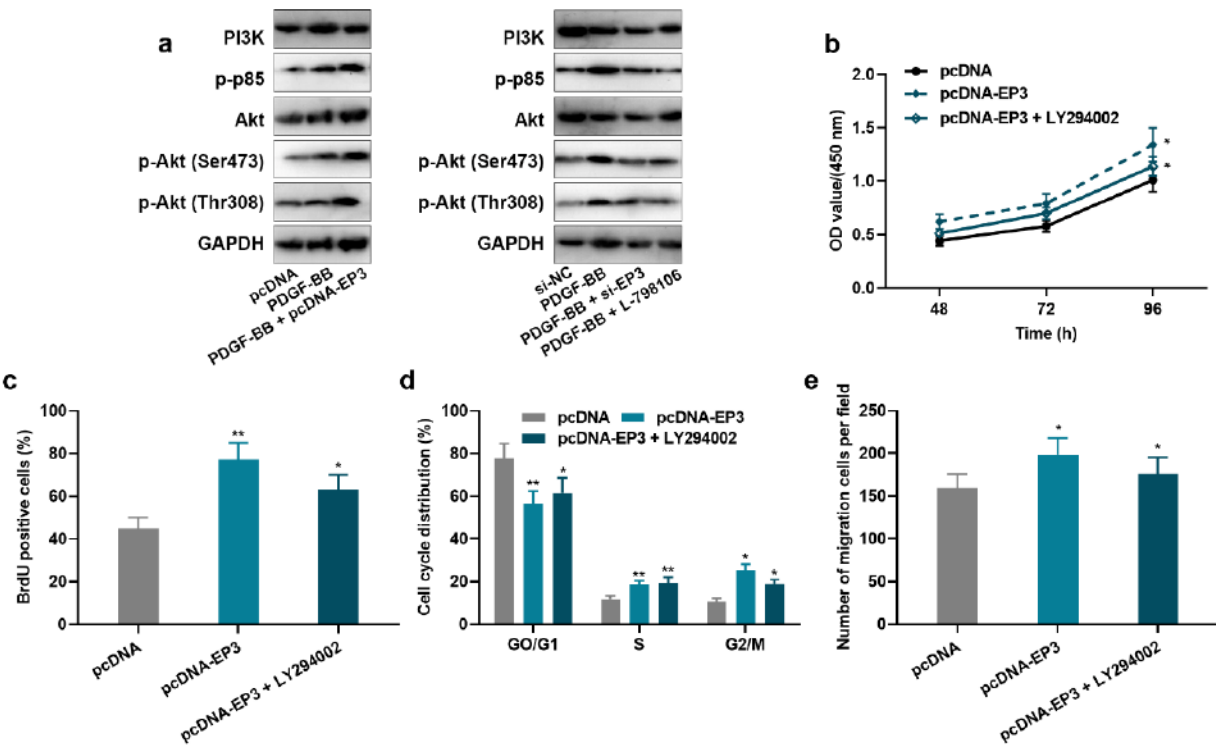

Fig. 5. *EP3 regulates the phnotypes of VSMCs via PI3K/Akt signaling.* ***A****) VSMCs were transfected with EP3 siRNAs or overexpression plasmids, and they were treated with PDGF-BB; additionally, PI3K/Akt inhibitor L-798106 was used to treat the VSMCs after PDGF-BB treatment. Then the expression levels of PI3K, p-p85, Akt, p-Akt in the VSMCs were detected by Western blotting.* ***B****) VSMCs were divided into three groups: pcDNA group, EP3 overexpression group, and EP3 overexpression + LY294002 group, then CCK-8 assay was performed to detect the viability of VSMCs.* ***C****) BrdU assay was performed to detect the proliferation of VSMCs.* ***D****) Flow cytometry was conducted to evaluate the cell cycle progression of VSMCs. F) Transwell assay was performed to examine the migration of VSMCs. *P<0.05 and **P<0.01.*

counteracted the effects of EP3 overexpression. Our findings partly explain the downstream mechanism by which EP3 regulates the phenotypes of VSMCs.

Our study reveals that EP3 up-regulation, induced by PDGF-BB stimulation, promotes the dysfunction of VSMCs via the PI3K/Akt pathway. Our data provide helpful clues to explain the pathogenesis of atherosclerosis and AMI.

Conflict of interest:

All authors declare that they have no conflict of interest.

Funding information:

This study is supported by the Science and Technology Development Plan of Suzhou City, China (SYS2019061), National Natural Science Foundation of China (82170831), Project of Clinical Outstanding Clinical Discipline Construction in Shanghai Pudong New Area (No. PWYgy2018-07), Project of Shanghai Municipality Key Medical Specialties Construction (No. ZK2019C08), Leading Talent Training in Shanghai Pudong New Area Health System (No. PWRl2018-08).

REFERENCES

1. Akyuz A. Exercise and Coronary Heart Disease. Adv Exp Med Biol 2020; 1228:169-79.
2. Sanchis-Gomar F, Perez-Quilis C, Leischik R, et al. Epidemiology of coronary heart disease and acute coronary syndrome. Ann Transl Med 2016; 4(13):256.
3. Moledina A, Tang KL. Socioeconomic Status, Mortality, and Access to Cardiac Services After Acute Myocardial Infarction in Canada: A Systematic Review and Meta-analysis. CJC Open 2021; 3(7):950-64.
4. Fahed AC, Jang IK. Plaque erosion and acute coronary syndromes: phenotype, molecular characteristics and future directions. Nat Rev Cardiol 2021; 18(10):724-34.
5. Chakraborty R, Chatterjee P, Dave JM, et al. Targeting smooth muscle cell phenotypic switching in vascular disease. JVS Vasc Sci 2021; 2:79-94.
6. Zurek M, Aavik E, Mallick R, et al. Epigenetic Regulation of Vascular Smooth Muscle Cell Phenotype Switching in Atherosclerotic Artery Remodeling: A Mini-Review. Front Genet 2021; 12:719456.
7. Bowen-Pope DF, Raines EW. History of discovery: platelet-derived growth factor. Arterioscler Thromb Vasc Biol 2011; 31(11):2397-401.
8. Inoue O, Hokamura K, Shirai T, et al. Vascular Smooth Muscle Cells Stimulate Platelets and Facilitate Thrombus Formation through Platelet CLEC-2: Implications in Atherothrombosis. PLoS One 2015; 10(9):e0139357.
9. Mitchell JA, Kirkby NS. Eicosanoids, prostacyclin and cyclooxygenase in the cardiovascular system. Br J Pharmacol 2019; 176(8):1038-50.
10. Peinhaupt M, Sturm EM, Heinemann A. Prostaglandins and Their Receptors in Eosinophil Function and As Therapeutic Targets. Front Med (Lausanne) 2017; 4:104.
11. Schaid MD, Wisinski JA, Kimple ME. The EP3 Receptor/G(z) Signaling Axis as a Therapeutic Target for Diabetes and Cardiovascular Disease. AAPS J 2017; 19(5):1276-83.
12. Schober LJ, Khandoga AL, Dwivedi S, et al. The role of PGE(2) in human atherosclerotic plaque on platelet EP(3) and EP(4) receptor activation and platelet function in whole blood. J Thromb Thrombolysis 2011; 32(2):158-66.
13. Mawhin MA, Tilly P, Fabre JE. The receptor EP3 to PGE2: A rational target to prevent atherothrombosis without inducing bleeding. Prostaglandins Other Lipid Mediat 2015; 121(Pt A):4-16.
14. Du M, Shi F, Zhang H, et al. Prostaglandin E2 promotes human cholangiocarcinoma cell proliferation, migration and invasion through the upregulation of beta-catenin expression via EP3-4 receptor. Oncol Rep 2015; 34(2):715-26.
15. Morimoto K, Shirata N, Taketomi Y, et al. Prostaglandin E2-EP3 signaling induces inflammatory swelling by mast cell activation. J Immunol 2014; 192(3):1130-7.
16. Israel DD, Regan JW. EP(3) prostanoid receptor isoforms utilize distinct mechanisms to regulate ERK 1/2 activation. Biochim Biophys Acta 2009; 1791(4):238-45.
17. Sorokin V, Vickneson K, Kofidis T, et al. Role of Vascular Smooth Muscle Cell Plasticity and Interactions in Vessel Wall Inflammation. Front Immunol 2020; 11:599415.

18. Chen J, Zhou Y, Liu S, et al. Biomechanical signal communication in vascular smooth muscle cells. J Cell Commun Signal 2020; 14(4):357-76.
19. Badran A, Nasser SA, Mesmar J, et al. Reactive Oxygen Species: Modulators of Phenotypic Switch of Vascular Smooth Muscle Cells. Int J Mol Sci 2020; 21(22):8764.
20. Albany CJ, Trevelin SC, Giganti G, et al. Getting to the Heart of the Matter: The Role of Regulatory T-Cells (Tregs) in Cardiovascular Disease (CVD) and Atherosclerosis. Front Immunol 2019; 10:2795.
21. Ishii S, Ashino T, Fujimori H, et al. Reactive sulfur species inhibit the migration of PDGF-treated vascular smooth muscle cells by blocking the reactive oxygen species-regulated Akt signaling pathway. Free Radic Res 2021; 55(2):186-97.
22. Biros E, Reznik JE, Moran CS. Role of inflammatory cytokines in genesis and treatment of atherosclerosis. Trends Cardiovasc Med 2022; 32(3):138-42.
23. Zhang J, Zou F, Tang J, et al. Cyclooxygenase-2-derived prostaglandin E2 promotes injury-induced vascular neointimal hyperplasia through the E-prostanoid 3 receptor. Circ Res 2013; 113(2):104-14.
24. Jadhav V, Jabre A, Lin SZ, et al. EP1- and EP3-receptors mediate prostaglandin E2-induced constriction of porcine large cerebral arteries. J Cereb Blood Flow Metab 2004; 24(12):1305-16.
25. van Rodijnen WF, Korstjens IJ, Legerstee N, et al. Direct vasoconstrictor effect of prostaglandin E2 on renal interlobular arteries: role of the EP3 receptor. Am J Physiol Renal Physiol 2007; 292(3):F1094-101.
26. Chen L, Miao Y, Zhang Y, et al. Inactivation of the E-prostanoid 3 receptor attenuates the angiotensin II pressor response via decreasing arterial contractility. Arterioscler Thromb Vasc Biol 2012; 32(12):3024-32.
27. Lu A, Zuo C, He Y, et al. EP3 receptor deficiency attenuates pulmonary hypertension through suppression of Rho/TGF-beta1 signaling. J Clin Invest 2015; 125(3):1228-42.
28. Valettas N, Herrmann HC. The role of platelets and platelet inhibition in acute myocardial infarction. Coron Artery Dis 2003; 14(5):357-63.

Multicenter clinical study on biocompatible artificial hair

A. Rateb Said[1], I. Salazar Reyes[2], M. Gara[3], B. Petrovic[4], S. Faddoul[5], C. Chaker[6], R. Romano[7], M. Giovannini[8], G. Griselli[9], B. Al Halabi[10], S. Kalivas[11], D. Kowalczick[12], W. Espinoza[13], Y. Gilony[14], A. Moga[15], L. De Fazio[16], M. Santiago[17], N. Serdev[18]

[1]Dermatologic Dept. University of Cairo, Egypt; [2]Biopel Clinic, Las Americas, Guadalupe, N.L., Mexico; [3]Dr Gara Clinic, Tel Aviv-Yafo, Israel; [4]CMG Clinic, Beograd, Serbia; [5]Dr Faddoul Dermatology Clinic, Lebanon; [6]Dr Rami Hamed Center, Dubai, UAE; [7]Dermaroma Clinic, Manila, Philippines; [8]Clinica Privata Villalba, Bologna, Italy; [9]Dermatologist, Private Practice, Ferrara, Italy; [10]Dr Basem Plastic Surgery, Dubai, UAE; [11]FM care Clinic, Lemesos, Cyprus; [12]DORMIO-Clinique, Warsaw, Poland; [13]Dr Espinoza Plastic Surgery, Lima, Peru; [14]Aesthetic beauty Clinic, Tel Aviv, Israel; [15]Medical Aesthetics Clinic, Paris, France; [16]LDF Hair Clinic, London, United Kingdom; [17]Plastic Surgeon, Private Practice, São Paulo, Brazil; [18]Serdev Clinic, Sofia, Bulgaria

Introduction: Baldness is a current problem in aesthetic medicine. This cosmetic defect can lead to serious psychological and emotional stress. Most of the time, the solution to this problem consists of removing or attenuating its cause: alopecia. Among the current hair restoration technique to treat alopecia, one is the biocompatible artificial hair implant.

Materials and Methods: The certified medical device used for this study is the biocompatible artificial hair Biofibre4.0. The clinical study was done by collecting clinical data from 18 clinics located in 15 different countries and 4 continents to evaluate the efficacy, safety, and performance of a new artificial hair device generation compared to previous artificial hair. Automatic and manual implanter were utilized by doctors participating in these trials. A new needles material was also used for this study. The standard medical protocol was applied with some differences in the doctor's personal experience, patient's situation, and climate.

Results: The data collected show that in a sample of about 1337 patients treated in 2020/2021, inflammation and infections are around 7%, and curling is <1%. There were no phenomena of fibre breakage. Itching appeared in about <3% of cases. The problems encountered in most cases were mild and resolvable with appropriate therapy, and only in rare cases (<1%) it was necessary to proceed with the total removal of the fibres. In some cases (<1%), it was just necessary to partially extract the fibres that cause recurrent discomfort for the patient. In most patients, satisfaction was 96%. The limitations in patient movement and lowering of the immune response in many of them caused by COVID SARS 2 might partially affect the final data.

Conclusion: This surgery does not imply scar formation and hospitalization. It can be used alone or with other treatments to provide psychological benefits and improve quality of life. Indications are poor donor area, request for immediate aesthetic result and scarce trauma. Patient selection, respect for medical protocol and proper aftercare must be complied with. Contraindicated cases must be avoided, and partial or total removal of fibres is required in case of recurrent problems. Additional improvements to this technique are expected to enable an ever vaster application.

Keywords: Alopecia, Baldness, hair Implant, Hair surgery, cosmetic surgery, artificial hair, hair loss

Corresponding author:
Dr Luca De Fazio,
LDF Hair Clinic,
9 Seagrave Road,
SW6 1RP London, United Kingdom
e-mail: drlucadefazio@gmail.com

0393-974X (2022)

Alopecia is common, has a multitude of etiologies, and affects all genders and age groups. Hair restoration can be surgical or non-surgical. Hair transplant (FUT/FUE) is the most common surgical treatment to correct alopecia. This surgery has gained popularity in the years due to continuously growing technical and aesthetic improvements.

The biocompatible artificial hair implant is listed in the arrays of alternative or complementary hair restoration techniques. Artificial hair is a long term implantable medical device, and it must comply with overall safety standard requirements to be certified and approved (1, 2). The implant procedure can be performed using automatic or manual devices. Biocompatible Artificial hair implant has multiple indications, including treating androgenic alopecia, depletion of a donor area, scalp scars or scalp burns (3-10). It can be used alone or with other hair restoration techniques such as FUE and FUT (11-16). It can also be used in combination with other hair treatment as PRP, Mesotherapy. Laser etc. (17). It is indicated for male and female patients to ensure immediate aesthetic results with psychological benefit and improved quality of life 18-26.

No surgical procedure is without complications. Similarly, this procedure also has certain limitations and side effects for different causes. Patients who are affected by skin diseases, diabetes, hepatitis, immune system deficits, and autoimmune diseases who do not comply with the right hygiene and psychological instability or with unrealistic expectations must be avoided. This technique is not indicated for an implant on the temples, low frontal hairline, scalp areas with very thin dermal tissue in case of no stabilized alopecia or in case of a pathologically atrophic scalp. The result of implants in unsuitable areas causes inflammation or infection.

A traumatic implant may be caused by excessive pressure of the implanter device on the scalp. That can cause small scalp injury that leads to infection in most cases. Implanting two or more fibres in the same hole leads to an infection if not removed. Space implanted fibres by 2 mm at least to avoid prospective groupings. Patients are often in a hurry to get a result, but gradual thickening is usually more natural and appreciable. In addition, it is strongly recommended not to implant more than 1500 fibres per session and wait 5 weeks between 2 sessions to allow healing of the scalp and reduce the risk of complications. The use of thin diameter and soft artificial hair fibres is propaedeutic to reduce sebum accumulation.

The timely removal of comedones, if they appear, is important to prevent infection and premature fall of the fibres. The patient's attitude is very important to maximize implant results. Patients must be informed about aftercare protocol and follow up. Use of forbidden treatment or wrong products and lack of proper hygiene can compromise implant results leading to fibre spoiling, local infection, or inflammation. These problems are solvable with appropriate therapy in the majority of cases. If problems are recurrent or not solvable satisfactorily, the partial or total removal of fibres is required.

MATERIALS AND METHODS

This randomized clinical study collected clinical data from 18 clinics spread across 15 countries and 4 continents to evaluate the efficacy, safety, and performance of the medical device Biofibre 4.0, a certified biocompatible artificial hair. The patients included in this trial are implanted with automatic and manual devices. As an additional novelty, a new improved needles material was used in this study. The clinical data are collected by sending to each clinic a form where multiple clinical information was requested to each clinic as:

- *number of patients treated,*
- *number of implanted fibres per session (average),*
- *total number of fibres for each patient (average)*
- *number of patients who perform post-operative controls,*
- *the annual rate of fall of fibres,*
- *number of patients with complications,*
- *type and grade of complications (mild, moderate, serious),*
- *percentage of solved cases,*
- *time of healing expressed on weeks (average),*
- *total number of patients in whom it was necessary for fibres removal,*
- *type of problem that required fibres removal*

Patient selection is compulsory to avoid the prospective

problem. The implant technique is based on small hooking needles that hook the artificial hair reversible knot and place it at the galea aponeurotic level to allow the fibrous tissue to avoid premature hair loss.

A test of 100 artificial hair is performed. After the test, it is recommended to wait 5 weeks to see if some reaction occurs. The area to be implanted is cleaned, disinfected, and draped; 2% xylocaine solution with adrenalin 1:100.000 is locally injected in the subdermal layer with 30G needles for local anaesthesia and vasoconstriction under strict aseptic conditions. There is hardly any bleeding. On concluding implantation, ice wrapped in gauze is applied for 5-10 mins to reduce implant inflammation. A broad-spectrum antibiotic is given, and the implanted area is disinfected. Normal activities were resumed immediately after implant without hospitalization. At home, cleaning and disinfection of the scalp are required with the prescribed products and 7-10 days of antibiotic intaking. The patient can start shampooing his hair from the third day onwards. A medical shampoo with Ketoconazole is recommended twice a week, at least for the first month after the implant, then once a week.

The hair should be washed frequently to remove dust, dirt, sebum and sweat. High-quality neutral shampoo can be used for this purpose. The first medical check-up is required at 4-5 weeks or before in the case of needs. The use of local anti-inflammatory therapies and systemic anti-stamina therapy is suggested in large implant sessions or cases of sensitive skin. Aftercare protocol might be adapted to the patient's situation and local climate.

RESULTS

The data collected show that on a sample of 1337 patients treated in 2020/2021. The incidence of inflammation and infections is around 7%, and curling is <1%. There was no evidence of fibre breakage. Itching appeared in about <3% of cases, but it was a transient situation resolved using medicated shampoo. The problems encountered in most cases were mild and resolvable with appropriate therapy, and only in rare cases (<1%) did patients show more pronounced complications that required the total removal of the fibres.

In some cases (<1%), it was just necessary to partially extract the fibres that cause recurrent discomfort for the patient. The average yearly fall is around 12%. Most patients are satisfied (96%) (Table I).

DISCUSSION

The clinical assessment of the patients before and after implantation of biocompatible artificial hair shows that it may be considered an effective alternative methodology with some good perspectives and some disadvantages.

The advantages are that it offers high hair density in a short time with a natural aesthetic result and with the related psychological and physical wellness for the patient (Fig. 3-6). In addition, it's a soft

Table I. *Data source 2020/2021.*

number of patients treated in this study	**1337**
average annual rate of fall of fibers	**12%**
no. of patients showing mild complications **no. of above mild complications cases resolved with therapy**	**73** **73 (100%)**
no. of patients showing moderate complications **no. of above moderate complications cases resolved with therapy or with partial fiber removal**	**19** **13 (68,42%)**
no. of patients where total removal of fibers was required	**6**
no. of patients showing frizzy hair problem	**<1%**
average of patients satisfied for the procedure	**96%**

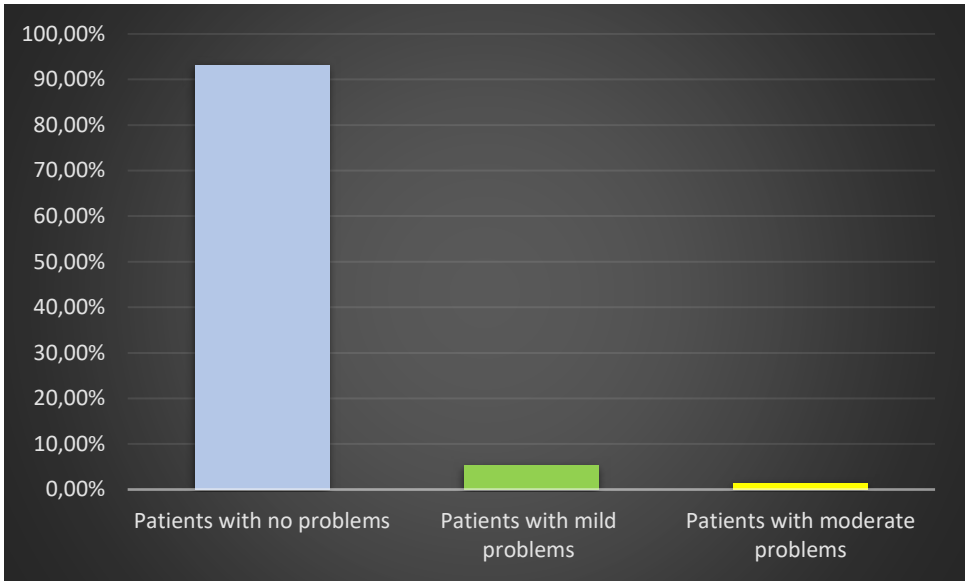

Patients with no problems	93,12%
Patients with mild problems	5,46%
Patients with moderate problems	1,42%

Fig. 1. *Classification rates of problems incurred .*

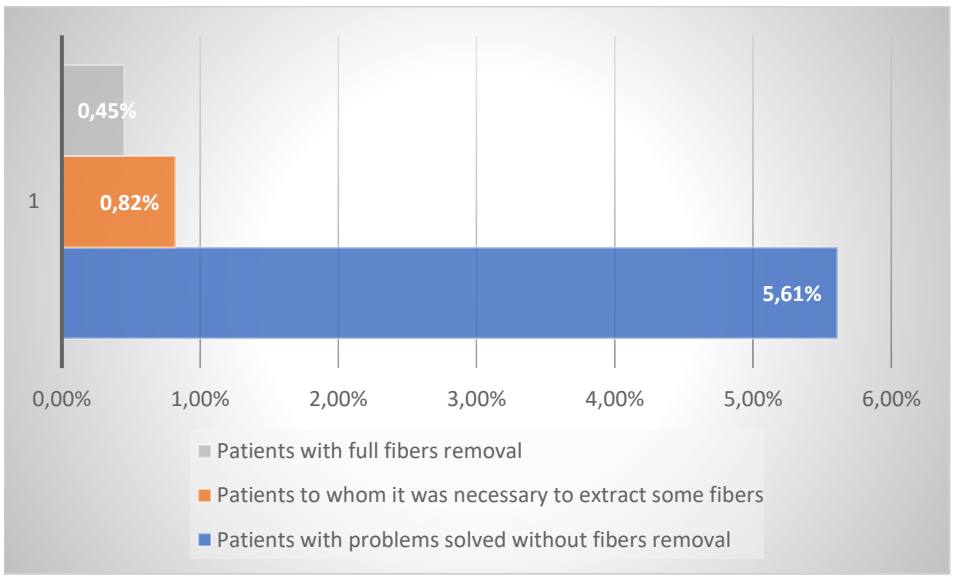

Patients with problems solved without fibers removal	5,61%
Patients to whom it was necessary to extract some fibers	0,82%
Patients with full fibers removal	0,45%

Fig. 2. *Fiber extraction rate*

outpatient procedure that allows the patient to return immediately to his normal social life. No donor area is required, and the artificial hair will not age. The disadvantage of this technique is that not all patients are good candidates, the artificial hair doesn't grow, not the whole scalp area can be implanted successfully, and periodical implant sessions are needed to maintain the expected results.

Aftercare maintenance is also required. Each doctor, according to its geographical location, the different ethnic groups treated, and the different uses, cultures, and habits of the patients, must face different problems.

Patients located far from the clinics have more difficulties in undergoing post-implantation check-ups. These patients have to strictly abide by the aftercare protocol necessary to reduce the risk of complications. Certain groups of patients are more prepared to develop a greater amount of sebum which often, due also to poor maintenance, accumulates at the base of the implanted fibres, creating unsightly sebum plugs. If not removed, it can lead to infection problems, and premature fibres fall. The sebum plugs can be removed directly from the clinic with forceps or can be prevented by following the instructions of

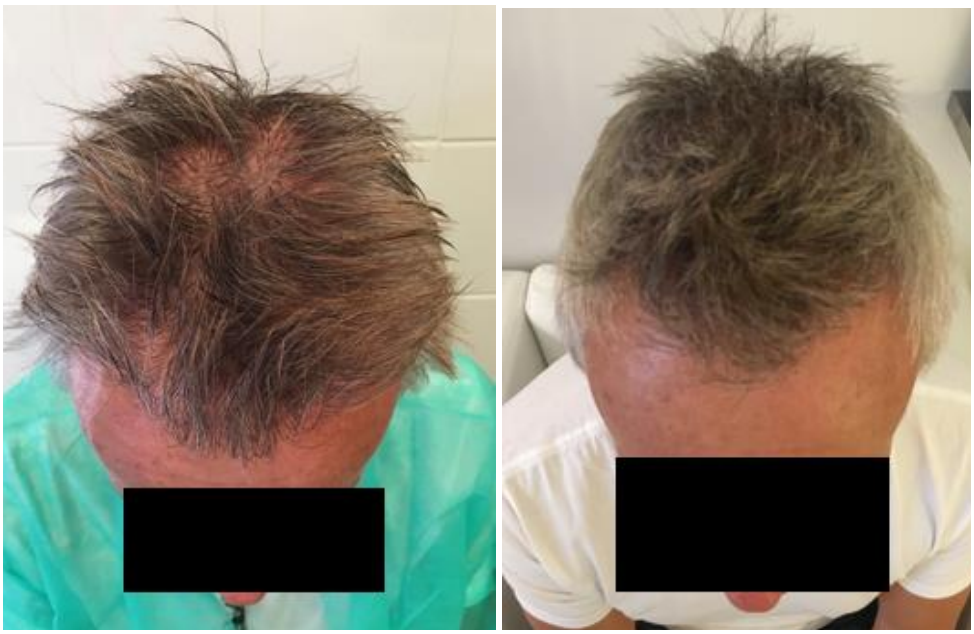

Fig. 3. *Male patient before and after implant of 1000 artificial hair implant.*

Fig. 4. *Female patient before and after implant of 1000 artificial hair implant.*

the post-implantation protocol. In case of prolonged and massive accumulation, these sebum plugs can sometimes create a skin roughness that can be attenuated or eliminated by localized infiltrations of organic silicious.

The use of new pharmacological treatments and specific post-implantation treatments (e.g., targeted use of PRP, LEDs, trace elements, etc.) further assisted in the control of the problems that might emerge after the procedure. The fall proved to be highly variable. The reduced possibility of going to the clinics caused by the COVID-19 lockdown had an impact and highlighted the limitations in movement and the lowering of the immune response in many patients caused by COVID-19; this could partially affect these data that would have been better as a result of a higher standard of biocompatibility of this new generation of artificial hair. It is also interesting to note that the number of explanted fibres is often inversely proportional to the doctor's experience. Less experienced doctors tend to remove fibres more frequently than experienced doctors, who can normally prevent or solve problems that may appear.

CONCLUSION

The data emerging from this multiple centre's clinical studies show the reliability of the medical device Biofibre 4.0. The aseptic prophylaxis and non-fragmenting, scarcely accessible to corrosion, non-migrating fibres are propaedeutic to prevent the risk of bacterial niche and related complications.

Fig. 5. *Young female patient before and after implant of 1500 artificial hair long/ curly.*

Fig. 6. *Front line after 500 artificial hair implants.*

Most of the unsatisfactory cases reported in this study are due to post-operative complications caused by wrong patient selection, implant in an unsuitable area and lack of proper aftercare. Patients' aftercare must include the indications that patients have to follow after implant and must provide a list of products and treatments that must be avoided. According to these premises, the authors might consider providing this procedure to an ever-greater number of patients.

Ethical statements:

The authors received no specific funding for this work.

The authors have declared that no conflict of interest exists.

The authors declared that they received approval and written informed consent.

REFERENCES

1. Universal Medical Device Nomenclature System, Prostheses, Hair, Universal Medical Device Code 16611.
2. Directive 93/42/EEC of the Council concerning Medical Devices.
3. Santiago M, Perez Rangel R, D'ugo A, Griselli G, Igitian G, Garcia Martin I, Nesheim GB, Saad Eddin U, Smith G, Brady GW, Chaker C. Artificial Hair Fiber Restoration in the Treatment of Scalp Scars, Dermatologic Surgery 2007; 33(1):35-44.
4. Franca K. Current and Emerging Therapies in Hair Transplantation and Hair Implants, Oxford Clinical Handbook, May 2017.
5. M. Roccia, K. França, D. Castillo, G. Tchernev, U. Wollina, M. Tirant, Y. Valle, C. Guarneri, M. Fioranelli, T. Lotti. Artificial Hair: By the Dawn to Automatic Biofibre® Hair Implant, OAMJMS, Global Dermatology-2, https://doi.org/10.3889/oamjms.2018.001, eISSN: 1857-9655
6. D'ugo A., Santiago M., Chaker C., Perez Rangel R., Saad Eddin U., Ramponi V. Safety of Biofibre® CE 0373/TGA artificial hair implants: importance of the scalp anchoring system. International Society of Hair Restoration Surgery, 10th Annual Meeting, Chicago, USA, October 9-13, 2002 G. Tchernev Et Al, Biofibre Hair Implant: What is New, What is True? JBRHA, 2016 Apr-Jun;30(2 Suppl 2):27-34
7. A. Rateb, B. Al Bzour, M. Santiago, G. Tchernev, U. Wollina, M. Agrawal, M. Rovesti, F. Satolli, J. Lotti, T. Lotti. Automatic Artificial Hair Implant: Safety and Efficacy in Androgenetic Alopecia. A Prospective Study with a Highly Biocompatible Fiber, OAMJMS, Global Dermatology-2, oamjms.2018.052 eISSN: 1857-9655
8. Gonzalez M. Biofibre hair replacement. ASAPS 35th Anniversary Meeting, Las Vegas, NV, USA, April 27-May 3, 2002
9. A. Rateb, Prosthetic hair fibers. Is there a role ? Twenty years' experience with artificial hair insertion for the treatment of alopecia, FACE Conference, 17-19 June 2017, London, UK
10. T Lotti, M Tirant, A Rateb Said, B Albzour, M Santiago, M Agrawal, A Dutta, T Van Nguyen, M Vadala', B Palmieri, A Vojvodic, M Fioranelli, Clinical updating Study at 3 years on 278 patients treated by modern Artificial hair Implant technique (Automatic Biofibre®) https://onlinelibrary.wiley.com/doi/abs/10.1111/dth.13194
11. Perez Rangel R., How and when to combine the different methods for baldness, 8th World Congress of Cosmetic Dermatology, Cancun, Mexico, February 2012
12. Careno N. - Injerto de pelo: qué hacer cuando no hay pelo donante?, Jornadas Universitarias de la Asociacion de Dermatologia de Chile, Santiago, Chile, 23 of June, 2015
13. Brady G., Case Presentation: 23 Years of Hair Restoration Procedures in a Single Patient, International Society of Hair Restoration Surgery, 11th Annual Meeting, New York, USA, October 15-19, 2003 – poster presentation
14. Seery G., Hair Repair. ISHRS Hair Transplant Forum International 2003; 13(1): 260-261
15. Brady G., Fukuta K., Santiago M., Shiell R., Synthetic Fibers in Hair Restoration: Potential Benefits, Patient Selection, Possible Complications, International Society of Hair Restoration Surgery, 11th Annual Meeting, New York, USA, October 15-19, 2003
16. Morselli M., D'ugo A., Griselli G., Ramponi V., Anichini N., How to achieve a good hair covering in patients without donor area after autotransaplantation, International Society of Hair

Restoration Surgery, 10th Annual Meeting, Chicago, USA, October 9-13, 2002

17. Melissa AB, Angela MC, Lindsey AB, Treatment Options for Primary Cicatricial Alopecia: established Therapies and New Concepts, International Journal of Cutaneous Disorders e Medicine, Vol 2, Issue 2, October 2019
18. Williamson D1, Gonzalez M, Finlay AY. The effect of hair loss on quality of life. J Eur Acad Dermatol Venereol. 2001 Mar;15(2):137-9.
19. Lotti T. Aesthetic Disability, SIME 38TH congress, 12-14 May 2017, Rome, Italy
20. França, et al. Psychological Impact of Scars. In Scars and Scarring. Ed Yongsoo Lee. NovaScience Publishers 2013
21. Rahoui M., Biofibre et Cicatrice de Brulure du cuir Chevelu, 6° Congres National Algérienne de Chirurgie Esthétique, 28-29 Avril 2016, Alger, Algérie
22. Cash TF1, Price VH, Savin RC. Psychological effects of androgenetic alopecia on women: comparisons with balding men and with female control subjects. J Am Acad Dermatol. 1993 Oct;29(4):568-75.
23. Van Der Donk J1, Hunfeld JA, Passchier J, Knegt-Junk KJ, Nieboer C. Quality of life and maladjustment associated with hair loss in women with alopecia androgenetica. Soc Sci Med. 1994 Jan;38(1):159-63.
24. Ramos Et Al, Biofibre Hair Implant – Impact on the Quality of Life, Journal of Biological Regulators & Homeostatic Agents, 2016 Apr-Jun;30(2 Suppl 2):21-5.
25. Santiago M., Fiber Hair Restoration – A Surgical Option to Treat Female Pattern Baldness, International Society of Hair Restoration Surgery, 11th Annual Meeting, New York, USA, October 15-19, 2003 – poster presentation
26. R. Dell'avanzato, B. Al Bzour, R. Perez Rangel, M. Agrawal, N. Serdev : Automatic Biofibre Hair Implant an Innovative Hair Restoration Technique for the Improvement of Quality of Life, Journal of Cosmetology and Trichology, Vol 4, Issue 1, ISSN:2471-9323 https://www.biofibre.com/wp-content/uploads/2018/08/186-dell-avanzato-et-al-JCTT.pdf.

Penehyclidine hydrochloride combined with fasudil reduces inflammation and improves kidney function in renal ischemia-reperfusion injury rats

X-Q. Shao[#], S-F. Sun[#,*], Q. Xu, T. Zhang, S-Q. Wei and D-D. Li

Department of Anesthesiology, Weifang Maternal and Child Health Hospital, Weifang, China

[#]These authors contributed equally to this work

Letter to the Editor,

Renal ischemia-reperfusion injury (RIRI) is a common injury in kidney surgery. It is one of the causes of surgical complications and one of the important factors affecting the success rate of surgery (1). In addition, RIRI has great harm to the normal physiological functions of kidneys in patients, which can lead to acute renal failure and even endanger patients' lives. Therefore, it is essential to prevent and improve RIRI.

During RIRI, the pathological reactions caused by ischemic and hypoxic injury are very complicated, including inflammation, apoptosis and toxic effect, which can further aggravate the ischemic and hypoxic injury, damaging the kidney tissues and affecting the normal physiological function of the kidney (2, 3). Meanwhile, severe damage can be caused to the kidney by complex pathology in RIRI, which is not conducive to the repair and functional recovery of kidney tissues after injury. In addition, previous evidence demonstrated that nuclear factor-κB (NF-κB) plays an essential regulatory role in inflammation after RIRI (4).

The combined application of phencyclidine hydrochloride (PHC) and fasudil was reported to improve microcirculation; however, the potential molecular mechanism remains unclear (5). Therefore, the present study aimed to explore the effects of PHC combined with fasudil on RIRI rats and to further investigate the underlying mechanism.

MATERIALS AND METHODS

RIRI animal models establishment and grouping

A total of 36 Sprague-Dawley rats (male: female=1:1) weighing about 200 g, purchased from Shanghai SLAC Laboratory Animal Co., Ltd. (Shanghai, China), were randomly divided into normal groups (n=12), model group (n=12), and treatment group (n=12). The Animal Ethics Committee approved this study of Weifang Medical University Animal Center. The rats were fed normally in the normal group. The RIRI model was established in the model group according to a previous study (4). PHC (0.2 mg/kg) combined with fasudil (30 mg/kg) was intraperitoneally injected into the RIRI rats in the treatment group. After intervention for 7 d, the samples were taken for detection. After successful anesthesia, the abdominal aortic blood was first drawn from each rat. Then, the kidney tissues were directly taken from 6 rats in each group.

Immunohistochemistry

The paraffin-embedded tissues were sliced into

Keywords: renal ischemia-reperfusion, inflammation, phencyclidine hydrochloride, fasudil

**Corresponding Author:*
Dr Shufang Sun
Department of Anesthesiology,
Weifang Maternal and Child Health Hospital,
407 Qingnian Road, Weicheng District,
Weifang, Shandong 261021, China
e-mail: sunshufang@stu.cpu.edu.cn

0393-974X (2022)

5 μm-thick sections, flattened in water at 42°C and prepared into paraffin sections. Then the sections were soaked and routinely deparaffinized in xylene solution and gradient alcohol, followed by adding the endogenous peroxidase blocker. After the sections were washed and sealed with goat serum for 20 min, the anti-NF-κB (1:200) primary antibody was added for incubation at 4°C overnight. On the next day, the sections were washed, incubated with the secondary antibody for 10 min and reacted with a streptavidin-peroxidase solution for 10 min, followed by colour development with diaminobenzidine (DAB) (Solarbio, Beijing, China). Finally, the sections were sealed and observed under a microscope after being counterstained with hematoxylin.

Western blotting

The kidney tissues were lysed with lysis buffer and then were centrifuged at 14,000 g for 10 min. The protein was quantified using the bicinchoninic acid (BCA) method (Pierce, Rockford, IL, USA). Protein samples with the adjusted same concentration were separated and then loaded on polyvinylidene fluoride membranes followed by being blocked with defatted milk (5%) for 2 h and subsequently incubated with primary antibodies at 4˚C overnight. After that, secondary antibodies were added for further incubation for 2h, followed by bands being exposed via an electrochemiluminescence (ECL) kit.

Quantitative real-time polymerase chain reaction (qRT-PCR)

TRIzol was used to extract the total RNA. *qRT-PCR* was performed according to the previously established instructions. Glyceraldehyde 3-phosphate dehydrogenase (GAPDH) was served as the internal control. The $2^{-\Delta\Delta Ct}$ method was used for the quantitative analysis. The primer sequences are shown in Table I.

Enzyme-Linked Immunosorbent Assay (ELISA)

After the abdominal aortic blood samples were centrifuged at 14,000 g for 10 min, ELISA was performed according to the manufacturers' instructions. Finally, the absorbance value was measured at 450 nm using a microplate reader. Next, the levels of serum creatinine (Cr) and blood urea nitrogen (BUN) in venous blood were determined using a full-automatic biochemical analyzer.

Statistical analysis

Statistical Product and Service Solutions (SPSS) 20.0 software (IBM, Armonk, NY, USA) was used for statistical analysis. Enumeration data were expressed as mean ± standard deviation. Comparison between multiple groups was made using a one-way ANOVA test followed by Post Hoc Test (Least Significant Difference). P values < 0.05 were considered statistically significant.

RESULTS

The positive rate of NF-κB expression was found to be lower in the normal group but higher in the other two groups. According to the statistical results (Fig. 1A), the mean optical density of NF-κB positive expression was significantly lower in

Table I. *Primer sequences*

Gene	Primer sequence
IL-6	F: 5'-GGCGCTTATAGCAATTGGGTTA-3' R: 5'-TTAGTAAGCCAATTCAGCCAAT-3'
IL-18	F: 5'-GGCGTTATCCGCAATAAGCCGT-3' R: 5'-AATCTGGCATCCATTGCCTAATC-3'
GAPDH	F: 5'-ACGGCAAGTTCAACGGCACAG-3' R: 5'-GAAGACGCCAGTAGACTCCACG-3'

the normal group than that in the other two groups, showing statistically significant differences (P<0.05). The protein expression of NF-κB was lower in the normal group but higher in the other two groups (Fig. 1B). According to the statistical results, the relative protein expression of NF-κB was significantly higher in the other two groups than that in the normal group (P<0.05). Additionally, treatment of PHC combined with fasudil remarkably inhibited the expression of NF-κB in RIRI rats (P<0.05).

The normal group had lower mRNA expressions of IL-6 and IL-18 than the other two groups (P<0.05). The treatment group also had significantly lower mRNA expressions of IL-6 and IL-18 than the model group (P<0.05) (Fig. 2A). The content of IL-6 and IL-18 was remarkably lower in the normal group than that in the other two groups (P<0.05), while it was also remarkably lower in the treatment group than that in the model group (P<0.05) (Fig. 2B). The content of BUN and Cr was markedly lower in the normal group than that in the other two groups (P<0.05). Furthermore, treatment of PHC combined with fasudil remarkably inhibited the levels of BUN and Cr after RIRI (P<0.05) (Fig. 2C).

DISCUSSION

The pathological reactions after RIRI are a series of complex cascade reactions, in which inflammation is a major one that has important influences on the further damage to kidney tissues after RIRI, repair of kidney tissues and recovery of kidney physiological function (6). Studies have demonstrated (7-9) that a large number of inflammatory factors, including IL-6 and IL-18, in kidney tissues will be released after RIRI in a hypoxic and ischemic environment. Furthermore, the inflammatory factors, such as IL-6 and IL-18, can enhance the release of other inflammatory factors and mediators, leading to worse destruction of the renal interstitium and accelerated glomerular sclerosis and

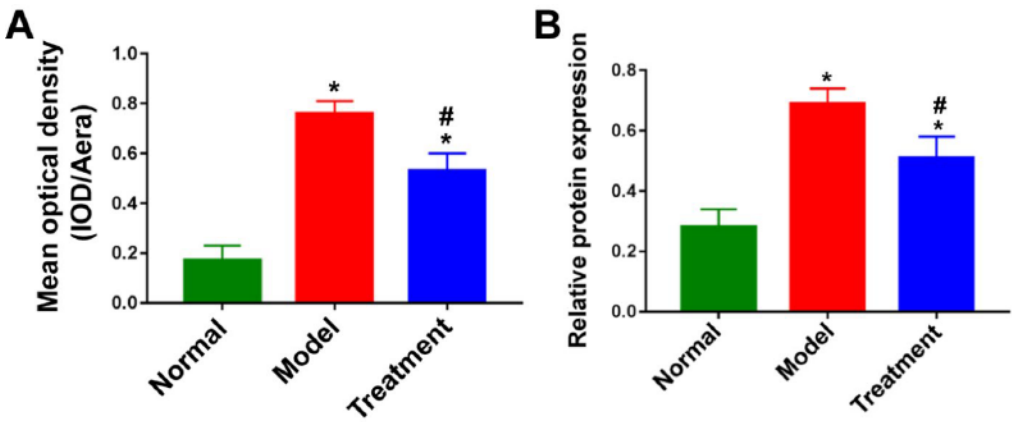

Fig. 1. Treatment of PHC combined with fasudil inhibited the expression of NF-κB in RIRI Rats; A) Mean optical density of positive expression of NF-κB via Immunohistochemistry in each group; B) Relative protein expression of NF-κB based on Western blotting results in each group. (*P<0.05 vs. normal group, #P<0.05 vs. model group).

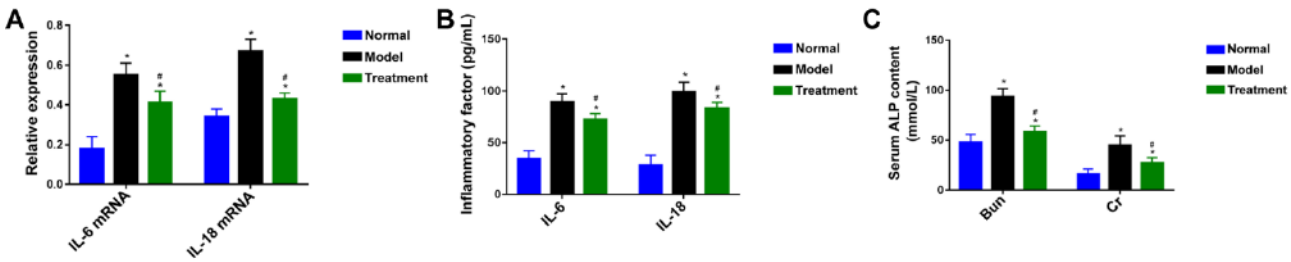

Fig. 2. Treatment of PHC combined with fasudil reduced inflammation and improved kidney function in RIRI Rats; A) mRNA expressions of IL-6 and IL-18 detected via qPCR; B) The content of IL-6 and IL-18 determined by ELISA; C) The levels of BUN and Cr in each group. (*P<0.05 vs. normal group, #P<0.05 vs. model group).

mesangial cell proliferation. As a nuclear transcription factor, NF-κB is widely expressed in renal tubular epithelial cells and mesangial cells (10-12). In the ischemic and hypoxic environment, a large number of cytokines and inflammatory factors will be released by injured tissues, thus further activating NF-κB. As a result, activated NF-κB enters the nucleus to bind to its corresponding sites, further activating downstream molecules and mediating inflammation.

This study found that the content of inflammatory factors IL-6 and IL-18 significantly rose, the NF-κB signaling pathway was activated, and the expression of NF-κB was significantly increased after RIRI. PHC and fasudil can well improve microcirculation and resist inflammation. This study further confirmed that PHC combined with fasudil exerted a specific inhibitory effect on the NF-κB signaling pathway after RIRI, reduced the expression of NF-κB and inhibited the inflammation after RIRI, which may be one of the important reasons for its improvement of kidney function. In conclusion, PHC combined with fasudil reduced inflammation and improved kidney function in RIRI rats *via* inhibiting the NF-κB signaling pathway.

Conflict of interest:

The authors declared no conflict of interest.

REFERENCES

1. Menting TP, Ergun M, Bruintjes MH, et al. Repeated remote ischemic preconditioning and isoflurane anesthesia in an experimental model of renal ischemia-reperfusion injury. Bmc Anesthesiol 2017; 17:14.
2. Pressly JD, Mustafa SM, Adibi AH, et al. Selective Cannabinoid 2 Receptor Stimulation Reduces Tubular Epithelial Cell Damage after Renal Ischemia-Reperfusion Injury. J Pharmacol Exp Ther 2018; 364:287-299.
3. Liu M, Xie J, Zheng X, Wang M, Chen G, Wang T, Lu Y. Correlation between Stromal Cell-Derived Factor 1 and the Prognosis of Transient Ischemic Attack. Iran Red Crescent Me 2021; 23: e348.
4. Zhang Y, Hu F, Wen J, et al. Effects of sevoflurane on NF-small ka, CyrillicB and TNF-alpha expression in renal ischemia-reperfusion diabetic rats. Inflamm Res 2017; 66:901-910.
5. Zeng P, Pi RB, Li P, et al. Fasudil hydrochloride, a potent ROCK inhibitor, inhibits corneal neovascularization after alkali burns in mice. Mol Vis 2015; 21:688-698.
6. Zhou S, Sun Y, Zhuang Y, et al. Effects of kallistatin on oxidative stress and inflammation on renal ischemia-reperfusion injury in mice. Curr Vasc Pharmacol 2015; 13:265-273.
7. Tadagavadi RK, Wang W, Ramesh G. Netrin-1 regulates Th1/Th2/Th17 cytokine production and inflammation through UNC5B receptor and protects kidney against ischemia-reperfusion injury. J Immunol 2010; 185:3750-3758.
8. McGinn J, Zhang F, Aziz M, et al. The Protective Effect of a Short Peptide Derived From Cold-Inducible RNA-Binding Protein in Renal Ischemia-Reperfusion Injury. Shock 2018; 49:269-276.
9. Gholampour H, Moezi L, Shafaroodi H. Aripiprazole prevents renal ischemia/reperfusion injury in rats, probably through nitric oxide involvement. Eur J Pharmacol 2017; 813:17-23.
10. Liu YQ, Xie YZ, Wu F, Ma B, Ren ZX, Tian Y. OTUD7B suppresses the progression of melanoma via inhibiting the activation of NF-kappa B signaling. J Biol Reg Homeos Ag 2021; 35:1939-1945.
11. Xu JJ, Li XQ, Hu XM, Chen MR, Chen QL, Wu WF, Quan K. Pogostone attenuates traumatic brain injury-induced inflammatory response and neurological damage via regulating NF-kappa B and PPAR-gamma pathways. J Biol Reg Homeos Ag 2021; 35:1245-1253.
12. Yeo JY, Hwang KW, Park S. Anti-inflammatory effect of neo-lignan isoamericanin A via suppression of NF-kappa B in liposaccharide-stimulated RAW 264.7 cells. Trop J Pharm Res 2020; 19:1857-1862.

A study on myocardial fibrosis in rats with post-myocardial infarction heart failure based on Luofengning No. 2 in the transforming growth factor-β/Smads pathway

X-Q. Yang[1#], X-Z. Wang[2#] and X. Wang[3*]

[1]Cardiovascular Department, Shunyi Hospital, Beijing Traditional Chinese Medicine Hospital, Beijing, China; [2]Department of Function Examination, Beijing University Chinese of Medicine Third Affiliated Hospital, Beijing, China; [3]Cardiovascular Insititute, Dongzhimen Hospital of Beijing University of Chinese Medicine, Beijing, China

[#]These authors contributed equally to this study

Objective: The present study aims to observe the effects of Luofengning No. 2 on cardiac function, histopathology, and the transforming growth factor-β (TGFβ)/Smads pathway in rat models.

Methods: A post-myocardial infarction heart failure (HF) model was constructed, and a total of 50 male Sprague Dawley rats were randomly divided into six groups: (1) the model group (n = 6), (2) the captopril group (n = 6), (3) the low-dose Luofengning No. 2 group (n = 6), (4) the medium-dose Luofengning No. 2 group (n = 7), (5) the high-dose Luofengning No. 2 group (n = 6), and (6) the sham operation group (n = 5). The serum N-terminal pro-brain natriuretic peptide (NT-proBNP) levels were detected using the enzyme-linked immunosorbent assay, and myocardial fibrosis (MF) was observed through Masson staining. In addition, the collagen volume fraction (CVF) was calculated, and the myocardial tissue TGFβ1, Smad2/3, collagen type I (Col-I), and collagen type III (Col-III) protein expressions were detected using Western blot testing.

Results: The general conditions of the rats in the drug administration groups were improved, and the heart weight index, left ventricular weight index, and serum NT-proBNP levels were significantly lower compared with the model group ($p<0.05$ or $p<0.01$). Furthermore, the TGFβ1, Smad2/3, Col-I, collagen type III (Col-III), and CVF protein levels in the drug administration groups were significantly lower compared with the model group ($p<0.05$ or $p<0.01$). There existed no statistically significant differences in NT-proBNP levels; TGFβ1, Smad2/3, Col-I, and Col-III protein levels; or MF degrees between the captopril group and the high-dose Luofengning No. 2 group ($p>0.05$).

Conclusion: Luofengning No. 2 might positively affect cardiac function and anti-MF improvement in rats with HF; this could be related to TGFβ1/Smad2/3.

Myocardial fibrosis (MF) refers to localized cardiomyocyte apoptosis in response to stimuli, such as ischemia and hypoxia, replaced by abnormal were higher and overdeposition of extracellular matrix, thus leading to an increase in myocardial stiffness and decrease in compliance. (1) Pathological heart diseases, such as myocardial infarction (MI) and hypertension, are important in MF development. Furthermore, MF is an important cause of chronic heart failure (CHF) (2). Previous studies have shown

Keywords: Chronic heart failure; Luofengning No. 2; Myocardial fibrosis; TGFβ/Smads pathway

*Corresponding Author:
Dr Xian Wang
Cardiovascular Insititute
Dongzhimen Hospital of Beijing University of Chinese Medicine,
No. 5. Haiyuncang Street, Dongcheng District,
100700 Beijing, China
e-mail: wx650515@163.com

0393-974X (2022)

that MF inhibition can delay CHF development and have important implications for patient outcomes (3). The transforming growth factor-β1 (TGFβ1) is an important fibrosis-promoting factor that plays a key role in myocardial remodelling (4). As one of the downstream signalling molecules of TGF-β, the Smads protein mediates intracellular TGFβ1 signalling. Moreover, the TGFβ1/Smads signalling pathway plays a key role in MF development; effective inhibition of this pathway is vital for MF prevention (5).

Luofengning No. 2 is prescribed on the therapeutic basis of "arming Yang and benefiting Qi, promoting blood circulation and inducing diuresis, expel wind and dredge collaterals. "Previous studies have revealed that Luofengning No. 2 can achieve significant clinical efficacy in patients' CHF treatment (6–9) and that it has a specific impact on CHF MF markers (10–11). The present study aims to observe the effects of Luofengning No. 2 on cardiac function, histopathology, and the influence of key factors, including TGFβ1, Smad2/3, collagen type I (Col-I), and collagen type III (Col-III), on the TGFβ1/Smads pathway in rats with heart failure (HF).

MATERIALS AND METHODS

Experimental animals

A total of 50 healthy male, SPF-grade Sprague Dawley rats, aged 12 weeks, with a weight of 200 ± 20 g, were purchased from the Experimental Animal Center of Hebei Medical University under the license number SCXK (Hebei) 2013-1-003 and the experimental animal use license number SYXK (Hebei) 2011-0057. The rats were housed at room temperature, had free drinking access, and were fed with standard rat chow.

Experimental drugs

Luofengning No. 2 was processed in the granular form by the Preparation Room of Shunyi Hospital, Beijing Chinese Medicine Hospital. The captopril tablet (Kaibotong) specifications were: 12. 5 mg/tablet, with CN CNS: H31022986, produced by the Sino-American Shanghai Squibb Pharmaceutical Co. promotes blood circulation and removes dampness; Bitter Apricot Kernel resolves sputum and soothes asthma; Tuckahoe, *Rhizoma atractylodis macrocephalae*, *Fructus amomi*, Dried Tangerine Peel, Sandalwood, and *Pinellia ternata* regulate Qi for phlegm elimination in the collaterals and fortify the spleen for dampness disinhibition; *Codonopsis pilosula*, *Astragalus membranaceus*, and *Salvia miltiorrhiza* can benefit Qi and promote blood circulation for blood stasis removal without vital Qi damage, and *Semen lepidii* and *Rhizoma alismatis* induce diuresis for edema alleviation. Furthermore, three wind-expelling herbs, *Cynanchum paniculatum*, *Stephania tetrandra,* and Pyrola, have a flying and fragrant nature; this can activate yang Qi and blood, clear Qi movement, and induce diuresis for edema alleviation. The herbs in this prescription cautiously watch the pathogenesis and differentiate among disease categories.

Main reagents and instruments

The main reagents used were as follows: (1) Masson staining solution, anhydrous ethanol, hematoxylin, and Lichon Red (Sinopharm Chemical Reagent Co. Ltd.); (2) N-terminal pro-brain natriuretic peptide (NT-proBNP) enzyme-linked immunosorbent assay (ELISA) kit (item # SEA598, Beijing Yi Aoming Technology Co.); (3) RIPA lysate (item # R0020), 30% acrylamide (item # A1010), 1M Tris-HCL (pH 6. 8) (item # T1010), 1. 5M Tris-HCL (pH 8. 8) (item # T1020), 2 × protein loading buffer (item # P1016) (Beijing Solebo Biotechnology Co.); pre-staining protein marker (item # 26616) (Thermo Co.); (4) polyvinylidene difluoride (PVDF) membrane (item # IPVH00010) (MILLPORE Company); intense ECL reagent kit (item # E411-04) (Nanjing Novozan Biotechnology Co.); (5) Col-III antibody (item # 84336S) and Smad2/3 antibody (item # 8685S) (Cell Signal Technology); (6) Col-III antibody (item # ab7778) and TGFβ1 antibody (item # ab179695) (Abcam Company); and (7) β-actin (Bioengineering Co.).

The instruments used were as follows: (1) embedding machine, pathology sectioning machine, tissue spreading machine (Zhejiang Jinhua Kedi Instruments & Equipment Co.); (2) upright optical microscope (produced by Nikon, Japan); (3) optical microscope (Olympus Corporation, model IX71); (4) Rat Ultrasound Imaging System (Canadian VisualSonics corporation, model Vevo 2100); (5) Rat Ultrasound Probe (Canadian VisualSonics corporation, model MS 250, frequency range 14–24 MHz); (6) MultiSkan FC enzymometer (Thermo Fisher Scientific Co. , Ltd.); (7) low-speed centrifuge (Beijing Leiboer Centrifuge Co. , Ltd.); (8) vortex mixer (Beijing Jinbeide

Industry and Trade Co. , Ltd.); (9) electronic balance (German Sartorius Corporation); (10) low-temperature refrigerator (−80°C) and low-temperature refrigerator (4°C) (Qingdao Haier); (11) deionized water meter (America PALL, Purelab Plus); (12) medical X-ray film (Kodak Corporation of America); (13) high-speed centrifuge and low-temperature centrifuge (Eppendorf Corporation of Germany); (14) transfer decoloring shaker (Haimen Qilin Bell Instrument Manufacturing Company); and (15) electrophoresis instrument, vertical electrophoresis tank, and transfer tank (Beijing Liuyi Instrument Factory).

Animal grouping

The rats included in the present study were randomly divided into six groups: (1) the model group (n =6), (2) the captopril group (n = 6), (3) the low-dose Luofengning No. 2 group (n = 6), (4) the medium-dose Luofengning No. 2 group (n = 7), (5) the high-dose Luofengning No. 2 group (n = 6 rats), and (6) the sham operation group (n = 5). The model group survival rate was 43/50 × 100% = 86%, with a successful modeling rate of 36/50 × 100% = 72%, and the sham operation group survival rate was 5/6 × 100% = 83. 3%. After 50 SD rats were modelled, 7 rats died within 48 hours after the operation. After ECG measurement, 3 unmodeled rats were excluded. And then 4 rats died due to administration.

Model preparation

The rats were anaesthetized using pentobarbital sodium, intubated via laryngotracheal intubation, and connected to a ventilator (assisted breathing at 80 times/min and a tidal volume of 0.7–0.8 ml) and an ECG oscillograph for monitoring. Left anterior descending artery (LAD) ligation was performed in the model group. (12–13) ECG was performed postoperatively, and the upward dorsal elevation of the ST segment in ECG lead I, together with the visually observed paling of the left ventricular myocardium wall in the ligation area, was regarded as a sign of successful ligation. The rats in the sham operation group were given only a loop in the LAD thread without ligation. A left ventricular ejection fraction (LVEF) of ≤45%, as measured by Doppler echocardiography 8 weeks after the operation, was considered a marker of a successful HF model. (14) The ECG I lead T-segment increased, and the ligation area left ventricular wall became pale (this was revealed via naked eye observation); both were signs of successful ligation. Once more, an LVEF of ≤45% (measured via Doppler echocardiography 8 weeks after the operation) was used as the mark of a successful HF model. We performed ECG after the rats were divided into model and sham operation groups. We performed Doppler echocardiography after the ligation operation for about 8 weeks. Heart failure is determined in the following ways: ST-segment increased in the ECG I lead, and the left ventricular wall in the ligation area became pale through naked eye observation, which was a sign of successful ligation. Furthermore, the left ventricular ejection fraction ≤ 45% was used as the successful mark of the heart failure model by Doppler echocardiography after 8 weeks.

Drug administration

The drug dosage was determined based on the bodyweight unit and a previous experimental study;(11) all groups underwent continuous gavage for 4 weeks.

The rats underwent gavage as follows: (1) the model group with 10 mL/kg double-distilled water; (2) the captopril group with 9. 322 mg/kg captopril; (3) the low-dose Luofengning No. 2 group with 3. 31g/kg Luofengning No. 2; (4) the medium-dose Luofengning No. 2 group with 6. 62g/kg Luofengning No. 2; (5) the high-dose Luofengning No. 2 group with 13. 24g/kg Luofengning No. 2; and (6) the sham operation group with 10mL/kg double-distilled water.

The activity level, food and water consumption, respiration, reaction sensitivity, fur characteristics (softness, neatness, and lustrousness), ear, paw, and tail colour, and the presence of edema were observed in each rat group.

Heart weight index and left ventricular weight index levels

Each rat was anaesthetized. Next, the heart was quickly removed; the whole heart mass was weighed, and the superficial vessels and atria were cut out. Next, the left ventricular mass was immediately weighed; the whole heart mass–body mass ratio was used as the heart weight index (HWI) (mg/g), and the left ventricular mass–body mass ratio was used as the left ventricular weight index (LVWI) (mg/g).

Serological indicator of N-terminal pro-brain natriuretic peptide

After 4 weeks of gavage, each rat was anaesthetized with blood collected from the abdominal aorta. The blood

specimen was centrifuged at 3.000 r/min for 10 min, and the supernatant was placed in a −80°C refrigerator for examination. The serum NT-proBNP level was detected using ELISA; the process was conducted in accordance with the kit instructions.

Masson staining and collagen volume fraction detection

The cross-sectional myocardium of the mid-left ventricle was selected from each rat; three paraffin-embedded tissue sections were subjected to Masson staining, and five fields of view were randomly selected from each section at a 400× bright field of view. The myocardial collagen area was calculated using the Image-Pro-Plus 6. 0 medical image analysis software, and the collagen tissue area percentage in the measured field of view was taken as the collagen volume fraction (CVF).

Myocardial tissue TGFβ1, Smad2/3, Col-I, and Col-III protein expression detection using Western blot

The left ventricular myocardium of all heart specimens was divided into two parts; these were perpendicular to the long axis from the apex. One was used for myocardial histopathological observation, and the other was used for Western blot analysis. The tissue from the upper part of the infarcted left ventricle region was removed from the −80°C refrigerator, and approximately 50 mg of tissue was weighed from each group. Next, 600 μl of the lysis solution (prepared as RIPA lysis solution-PMSF-phospho-protease inhibitor at a 100:1:1 ratio) was added to the specimen in each group. The specimen was ground with a glass homogenizer, left to stand still, and centrifuged. Next, the supernatant was taken to obtain the total sample protein. Protein quantification was performed using the bicinchoninic acid method (the process was conducted according to the instructions), and the protein concentration in each sample was calculated by measuring the A at 562 nm in each well using an enzymometer. A 2 × sample buffer was added and boiled for 12 min. Next, the samples were added to the sodium dodecyl sulphate-polyacrylamide gel electrophoresis, first at 80 V constant pressure for approximately 30 min, and then to perform the electrophoresis at 110 V constant pressure until the marker strip was separated. The desired target strip was cut off, and a 250-mA constant-current membrane transfer was performed for 100 min using the double sandwich method with a white plastic plate–sponge–4-layer, filter paper–PVDF membrane-target glue–4-layer, filter paper-sponge–black plastic plate structure. It was then sealed with 5% skimmed milk for 1 h combined with a non-specific background. The primary antibody was added at 4°C overnight on a shaker and washed with Tris-buffered saline with Tween (TBST) three times for six min. After adding the secondary antibody, the specimens were incubated at room temperature for 1 h and washed with TBST again three times for six min. The ECL solution was added for colour development, and a chemiluminescence imaging developer scanned the sample. Grayscale scans of the target bands were performed using the ImageJ software, and the expression levels of the target protein were shown as the grayscale ratio to the internal reference glyceraldehyde-3-phosphate dehydrogenase.

Rat cardiac structure and function change detection in each group using echocardiography

Each rat was anaesthetized, and echocardiography was performed in each group after a 4-week gavage. The raw data from each group comprised the averaged value of three consecutive cardiac cycles. The detection indicators included the left ventricular end-systole dimension (LVDs), left ventricular end-diastole dimension (LVDd) and LVEF.

Statistical analysis

The experimental data were expressed as means ± standard deviations ($\bar{x}\pm s$), and the Statistical Package for Social Sciences 17. 0 software was used for data analysis. Data that met the normal distribution (tested using the Shapiro–Wilk test) were compared among multiple groups using the one-way Analysis of Variance (ANOVA). The data that did not conform with the normal distribution was first logarithmically transformed into data that did conform with the normal distribution, then used for the mean comparison between multiple groups using the one-way ANOVA. The Least Significant Difference method was used for multiple comparisons of equal variance data, and the Games–Howell method was used for multiple comparisons of variable data. Data that could not be converted to a normal distribution using the aforementioned function were compared among multiple groups using the non-parametric Kruskal–Wallis H test. The corrected α' value (α' = 0.05/two-two comparison times) was adopted to make statistical judgments regarding the significance levels of multiple comparisons among different groups. A p-value of <0.05 was considered statistically significant.

Ethics approval and consent to participate

This study was conducted with approval from the Ethics Committee of Dongzhimen Hospital, Beijing University of Chinese Medicine, in accordance with the declaration of Helsinki. All animals were treated in compliance with the National Research Council's Guide for the Care and Use of Laboratory Animals (1996).

RESULTS

General rat conditions

The rats in the sham operation group were lively and active, with a regular diet and drinking pattern and even breathing and reasonable response. Their fur was soft, neat, and glossy, and their ears, claws, and tails were red without oedema. There is no weight change during the experimental period, so there is no need to change the dose.

The rats in the model group were unresponsive and almost inactive; they often curled up tiredly and had a low food and water intake. A noticeable wheezing sound could be heard in the larynx, and the respiratory rate increased significantly with small respiratory movement amplitude. Their fur was messy and lusterless. Their paws showed nasolabial cyanosis and visible oedema; some rats also had visible tail oedema; the rats in the captopril group presented with an average activity level, normal or slightly increased respiration, and sensitive response. No wheezing sound could be heard in the larynx. The fur was soft and shiny; however, less than in the sham operation group. The ears, paws, and tails were relatively red and moist, with no oedema.

The low-dose Luofengning No. 2 rats were unresponsive and presented with a lowered activity level, reduced diet and drinking habits, and shortness of breath. A wheezing sound could be heard in the larynx upon listening carefully; however, the sound was not as evident as in the model group. The rats had messy, less lustrous fur. The paws and tails were dark and slightly purple. Oedema was visible in the paws, but the swelling degree was lighter than the model group; the middle-dose Luofengning No. 2 group presented lower activity levels than the high-dose group, with shortness of breath and a reduced

Table I. *Comparison of the levels of HWI and LVWI in rats among different groups ($\bar{x}\pm s$, mg/g)*

Group (G)	n	HWI	LVWI	NT-proBNP（pg/ml）	CVF（%）
Sham operation (G)	5	2.92±0.89	1.45±0.04	167.73±8.45	5.73±0.21
Model (G)	6	3.89±0.11**	2.69±0.33**	493.56±12.60**	33.61±0.63**
Captopril (G)	6	3.09±0.13$^{*\#\#▲•}$	2.03±0.14$^{*\#\#▲•}$	198.93±7.34$^{*\#\#}$	9.23±0.34$^{*\#\#}$
Low-dose Luofengning No.2 (G)	6	3.53±0.88$^{**\#\#△}$	2.38±0.76$^{**\#△}$	322.37±8.07$^{**\#\#△••}$	21.57±0.17$^{**\#\#△••}$
Medium-dose Luofengning No.2 (G)	7	3.47±0.07$^{**\#\#△}$	2.33±0.91$^{**\#△}$	248.05±10.13$^{*\#\#△▲▲}$	14.00±0.13$^{*\#\#△▲▲}$
High-dose Luofengning No.2 (G)	6	3.19±0.08$^{*\#\#▲•}$	2.19±0.54$^{*\#\#▲•}$	218.45±9.15$^{*\#\#▲▲•}$	10.61±0.28$^{*\#\#▲▲•}$

Note: Compared with the model group, $^{\#}$means P<0.05, $^{\#\#}$means P<0.01; Compared with the sham operation group, *means P<0.05, **means P<0.01; Compared with the captopril group, $^{△}$means P<0.05, $^{△△}$means P<0.01; Compared with the low-dose Luofengning No. 2 group, $^{▲}$means P<0.05, $^{▲▲}$ means P<0.01; Compared with the medium-dose Luofengning No. 2 group, $^{•}$means P<0.05, $^{••}$means P<0.01.

diet and water intake. The wheezing sound in the larynx was difficult to hear. The rats had a slower response and less tidy and lustrous fur than the rats in the low-dose group; the ears, claws, and tails were also darker in colour, and slight claw oedema was visible in some rats.

The high-dose Luofengning No. 2 group had a lowered response and good activity level. The conditions were similar to the captopril group; the rats presented with normal eating and drinking habits. Their respiration was slightly faster, and no wheezing sound could be heard. The fur was soft and shiny, and the ears, paws, and tails were relatively red in colour, moist, and without oedema.

HWI and LVWI levels

The HWI and LVWI levels were measured after 4 weeks of drug intervention. The results were as follows: the levels were (1) significantly higher in the model group than in the sham operation group ($p<0.01$); (2) significantly lower in each drug intervention group than in the model group ($p<0.05$ or $p<0.01$); and significantly lower in the high-dose Luofengning No. 2 group than in the low-dose and medium-dose groups ($p<0.05$). There were no statistically significant differences between the low-dose group and the medium-dose group ($p>0.5$) or the high-dose group and the captopril group ($p>0.05$) (Table I).

Serological indicator NT-proBNP

The rat serum NT-proBNP levels were measured after 4 weeks of drug intervention. The results were as follows: the levels were (1) significantly changed in the model group compared with the sham operation group ($p<0.01$); (2) significantly higher in each drug administration group than in the sham operation group ($p<0.05$ or $p<0.01$); (3) significantly lower in each drug administration group than in the model group ($p<0.01$); (4) significantly lower in the high-dose Luofengning No. 2 group than in the medium-dose group ($p<0.05$); and (5) significantly lower in the medium-dose group than in the low-dose group ($p<0.01$). There was no statistically significant difference between the high-dose and the captopril groups ($p>0.05$) (Table I).

Masson staining and CVF detection

The left ventricular myocardium was assessed for collagen fraction. Furthermore, the slices of the heart were the same among all groups. The results showed no collagen around the blood vessels in the sham group and a large amount of collagen around the blood vessels. The degree of fibrosis around the blood vessels in the drug intervention group was lower than in the model group while the low-dose luofengning 2 group was similar to the model group. As Luofengning No. 2 increased, collagenesis significantly reduced, and the collagen content in the captopril group and the high-dose group of Luofengning No. 2 was significantly lowered compared with the model group.

After 4 weeks of drug intervention, Masson staining was conducted on the myocardium of each rat; this showed the myosin fibres in red and myocardial fibres in blue. The results showed a small amount of extracellular collagen in the sham operation group and a large amount of collagen hyperplasia in the model group. The cardiomyocyte fibrosis degree was lower in the drug intervention group than in the model group; however, the degrees in the low-dose Luofengning No. 2 group and the model group were similar. As the Luofengning No. 2 dosage was increased, the collagenesis became significantly reduced, and the collagen content was significantly lower in the captopril group and the high-dose Luofengning No. 2 group than in the model group. The results are shown in Fig. 1.

The results further showed that CVF was (1) significantly higher in the model group than in the sham operation group ($p<0.01$); (2) significantly lower in each drug administration group than that in the model group ($p<0.05$ or $p<0.01$); (3) significantly lower in the high-dose Luofengning No. 2 group than in the medium-dose group ($p<0.05$); and (4) significantly lower in the medium-dose group than in the low-dose group ($p<0.01$). There was no statistical difference between the high-dose Luofengning No. 2 group and the captopril group ($p>0.05$). The comparisons are shown in Table I.

Myocardial tissue TGFβ1 and Smad2/3 protein expression Western blot measurement

The rat myocardial tissue TGFβ1 protein levels were measured after 4 weeks of drug intervention. The

results were as follows: the levels were (1) significantly changed in the model group compared with the sham operation group ($p<0.01$); (2) significantly higher in the captopril group, low-dose Luofengning No. 2 group, and medium-dose Luofengning No. 2 group than in the sham operation group ($p<0.05$ or $p<0.01$); (3) significantly lower in the captopril group, low-dose Luofengning No. 2 group, medium-dose Luofengning No. 2 group, and high-dose Luofengning No. 2 group than in the model group ($p<0.05$ or $p<0.01$); (4) lower in the high-dose Luofengning No. 2 group than in the low-dose Luofengning No. 2 group and the medium-dose Luofengning No. 2 group ($p<0.05$); (5) lower in the medium-dose group than in the low-dose group ($p<0.05$); and (6) lower in the high-dose group than in the captopril group ($p<0.05$). There was no statistically significant difference between the high-dose and the sham operation groups ($p>0.05$). The comparisons are shown in Fig. 2.

The rat myocardial tissue Smad2/3 protein levels were measured after 4 weeks of drug intervention. The results were as follows: the levels were (1) significantly higher in the low-dose Luofengning No. 2 group and the medium-dose Luofengning No. 2 group than in the sham operation group ($p<0.05$ or $p<0.01$); (2) significantly lower in the captopril group and the high-dose Luofengning No. 2 group than in the model group ($p<0.05$); and (3) significantly lower in the high-dose Luofengning No. 2 group than in the low-dose Luofengning No. 2 group and the medium-dose Luofengning No. 2 group ($p<0.05$). There were no statistically significant differences in (1) the captopril group and the high-dose Luofengning No. 2 group when compared with the sham operation group ($p>0.05$); (2) the medium-dose Luofengning No. 2 group when compared with the low-dose Luofengning No. 2 group ($p>0.05$); and (3) the high-dose group when compared with the captopril group ($p>0.05$). The comparisons are shown in Fig. 3.

Myocardial tissue Col-I and Col-III protein expression
Western blot measurement

The rat myocardial tissue Col-I protein levels were measured after 4 weeks of drug intervention. The results were as follows: the levels were (1) significantly changed in the model group compared with the sham operation group ($p<0.01$); (2) significantly higher in the low-dose Luofengning No. 2 group than in the sham operation group ($p<0.01$); (3) significantly higher in the low-dose Luofengning No. 2 group than in the

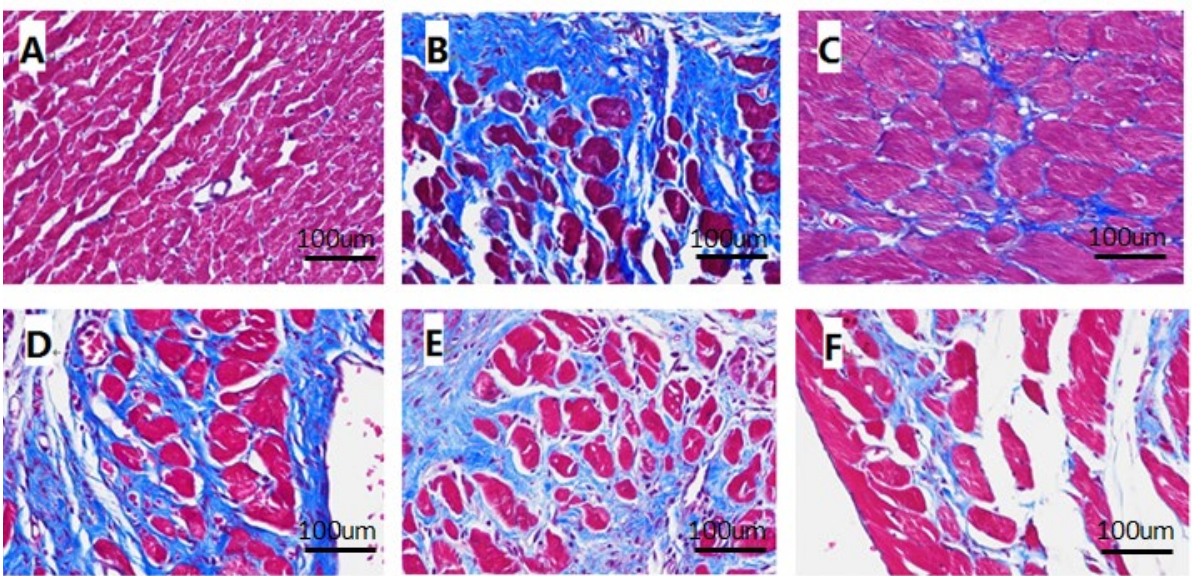

Fig. 1. *Rat cardiomyocyte collagen fiber expression group comparisons (Masson staining, 400×): **A**) sham group; **B**) model group; **C**) captopril group; **D**) low-dose Luofengning No. 2 group; **E**) middle-dose Luofengning No. 2 group; and **F**) high-dose Luofengning No. 2 group.*

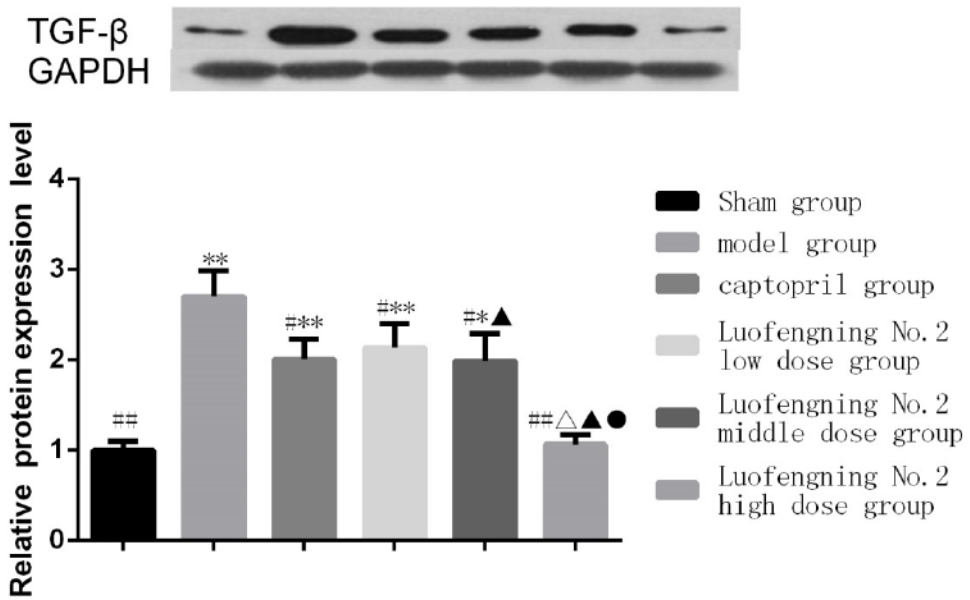

Fig. 2. *Rat myocardial tissue TGFβ1 protein expression in different groups. In model group comparisons, # means p<0.05 and ## means p<0.01; in sham operation group comparisons, * means p<0.05, and ** means p<0.01; in captopril group comparisons, △ means p<0.05 and △△ means p<0.01; in low-dose Luofengning No. 2 group comparisons, ▲ means p<0.05 and ▲▲ means p<0.01; in medium-dose Luofengning No. 2 group comparisons, ● means p<0.05 and ●● means p<0.01*

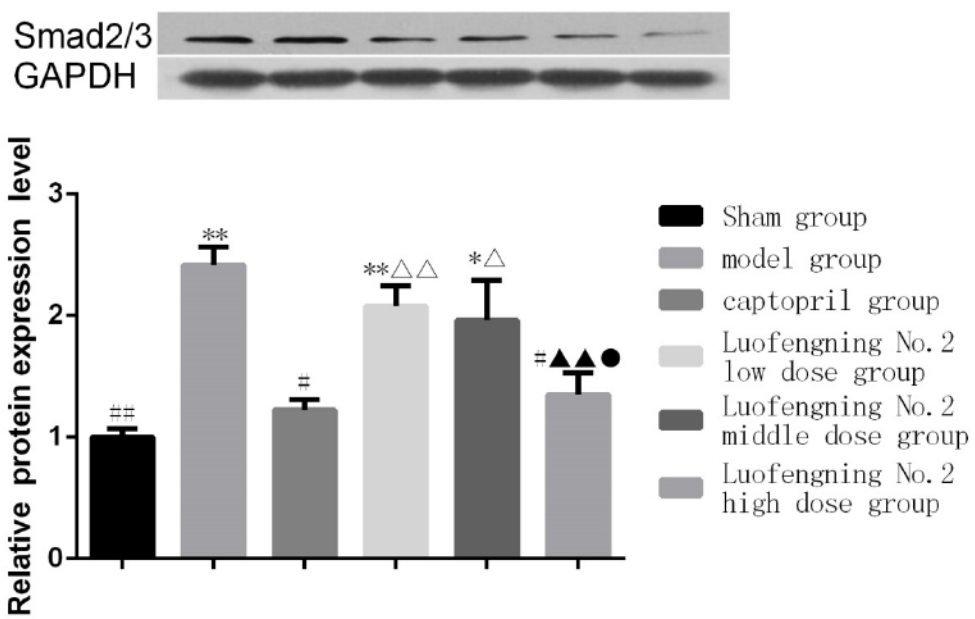

Fig. 3. *Rat myocardial tissue Smad2/3 protein expression in different groups. In model group comparisons, # means p<0.05 and ## means p<0.01; in sham operation group comparisons, * means p<0.05, and ** means p<0.01; in captopril group comparisons, △ means p<0.05 and △△ means p<0.01; in low-dose Luofengning No. 2 group comparisons, ▲ means p<0.05 and ▲▲ means p<0.01; in medium-dose Luofengning No. 2 group comparisons, ● means p<0.05 and ●● means p<0.01*

captopril group ($p<0.01$); and (4) significantly lower in the high-dose Luofengning No. 2 group and the medium-dose Luofengning No. 2 group than in the low-dose Luofengning No. 2 group ($p<0.001$ or $p<0.05$). There were no statistically significant differences in (1) the captopril group, the medium-dose Luofengning No. 2 group, and the high-dose Luofengning No. 2 group when compared with the sham operation group ($p>0.05$); (2) the medium-dose Luofengning No. 2 group when compared with the high-dose Luofengning No. 2 group ($p>0.05$); and (3) the medium-dose Luofengning No. 2 group and high-dose Luofengning No. 2 group when compared with the captopril group ($p>0.05$). The comparisons are shown in Fig. 4.

The rat myocardial tissue collagen type III protein levels were detected after 4 weeks of drug intervention. The results were as follows: the levels were (1) significantly higher in the low-dose Luofengning No. 2 group and the medium-dose Luofengning No. 2 group than in the sham operation group ($p<0.05$ or $p<0.01$); and (2) significantly lower in each drug administration group than in the model group ($p<0.05$ or $p<0.01$). There were no statistically significant differences in the captopril group and the high-dose Luofengning No. 2 group compared with the sham operation group ($p>0.05$). The comparisons are shown in Fig. 5.

Echocardiography

After 4 weeks of drug intervention, the rat's left ventricles were enlarged, and the contractile function of the whole heart was reduced. The LVDd and LVDs were significantly increased ($p<0.01$), and the LVEF was significantly reduced ($p<0.01$) in the model group when compared with the sham group; this suggested successful modelling. Compared with the model group, the rat LVDd was significantly reduced in the captopril group, middle-dose Luofengning No. 2 group, and high-dose Luofengning No. 2 group ($p<0.05$). The LVDs in the high-dose Luofengning No. 2 group was

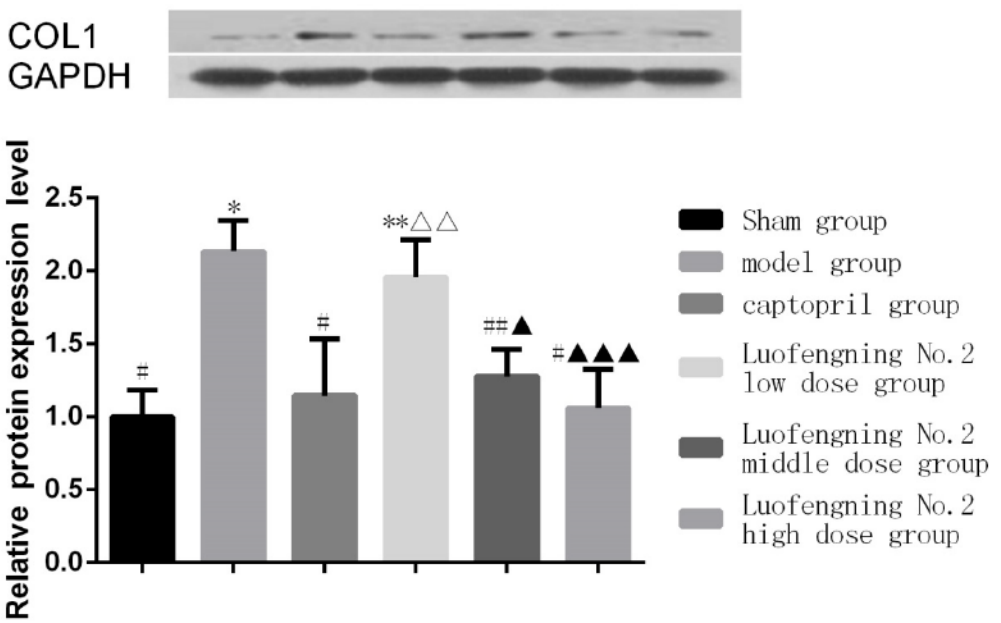

Fig. 4. *Rat myocardial tissue Col-I protein expression in different groups. In model group comparisons, # means $p<0.05$ and ## means $p<0.01$; in sham operation group comparisons, * means $p<0.05$, and ** means $p<0.01$; in captopril group comparisons, △ means $p<0.05$ and △△ means $p<0.01$; in low-dose Luofengning No. 2 group comparisons, ▲ means $p<0.05$ and ▲▲ means $p<0.01$; in medium-dose Luofengning No. 2 group comparisons, ● means $p<0.05$ and ●● means $p<0.01$*

significantly reduced ($p<0.05$), with no significant differences among the other drug-administered groups ($p<0.05$). Compared with the model group, the rat LVEF was significantly increased in the captopril group, middle-dose Luofengning No. 2 group, and high-dose Luofengning No. 2 group ($p<0.05$). The rat LVEF was increased in the low-dose Luofengning No. 2 group; however, there were no statistically significant differences compared with the other groups ($p>0.05$). The comparisons are shown in Table II and Fig. 6.

DISCUSSION

In the present study, coronary artery ligation in rats was used to create a post-MI HF model. In rats, coronary artery ligation can lead to similar pathological MF changes as those observed in humans; this makes it a suitable animal model for studying HF or MF (15). After experimental modelling, all rats in the model group showed CHF signs and symptoms, such as lying down lazily, shortness of breath, and oedema of the paws and tails (16). Meanwhile, the rats in the sham operation group did not present with any of the above-listed signs; this, combined with the LVEF ≤ 45% echocardiography result (16) and the HWI and LVWI levels 8 weeks after modelling, further proved the successful establishment of the rat model, meaning that the experiments could be carried out.

Myocardial hypertrophy is a compensatory myocardial response to pressure or volume overload; it is also a necessary CHF developmental stage. The HWI and LVWI levels were significantly higher in all model group rats than in the sham operation group rats, proving successful modelling. Furthermore, the HWI and LVWI levels were significantly lower in each drug administration group than in the model group; this suggested that pathological rat myocardial hypertrophy could be significantly improved via drug therapy. Sound therapeutic effects were observed among the treatment groups in the captopril group and the high-dose Luofengning No. 2 group.

The serum NT-proBNP level may reflect end-

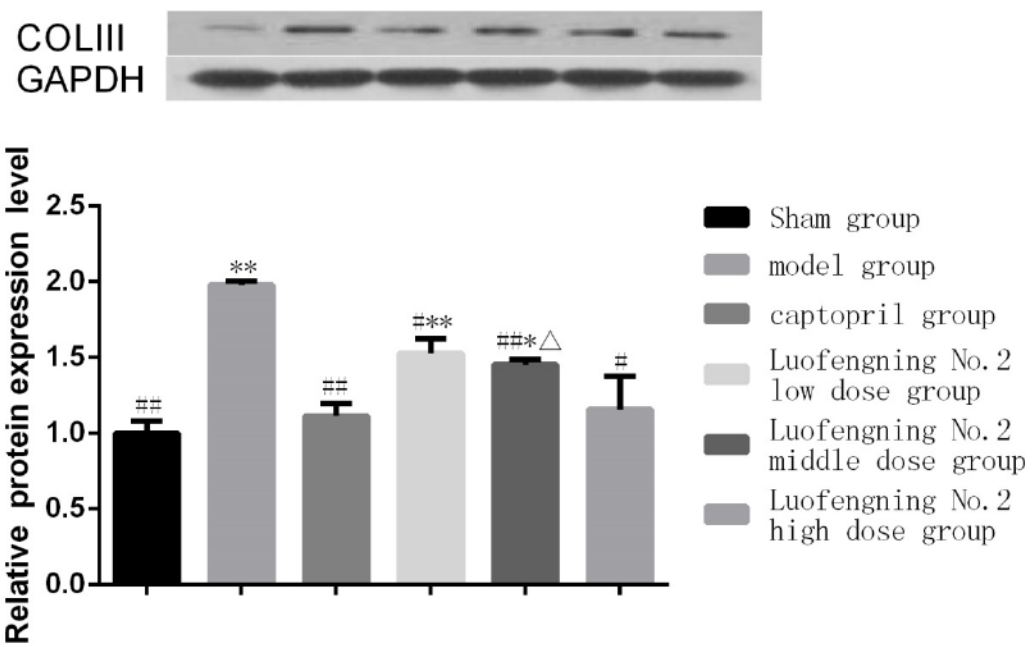

Fig. 5. *Rat myocardial tissue Col-III protein expression in different groups. In model group comparisons, # means $p<0.05$ and ## means $p<0.01$; in sham operation group comparisons, * means $p<0.05$, and ** means $p<0.01$; in captopril group comparisons, △ means $p<0.05$ and △△ means $p<0.01$; in low-dose Luofengning No. 2 group comparisons, ▲ means $p<0.05$ and ▲▲ means $p<0.01$; in medium-dose Luofengning No. 2 group comparisons, ● means $p<0.05$ and ●● means $p<0.01$*

Table II. *Morphologic change and heart function of rats in different groups ($\bar{x}\pm s$)*

	Sham group	Model group	Captopril group	Loufengning No.2 Low Dose group	Loufengning No.2 Middle Dose group	Loufengning No.2 High Dose group
LVDd(mm)	5.81±0.78$^{\#\#}$	7.27±1.83	6.21±1.25$^{\#}$	6.51±1.42	6.21±1.25$^{\#}$	5.84±0.82$^{\#}$
LVDs(mm)	2.84±0.83$^{\#\#}$	6.06±1.24	5.19±0.78	5.41±1.10	5.22±1.81	4.97±1.07$^{\#}$
LVEF(%)	79.07±3.21$^{\#\#}$	39.98±14.80	51.49±14.94$^{\#}$	49.63±7.88	53.34±21.01$^{\#}$	53.95±11.59$^{\#}$

Note: Compared with the model group, $^{\#}$ means P<0.05, $^{\#\#}$ means P<0.01; compared with the sham operation group, * means P<0.05, ** means P<0.01.

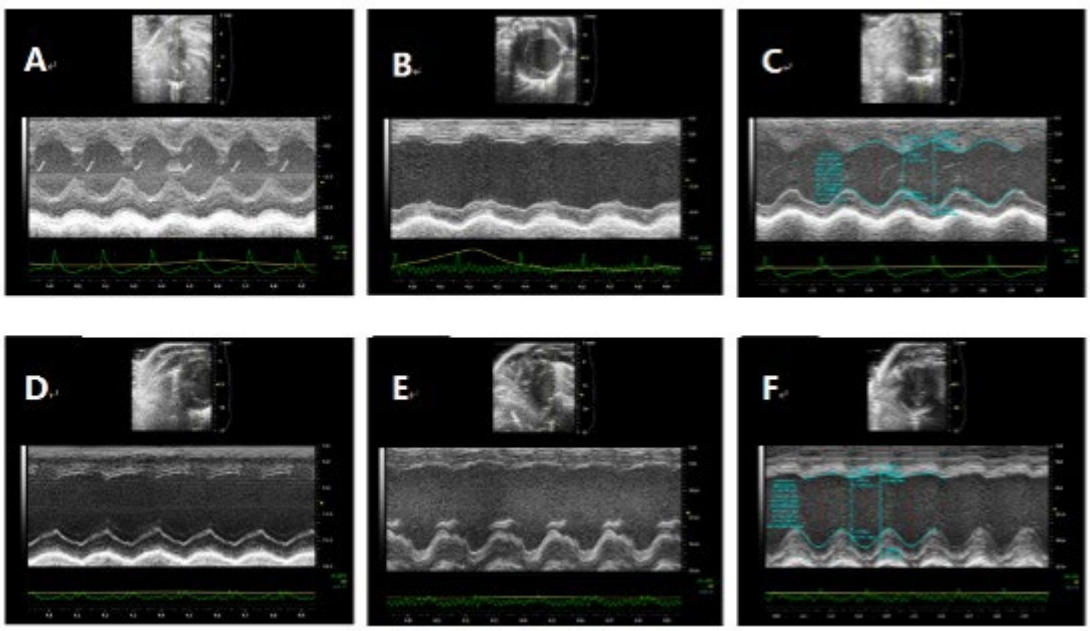

Fig. 6. *Ultrasonic rat cardiograms in different groups: (**A**) sham group; (**B**) model group; (**C**) captopril group; (**D**) low-dose Luofengning No. 2 group; (**E**) middle-dose Luofengning No. 2 group; and (**F**) high-dose Luofengning No. 2 group.*

diastolic volume load and cardiac function; it can also be used to determine CHF severity. (17) Studies conducted in recent years have shown that the serum NT-proBNP level can be used as an indicator to achieve early diagnosis and assess MF severity (18). In the present study results, the serum NT-proBNP levels were significantly higher in the model group than in the sham operation group, indicating HF presence in the model group. They were significantly lower in the drug intervention group than in the model group, indicating that captopril and Luofengning No. 2 intervention could lower NT-proBNP expression and proving that captopril and Luofengning No. 2 use could significantly improve cardiac function in rats with HF. The group comparison showed that Luofengning No. 2 on cardiac function was positively correlated with the dosage and that the effects of high Luofengning No. 2 and captopril doses were comparable in cardiac function improvement in rats with CHF.

The present study results showed that the collagen hyperplasia degree was (1) lower in the drug intervention group than in the model group. As the traditional Chinese medicine dose increased, the collagen hyperplasia reduced significantly; (2) more obviously reduced in the captopril group and

the high-dose Luofengning No. 2 group than in the model group, indicating that both captopril and a high Luofengning No. 2 dose could inhibit collagen hyperplasia in rats and that the inhibitory effect was relatively strong. MF development was effectively inhibited by the captopril and Luofengning No. 2 interventions. The comparison between the groups proved that MF inhibition using Luofengning No. 2 was dose-dependent; there was no significant difference in MF between the high-dose Luofengning No. 2 group and the captopril group.

Furthermore, the present study results showed increased rat cardiomyocyte TGFβ1 and Smad2/3 expressions in the model group compared with the sham operation group, indicating myocardium TGFβ1/Smad2/3 signalling pathway activation in rats with post-MI HF and a significantly increased MF degree. (19-24) Although the difference between the medium-dose Luofengning No. 2 group and the high-dose Luofengning No. 2 group was not statistically significant, the histogram trend showed that Luofengning No. 2 on Col-I protein expression reduction was, to a certain extent, positively correlated with the dosage. Furthermore, there was a significant increase in Col-I protein levels in the low-dose Luofengning No. 2 group compared with the captopril group and comparable Col-I protein level reductions in the medium-dose Luofengning No. 2, high-dose Luofengning No. 2 group, and captopril group. Luofengning No. 2 on Col-I protein level reduction in the low-dose group was not significant; this might be due to the low concentration of the drug and the fact that the low dosage was far from the effective threshold dosage of this traditional Chinese medicine (25).

The results further showed that Luofengning No. 2 could improve cardiac function and exert an anti-MF effect in rats with HF; this reduces collagen synthesis and secretion by down-regulating TGFβ1/Smads expression, thus delaying MF progression playing a positive role in cardiac protection. Moreover, this effect might positively correlate with the traditional Chinese medicine dosage within a specific range.

Inflammatory response plays an important role in MF progression, and preliminary clinical studies have suggested that Luofengning No. 2 might block or inhibit the inflammatory state in patients with HF. (26-30) Therefore, it can be speculated that the use of Luofengning No. 2 and captopril plays a cardioprotective role by inhibiting the chronic inflammatory state in patients with HF, improving or even reversing the myocardium's fibrotic process as well as improving its systolic and diastolic functions. In future research, this speculation may be explored in-depth concerning the crosstalk relationship between MF and inflammation, as the action mechanism through which low frequency generated noise (LFG) mediates its beneficial cardiac effects remains to be demonstrated despite the finding that the LFG was lowered TGFβ/Smads.

Conflicts of interests:

The authors declare that they have no conflicts of interest.

REFERENCES

1. Li L, Zhao Q, Kong W. Extracellular matrix remodeling and cardiac fibrosis. Matrix Biol 2018, 68-69:490-506.
2. Fonseca C, Maggioni AP, Marques F, et al. A systematic review of in-hospital worsening heart failure as an endpoint in clinical investigations of therapy for acute heart failure. Int J Cardiol 2018, 250:215-222.
3. Shanbhag SM, Greve AM, Aspelund T, et al. Prevalence and prognosis of ischaemic and non-ischaemic myocardial fibrosis in older adults. Eur Heart J 2019, 40(6):529-538.
4. Bhandary B, Meng Q, James J, et al. Cardiac fibrosis in proteotoxic cardiac disease is dependent upon myofibroblast TGF-βsignaling. J Am Heart Assoc 2018, 7:e010013.
5. Tecalco-Cruz AC, Ríos-López DG, Vázquez-Victorio G, et al. Transcriptional cofactors Ski and SnoN are major regulators of the TGF-β /Smad signaling pathway in health and disease. Signal Transduct Target Ther 2018, 3:15.
6. Yang X, Li X, Wang X, Zhu H, Jing G, Liu D, Zhou H, Guo J. Effect of Luofengning No. 2 and its split prescription on the quality of life of patients with heart and kidney syndrome. J Trad Chin Med 2013, 54(23):2024-2027.
7. Schwarz PEH, Timpel P, Harst L, Greaves CJ, Ali MK, Lambert J, Weber MB, Almedawar MM, Morawietz H. Blood Sugar Regulation for

Cardiovascular Health Promotion and Disease Prevention: JACC Health Promotion Series. J Am Coll Cardiol 2018;72(15):1829-1844.
8. Yang X, Li X, Wang X, Zhu H, Jing G, Liu D, Zhou H, Guo J. Effects of Luofengning No. 2 formula on patients with heart and kidney syndrome. Chin J Evid Based Cardiovasc Med 2013, 6:635-638.
9. Bedada FB, Wheelwright M, Metzger JM. Maturation status of sarcomere structure and function in human iPSC-derived cardiac myocytes. Biochim Biophys Acta 2016; 1863(7 Pt B):1829-38.
10. Yang X, Wang X. Anti-myocardial fibrosis effect of Luofengning No. 2 formula from the pathogenesis of Luo Feng internal movement. Chin J Evid Based Cardiovasc Med, 2017, 9(5):614-619.
11. Li X, Yang X, Wang X, Zhao H, Zheng X. Effects of Luofenin 2 on cardiac function in rats with heart failure. Chin J Evid Based Cardiovasc Med 2013, 5(5):510-512.
12. Zhang L, Gan Z K, Han L N, et al. Protective effect of heme oxygenase-1 on Wistar rats with heart failure through the inhibition of inflammation and amelioration of intestinal microcirculation. J Geriatr Cardiol 2015, 12(4):353-365.
13. Wagenaar A, Wiegerinck R F, Heijnen V V, et al. Percutaneous microembolization of the left coronary artery to model ischemic heart disease in rats. Lab Anim 2015, 45 (1): 20-27.
14. Wang XF, Qu XQ, Zhang TT, et al. Testosterone suppresses ventricular remodeling and improves left ventricular function in rats following myocardial infarction. Exp Ther Med 2015, 9(4):1283-1291.
15. He Q, Cheng J, Wang Y. Chronic CaMK inhibition reverses cardiac function and cardiac reserve in HF mice. Life Sci 2019, 219(1):122-128.
16. Yang X, Wang X. Effect of Luofengning No. 2 formula on cardiac function and myocardial fibrosis in rats with heart failure after heart attack. Chin J Evid Based Cardiovasc Med 2020, 12(2):192-196.
17. Davidovski FS, Goetze JP. ProANP and proBNP in plasma as biomarkers of heart failure. Biomark Med 2019, 13(13):1129-1135.
18. Pandey A, Golwala H, Devore AD, et al. Trends in the use of guideline-directed therapies among dialysis patients hospitalized with systolic heart failure: findings from the American heart association get with the guidelines-heart failure program. JACC Heart Fail 2016, 4(8): 649-661.
19. Wu J, Jackson-Weaver O, Xu J. The TGFβ superfamily in cardiac dysfunction Acta Biochim Biophys Sin 2018, 50(4):323-335.
20. Moore-Morris T, Cattaneo P, Puceat M, et al. Origins of cardiac fibroblasts. J Mol Cell Cardiol 2016, 91:1-5.
21. Gao H, Bo Z, Wang Q, et al. Salvanic acid B inhibits myocardial fibrosis through regulating TGF-β1/Smad signaling pathway. Biomed Pharmacother 2019, 110:685-691.
22. Gyöngyösi M, Winkler J, Ramos I, et al. Myocardial fibrosis: biomedical research from bench to bedside. Eur J Heart Fail 2017, 19(2):177-191.
23. Wang HB, Yang X, Yang QQ, et al. Parp-1 inhibition attenuates cardiac fibrosis induced by myocardial infarction through regulating autophagy. Biochem Biophys Res Commun 2018, 503(3):1625-1632.
24. Liu JC, Wang F, Xie ML, et al. Osthole inhibits the expressions of collagen and through Smad signaling pathway after treatment with TGF-β1 in mouse cardiac fibroblasts. Int J Cardiol 2017, 228(2):388-393.
25. Wu T, Jia C. The relationship between quantity and effect of Chinese medicine characteristics. J Beijing Uni Chin Med 2018, 41(11):900-904.
26. Wang X, Lin ZX, Ge JB, Zhang ZX, Shen L. Relationship between Traditional Chinese Medicine Syndrome Type and Coronary Arteriography of Acute Coronary Syndrome. CJIM 2003, 9(2):116-119.
27. Wang X, Hu D. Acute coronary syndromes: A clinical study of the hypothesis of "complex wind and internal movement". J Trad Chin Med, 2008, 23(3):204-208.
28. Hu D, Ma C, Wang X. Heart Failure Chapter. Cardiology Practice 2010-Integrated Chinese and Western Medicine Volume. Cardiology Practice 2010-Integrated Chinese and Western Medicine Volume.
29. Wang X. Reflections on the diagnosis and study of coronary heart disease: The "complex wind and internal motion" hypothesis of atherosclerosis and its practice. Chin J Integ Med 2011, 31(3):310-312.
30. Wang X, Zhang C, Yang R, Zhu HY, Zhao HB. Clinical study of the hypothesis of endogenous collateral wind on acute coronary syndrome. Afr J Tradit Complem Altern Med 2014, 11(1): 121-126.

A type II Abernethy malformation that started with hypersplenism: a case report

Y. Lu[1], X. Wang[1], Y. Yuan[2], B. Wei[3] and Y. Xing[1*]

[1]Department of Infectious Disease, Zibo Central Hospital, Zibo City, Shandong Province, China; [2]Department of Neurology, Gucheng County Hospital, Hengshui, Hebei Province, China; [3]Hepatobiliary Surgery, Zibo Central Hospital, Zibo City, Shandong Province, China

BACKGROUND: Abernethy malformations are rare congenital vascular malformations defined by diverting portal blood away from the liver. We present a case of Abernethy malformation that started with hypersplenism.

CASE DISCUSSION: A 44-year-old female had leukopenia and thrombocytopenia 14 years ago and was diagnosed with hypersplenism without manifestations of cirrhosis. Since then, the disease gradually progressed, and the number of erythrocytes, leukocytes, and platelets significantly decreased. In addition, liver perfusion was insufficient for an extended period due to portosystemic shunt, and abnormal liver function was observed. The laboratory investigation excluded viral, alcoholic, drug, and autoimmune factors; magnetic resonance imaging and colour ultrasonography revealed a splenorenal shunt, and type II Abernethy malformation was considered. After shunt ligation, the leukocyte and platelet counts and haemoglobin level quickly returned to normal values, improving liver function. In this report, we discuss the common clinical manifestations, associated anomalies, diagnostic workup, and treatment options of this disorder.

CONCLUSION: Abernethy malformation is a rare congenital vascular malformation. This vascular abnormality's clinical importance and manifestations range from asymptomatic cases to liver or metabolic dysfunctions of various degrees. Treatment strategies are decided according to shunt types, locations, symptoms, severities, and clinical course shunt closure should be advised to cure or prevent complications for type II Abernethy malformation. Long-term follow-up is indicated for all patients.

Congenital extrahepatic portosystemic shunt (CEPS), also termed Abernethy malformation, is a rare congenital vascular malformation in which splenomesenteric blood drains directly into a systemic vein bypassing the liver through a complete or partial extrahepatic shunt. In 1793, John Abernethy first reported the congenital absence of the portal vein and congenital mesentericocaval shunt (1). Abernethy malformation is the congenital diversion of portal blood away from the liver by either an end-to-side or a side-to-side shunt (2). Morgan and Superina (3) have classified CEPSs into two types: type 1 consists of complete portosystemic shunts and the liver is not perfused with portal blood, whereas type 2 consists of shunts where a certain proportion of portal blood is perfused to the liver and the remaining portal flow bypass the liver and is diverted into a systemic vein through a partial shunt (4,5). The clinical importance of this vascular abnormality lies in its broad spectrum of symptoms and complications, ranging from incidentally discovered asymptomatic cases to liver or metabolic dysfunctions of various degrees and even severe clinical scenarios, which are caused by variations in sites or shunt types (6). Here, we report a

Keywords: congenital extrahepatic portosystemic shunt (CEPS), Abernethy malformation, hypersplenism, surgical ligation

**Corresponding author:*
Dr Yanqing Xing
Department of Infectious Disease, Zibo Central Hospital,
No.54 Gongqingtuan West Road,
Zhangdian District, Zibo City,
Shandong Province, 255036 China.
e-mail: yanqingxing@163.com

0393-974X (2022)

case of a patient with Abernethy malformation, which started with hypersplenism, admitted to our hospital.

Case presentation

A 44-year-old female had leukopenia and thrombocytopenia in a medical examination in March 2007, without other discomforts. Bone marrow puncture showed mildly active myeloproliferation and normal erythrocyte, leucocyte, and platelet counts, and no special treatment was provided. Since then, the patient underwent reexaminations intermittently, with leukocyte and platelet counts in the range of 1.5–1.8 × 10^9/L and 60–70 × 10^9/L, respectively. In May 2021, the patient visited another hospital for "oedema of both lower extremities"; routine blood tests showed a severe decline in the three systems; routine biochemical tests showed decreased albumin levels and prolonged prothrombin time; however, alpha-fetoprotein, carcinoembryonic antigen, and carbohydrate antigen (CA) 19-9 were within normal ranges. The levels of CA 125 and brain natriuretic peptide were 226.6 U/mL and 84 ng/L, respectively. Color Doppler ultrasonography revealed megalosplenia, ascites, bilateral pleural effusion and atherosclerotic plaques in both limbs. A liquid dark area was detected in the abdominal cavity, with a maximum depth of approximately 11.6 cm.

Echocardiography showed left heart enlargement, mild mitral regurgitation, mild tricuspid regurgitation, mild aortic regurgitation, and decreased left ventricular diastolic function. Gynaecological sonography showed reduced uterine volume. Abdominal puncture and drainage, diuresis, plasma infusion, albumin supplementation, and hepatoprotective treatment were performed. The patient was admitted to our department on June 19, 2021. The patient was emaciated and showed a moderately anaemic appearance. The patient was positive for mobile dullness; mild oedema of the lower limbs and visible pigmentation was observed. Routine blood tests showed seriously reduced erythrocyte, leukocyte, and platelet counts. Liver function test showed reduced albumin levels, mildly increased bilirubin levels, and prolonged prothrombin time. The percentage of reticulocytes was 1.52%, and the number of absolute reticulocytes was 0.052 × 10^{12}/L. On June 20 2021, an MRI showed megalosplenia, ascites, portal hypertension, collateral circulation formation, thin portal vein branches, and thickened gallbladder wall.

The patient was diagnosed with "portal hypertension and hypersplenism" with unknown causes. The patient had no apparent manifestations of cirrhosis. MRI of the patient (Fig. 1) showed a splenorenal venous shunt. Later, colour Doppler ultrasonography showed a dilated portal vein system with an inner diameter of the main trunk of 17 mm, and that of a splenic vein in the splenic portal area of 18 mm. A vascular echo was observed between the splenic and left renal veins, showing ectasia in 38×33 mm.

CEPS (type II Abernethy malformation) was considered the potential cause of portal hypertension. The significant problem was the seriously reduced erythrocyte, leukocyte, and platelet counts. Surgery was indicated, and liver tissue could be obtained for pathological examination to screen the causes of the disease further. Symptomatic therapies were

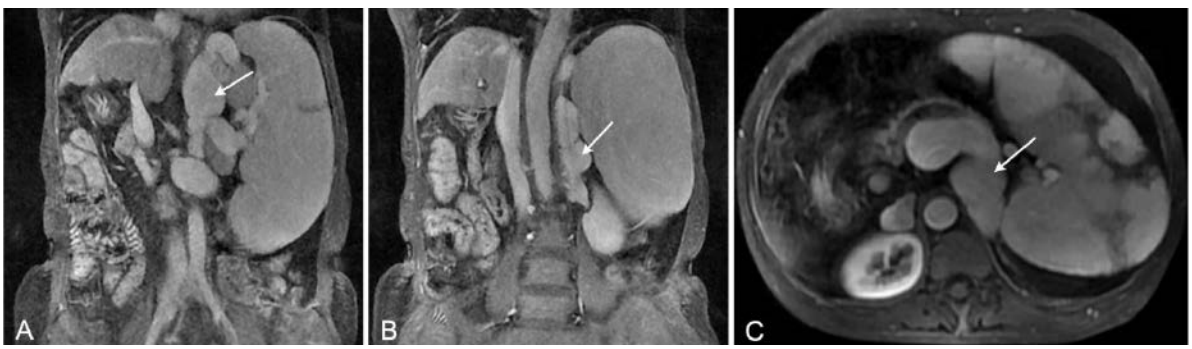

Fig. 1. ***A)*** *Significantly enlarged spleen and multiple tortuous and thickened vascular shadows in the splenic hilum (the shear head is shown).* ***B)*** *Splenorenal shunt.* ***C)*** *Splenorenal shunt.*

provided, including transfusion of erythrocytes and plasma, leucocyte-increasing agents, diuresis, and liver protection. The patient was transferred to the Hepatobiliary Surgery Department on July 8, 2021. Six units of homotypic erythrocytes were transfused in 3 days to prepare for surgery. Then, the retest showed gradually increasing bilirubin parameters, which might be caused by hemolytic jaundice due to the accelerated destruction of erythrocytes in the spleen after erythrocyte transfusion. Therefore, the surgery should be performed as soon as possible.

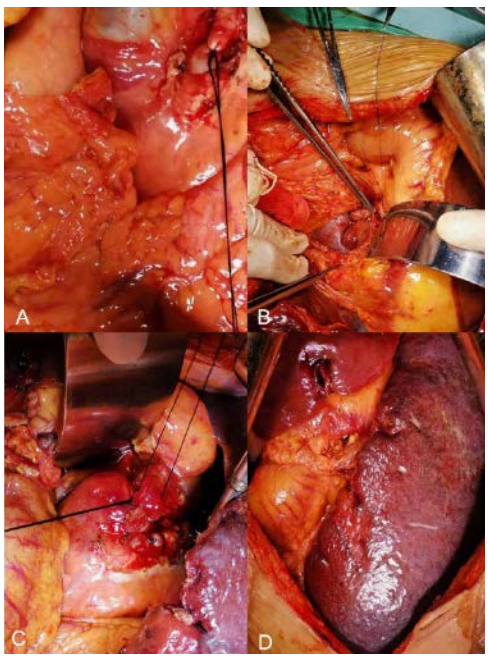

Fig. 2. ***A****) Ligation of splenic artery;* ***B****) Splenorenal venous shunt;* ***C****) Ligation of abnormal varicose veins on the upper edge of the pancreas;* ***D****) Liver biopsy.*

Intraoperative exploration on July 21, 2021, revealed reduced liver size, a dark red liver, no apparent cirrhotic nodule, and medium texture; spleen size was approximately 30 × 20 × 10 cm with a brittle texture; the superior margin of the pancreas had a dilated vein with a 3-cm diameter; no varicose veins in the oesophagus or fundus of the stomach were observed. The splenic artery, splenic vein, splenorenal venous shunt, and abnormal venous outflow tract were ligated, and a liver tissue biopsy was performed. Moreover, the ligation of the splenic artery, splenic vein, splenorenal vein shunt, abnormal venous outflow tract and liver biopsy was decided. The gastrocolonic belt was cut, and the main splenic artery was separated along line 7 of the pancreatic tail. The lower part of the pancreas was separated, the right side of the portal vein of the superior of 2.0 cm, and the splenic portal was separated using a 3-0 PROLENE suture. The splenic vein diameter was 2.0 cm, and the wall was thin. The retroperitoneal tissue was separated from the back of the pancreas to the blood vessel. The diameter was approximately 1.0 cm. The blood supply was good. The abnormally dilated vein on the pancreas was separated by a double knot of line 7. During the operation, ultrasonography showed that the splenic shunt was standard, the portal vein diameter was dilated before the operation, and

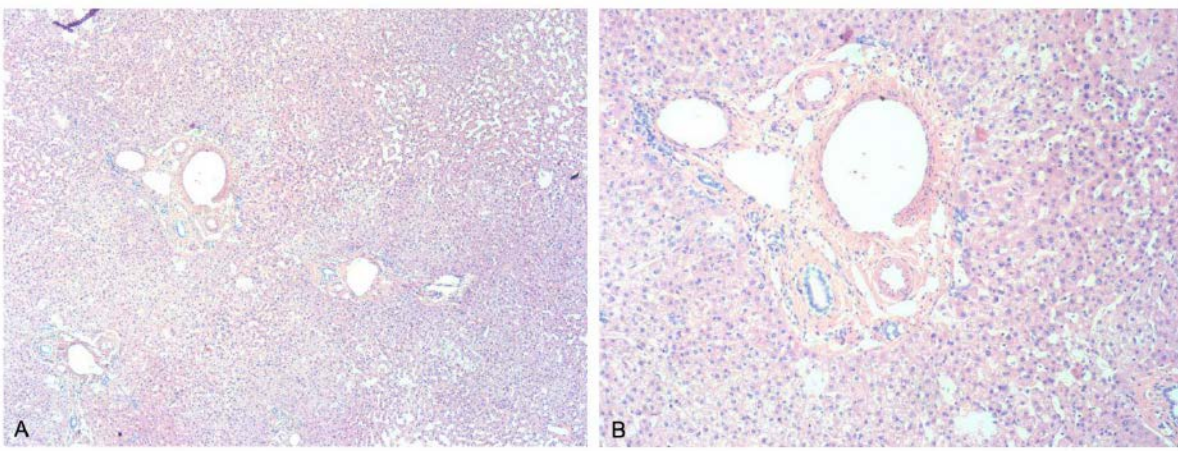

Fig. 3. *Partially mild dilation of liver sinusoids, small bile duct hyperplasia in the portal area, lymphocyte infiltration, no obvious pseudolobule formation.* ***A****) Magnification 4 × 10 hematoxylin and eosin (H&E).* ***B****) Magnification 10 × 10 H&E.*

the superior mesenteric vein was connected. The left lateral lobe of the liver was cut down, and a tissue biopsy revealed that the size was approximately 1 × 1 cm (Fig. 2).

The pathological findings of liver tissue biopsy were as follows: partially mild dilation of liver sinusoids, small bile duct hyperplasia in the portal area, lymphocyte infiltration, and no obvious pseudolobule formation (Fig. 3).

Postoperatively, patient parameters gradually improved. On September 22, 2021, a retest revealed the leukocyte, neutrophil, erythrocyte, haemoglobin, and platelet levels were 5.10 × 10^9/L, 2.98 × 10^9/L, 3.90 × 10^{12}/L, 111.0 × 10^9g/L, and 200× 10^9/L, respectively (Table I). The patient is still followed up.

DISCUSSION

Malformations of the portal venous system consist of congenital and acquired anomalies. Congenital portosystemic shunts are rare vascular developmental anomalies, commonly classified into extrahepatic portosystemic shunts and intrahepatic portosystemic shunts (IHPS) (7). An IHPS may either seal spontaneously within the first 2 years of life or persist. Abernethy malformations are characterized by abnormal communication between the portal vein (or its branches) and inferior vena cava, resulting in a complete or partial shunt of blood flow from the portal vein system into the systemic circulation. In 1994, Morgan and Superina (8) classified Abernethy malformations into two types based on the presence of an intrahepatic portal vein shunt and different types of portosystemic shunts:

Type I: a complete absence of an intrahepatic portal vein or type II: partial portal vein blood flow flows into the liver, and the remaining blood flows bypassed the liver and delivered into a systemic vein through abnormal branches, such as gastrorenal and splenorenal shunts. Type I is mainly related to other congenital malformations; cardiac malformations are the most related, followed by muscle and bone abnormalities.

Type II malformations are mostly not accompanied

Table I. *Clinical blood routine results during hospitalization.*

	WBC ×10^9/L	N ×10^9/L	RBC ×10^{12}/L	HGB g/L	PLT ×10^9/L	ALT U/L	AST U/L	ALP U/L	GGT U/L	ALB U/L	TBIL umol/L	DBIL umol/L	IBIL umol/L	PTs	INR	NH3 ug/dl
2007.03.15	1.54	0.92	4.33	112	46	50.9	25.6	89.9	45.3	43	26.6	7.2	19.39	13.5	1.13	
2021.05.16	0.74	0.37	2.77	47	35	19	25	125	18	21.4	39.6	21.5	18.1	18.6	1.61	
2021.06.20	1.08	0.55	3.42	67	42	19	25.2	162	18.8	24.8	51.4	16.5	34.9	18.7	1.56	
2021.06.27	0.77	0.48	3.64	80	23	22.5	24.5	163	23.3	28.5	58.7	16.3	42.4	17.9	1.5	
2021.07.06	0.37	0.17	3.27	75	30	25.3	35.8	172	33.8	32.4	33.9	11.2	22.7	22.3	1.86	
2021.07.11	1.55	1.08	3.78	94	31	34.8	46.8	244	46.9	30.5	82	25.4	56.6	16.8	1.41	
2021.07.13	1.25	0.89	4.09	103	29	52.2	61.7	257	57.7	37.3	96.5	28.2	68.3	18.3	1.53	127
2021.07.18	1.04	0.53	4.41	114	24	28.3	26.9	253	47.7	35.1	79.6	23.7	55.9	19.6	1.64	
2021.07.20	2.17	1.69	4.41	114	24	30.2	31.2	237	51	37.9	99.1	32.3	66.8	16.1	1.35	
2021.07.21	0.83	0.48	4	105	22	33	47	130	42	29.9	102	15.9	61.9	17.3	1.45	11
2021.07.22	1.24	0.96	3.12	81	31	31.5	65.2	171	44.1	34.9	86.4	33.6	52.8	13.9	1.17	
2021.07.24	2.32	1.56	3.01	82	30	37.2	36.4	132	35.1	34.5	62.4	21.5	40.9	16.2	1.36	37
2021.07.29	2.3	0.53	3.51	95	67	18.3	19.8	127	38.4	33	66.5	27.7	38.8	17	1.42	37
2021.08.01	2.52	1.31	3.36	93	73	12.9	29.1	168	46.3	34.4	74.4	30.2	44.2	15	1.26	
2021.08.04	2.26	1.26	3.38	94	92	10.5	35.9	190	51.1	32.2	68.9	28.1	40.8	14.4	1.25	
2021.08.09	5.81	4.11	3.63	103	155	12.8	38.6	259	67.5	34.4	65.5	28.5	37	16.3	1.37	
2021.8.25	6.59	4.63	3.48	103	232	19.6	35.8	292.2	89.8	38.3	57.6	20.4	37.2	15.4	1.34	
2021.9.22	5.1	2.98	3.90	111	200	21.3	31.8	303.2	81.9	32.5	39.3	11.0	28.3	17.7	1.48	

WBC: white blood cells; N: neutrophil; RBC: red blood cells; HGB: hemoglobin; PLT: Platelets; ALT: Alanine transaminase; AST: Aspartate aminotransferase; ALP: Alkaline phosphatase; GGT: gamma-glutamyl transpeptidase; ALB: albumin; TBIL: total bilirubin; DBIL: direct bilirubin; IBIL: indirect bilirubin; PTs: prothrombin time; INR: international normalized ratio.

by malformations in other sites. Suppose the intrahepatic portal vein is present with abnormal extrahepatic communication vessels between the portal vein and vena cava systems, whether the communication vessels are direct or indirect and single or multiple. In that case, all of these are defined as type II Abernethy malformation (9). The patient in this case report had an intrahepatic portal vein and abnormal extrahepatic communication vessel between the portal vein and vena cava systems, that is, a splenorenal shunt, so the patient was diagnosed with type II Abernethy malformation.

Since CEPS was first described, the number of cases reported in the literature has progressively increased due to advances in imaging techniques and neonatal screening. The proportion of extrahepatic shunts is not significantly different between males and females; however, most cases of intrahepatic shunts were male (7,10). In addition, a limited number of studies have explored the etiological mechanisms of CEPS (11). Two possible explanations have dominated the literature on CEPS development:

i) a genetic origin and complex congenital malformation processes: such malformations are considered to originate from an insult occurring in weeks 4–10 of embryological development, which is a crucial stage for hepatic and systemic vessel formation (12);

ii) the absence of ductus venosus during the fetal stage: abnormal vessels may develop associated with occlusions or agenesis of ductus venosus. Afterwards, certain vessels may persist and develop into an abnormal shunt, resulting in a hypoplasia of the portal venous system (13, 14).

Spectra of clinical variants of CEPS range from entirely asymptomatic forms to severe forms of hepatic encephalopathy, hepatopulmonary syndrome, and pulmonary arterial hypertension (11).

According to the different types and sites of portosystemic shunts, Abernethy malformation may have different manifestations and can be classified into the following three types:

(1) shunt hypertension-related symptoms, such as recurrent hemafecia and variceal haemorrhage. Recurrent hemafecia is relatively common, mainly related to the obstruction of rectal venous plexus reflux and can be easily misdiagnosed as haemorrhoids;

(2) Extrahepatic portal vena cava shunt-related symptoms, such as hyperammonemia, hepatic encephalopathy, hepatopulmonary syndrome, pulmonary hypertension, hypergalactosemia, glomerulonephritis, and nephrotic syndrome;

(3) Liver ischemia-related symptoms: the long-term insufficient liver perfusion due to portosystemic shunt can result in liver dysfunction, cirrhosis, and liver nodules, among others. The patient in this case report had relatively mild symptoms and slow onset. The early-stage manifestations of the disease included megalosplenia and hypersplenism secondary to portal hypertension. As the disease progressed, the patient had liver dysfunction because of insufficient liver perfusion caused by a portosystemic shunt (9).

Early diagnosis of Abernethy malformation is challenging because no specific symptoms are available, and various imaging examinations are essential for diagnosing and differential diagnosis of Abernethy malformation and the screening of related complications. Doppler ultrasonography can reveal abnormal shunts between the portal and systemic veins; can assess liver morphology, liver nodules, and the relationship with other malformations; and has the advantages of noninvasiveness and low cost. Moreover, Doppler ultrasonography can be used as the first-choice examination method for Abernethy malformation and follow-up before and after treatment. However, it might fail to detect inapparent or small shunts accurately. Traditionally, conventional angiography is a gold standard for detecting portomesenteric vasculature. However, improvements in CT and MRI techniques have changed the situation.

Currently, conventional angiography is not necessarily a must in CEPS diagnosis, as CT and MRI can provide accurate diagnoses in most cases (11). For the accurate diagnosis of CEPS, one should first exclude potential acquired portosystemic shunts, such as patients with hepatic cirrhosis, those with or without concomitant presentations of portal hypertension (15), and those with surgically created portosystemic shunts (16). In the portosystemic shunt that developed after cirrhosis and portal hypertension, liver cirrhosis occurs first, followed by portal hypertension-related manifestations, so the shunt is acquired.

While in Abernethy malformation, extrahepatic portosystemic shunt happens first, which results in reduced liver blood perfusion, followed by portal hypertension, which results in liver nodules, hepatic encephalopathy, and liver cirrhosis. Furthermore, patients with cirrhosis and portal hypertension usually have other diseases that cause cirrhosis, such as viral hepatitis and alcoholic liver disease. Adult Abernethy malformation should be differentiated from a cavernous transformation of the portal vein (CTPV). In imaging findings, CTPV can be presented as several vascular plexuses formed in and around the main or branch of the portal vein. CTPV and MRA can also reveal the distribution of portal vein thromboses. The patient in this case report has no history of abdominal surgery or abdominal trauma, no apparent cirrhosis, and no obvious widening of the portal vein or CTPV manifestations; thus, the possibility of this disease is not considered, so this disease was not diagnosed more than 10 years ago. Recently, a splenorenal shunt was observed, and the intrahepatic portal vein is thin, so type II Abernethy malformation was diagnosed.

Currently, there is no standard therapeutic approach for CEPS. Treatment strategies are decided according to shunt types, locations, symptoms severities, and clinical course. Generally, liver transplantation is the most effective and practical for type I CEPS, whereas cure can be ensured by surgical closure or interventional radiology (coil embolization or catheter-device closure) for type 2 CEPS (17). Multiple studies have shown the capacity of the liver to re-expand or develop new portal veins following shunt closure (18,19–21).

Shunt closures must always be considered for symptomatic patients and should also be regarded as a prophylactic treatment early in the evolution of the disease to prevent the development of severe complications (11). Earlier studies have shown that for shunt occlusions, interventional embolization and surgical ligations (open or laparoscopic surgical techniques) are treatment options that rapidly reduce symptoms and normalize ammonia levels (22,23). Whether an interventional embolization or a surgical ligation depends on medical expertise, shunt vessel anatomy and sizes, and individual general conditions (18, 24, 25); for patients with wide and short shunt vessels or those who fail to receive embolization, surgical ligation will be preferred (26). The critical problem for this patient is the significant reduction in the number of erythrocytes, leukocytes, and platelets. The patient has surgical indications, and after the shunt of the splenic artery, splenic vein, splenorenal venous, and the ligation of the abnormal venous outflow tract, the abnormal parameters of the patient were quickly recovered, and his general conditions were improved. The therapeutic effect is ideal, and the patient is being followed up.

We report a case of a patient with type II Abernethy malformation with megalosplenia and hypersplenism. Surgical ligation led to a rapid recovery of the patient. Correct diagnosis and appropriate management may lead to improved prognosis and continued close, and long-term follow-up after shunt closure is required.

Consent

Written informed consent was obtained from the patient to publish this case report and all accompanying images.

Authors' contributions

YL and YX carried out the conception and design of the research, and XW participated in the Acquisition of data. YY carried out the analysis and interpretation of data. BW participated in the design of the study and performed the statistical analysis. YL and YX conceived of the study, participated in its design and coordination, and helped draft and revise the manuscript. The authors read and approved the final manuscript and declared that they have no conflict of interest.

REFERENCES

1. Abernethy J. Account of two instances of uncommon formation in the viscera of the human body: From the Philosophical Transactions of the Royal Society of London. Med Facts Obs 1797; 7:100-8.
2. Howard ER, Davenport M. Congenital extrahepatic portocaval shunts–the Abernethy malformation. J Pediatr Surg 1997; 32(3):494–7.
3. Morgan G, Superina R. Congenital absence of the portal vein: two cases and a proposed classification

system for portasystemic vascular anomalies. J Pediatr Surg 1994; 29(9):1239–41.
4. Mathai SV, Kondray V, Salloum E, et al. Role of interventional radiology in the diagnosis and management of congenital extrahepatic portosystemic shunts: Two case reports. Indian J Radiol Imaging 2019; 29(2):219-22.
5. Sakamoto S, Shigeta T, Fukuda A, et al. The role of liver transplantation for congenital extrahepatic portosystemic shunt. Transplantation 2012; 93(12):1282-7.
6. Matthews TJ, Trochsler MI, Bridgewater FH, et al. Systematic review of congenital and acquired portalsystemic shunts in otherwise normal livers. Br J Surg 2014; 101(12):1509-17.
7. Stringer MD. The clinical anatomy of congenital portosystemic venous shunts. Clin Anat 2008; 21(2):147–57.
8. Morgan G, Superina R. Congenital absence of theportalvein: Two cases and a proposed classification system for portasystemic vascular anomalies. J Pediatr Surg 1994; 29(9):1239-41.
9. Zhao X, Zheng J, Li P, et al. Congential extrahepatic portosystemic shunt in adults: A report of three cases. J Clin Hepatol 2021; 37(4):910-3.
10. Sokollik C, Bandsma RH, Gana JC, et al. Congenital portosystemic shunt: characterization of a multisystem disease. J Pediatr Gastroenterol Nutr 2013; 56:675-81.
11. Tang H, Song P, Wang Z, et al. A basic understanding of congenital extrahepatic portosystemic shunt: incidence, mechanism, complications, diagnosis, and Itreatment. Intractable Rare Dis Res 2020; 9(2):64-70.
12. Guerin F, Blanc T, Gauthier F, et al. Congenital portosystemic vascular malformations. Semin Pediatr Surg 2012; 21(3):233-44.
13. Acherman RJ, Evans WN, Galindo A, et al. Diagnosis of absent ductus venosus in a population referred for fetal echocardiography: association with a persistent portosystemic shunt requiring postnatal device occlusion. J Ultrasound Med 2007; 26(8):1077-82.
14. Shen O, Valsky DV, Messing B, et al. Shunt diameter in agenesis of the ductus venosus with extrahepatic portosystemic shunt impacts on prognosis. Ultrasound Obstet Gynecol 2011; 37(2):184-90.
15. Konstas AA, Digumarthy SR, Avery LL, et al. Congenital portosystemic shunts: imaging findings and clinical presentations in 11 patients. Eur J Radiol 2011; 80(2):175- 81.
16. Hu GH, Shen LG, Yang J, et al. Insight into congenital absence of the portal vein: is it rare? World J Gastroenterol 2008; 14(39):5969-79.
17. Gonçalves I, Barros D, Araújo M, et al. Type II Abernethy Malformation: A Rare Cause of Hepatic Encephalopathy in Adulthood. Eur J Case Rep Intern Med 2022; 9(1):003145.
18. Kanazawa H, Nosaka S, Miyazaki O, et al. The classification based on intrahepatic portal system for congenital portosystemic shunts. J Pediatr Surg 2015; 50(4):688–95.
19. Bernard O, Franchi-Abella S, Branchereau S, et al. Congenital portosystemic shunts in children: recognition, evaluation, and management. Semin Liver Dis 2012; 32(4): 273–87.
20. Chocarro G, Amesty MV, Encinas JL, et al. Congenital portosystemic shunts: clinic heterogeneity requires an individual management of the patient. Eur J Pediatr Surg 2016; 26(1):74–80.
21. Bruckheimer E, Dagan T, Atar E, et al. Staged transcatheter treatment of portal hypoplasia and congenital portosystemic shunts in children. Cardiovasc Intervent Radiol 2013; 36(6): 1580–5.
22. Morikawa N, Honna T, Kuroda T, et al. Resolution of hepatopulmonary syndrome after ligation of a portosystemic shunt in a pediatric patient with an Abernethy malformation. J Pediatr Surg 2008; 43(2):e35-8.
23. Kimura T, Soh H, Hasegawa T, et al. Laparoscopic correction of congenital portosystemic shunt in children. Surg Laparosc Endosc Percutan Tech 2004; 14(5):285-8.
24. Papamichail M, Ali A, Quaglia A, et al. Liver resection for the treatment of a congenital intrahepatic portosystemic venous shunt. Hepatobiliary Pancreat Dis Int. 2016; 15(3):329-33.
25. Papamichail M, Pizanias M, Heaton N. Congenital portosystemic venous shunt. Eur J Pediatr 2018; 177(3):285-94.
26. Kamimatsuse A, Onitake Y, Kamei N, et al. Surgical intervention for patent ductus venosus. Pediatr Surg Int. 2010; 26(10):1025-30.

Isoquercitrin alleviates inflammation in diabetic nephropathy by inhibiting TLR4/NF-κB signaling pathway

Y. Wu*, H. Deng, J. Sun and Y. Xu*

Department of Endocrinology, Zhongnan Hospital of Wuhan University, Wuhan, Hubei, P.R. China

Received November 23, 2021 – Accepted March 31, 2022

OBJECTIVE: The present study aimed to functionally investigate the protective effects and potential mechanisms of action of ISO (Isoquercitrin) in diabetic nephropathy using *in vivo* and *in vitro* experiments.

METHODS: The mRNA and protein expression levels of markers of fibrosis and inflammation, including TGF-β1, Collagen 1, PAI-1, IκBα, NF-κB, and p-NF-Kb, were analyzed by reverse transcription-PCR analysis and western blotting. In addition, histopathological examination was used to confirm the renal injury. ELISA was used to measure biochemical markers of renal injury, including TNF-α, IL-1β, adhesion molecule 1 (ICAM-1) and vascular cell adhesion molecule 1 (VCAM-1).

RESULTS: Our study demonstrated that ISO decreased the levels of glucose, urinary protein, serum creatinine and blood urea nitrogen and alleviated the histopathological abnormalities in the kidney of rats with streptozocin (STZ)-induced D.N. ISO also suppressed STZ-induced activation of NF-κB signaling pathway and decreased the STZ-induced increase in the levels of the markers of fibrosis and inflammatory response, including TGF-β1, collagen I, plasminogen activator inhibitor-1, TNF-α, IL-1β, ICAM-1 and VCAM-1 in D.N. rats. ISO also exerted similar protective effects on high glucose (H.G.)-treated HK-2 cells. Finally, exogenous TAK-242, a selective inhibitor of Toll-like receptor 4 (TLR4), enhanced the protective effects of ISO on HG-treated HK-2 cells.

CONCLUSION: In summary, our study demonstrated that ISO alleviates D.N. by suppressing fibrosis and inflammatory responses. The protective effects seem to be mediated by inhibiting the activation of the TLR4/NF-κB signaling pathway. Our data suggest that ISO has promising therapeutic benefits for patients with D.N.

Diabetic nephropathy (D.N.) is a highly prevalent vascular complication in the kidney of type 1 or type 2 diabetes mellitus (D.M.) patients, and it is the main cause of the end-stage renal disease (1, 2). However, due to the insufficient understanding of D.N.'s pathogenesis, there are currently no specific strategies for preventing the development and progression of D.N.

Accumulating evidence has indicated the involvement of inflammatory processes in the pathogenesis of D.N. (3, 4), which could lead to fibrosis and renal failure. Natural flavonoid isoquercitrin (quercetin-3-O-β-d-glucopyranoside; ISO) is commonly found in medicinal herbs, fruits, vegetables and plant-derived foods and beverages (5).

Keywords: isoquercitrin; diabetic nephropathy; Toll-like receptor 4/NF-κB signaling pathway

**Corresponding Authors*:
Dr Yancheng Xu and Dr Yuwen Wu,
Department of Endocrinology,
Zhongnan Hospital of Wuhan University,
Donghu Road No.169, Wuchang District,
Wuhan, Hubei 430071, P.R. China
e-mail [Y.X.]: xjl100901@whu.edu.cn
e-mail [Y.W.]: zenda@126.com

0393-974X (2022)

ISO has pleiotropic chemoprotective effects against cancer, oxidative stress, cardiovascular disorders, D.M. and allergic reactions through its anti-allergic, anti-inflammatory and antioxidant properties (5-7). It was recently demonstrated that ISO might be used as a possible therapeutic agent in D.M. (8). Further study indicated that the upregulation of antioxidant genes and inhibition of inflammatory cytokines by ISO contributes to the antidiabetic effect in streptozotocin-induced diabetic rats (9). However, whether ISO could exert beneficial effects on the D.N. in diabetes remains investigated.

Toll-like receptors (TLRs) are a conserved family of pattern recognition receptors involved in activating pro-inflammatory signalling pathways by exogenous microbial pathogens and agonists of non-microbial origin (10). TLR4, which is mainly distributed in the glomerular mesangial cells and renal tubular epithelial cells of kidney tissues (10), has been implicated in the pathogenesis of diverse diseases, including acute kidney injury (11), central nervous system autoimmune diseases (12), other autoimmune diseases (13). The activation of TLR4 promotes tubular inflammation (14), podocyte injury and interstitial fibrosis (15), and its antagonists may attenuate renal injury in D.N. (16). In addition, evidence has shown that the expression of TLR4 is increased by high glucose (H.G.) and angiotensin II, which activates the downstream p38-MAPK and NF-κB pathways and promotes the release of pro-inflammatory cytokines and chemokines, including IL-6, IL-1β and monocyte chemotactic protein 1, thereby aggravating kidney injury (9-11). Among those factors, NF-κB seems to serve as a key transcription factor activated by proteinuria and angiotensin II and regulates the expression of genes implicated in D.N. progression (17).

Based on these previous findings, the present study systematically evaluated the protective effect of ISO in streptozotocin (STZ)-induced rat model of D.N. and HG-treated HK-2 cells, to elucidate the mechanism underlying the protective effect of ISO in the pathogenesis of D.N. Our study demonstrated that ISO alleviates D.N. by suppressing fibrosis and inflammatory responses. The protective effects seem to be mediated by inhibiting the activation of the TLR4/NF-κB signaling pathway. Our data suggest that ISO has promising therapeutic benefits for patients with D.N.

MATERIALS AND METHODS

Groups and rat model of D.N.

Animal experiments were conducted according to the Guidelines for the Care and Use of Laboratory Animals by the National Research Council of the National Academies and were approved by the Animal Ethics and Welfare Committee of Zhongnan Hospital of Wuhan University (Approval number:2020045)

Thirty male Sprague-Dawley rats of specific pathogen-free grade, aged 8±1 weeks and weighing 275±25 g, were obtained from the Center for Disease Control and Prevention (Wuhan, China). The rats were maintained under conditions of 21±2˚C temperature and 55±2% humidity, with a 12-h light/dark cycle, with free access to food and water. The rats were divided into normal control (N.C., n=12) and D.N. groups (n=18). After 1 week, the rats in the D.N. group were intraperitoneally injected with 55 mg/kg STZ (Sigma-Aldrich; Merck KGaA) dissolved in sodium citrate buffer (pH 4.5). Mice in the N.C. group were injected with sodium citrate buffer. One week after STZ injection, blood was collected daily from the tail vein (5 mL) for 3 consecutive days. The successful construction of the diabetic rat model was verified when the plasma glucose concentrations were ≥16.67 mM over 3 consecutive days.

The rats, including 18 diabetic rats and 12 N.C. rats, were grouped as follows (n=6 per group): N.C., NC + high-dose ISO (ISO-H), D.N., D.N. + low-dose ISO (ISO-L) and D.N. + ISO-H. The rats in N.C. + ISO-H, D.N. + ISO-L and D.N. + ISO-H groups were intragastrically administered with ISO at 80, 40 and 80 mg/kg/day (dissolved in water), respectively, for 8 weeks, while the rats in the N.C. and D.N. groups received the same dose of normal saline. At 12 weeks after STZ injection, all rats were housed in metabolic cages for 24-h urine collection, and their body weight was measured. Subsequently, the animals were sacrificed by anesthesia (10% chloral hydrate, 480mg/kg), and blood samples were collected. The serum was obtained by centrifugation (37 ˚C, 3000rmp, 15 min) and stored at -20˚C. Kidney tissues were dissected, weighed and stored in liquid nitrogen or fixed in 4% paraformaldehyde for 24h at 37 ˚C. The concentration of ISO used in this study was determined according to a previous study (8).

Measurements of renal biochemical markers and TNF-α, IL-1β, ICAM-1 and VCAM-1

The urinary protein, creatinine, and blood urea nitrogen concentrations were measured using the sulfosalicylic acid precipitation method and commercial assay kits from Nanjing Jiancheng Institute of Biotechnology (No. C035-1-1). The levels of TNF-α, IL-1β, ICAM-1 and VCAM-1 in renal tissues or HK-2 cell culture medium were determined by corresponding ELISA kits: anti-TNF-α (cat. no. SEKH-0047), anti-IL-1β (cat. no. SEKH-0002), anti-ICAM-1 (cat. no. SEKH-0053) and anti-VCAM-1 (cat. no. SEKH-0055; Beijing Suolaibao Technology Co., Ltd.).

Histopathological examination

The kidney tissues were fixed in 4% paraformaldehyde for 24h at 37 ˚C, embedded in paraffin and cut into 4-μm sections. The tissue sections were stained with hematoxylin-eosin (HE) (fixed with 95% ethanol for 20 min, washed with PBS 3 times, and then stained with hematoxylin for 3 min and Eosin for 5 min). For periodic acid Schiff (PAS) staining, the tissues were fixed with 70% ethanol for 20 min, washed with PBS 3 times, and then stained with Periodic acid and Schiff). All tissues sections were examined under a light microscope (Olympus Corporation, ×200).

Reverse transcription PCR (RT-PCR)

Total RNA was extracted from HK-2 cells and tissues using TRIzol® reagent (GenMed) according to the manufacturer's protocol. By using a cDNA synthesis kit (Invitrogen; Thermo Fisher Scientific, Inc.), 1 μg of total RNA was reversely transcribed into cDNA. qPCR was performed using Premix Ex Taq Master Mix (Takara Bio, Japan) on the ABI 7500 Real-Time PCR System (Applied Biosystems, USA). $2^{-\triangle\triangle Ct}$ method was applied to measure the relative gene expression. GAPDH was used as an internal reference. Primers used in this study:

Mouse:

GAPDH: F-AGGTCGGTGTGAACGGATTTG;
GAPDH: R-GGGGTCGTTGATGGCAACA;
TGFb1: F-CCACCTGCAAGACCATCGAC;
TGFb1: R-CTGGCGAGCCTTAGTTTGGAC;
Collagen 1: F-GCTCCTCTTAGGGGCCACT;
Collagen 1: R-ATTGGGGACCCTTAGGCCAT;
TLR4: F-ATGGCATGGCTTACACCACC;
TLR4: R-GAGGCCAATTTTGTCTCCACA;
PAI-1: F-TTCAGCCCTTGCTTGCCTC;
PAI-1: R-ACACTTTTACTCCGAAGTCGGT.

Human:

GAPDH: F-CAACTTTGGTATCGTGGAAGG;
GAPDH: R-GCCATCACGCCACAGTTTC;
TGFb1: F-TAATGGTGGAAACCCACAACG;
TGFb1: R-ATCGCCAGGAATTGTTGCTG;
Collagen 1: F-GAGGGCCAAGACGAAGACAT;
Collagen 1: R-CAGATCACGTCATCGCACAA;
TLR4: F-AGACCTGTCCCTGAACCCTAT;
TLR4: R-CGATGGACTTCTAAACCAGCC;
PAI-1: F-GCACCACAGACGCGATCTT;
PAI-1: R-ACCTCTGAAAAGTCCACTTGC.

Western blot assay

Cells and tissues were lysed with RIPA lysis buffer (Beyotime Institute of Biotechnology). Total protein was quantified using the BSA kit (Beyotime, China), and 20 μg of protein samples were separated by 10% SDS-PAGE and transferred to PVDF membranes (Bio-Rad Laboratories, Inc.). The membranes were then blocked with 5% skimmed milk for 1h and incubated with the following primary rabbit antibodies at 4˚C overnight: Anti-TGF-β1 (18978-1-AP, 1:1000, ProteinTech Group, Inc.), anti-collagen I (ab34710, 1:1000, Abcam), anti-plasminogen activator inhibitor (PAI)-1 (ab66705, 1:500, Abcam), anti-p-NF-κB p65 (ab28856, 1:500, Abcam), anti-NF-κB p65 (ab16502, 1:500, Abcam), anti-NF-κB inhibitor (IκB) α (ab32518, 1:500, Abcam), anti-Histone H3 (#37988, 1:1000, Signalway Antibody LLC) and anti-GAPDH (ab9485, 1:500, Abcam). Subsequently, the membranes were incubated with HRP-conjugated secondary antibody (goat anti-rabbit IgG; 1:2000, ab6721, Abcam) for 1h. The bands were developed using Horseradish Peroxidase Color Development Kit (Solarbio, China), and protein bands were developed in a dark room.

Cell culture and treatment

Human renal tubular epithelial HK-2 cells were obtained from the Cell Bank of Shanghai Institute (Shanghai, China) and cultured in DMEM (Gibco; Thermo Fisher Scientific, Inc.) containing 5.5 mM glucose (normal glucose, N.G.), supplemented with 10% FBS (Gibco; Thermo Fisher Scientific, Inc.) and 0.1% penicillin/streptomycin in a 5% CO_2 incubator at 37˚C. Cells were sub-cultured when every three days. In order to evaluate the effect of ISO on high glucose treatment, the following experimental conditions

were set up: N.C. (untreated control), H.G. (High glucose: 30 mmol/l D-glucose), HG + 5 μM ISO, HG + 10 μM ISO, HG + 20 μM ISO, HG + 40 μM ISO, HG + 80 μM ISO, NC + 20 μM ISO, HG + TAK-242 (1 μM) and H.G. + TAK-242 + **20** μM ISO.

Cells were cultured for 72 h in an H.G. medium containing 30 mmol/l D-glucose. ISO (at concentrations of 5, 10, 20, 40 or 80 μM) was added when the cell culture medium after H.G. treatment. In HG + TAK-242 and H.G. + TAK-242 + ISO groups, cells were also pretreated with 1μM TAK-242. TAK-242, a cyclohexene derivative, can bind to Cys747 in the Toll/interleukin-1 receptor (TIR) domain of TLR4 and selectively inhibit TLR4 (18), thereby disrupting the association between TLR4 and TIR adaptor protein (19).

Cell viability assay

HK-2 cells were seeded into 96-well plates ($4x10^3$ cells/well) and were subject to indicated treatment for 2 days. Next, 10 μl of CCK-8 solution (Dojindo Molecular Technologies, Inc.) was added, and the cells were incubated for 3 h. Finally, a microplate reader measured the optical density value of each condition at 450 nm by a microplate reader.

Statistical analysis

All results are shown as means ± S.D. and were analyzed by SPSS version 20.0 (IBM Corp.) and GraphPad Prism 7 (GraphPad Software, Inc.). Comparisons between two or multiple groups were performed using Student's t-test or one-way ANOVA. $P<0.05$, $P<0.01$ or $P<0.001$ were considered statistically significant.

RESULTS

Effects of ISO on STZ-induced DN rats

Following ISO-H treatment, glucose, urinary protein, serum creatinine and blood urea nitrogen were increased, but the bodyweight was decreased in D.N. rats compared with the N.C. group ($P<0.001$; Fig. 1). Low concentration of ISO (ISO-L) decreased the levels of glucose, urinary protein, serum creatinine and blood urea nitrogen ($P<0.05$; Fig. 1A and C-E) and increased body weight ($P<0.05$; Fig. 1B) in D.N. rats. Moreover, a high concentration of ISO (ISO-H) generated more profound protective effects than ISO-L. We also examined the renal tissues by HE staining and PAS staining. D.N. group showed significant glomerular hypertrophy, diffusely expanded mesangial region and the thickening of the glomerular basement membrane. Similarly, the results of PAS staining revealed glomerular basement membrane thickening and mesangial expansion in D.N. rats (Fig. 1F). Interestingly, ISO treatment (both ISO-H group and ISO-L) ameliorated these histopathological abnormalities in the renal tissues (Fig. 1F). As hyperglycemia is a major factor contributing to renal abnormality in diabetes, we next examined the effect of high glucose (H.G.) on HK-2 cells, a tubular cell line derived from a normal kidney. HK-2 cells in N.C. exhibited a cobble-shaped morphology (Fig. 1G). In addition, cells exposed to H.G. exhibited an elongated, fibroblast-like phenotype. Treatment with ISO (20 μM) prevented the morphological changes in most HK-2 cells (Fig. 1G). These data suggest that ISO may improve the renal histopathological abnormalities observed in D.N. rats.

Effects of ISO on the NF-κB signaling pathway in STZ-induced DN rats

As shown in Fig. 2A, the mRNA levels of TGF-β1, collagen I and PAI-1 were significantly higher in renal tissues of D.N. rats compared with N.C. rats. However, ISO treatment (both ISO-H and ISO-L) attenuated the upregulation of these genes. The western blotting analysis yielded similar results (Fig. 2B). ELISA further revealed that the levels of TNF-α, IL-1β, ICAM-1 and VCAM-1 were higher in renal tissues of D.N. rats, whereas ISO treatment (both ISO-H and ISO-L) reduced their expression levels (Fig. 2C). In addition to the induction of the pro-inflammatory cytokines, we further examined the changes in the NF-κB pathway. The phosphorylation level of NF-κB p65 (p-NF-κB p65) was increased, and that of IκB**α was decreased in D**.N. rats compared with N.C. rats (Fig. 2D). However, ISO treatment partially reversed these changes (Fig. 2D). Furthermore, the cytoplasmic/nuclear fraction analysis indicated that a relatively higher amount of NF-κB p65 was translocated into the nucleus in renal tissues of D.N. rats, whereas ISO partially rescued these effects (Fig. 2E). Together, these data suggest

that ISO attenuates the activation of the NF-κB signaling pathway in STZ-induced DN rats.

Effects of ISO on the expression of the markers of fibrosis and inflammatory response in HG-treated HK-2 cells

We next investigated the effect of ISO using an *in vitro* cell model of HK-2 cells induced by high glucose (H.G.). As shown in Fig. 3A, H.G. treatment significantly decreased the viability of HK-2 cells, which was protected by ISO administration. The addition of 20 μM ISO achieved the highest cell viability and was used in the following analysis. As shown in Fig. 3B and C, the mRNA and protein expression levels of TGF-β1, collagen I and PAI-1 were upregulated in HG-treated HK-2 cells, and ISO treatment attenuated their upregulation. In addition, ELISA demonstrated that the levels of TNF-α, IL-1β,

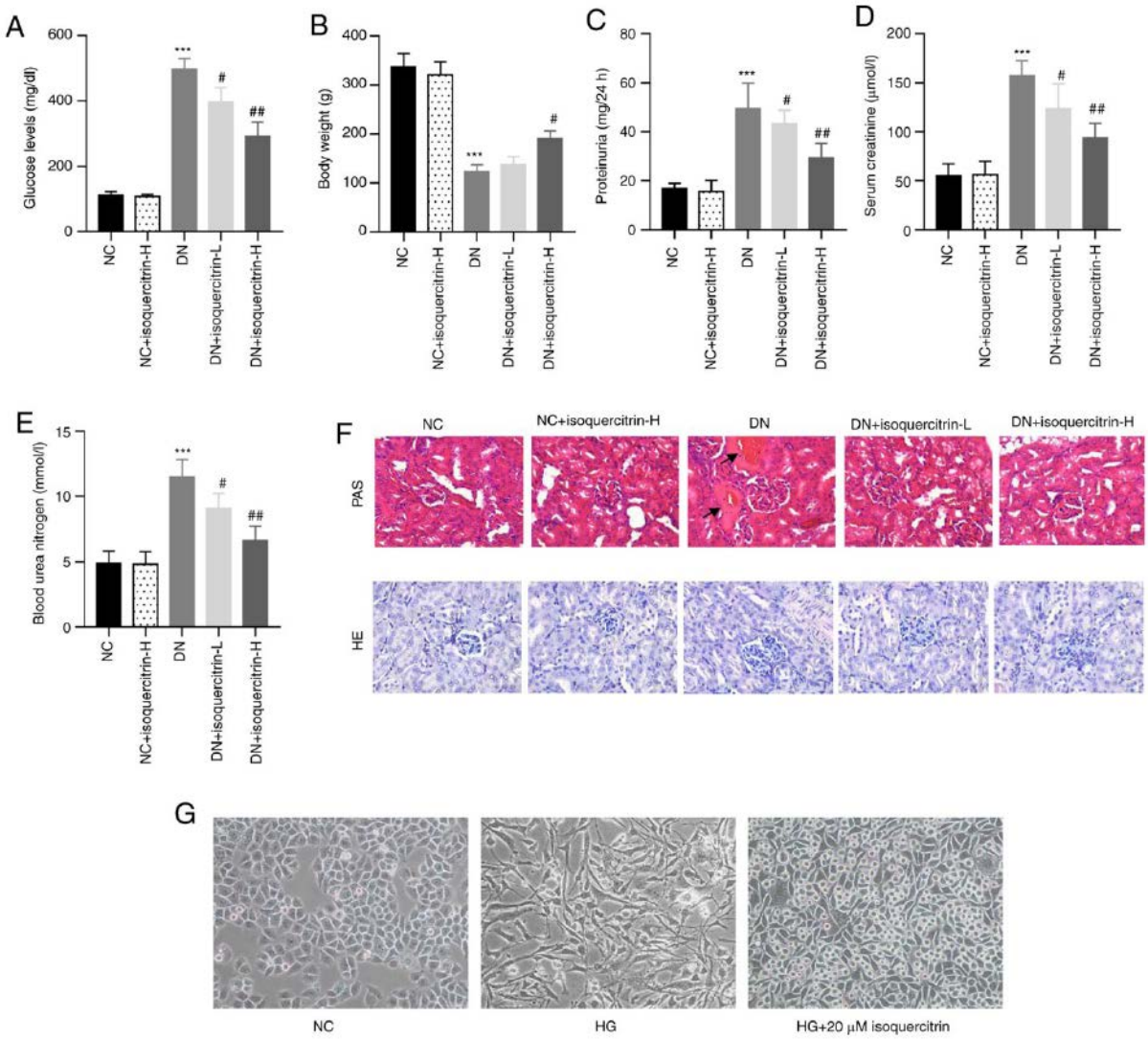

Fig. 1. *Effects of ISO on streptozocin-induced D.N. rats. (A) Glucose levels, (B) rat body weight, (C) urinary protein, (D) serum creatinine and (E) blood urea nitrogen levels were measured. (F) HE and PAS staining was used for renal histopathology analysis (scale bar, 50 μm, ×200); arrows, glomerular hypertrophy. (G) Phase-contrast microscopy was used to examine HK-2 cell morphology following exposure to N.C., HG, or HG + 20 μM ISO (scale bar, 100 μm×100). ***P<0.001 compared to N.C. group, #P<0.05 and ##P<0.01 compared to D.N. group. ISO, isoquercitrin; D.N., diabetic nephropathy; N.C., normal control; H.G., high glucose; HE, hematoxylin-eosin; PAS, periodic acid Schiff.*

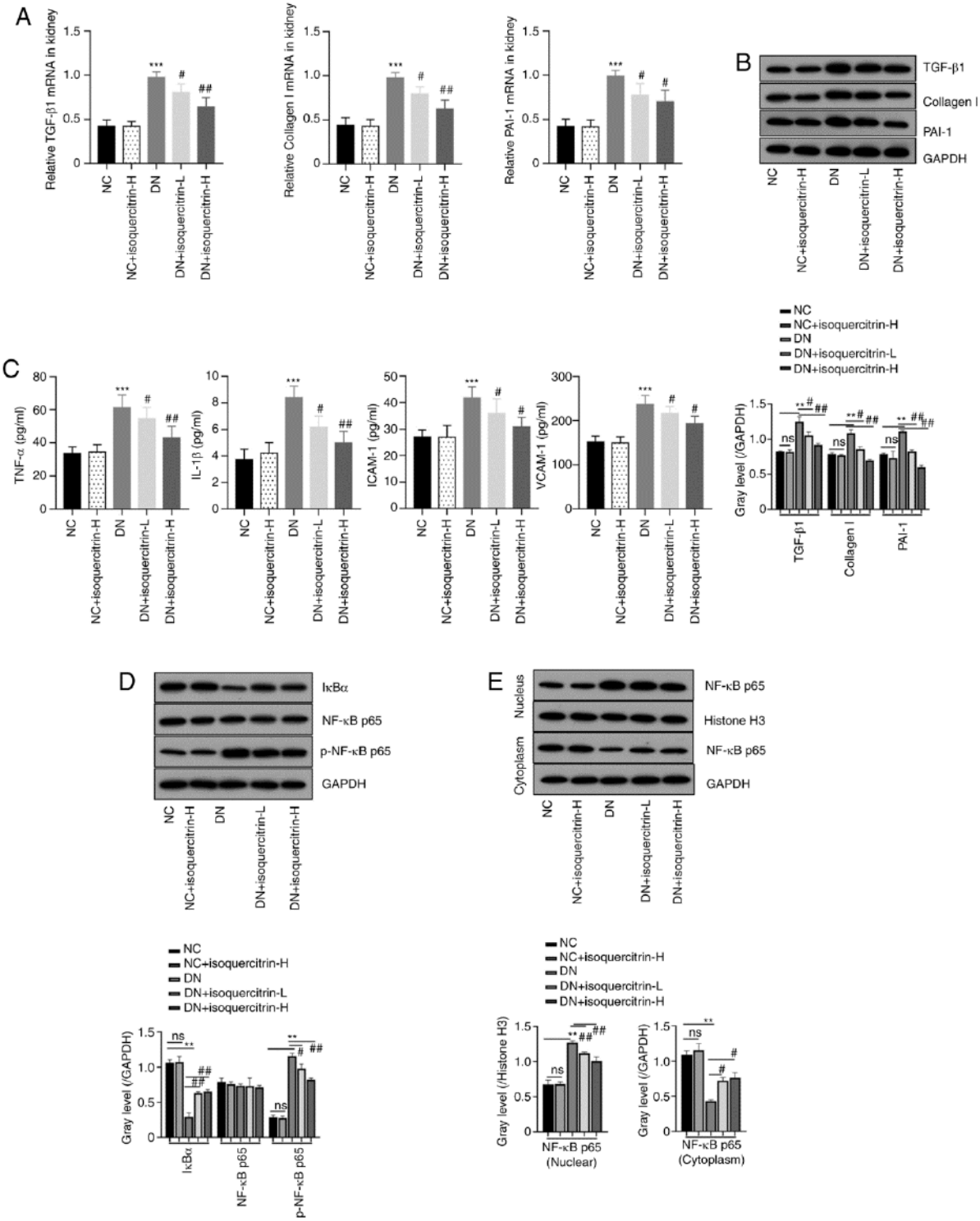

Fig. 2. *Effects of ISO on the NF-κB signaling pathway in streptozocin-induced D.N. rats. (A) mRNA and (B) protein expression levels of TGF-β1, collagen I and PAI-1 in rats. (C) ELISA was used to measure the levels of TNF-α, IL-1β, ICAM-1 and VCAM-1 in renal tissues from rats. (D) Protein expression levels of p-NF-κB p65, NF-κB p65 and IκB**α** in rats. (E) Nuclear and cytoplasmic protein expression levels of NF-κB p65 in renal tissues from rats.* $^{***}P<0.001$ *compared to NC group,* $^{\#}P<0.05$ *and* $^{\#\#}P<0.01$ *compared to DN group; ns, non-significant. ISO, isoquercitrin; D.N., diabetic nephropathy; N.C., normal control; PAI-1, plasminogen activator inhibitor-1; ICAM-1, intercellular adhesion molecule 1; VCAM-1, vascular cell adhesion molecule 1; IκB**α**, NF-κB inhibitor **α**.*

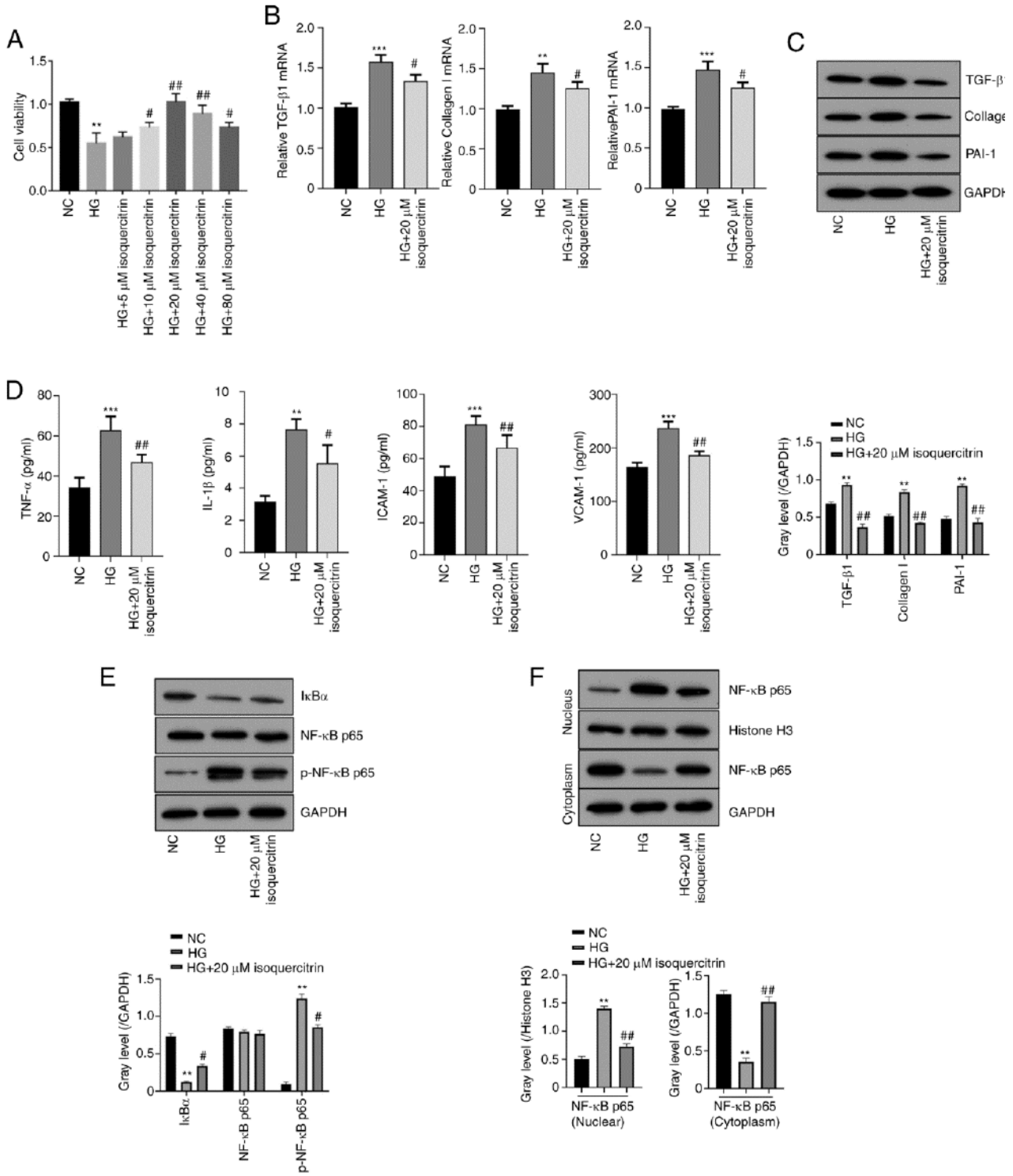

Fig. 3. *Effects of ISO on the expression of markers of fibrosis and inflammatory response in HG-treated HK-2 cells. (A) HK-2 cell viability was measured by the Cell Counting Kit-8 assay. (B) mRNA and (C) protein expression levels of TGF-β1, collagen I and PAI-1 in HK-2 cells. (D) ELISA was used to measure the levels of TNF-α, IL-1β, ICAM-1 and VCAM-1 in HK-2 cells. (E) Protein expression levels of p-NF-**κB p65, NF-κB p65 and** IκB**α in HK-2 cells. (F) Nuclear and cytoplasmic protein expression levels of NF-κB p65 in HK-2 cells.* $^{***}P<0.001$ *compared to N.C. group,* $^{\#}P<0.05$ *and* $^{\#\#}P<0.01$ *compared to H.G. group. ISO, isoquercitrin; N.C., normal control; H.G., high glucose; PAI-1, plasminogen activator inhibitor-1; ICAM-1, intercellular adhesion molecule 1; VCAM-1, vascular cell adhesion molecule 1; IκB**α,** NF-κB inhibitor **α.***

ICAM-1 and VCAM-1 induced by H.G. treatment were decreased by ISO (Fig. 3D). Consistently, ISO treatment also mitigated the increase of p-NF-κB p65 level and increased IκB**α level in HG-treated HK-2 cells (Fig. 3E).** However, this was accompanied by an impaired nuclear translocation of NF-κB p65 upon ISO treatment in HG-treated HK-2 cells (Fig. 3F).

TAK-242 enhances the protective effect of ISO on HG-treated HK-2 cells

To explore the mechanism underlying the function of ISO, TAK-242, a novel selective TLR4 signal transduction inhibitor, was applied together with ISO in HG-treated HK-2 cells (Fig. 4 and 5). As shown in Fig. 4A, TAK-242 significantly decreased the protein levels of TLR4 in HG-treated HK-2 cells. In addition, TAK-242 significantly enhanced the protective effect of ISO on HG-treated HK-2 cells. Furthermore, the addition of TAK-242 further reduced the mRNA and protein expression levels of TGF-β1 (Fig. 4B and E), collagen I (Fig. 4C and E) and PAI-1 (Fig. 4D and E), as well as the levels of TNF-α (Fig. 4F), IL-1β (Fig. 5A), ICAM-1 (Fig. 5B) and VCAM-1 (Fig. 5C), when compared to the group with ISO treatment alone. Furthermore, TAK-242 addition also caused additive effects on the reduction of p-NF-κB p65 level and the increase of IκB**α level by ISO in HG-treated cells (Fig. 5D), as well as on the nuclear translocation** of NF-κB p65 (Fig. 5E). These data suggest that ISO could act synergistically with TRL4 inhibitor on HG-treated HK-2 cells.

DISCUSSION

It has been reported that abnormal renal function in D.N. is mainly caused by mesangial cell proliferation and basement membrane thickening in the glomerulus, microalbuminuria, excessive accumulation of extracellular matrix proteins and epithelial hypertrophy in the glomerulus and tubules (20). In the present study, STZ was used to induce D.N. in a rat model, and the results of PAS and HE staining indicated renal injury in D.N. rats compared with the N.C. group. Interestingly, ISO treatment decreased these histopathological abnormalities. In addition, the markers of renal malfunction (glucose, urinary protein, serum creatinine and blood urea nitrogen levels) were increased in D.N. rats, and the bodyweight was decreased compared with the N.C. group. These observations were consistent with previous studies (21,22), suggesting the successful induction of the D.N. rat model. These changes were partially rescued by ISO treatment, indicating the protective role of ISO against renal injury in D.N. rats.

ISO or plants containing high amounts of flavonols have been reported to stabilize atherosclerotic plaques (23). In *in vitro* experiments, ISO was also described as a possible inhibitor of ACE (angiotensin-converting enzyme), a dipeptidyl peptidase (protease) that is widely distributed in the cardiovascular system and various non-cardiovascular tissues (24). A previous study suggested that the action of ISO is similar to that of glibenclamide, as supplementation with ISO could maintain the homeostasis of blood sugar levels and regulate expressions of insulin signalling pathway-related genes and carbohydrate metabolizing enzymes (8). Furthermore, ISO also inhibits the oxidative stress elicited by STZ by regulating antioxidant genes and alleviates hyperlipidemia and inflammation in STZ-induced diabetic rats (9).

Our study also suggests that ISO exerts protective effects in the STZ-induced DN rat model and HG-treated HK-2 cells by attenuating the activation of the NF-κB signaling pathway. It has been demonstrated that TLR4 can activate NF-κB downstream pathways and promote the release of pro-inflammatory cytokines and chemokines (9-11), which is strongly associated with D.N. progression (17). Our results showed that ISO treatment mitigates the STZ-induced levels of fibrotic markers and inflammatory factors, including TGF-β1, collagen I, PAI-1, TNF-α, IL-1β, ICAM-1 and VCAM-1, in D.N. rats. ISO achieved similar results in HG-treated HK-2 cells, consistent with previous reports (25-27). TGF-β1, collagen I and PAI-1 are pro-fibrogenic factors, whereas TNF-α, IL-1, ICAM-1 and VCAM-1 are important factors in inflammatory responses. These findings indicate that ISO alleviates D.N. by suppressing fibrosis and exerting anti-inflammatory effects. In addition, exogenous TAK-242 (TLR4 inhibitor) enhances the protective effects of ISO on HG-treated HK-2 cells. Our study suggests that ISO

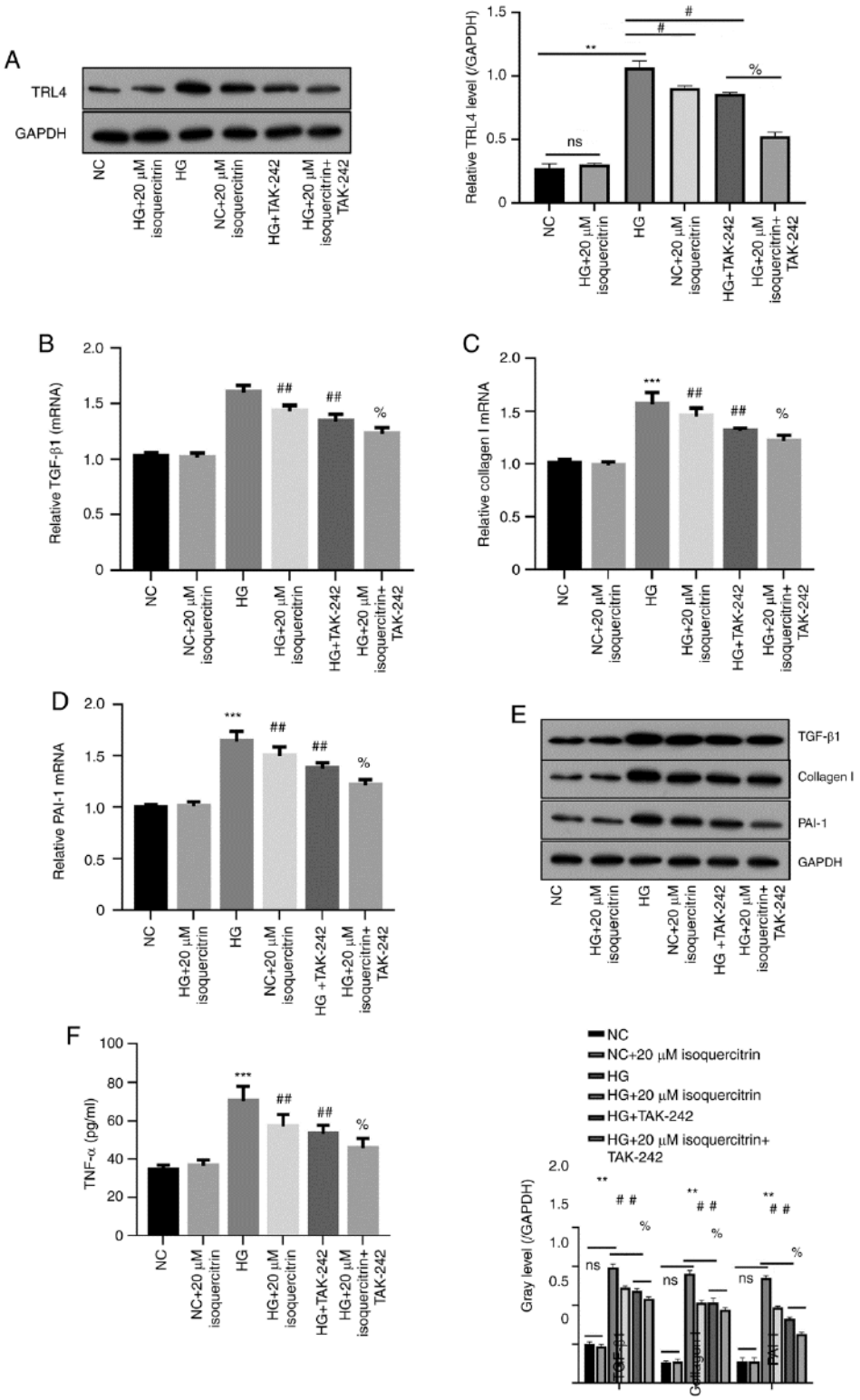

Fig. 4. *TAK-242 enhanced the suppressive effects of ISO on the levels of TGF-β1, collagen I, PAI-1 and TNF-α in HG-treated HK-2 cells. (A) TLR4 protein expression was detected by western blotting. (B-E) mRNA and protein expression levels of TGF-β1, collagen I and PAI-1 in HK-2 cells. (F) ELISA was used to measure the levels of TNF-α in HK-2 cells. $^{***}P<0.001$ compared to NC group, $^{\#}P<0.05$ and $^{\#\#}P<0.01$ compared to HG group, $^{\%}P<0.05$ compared to HG + TAK242 group; ns, non-significant. ISO, isoquercitrin; N.C., normal control; H.G., high glucose; PAI-1, plasminogen activator inhibitor-1.*

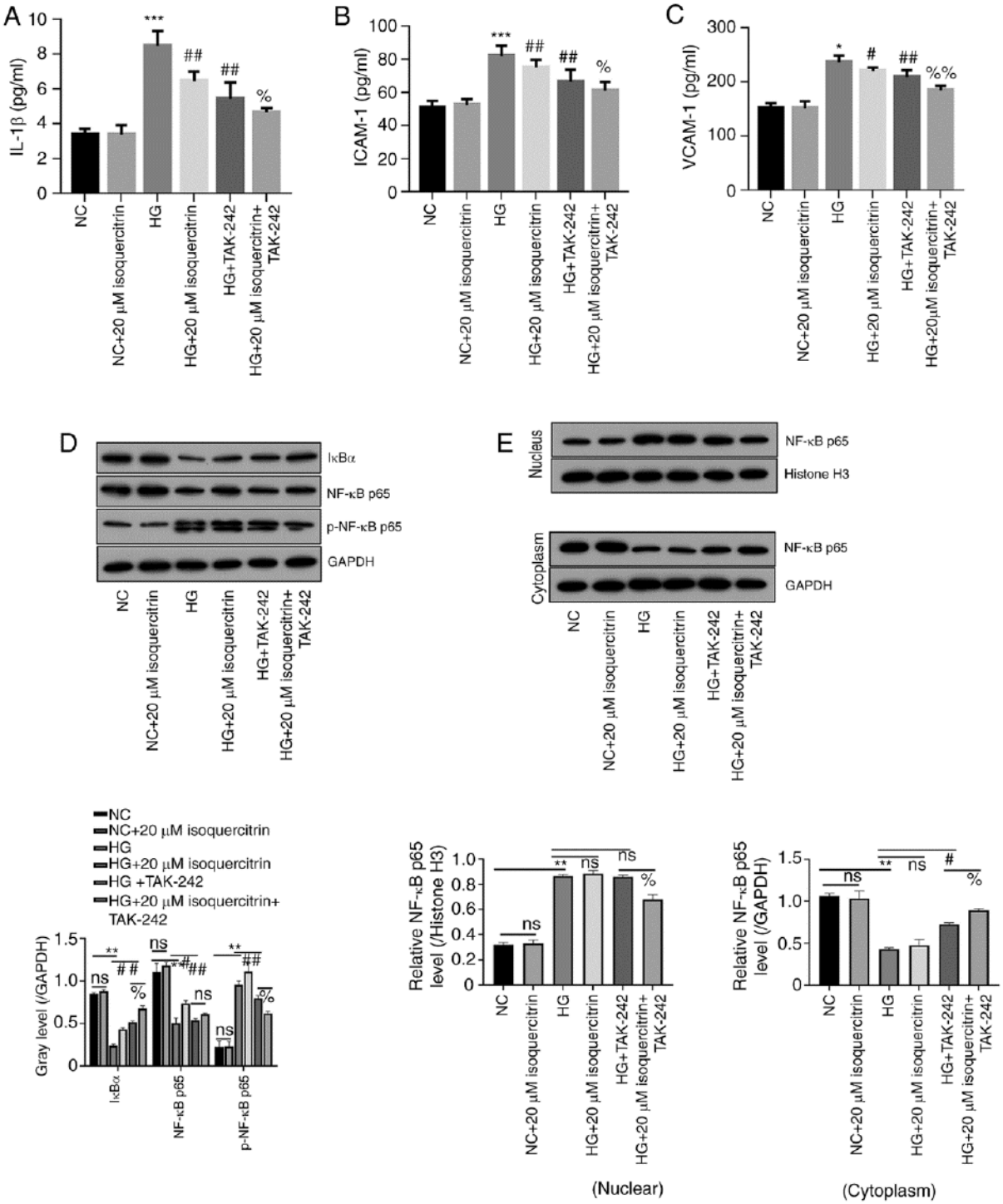

Fig. 5. *TAK-242 enhanced the suppressive effects of ISO on the levels of IL-1β, ICAM-1 and VCAM-1 and NF-κB signaling pathway in HG-treated HK-2 cells. ELISA was used to measure the levels of (A) IL-1β, (B) ICAM-1 and (C) VCAM-1 in HK-2 cells. (D) Protein expression levels of p-NF-κB p65, NF-κB p65 and IκB**α** in HK-2 cells. (E) Nuclear and cytoplasmic protein expression levels of NF-κB p65 in HK-2 cells.* $^{***}P<0.001$ *compared to NC group,* $^{\#}P<0.05$ *and* $^{\#\#}P<0.01$ *compared to HG group,* $^{\%}P<0.05$ *and* $^{\%\%}P<0.01$ *compared to HG + TAK242 group; ns, non-significant. ISO, isoquercitrin; N.C., normal control; H.G., high glucose; ICAM-1, intercellular adhesion molecule 1; VCAM-1, vascular cell adhesion molecule 1; IκB**α**, NF-κB inhibitor **α**.*

alleviates D.N. by inhibiting the activation of the TLR4/NF-κB signaling pathway.

A previous study reported that c-Jun and SP1 synergistically promote TGF-β1 expression in the development of D.N. through autoregulation, cross-activation and phospho-modification (28). This finding suggested that other signalling pathways may also be implicated in D.N. development, which requires further clarification. Furthermore, in PMACI-stimulated KU812 cells, ISO reduces the production of histamine and pro-inflammatory cytokines, such as IL-6, IL-8, IL-1β and TNF-α (27). Finally, in a rat model of acute myocardial infarction, ISO increased the levels of endothelial nitric oxide synthase (NOS), reduced inducible NOS and suppressed the TLR4/NF-κB signalling pathway (29).

There are some limitations in the current study. The effect of ISO should also be evaluated in the type 2 diabetic model to study whether ISO can be used as a general antidiabetic natural product. In addition, the synergistic effect of TLR4 inhibitor and ISO could be investigated in the D.N. rat model as well to evaluate the potential as a combinatory therapy for D.N. Future transcriptomic analysis of ISO effect in D.N. rat could further reveal additional pathways or gene programs regulated by ISO. Since we only observed the partial rescue effect of ISO in our study, we propose ISO as a potential supplement to mitigate the complications of D.N. Nevertheless, since ISO seems to dampen inflammatory responses, it is worth further evaluating whether ISO also negatively regulates other beneficial immune responses such as anticancer immunity or antiviral infection in diabetic patients, which could provide more clinical evidence for the safety of ISO in diabetic patients.

In summary, the present study's findings indicated that ISO might alleviate D.N. by suppressing fibrosis and exerting anti-inflammatory effects via inhibiting the activation of the TLR4/NF- B signaling pathway, thus establishing its potential as a new therapeutic method for patients with D.N. However, further investigations must be performed to elucidate the underlying mechanism and explore the complexity of D.N.

Funding

This study was supported by the Chinese National Project in Science and Technology (81970718) and the Health Commission of Hubei Province scientific research project (WJ2021M161).

Availability of data and materials

All datasets generated and/or analyzed during the present study are available on request.

Authors' contributions

Y.W. and Y.X. conceived the study. H.D. conducted the investigation. J.S. prepared the materials for the study. Y.W. analyzed the data and wrote the manuscript. All the authors have read and approved the final manuscript. In addition, Y.X. have seen and confirmed the authenticity of the raw data.

Ethics approval and consent to participate

All the experimental protocol involving human data was following the guidelines of the Declaration of Helsinki in the manuscript, and all experimental animal protocols were reviewed and approved by the Animal Ethics and Welfare Committee of Zhongnan Hospital of Wuhan University

Competing interests

The authors declare that they have no competing interests.

REFERENCES

1. Zhang L, Long J, Jiang W, et al. Trends in Chronic Kidney Disease in China. N Engl J Med 2016; 375(9):905-6.
2. Salman M, Khan AH, Adnan AS, et al. Attributable causes of chronic kidney disease in adults: a five-year retrospective study in a tertiary-care hospital in the northeast of the Malaysian Peninsula. Sao Paulo Med J 2015;133(6):502-9.
3. Verzola D, Cappuccino L, D'Amato E, et al. Enhanced glomerular Toll-like receptor 4 expression and signaling in patients with type 2 diabetic nephropathy and microalbuminuria. Kidney Int 2014; 86(6):1229-43.
4. Sun B, Hu S, Li Y, et al. Triptolide contributes to decrease in TLR4 expression by upregulating miR-224-3p to inhibit the inflammatory reaction in

diabetic nephropathy. [Retracted] Oncotarget 2016; 7(51):85675.
5. King CA, Marshall JS, Alshurafa H, Anderson R. Release of Vasoactive Cytokines by Antibody-Enhanced Dengue Virus Infection of a Human Mast Cell/Basophil Line. J Virol 2000; 74(15):7146-50.
6. Kim AR, Jin Q, Jin HG, Ko HJ, Woo ER. Phenolic compounds with IL-6 inhibitory activity fromAster yomena. Arch Pharm Res 2014; 37(7):845-51.
7. Falcone FH, Haas H, Gibbs BF. The human basophil: a new appreciation of its role in immune responses. Blood 2000; 96(13):4028-38.
8. Jayachandran M, Zhang T, Ganesan K, Xu B, Chung SSM. Isoquercetin ameliorates hyperglycemia and regulates key enzymes of glucose metabolism via insulin signaling pathway in streptozotocin-induced diabetic rats. Eur J Pharmacol 2018; 829:112-120.
9. Jayachandran M, Wu Z, Ganesan K, Khalid S, Chung SM, Xu B. Isoquercetin upregulates antioxidant genes, suppresses inflammatory cytokines and regulates AMPK pathway in streptozotocin-induced diabetic rats. Chem Biol Interact 2019; 303:62-69.
10. Lin M, Yiu WH, Wu HJ, et al. Toll-Like Receptor 4 Promotes Tubular Inflammation in Diabetic Nephropathy. J Am Soc Nephrol 2012; 23(1):86-102.
11. Shah N, Mohamed FE, Jover-Cobos M, et al. Increased renal expression and urinary excretion of TLR4 in acute kidney injury associated with cirrhosis. Liver Int 2013; 33(3):398-409.
12. Kerfoot SM, Long EM, Hickey MJ, et al. TLR4 Contributes to Disease-Inducing Mechanisms Resulting in Central Nervous System Autoimmune Disease. J Immunol 2004; 173(11):7070-7.
13. Liu Y, Yin H, Zhao M, Lu Q. TLR2 and TLR4 in Autoimmune Diseases: A Comprehensive Review. Clin Rev Allergy Immunol 2014; 47(2):136-47.
14. Lin M, Yiu WH, Wu HJ, et al. Toll-like receptor 4 promotes tubular inflammation in diabetic nephropathy. J Am Soc Nephrol 2012; 23(1):86-102.
15. Ma J, Chadban SJ, Zhao CY, et al. TLR4 Activation Promotes Podocyte Injury and Interstitial Fibrosis in Diabetic Nephropathy. PLoS One 2014; 9(5):e97985.
16. Lin M, Yiu WH, Li R.X., et al. The TLR4 antagonist CRX-526 protects against advanced diabetic nephropathy. Kidney Int 2013; 83(5):887-900.
17. Mezzano S, Aros C, Droguett A, et al. NF-κB activation and overexpression of regulated genes in human diabetic nephropathy. Nephrol Dial Transplant 2004; 19(10):2505-12.
18. Kawamoto T, Ii M, Kitazaki T, Iizawa Y, Kimura H. TAK-242 selectively suppresses Toll-like receptor 4-signaling mediated by the intracellular domain. Eur J Pharmacol 2008; 584(1):40-8.
19. Matsunaga N, Tsuchimori N, Matsumoto T, Ii M. TAK-242 (resatorvid), a small-molecule inhibitor of Toll-like receptor (TLR) 4 signaling, binds selectively to TLR4 and interferes with interactions between TLR4 and its adaptor molecules. Mol Pharmacol 2011; 79(1):34-41.
20. Sato S, Sasaki Y, Adachi A, Ghazizadeh M. Validation of Glomerular Basement Membrane Thickness Changes with Aging in Minimal Change Disease. Pathobiology 2010; 77(6):315-9.
21. Zhou Y, Wang Q, Qing G, Guo F, Zhang Y, Wu L. [Effect and mechanism of FoxO1 overexpression in rats with diabetic nephropathy.] [Chinese] Chine J Endocri Meta 2015; 31(2):155-161.
22. Ryu HH, Kim HL. Therapeutic effects of epigallocatechin gallate on streptozotocin-induced diabetic nephropathy in mice. Kidney Res Clin Pract 2012; 31(2):A45.
23. Enkhmaa B, Shiwaku K, Katsube T, Kitajima K, Anuurad E, Yamasaki M, Yamane Y. Mulberry (Morus alba L.) Leaves and Their Major Flavonol Quercetin 3-(6-Malonylglucoside) Attenuate Atherosclerotic Lesion Development in LDL Receptor-Deficient Mice. J Nutr 2005; 135(4):729-34.
24. Lacaille-Dubois MA, Franck U and Wagner H: Search for potential angiotensin converting enzyme (ACE)-inhibitors from plants. Phytomedicine 2001; 8(1):47-52.
25. Noh HJ, Kim HC, Lee SS, Kang YN, Chae YM, Park KK. The Inhibitory Effect of siRNAs on The High Glucose-Induced Overexpression of TGF-β1 in Mesangial Cells. J Korean Med Sci 2006; 21(3):430-5.
26. Tsuchida KI, Zhu Y, Siva S, Dunn SR and Sharma K: Role of Smad4 on TGF-—induced extracellular matrix stimulation in mesangial cells. Kidney Int 2003; 63(6):2000-9.
27. Ko GJ, Kang YS, Han SY, et al. Pioglitazone attenuates diabetic nephropathy through an anti-inflammatory mechanism in type 2 diabetic rats.

Nephrol Dial Transplant 2008; 23(9):2750-60.
28. Gao P, Wei Y, Zhang Z, et al. Synergistic effects of c-Jun and SP1 in the promotion of TGFβ1-mediated diabetic nephropathy progression. Exp Mol Pathol 2016; 100(3):441-50.
29. Ma C, Jiang Y, Zhang X, Chen X, Liu Z, Tian X. Isoquercetin ameliorates myocardial infarction through anti-inflammation and anti-apoptosis factor and regulating TLR4-NF-κB signal pathway. Mol Med Rep 2018; 17(5):6675-80.

Comparative studies of mouse acute lung injury models induced by lipopolysaccharide and polyinosinic-polycytidylic acid

L. Zhang, Y. Ye, H. Kang, J. Pan, Q. Xu, H. Zhu, G. Liu* and W. Gu*

Department of Biochemistry and Molecular Biology, School of Laboratory Medicine, and Anhui Province Key Laboratory of Translational Cancer Research, Bengbu Medical College, Bengbu, Anhui Province, P.R. China

Acute lung injury (ALI), its severe form, acute respiratory distress syndrome (ARDS), is a clinical syndrome characterized by acute hypoxic respiratory failure, bilateral lung infiltration with edema, and normal cardiac filling pressure. There is no effective treatment for ALI/ARDS, and our understanding of its pathogenesis is partially based on animal models. With the widely use of Lipopolysaccharide (LPS) for bacterial infection-induced ALI, models for a viral infection-induced ALI are relatively rare. This study established ALI models using Polyinosinic-polycytidylic acid [poly(I:C)] and LPS intra-tracheal installation, respectively, and systematic evaluations were conducted. Firstly, histological studies by hematoxylin and eosin (HE) staining showed that poly(I:C) and LPS could induce inflammatory cell infiltration and structural changes. The lung injury was confirmed with the Wet/Dry ratio in both treatments with a significantly higher ratio in poly(I:C) group. Total protein concentration in Bronchoalveolar Lavage Fluid (BALF) from poly(I:C) and LPS treated groups were also significantly increased, while more protein concentration in LPS group than that in poly(I:C) group. Flow cytometry showed that LPS promoted more alveolar neutrophil infiltration than poly(I:C). Secondly, quantitative PCR showed that poly(I:C) treatment promoted more expression of inflammatory factors, IL-1α, IL-6, TNF-α, and ICAM-1, with decreased expression of CCL-2. Finally, lung ventilation experiments showed that both poly(I:C) and LPS caused similar lung function loss with increased Newton resistance in poly(I:C) induced lung injury. In conclusion, poly(I:C) and LPS-induced ALIs were systematically evaluated, and distinct characteristics were associated with poly(I:C) induced lung injury. Our studies may provide the foundation for understanding the viral infection-induced ALI.

Acute lung injury (ALI) is a clinical syndrome characterized by acute hypoxic respiratory failure, bilateral lung infiltration with leukocytes and fluids (edema), and severe symptoms that may be acute respiratory distress syndrome (ARDS) (1, 2). Despite recent advances in the diagnosis and treatment of ALI/ARDS, the mortality rate is still around 40% and up to 60% in patients over 85 years of age (3, 4). At present, there is no effective treatment for ARDS. The injury could induce ALI to pulmonary vascular endothelial cells and alveolar epithelial cells, which results in increased vascular permeability, excessive production of cytokines and leukocyte aggregation, pulmonary interstitial and alveolar edema, alveolar collapse, and hypoxemia (5). Nevertheless, the pathogenesis of ALI is not fully understood. Therefore, the mouse ALI models are good tools for exploring the pathogenesis and treatment of ALI.

Keywords: poly(I:C); LPS; ALI/ARDS; inflammation

**Corresponding Author:*
Dr Guoquan Liu and Dr Wei Gu,
Department of Biochemistry and Molecular Biology,
School of Laboratory Medicine, Bengbu Medical College,
2600 Donghai Street, Bengbu,
233030 Anhui Province, People's Republic of China.
e-mail: guoquanliu@bbmc.edu.cn; guwei@bbmc.edu.cn

0393-974X (2022)

ALI can be caused by multiple pathogen infections (bacterial, viral and fungal), poisoning, trauma, shock, and immune response, and bacterial and viral infections are the main pathogenic factors (2). Lipopolysaccharide (LPS) is an essential component of the outer membrane of gram-negative bacteria, which stimulates innate immunity, and promotes the release of a variety of inflammatory factors. LPS is often used as an inducer to establish bacterial infection-induced ALI models in animals (6). Poly(I:C) is a synthetic double-stranded RNA that may stimulate the host immune response and is frequently employed as a virus mimic in studying the host immune system response produced by the virus infection (7). While more studies are carried out in the mature LPS-induced ALI, poly(I:C) induced ALI is relatively new and rarely used. The emergence of COVID-19 addresses the necessity and neediness of ALI models from a viral infection, and poly(I:C) produced ALI may serve the aims.

Nevertheless, characterizing the similarities and differences between poly(I:C) and LPS induced ALIs may provide a new strategy and base for treating virus-induced ALI. In this study, ALI models established by poly(I:C) and LPS, respectively, were characterized. Total protein quantization and neutrophil proportion detection of bronchoalveolar lavage fluid (BALF) were performed. The lungs Wet/Dry ratio (W/D), pathological analysis and cytokine determination of lung tissue, and lung ventilation test of mice. ALIs induced by poly(I:C) and LPS were systematically evaluated to provide the pathological difference between them and an additional theoretical basis for treating ALI differently.

MATERIALS AND METHODS

Experimental animals

This study was performed following the China Council on Animal Care and Protocol guidelines. In addition, the procedures for animal care and use were approved by the Ethics Committee of Bengbu Medical College, and all applicable institutional and governmental regulations concerning the ethical use of animals were followed. C57BL/6 mice were purchased from SKbex Biotechnology (Henan, China). Mice weight 18~25 g and were aged 7~8 weeks.

Intra-tracheal installation of acute lung injury models

C57BL/6 mice were randomly divided into control group, LPS (*Escherichia coli* 055: B5; Sigma Aldrich, St. Louis, Missouri), and poly(I:C) (APExBIO, Houston, Texas) group. The mice were weighed and anaesthetized with pentobarbital sodium (10 mg/kg) and tracheotomized, and a trimmed sterile 18-gauge needle was inserted caudally into the tracheal lumen. LPS (2.5 mg/kg), poly(I:C) (2.5 mg/kg), and equal-volume endotoxin-free PBS as control, respectively, through intratracheally administered injection for 6 h, the BALF and lung tissues were collected for subsequent experiments.

Histopathology of Lung tissue processing

Lung tissues were collected and fixed in 5% paraformaldehyde, cut into 5-μm slices, and stained with hematoxylin and eosin (Sigma Aldrich, St. Louis, Missouri, USA). The sections were observed with a light microscope for lung histopathology.

Lung Wet/Dry Ratio

Mouse lungs were isolated, and the weights of lungs were recorded as the wet weight. After the lungs were dried at 60°C for 72 h, the weight was recorded as dry-weight. The lung wet/dry (W/D) ratio was calculated.

Collection of bronchoalveolar lavage fluid (BALF) and total protein analysis

The chest cavity was exposed for bronchoalveolar lavage collection, the lung was repeatedly rinsed with PBS and withdrawn, and the alveolar lavage fluid was collected. The collected solutions were centrifuged at 1000 × g for 10 min at 4 °C. After centrifugation, the supernatant and precipitate were collected. The BCA kit determined the total protein concentration of cell-free BALF (Beyotime, Jiangsu, China).

Flow Cytometry analysis

Quantitative analysis of neutrophils was carried out using fluorescent-labelled antibodies by flow cytometry. Unconjugated anti-mouse CD16/CD32 was used to block Fc receptors, APC-labeled anti-mouse Ly-6G/Ly-6C (Gr-1) (Biolegend, San Diego, California) performed for neutrophils. The cells, protected from light, were incubated with antibodies for 30 min on ice, then washed with PBS three times by centrifugation. The labelled neutrophils were

counted by flow cytometry, and the data were analyzed by FlowJo7.6 software.

RNA Isolation and Quantitative RT-PCR

Total RNA isolation from lung tissues using was conducted with TRIzol reagent (Invitrogen, Carlsbad, CA, USA), following the manufacturer's instructions. One thousand nanograms of total RNA from each sample were reverse-transcribed into single-stranded cDNA in a 10 µl reaction mixture, using BeyoRT™ III First Strand cDNA Synthesis Kit from BeyoRT (Beyotime, Shanghai, China), following the manufacturer's instructions. Real-time PCR using the ChamQ Universal SYBR qPCR Master Mix (Vazyme, Nanjing, China) was performed on the cDNA samples, as directed by the manufacturer, on a Roche lightcycler96 instrument. Expression of a specific gene was standardized to that of the control sample, GAPDH was used as internal control, and fold change was calculated using the $2^{-\Delta\Delta Ct}$ method. All experiments were performed in triplicate. Sequence information of the primers used is listed in Table I.

Respiratory mechanics

Six hours after the administration, mice were anaesthetized with pentobarbital sodium (10 mg/kg), secured in place with a nylon suture. The mouse was then connected via the cannula to the flexiVent computer-controlled piston ventilator (SCIREQ Scientific Respiratory Equipment Inc., Montreal, Canada). The parameters obtained from this sequence are integrated by default in the operating software (flexiWare v.7.6.4).

Statistical analysis

Statistical analysis was performed using GraphPad Prism 5.0 (GraphPad Software, United States). Statistical significance was analyzed using one-way ANOVA, and the post hoc test (Tukey method) was applied to investigate the differences between the two groups. P-value of less than 0.05 ($*P < 0.05$, $**P < 0.01$, $***P < 0.001$) was considered as statistically significant.

RESULTS

Histopathological studies of poly(I:C) and LPS-Induced lung injury

In order to investigate the effects of poly(I:C) and LPS-induced ALI, lung histopathological changes were first detected by HE staining, and acute lung injury featuring neutrophilic inflammation and interstitial edema were observed. The histological studies showed that the alveolar structure in the control group was complete with a clear alveolar cavity, and no noticeable swelling and inflammatory infiltration in the alveolar septum was also noticed (Fig. 1A). However, in the poly(I:C) treated group, erythrocytic infiltration, inflammatory cell infiltration, alveolar wall thickening, less blood filling, and edema were observed in the lung tissues (Fig. 1B). On the other hand, in the LPS treated group, erythrocytic and inflammatory cell infiltration in the lung interstitium and alveolar cavity, prominent thickening of alveolar wall, a large amount of blood filling, and swelling in lung tissue were observed (Fig. 1C). Together, these

Table I. *RT-PCR primer sequences used in this study*

Gene	Forward primer (5'-3')	Reverse primer (5'-3')
GAPDH	CCTTCCGTGTTCCTACCC	GCCCAAGATGCCCTTCAGT
IL-1α	TGGCCAAAGTTCCTGACTTGTTTG	CAGGTCATTTAACCAAGTGGTGCT
IL-6	ATGGCAATTCTGATTGTATG	GACTCTGGCTTTGTCTTTCT
TNF-α	CTTGTGGCAGGGGCCACCAC	CCATGCCGTTGGCCAGGAG
ICAM-1	CTGGGCTTGGAGACTCAGTG	CCACACTCTCCGGAAACGAA
CCL-2	CCTCGAGAGCCTGACTCCACCC	ATTTGCGGCCGCTTCAATAGTTAC

results suggest that, like LPS, poly(I:C) can also induce lung injury.

Increased lung W/D Ratio induced by poly(I:C) and LPS treatment

The W/D ratio of lung tissue is an important index to reflect the severity of pulmonary edema in mice, which can be used to evaluate the severity. The effects of poly(I:C) and LPS induced lung W/D ratio were detected in this study. The W/D ratio in the poly(I:C) group and LPS group were higher than that in the PBS group (as shown in Fig. 2A), indicating that the poly(I:C) and LPS induced pulmonary edema in mice. Furthermore, the results showed that poly(I:C) and LPS caused different degrees of pulmonary edema, and poly(I:C) induced more severe pulmonary edema than LPS.

Increase of protein concentration and neutrophil infiltration in BALF

The change of total BALF protein concentration reflects the integrity of the lung blood-gas barrier. After centrifugation, the supernatant of the BALF was collected and the total protein concentration was determined. The results showed that total protein concentration in BALF was higher than in the poly(I:C) group than in the PBS group ($P < 0.05$), and total protein concentration in BALF was significantly higher in the LPS group than in the PBS group ($P < 0.001$). In addition, the total protein concentration in bronchoalveolar lavage fluid in the group of LPS was higher than that in the group of poly(I:C) ($P < 0.05$, Fig. 2B). The results suggested that LPS treatment might induce more severe ALI than poly(I:C) treatment.

To further confirm the lung injury caused by poly(I:C), we next examined the infiltration of neutrophils in the BALF with flow cytometry analysis. Poly(I:C) or LPS alone induced a high number of leukocytes collected in the BALF; about 51.3±4.6% and 63.9±2.4% of the cells were the neutrophils, respectively (Fig. 3C-D). These suggested that the poly(I:C), like LPS, stimulated the infiltration of neutrophils. Furthermore, the infiltration of neutrophils in BALF is also closely associated with the severity.

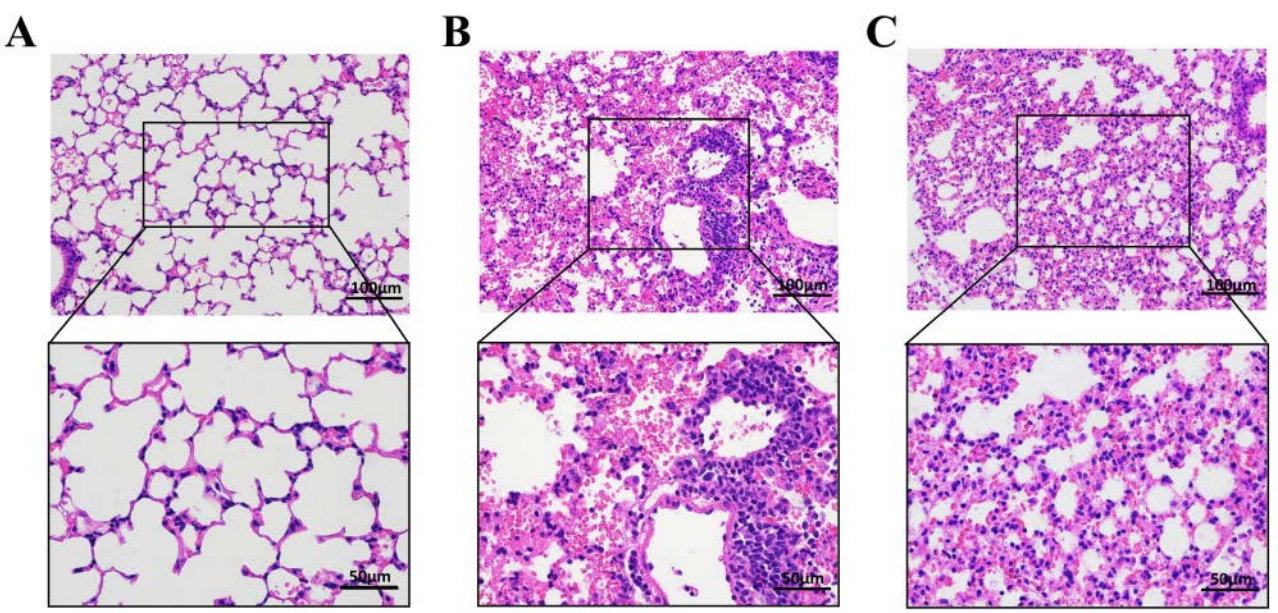

Fig. 1. *Histologic features of lung injury and interstitial pneumonia induced by poly(I:C) and LPS at 6h after challenge. Representative histological changes of lung obtained from mice of different groups. (A) Control group (n=3), (B) poly(I:C) group (n=3), (C) LPS group (n=3).*

Comparison of the expression levels of inflammatory factors in lung tissue

Inflammatory factors such as IL-1α, IL-6, TNF-α, CCL-2 and ICAM-1, play an essential role in the inflammatory response. Among them, IL-1α and TNF-α is the key pro-inflammatory factor, TNF-α is considered by many as ALI inflammatory promoter (8). After ALI, the inflammatory factors changed in different degrees. In order to understand the molecular pathology of poly(I:C) and LPS-induced lung injury, cytokine profiles were performed. Lung tissues of the poly(I:C) or LPS treated groups were collected, total RNA was extracted and reversed transcribed into DNA, and the expression levels of inflammatory factors in lung tissues were detected, respectively. The results showed that the mRNA expressions of inflammatory factors IL-1α, IL-6, TNF-α, and ICAM-1 were significantly increased ($P < 0.05$, $P < 0.001$, as shown in Fig. 3A-C), suggesting that poly(I:C), like LPS, was able to induce the production of these pro-inflammatory factors.

Respiratory mechanics parameters (respiratory system resistance) in poly(I:C) and LPS-induced mouse lung injury

ALI is a devastating disease characterized by impaired respiratory function. For instance, parameters derived from the forced expiratory manoeuvres. Therefore, to examine changes to the biophysical properties of the lung throughout poly(I:C) or LPS-induced lung injury, we mechanically ventilated mice via tracheostomy and performed several forced

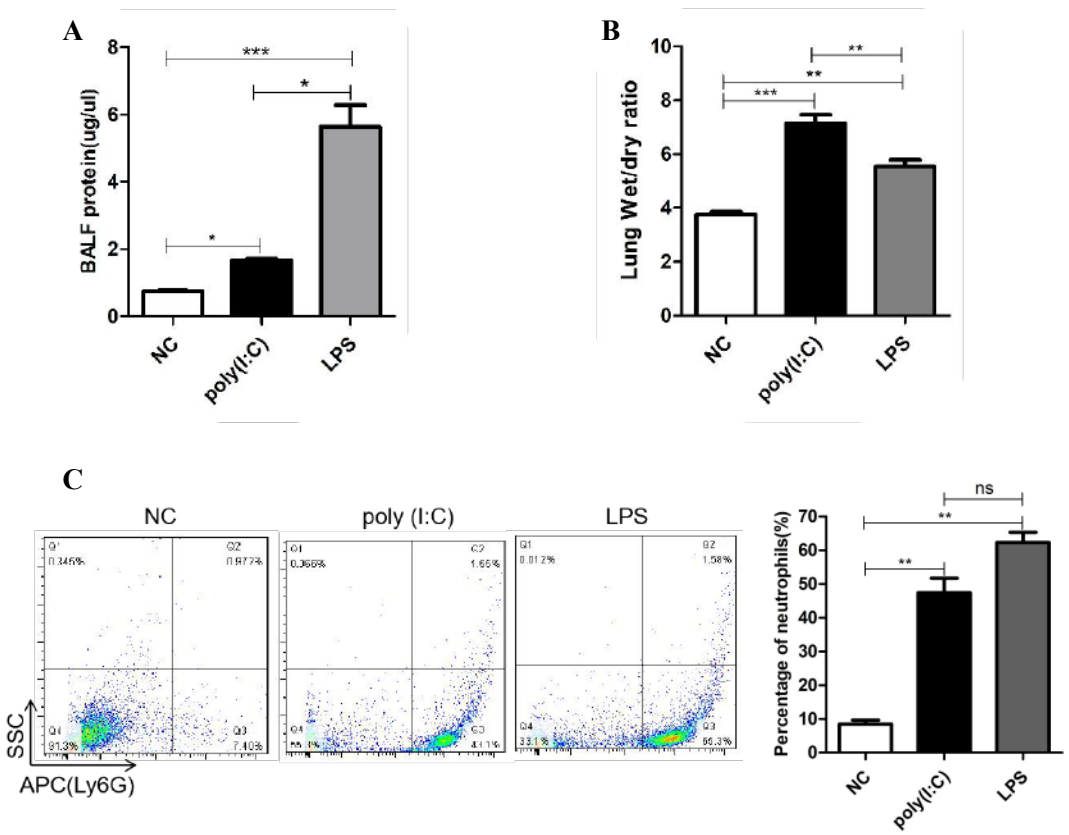

Fig. 2. *Poly(I:C) and LPS-induced lung injury. Total BALF protein (A) and lung wet/dry ratio (B) were significantly higher in the poly(I:C) and LPS-induced mice than that challenged with PBS. Flow cytometry (C) The total BALF cells and neutrophils were measured and counted based on flow cytometry analysis. The neutrophils were remarkably increased in poly(I:C) and LPS-induced mice than that in PBS mice. Data are the mean ± SEM from three independent experiments (* P< 0.05, **P< 0.01; *** P< 0.001).*

oscillation tests to determine various respiratory mechanics parameters (Fig. 4A-H).

The results showed that the inspiratory capacity, quasi-static compliance, and hysteresis area of poly(I:C) or LPS treated groups were significantly reduced compared with those of the control group while the LPS group decreased even more (Fig.4A, E, F). Meanwhile, resistance, elastance, tissue damping, and tissue elastance significantly increased in both treated groups (Fig. 4B, C, G, H). Interestingly, Newtonian resistance (Rn), a parameter of the Constant Phase Model (CPM) and representing the resistance of the central or conducting airways, was significantly increased in poly(I:C) treated group in comparison to the control and LPS treated groups (Fig. 4D), suggesting that, unlike LPS, poly(I:C) induced lung injury might also alter the function of central airways.

DISCUSSION

ALI/ARDS is a devastating lung disease characterized by acute onset of diffuse alveolar and interstitial edema, leading to severe hypoxemia ($PaO2/FiO2 \leq 300$) and infiltration of inflammatory cells in the lungs (9). Pulmonary edema caused by ALI could be due to injured endothelial cells and/or epithelial cells (10), and activation and recruitment of neutrophils play a key role in the progression of ALI and are closely related to its severity and prognosis (11). Bacterial and viral infections are the most common causes of ALI/ARDS. For instance, Gram-negative bacilli were found to be the main pathogenic bacteria in children ALI (12), and severe acute respiratory syndrome Coronavirus 2 (SARS-COV-2) causes COVID-19, including pneumonia,

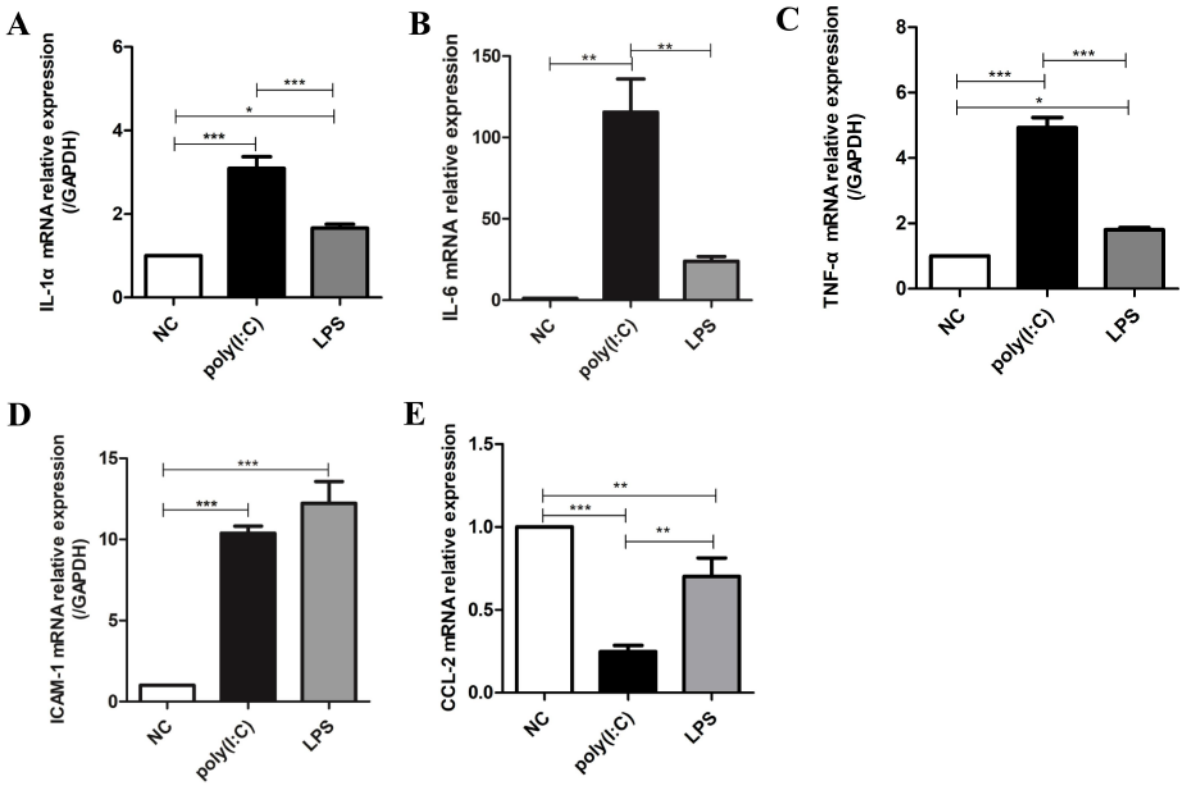

Fig. 3. *The expression of IL-6, TNF-α, IL-1α, ICAM-1, CCL-2 mRNA in poly(I:C) and LPS-induced mouse lung injury. The qPCR results showed that cytokines IL-1α(A), IL-6 (B), TNF- α(C), ICAM-1 (D) and CCL-2(E) expression exhibited a high level after stimulation by poly(I:C) and LPS in mouse lung injury. The results indicated that the expression of CCL-2 (E) protein was decreased by poly(I:C) and LPS in in mouse lung injury. GAPDH was used as internal control. Data are the mean ± SEM from three independent experiments (* P < 0.05, **P< 0.01; *** P< 0.001).*

ARDS, and multiple organ failure in the elderly (13). So far, no effective drugs have been developed for COVID-19. Establishing a highly safe, non-infectious viral analogue induced mouse acute lung injury model may be helpful for a pathological understanding of viral infection-induced ALI and future related drug development. Therefore, this study used poly(I:C) as a virus simulator to induce mouse lung injury.

We compared ALI models established by poly(I:C) and LPS, respectively, and systematic evaluation was conducted. HE's histological results are staining of lung tissue showed that poly(I:C) and LPS induced ALI with leukocyte infiltration. Protein concentration on BALF and W/D ratio confirmed the ALI induced poly(I:C) and LPS treatments. Interestingly, while the total protein concentration of BALF in the LPS group

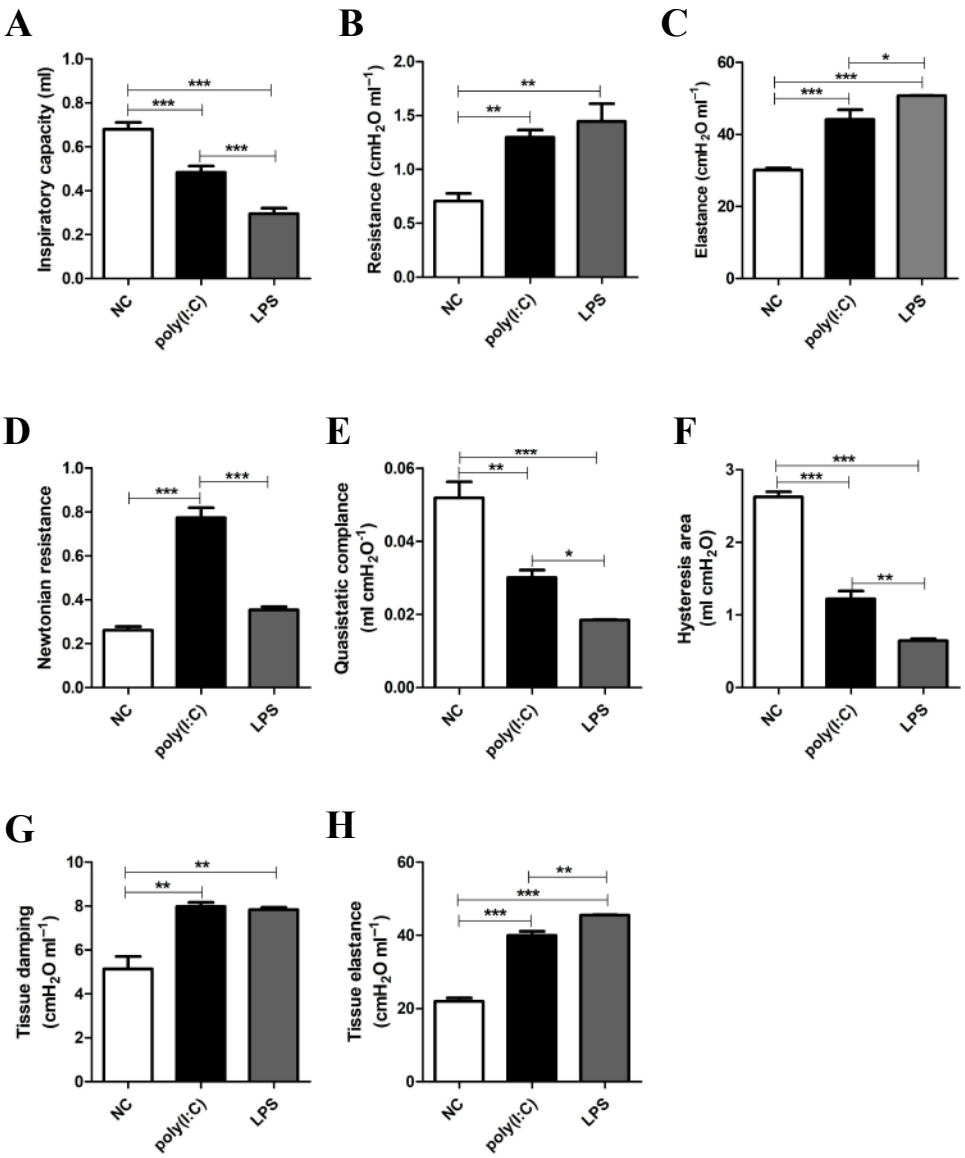

Fig. 4. *Respiratory mechanics parameters (respiratory system resistance) in poly(I:C) and LPS-induced mouse lung injury. (A) Inspiratory capacity (ml), (B) Resistance ($cmH_2O\ ml^{-1}$), (C) Elastance ($cmH_2O\ ml^{-1}$), (D) Newtonian resistance ($cmH_2O\ ml^{-1}$), (E) Quasistatic compliance ($cmH_2O\ ml^{-1}$), (F) Hysteresis area, (G) Tissue damping ($cmH_2O\ ml^{-1}$), (H) Tissue elastance (cmH_2O ml-1). Data are the mean ± SEM from three independent experiments (* P < 0.05, **P< 0.01; *** P< 0.001).*

was significantly higher than that in poly(I:C) group, the W/D ratio of poly(I:C) group was significantly higher than that of LPS group, suggesting the subtle difference of these two ALI models, which we believe may be related to changes in lung permeability induced by poly (I:C) and LPS. The difference was further confirmed by the fact that more alveolar neutrophil infiltration. It was well known that some cytokines' levels in mice could reach the highest levels 2 hours after LPS administration (14). However, we found that when LPS or poly(I:C) was induced for 6h, there were significant differences in morphological changes, neutrophil infiltration and respiratory mechanics results of the two ALI models. Furthermore, the relatively high expression of IL-1α, IL-6, TNF-α in poly(I:C) treated group suggested the formation of cytokine storm, despite similar ICAM-1 in both groups, which is an indicator of lung inflammatory.

Furthermore, poly(I:C) significantly decreased the mRNA expression of CCL-2, suggesting poly(I:C) treatment might cause a much more unbalanced cytokine expression. Previous experiments reported a novel role of ICAM-1 in the downregulation of miR-124 mediated expression of MCP-1, a key regulator molecule in monocyte recruitment, in both lungs and macrophages (15, 16). Lung functional studies also indicated the similarity of lung injury caused by poly(I:C) and LPS, except for Newtonian Resistance (Rn), which was significantly increased in poly(I:C) treated mice. This increase in Rn suggests that poly(I:C) treatment produced more profound lung damage than LPS.

Although poly(I:C) and LPS both are PAMPS, they exert different signalling to cells. Toll-like receptors (TLRs) are, as a part of the innate immune system, key elements in recognizing viral and bacterial PAMPs (17). LPS, present on the surface of Gram-negative bacteria, recognizes Toll-like receptor 4 (TLR4) (18, 19) and activates TLR4 mediating signalling, resulting in the immune response, including local infiltrating of neutrophils and macrophages, releasing of inflammatory factors, such as IL-1β, IL-6 and TNF-α, and aggravating lung injury. TNF-α, as one of the main pro-inflammatory factors, is considered as an ALI inflammatory promoter (20, 21). The poly(I:C) is a synthetic analogue of viral dsRNA and has been used as a viral mimic or an immune stimulant in various *in vitro* or *in vivo* studies, such as eliciting inflammatory responses in lungs and pulmonary allergic reactions in animal models (22).

One of the major inflammatory signalling pathways activated by the virus is the TLR3 pathway, which poly(I:C) recognizes. Thus poly(I:C) is often used as a viral mimetic and a TLR3 agonist (23). TLR3 activation induces the production of Type I interferon, which triggers an inflammatory response via downstream myeloid differentiation factor 88 (MyD88) protein or Tir-domain containing adaptor receptor Interferon-β (TRIF) (24). TLR3 activation by poly(I:C) modulates the local inflammatory response to the lung and results in lung function impairment (25). Some studies have examined the effects of poly(I:C) combined with the recombinant Spike Protein (S) of COVID-19 in mice, and it was found that the combination caused ARDS, with neutrophil inflammation, interstitial edema, and significantly increased expressions of TNF-α and IL-6 (26). However, it is also found that the poly(I:C) confers protection against a bacterial infection with a Gram-negative pathogen (27). Clearly, with our results, poly(I:C) induced lung injury may present some difference from LPS.

In summary, our comparative studies on the poly(I:C) and LPS induced mouse ALI models were systematically evaluated at the cellular and pathological levels and the inflammatory cytokine expression and lung functions. Our results suggest that there is a difference between these two models. Furthermore, our results may provide a more detailed foundation for using these models in ALI studies and a theoretical basis for developing ALI/ARDS treatment and drugs in the future.

Conflict of interest

All authors declare that they have no conflict of interest.

ACKNOWLEDGEMENTS

This project was supported financially by the National Natural Science Foundation of China (NSFC) Grants 82104178 (W. Gu), Bengbu Medical College

Scientific and Technology Self-Innovation Foundation Program, Grants BYKC201903 (G. Liu) and the Natural Science Research Project of Anhui Educational Committee, Grants KJ2021A0768 (W. Gu).

REFERENCES

1. Matute-Bello G, Frevert CW, Martin TR. Animal models of acute lung injury. Am J Physiol Lung Cell Mol Physiol 2008; 295(3): L379-99.
2. D'Alessio FR. Mouse Models of Acute Lung Injury and ARDS. Methods Mol Biol 2018; 1809: 341-350.
3. Rubenfeld GD, Caldwell E, Peabody E, et al. Incidence and outcomes of acute lung injury. N Engl J Med 2005; 353(16):1685-93.
4. Máca J, Jor O, Holub M, et al. Past and Present ARDS Mortality Rates: A Systematic Review. Respir Care 2017; 62(1):113-22.
5. Chen H, Bai C, Wang X. The value of the lipopolysaccharide-induced acute lung injury model in respiratory medicine. Expert Rev Respir Med 2010; 4(6): 773-83.
6. Quan C, Wang M, Chen H, et al. Extracellular vesicles in acute respiratory distress syndrome: Recent developments from bench to bedside. Int Immunopharmacol 2021; 100:108118.
7. Jin S, Ding X, Yang C, Li et al. Mechanical Ventilation Exacerbates poly(I:C) Induced Acute Lung Injury: Central Role for Caspase-11 and Gut-Lung Axis. Front Immunol 2021; 12:693874.
8. Imamura S, Matsukawa A, Ohkawara S, et al. Involvement of tumor necrosis factor-alpha, interleukin-1 beta, interleukin-8, and interleukin-1 receptor antagonist in acute lung injury caused by local Shwartzman reaction. Pathol Int 1997; 47(1): 16-24.
9. ARDS Definition Task Force, Ranieri VM, Rubenfeld GD, et al. Acute respiratory distress syndrome: the Berlin Definition. JAMA 2012; 307(23): 2526-33.
10. Mokra D, Kosutova P. Biomarkers in acute lung injury. Respir Physiol Neurobiol 2015; 209: 52-8.
11. Grommes J, Soehnlein O. Contribution of neutrophils to acute lung injury. Mol Med 2011; 17(3-4):293-307.
12. Ye R, Liu Z. ACE2 exhibits protective effects against LPS-induced acute lung injury in mice by inhibiting the LPS-TLR4 pathway. Exp Mol Pathol 2020; 113: 104350.
13. Szturmowicz M, Demkow U. Neutrophil Extracellular Traps (NETs) in Severe SARS-CoV-2 Lung Disease. Int J Mol Sci 2021; 22(16): 8854.
14. Kabir K, Gelinas JP, Chen M, et al. Characterization of a murine model of endotoxin-induced acute lung injury. Shock 2002; 17(4):300-3.
15. Liu J, Hou M, Yan M, et al. ICAM-1-dependent and ICAM-1-independent neutrophil lung infiltration by porcine reproductive and respiratory syndrome virus infection. Am J Physiol Lung Cell Mol Physiol 2015; 309:L226–L236.
16. Gu W, Yao L, Li L, et al. ICAM-1 regulates macrophage polarization by suppressing MCP-1 expression via miR-124 upregulation. Oncotarget 2017; 8(67):111882-111901.
17. Starkhammar M, Kumlien Georén S, Swedin L, et al. Intranasal administration of poly(I:C) and LPS in BALB/c mice induces airway hyperresponsiveness and inflammation via different pathways. PLoS One 2012; 7(2): e32110.
18. Chow JC, Young DW, Golenbock DT, et al. Toll-like receptor-4 mediates lipopolysaccharide-induced signal transduction. J Biol Chem 1999; 274(16):10689-92.
19. Ye R, Liu Z. ACE2 exhibits protective effects against LPS-induced acute lung injury in mice by inhibiting the LPS-TLR4 pathway. Exp Mol Pathol 2020; 113:104350.
20. Tang J, Xu L, Zeng Y, et al. Effect of gut microbiota on LPS-induced acute lung injury by regulating the TLR4/NF-kB signaling pathway. Int Immunopharmacol 2021; 91:107272.
21. Meng L, Li L, Lu S, et al. The protective effect of dexmedetomidine on LPS-induced acute lung injury through the HMGB1-mediated TLR4/NF-κB and PI3K/Akt/mTOR pathways. Mol Immunol 2018; 94:7-17.
22. Ali MI, Li L, Li L, et al. The tissue specific regulation of miR22 expression in the lung and brain by ribosomal protein L29. Sci Rep 2020; 10(1):16242.
23. Kang I, Harten IA, Chang MY, et al. Versican Deficiency Significantly Reduces Lung Inflammatory Response Induced by Polyinosine-Polycytidylic Acid Stimulation. J Biol Chem 2017; 292(1):51-63.
24. Zhou ZX, Zhang BC, Sun L. Poly(I:C) induces antiviral immune responses in Japanese flounder (Paralichthys olivaceus) that require TLR3 and MDA5

and is negatively regulated by Myd88. PLoS One 2014; 9(11): e112918.
25. Stowell NC, Seideman J, Raymond HA, et al. Long-term activation of TLR3 by poly(I:C) induces inflammation and impairs lung function in mice. Respir Res 2009; 10(1):43.
26. Gu T, Zhao S, Jin G, et al. Cytokine Signature Induced by SARS-CoV-2 Spike Protein in a Mouse Model. Front Immunol 2021; 11:621441.
27. Ribes S, Arcilla C, Ott M, et al. Pre-treatment with the viral Toll-like receptor 3 agonist poly(I:C) modulates innate immunity and protects neutropenic mice infected intracerebrally with Escherichia coli. J Neuroinflammation 2020; 17(1):24.

MiR-185-induced autophagy is associated with triglyceride accumulation

L. Zhou[1], A. Ma[1], Y. Wang[2,3], S. Liu[2,3] and J. Cheng[2,3]*

[1]Department of Infectious Disease China-Japan Friendship Hospital, Beijing, China; [2]Beijing Key Laboratory of Emerging Infectious Diseases, Beijing, China; [3]Insitiute of Infectious Diseases, Beijing Ditan Hospital, Capital Medical University, Beijing, China

Received November 2, 2021 – Accepted April 1, 2022

Studies have demonstrated that miRNA-185 may be a promising therapeutic target for NAFLD. However, the underlying mechanisms have not been fully clarified. Autophagy, an evolutionarily conserved catabolic process, maintains cellular homeostasis under stressful conditions, and it is closely associated with metabolic disorders. We previously reported that miR-185 could regulate autophagy for the first time via decreasing target genes (RHEB and RICTOR). The present study found that miR-185-induced autophagy is responsible for triglyceride (TG) accumulation. Firstly, we confirmed the regulatory relationship between miR-185 and lipid metabolism. Then, we found that nutrient deprivation upregulated the miR-185 level, which is associated with a remarkable downregulation of SREBP1C and FASN, as the main genes of TG synthesis, and also RHEB and RICTOR. Furthermore, the downregulated expression levels of SREBP1C and FASN confirmed that nutrient deprivation could decrease lipid storage. The downregulated expression levels of RHEB and RICTOR and increasing LC3 II/LC3-I ratio suggested that autophagy plays a role in lipid accumulation. The results highlighted an important potential role for miR-185-induced autophagy in TG accumulation. Additionally, it was found that the autophagosome level was upregulated with si-RHEB or si-RICTOR, which was consistent with the conversion of LC3-I to LC3-II. The downregulated expression levels of SREBP1C and FASN confirmed that the down-expression of RHEB or RICTOR could decrease TG accumulation. Therefore, the promotion of autophagy may be a promising therapeutic strategy for NAFLD, and miR-185 is a promising miRNA that can be developed and assessed for its significant clinical effects on NAFLD.

Non-alcoholic fatty liver disease (NAFLD) is one of the most common chronic diseases worldwide, seriously threatening public health. It also increases the incidence of liver and cardiovascular diseases, such as liver cirrhosis, hepatocellular carcinoma (HCC), and coronary artery disease (1, 2). Although the molecular mechanisms of NAFLD have been extensively studied, no therapy has been approved to reverse non-alcoholic steatohepatitis (NASH) and its consequences (3-5).

MicroRNAs (miRNAs) are a class of short non-coding RNAs with posttranscriptional regulatory functions. Growing evidence demonstrated that miRNAs are involved in the pathogenesis of NAFLD (6-8). MiR-185, playing a pivotal role in cancer progression (9-11), is located at chromosome

Keywords: triglyceride accumulation; microRNA-185; RHEB; RICTOR; autophagy

*Corresponding authors:
Dr Jun Cheng,
Institute of Infectious Diseases, Beijing Ditan Hospital,
Capital Medical University, Beijing Key Laboratory of Emerging Infectious Diseases, NO. 8 East Jingshun St,
Chaoyang, Beijing 100015, China
e-mail: chengj0817@sina.cn

0393-974X (2022)

22q11.21. Accumulating evidence revealed the close relationship between different types of cancer and disorders of glucose and lipid metabolism (12-15). Following that, a great number of studies have concentrated on the regulation of glucose and lipid metabolism by miR-185 (16-18). For instance, it was reported that miR-185 could mediate the inhibition of low-density lipoprotein (LDL) uptake, and HMG-CoA reductase activity could be involved in the dysregulation of cholesterol homeostasis associated with various metabolic disorders (e.g., diabetes) (19). Wang et al. found that miR-185 plays an important role in regulating fatty acid metabolism and cholesterol homeostasis in hepatocytes and improving insulin sensitivity, both *in vitro* and *in vivo* (17). A previous study showed that the hepatitis C virus (HCV) core protein decreases the expression of miR-185-5p. Another study revealed that miR-185-5p could negatively regulate the expression of SREBP2 as a result of interaction with the SREBP2 mRNA 3'-UTR (18). These studies confirmed that miR-185 is closely associated with lipid metabolism.

However, the exact clinical-pathologic correlations and biological functions of miR-185 in NAFLD have not been fully clarified yet. Numerous researches demonstrated that autophagy plays a critical role in lipid metabolism (20-22). In our previous study, we found that miR-185 could induce potent autophagy in HCC by directly interacting with 3'- UTRs of the Ras homolog enriched in the brain (RHEB) and the rapamycin-insensitive companion of the mammalian target of rapamycin (RICTOR) mRNAs for the first time (23). RHEB and RICTOR play substantial roles in regulating two protein complexes (mammalian target of rapamycin complex 1 (mTORC1) and mTORC2) (24). In the past decade, several studies have demonstrated that mTORC1 and mTORC2 participate in lipid metabolism (25-27).

The present study aimed to assess whether miR-185-induced autophagy could play a role in lipid metabolism. Firstly, we confirmed the regulatory relationship between miR-185 and lipid metabolism. Secondly, we found that in nutritional deficiency, autophagosomes significantly increased, triglycerides (TG) level decreased, and the expression of miR-185 increased, which also suggested that the differential expression of miR-185 could be reduced be closely associated with autophagy and lipid metabolism. Then, we detected the effects of RHEB and RICTOR on autophagy and lipid metabolism. When the expression of RHEB or RICTOR decreased, the results were similar to overexpression of miR-185, which confirmed that RHEB and RICTOR could be the target genes of miR-185 and could play an important role in autophagy and TG accumulation. Finally, when the expression of RHEB or RICTOR was silenced, miR-185 was highly expressed simultaneously, and our results showed that autophagy increased more dramatically, and mRNA levels of genes involved in TG synthesis were downregulated.

MATERIALS AND METHODS

Cell culture and transfection

The HepG2 and L02 cells were maintained in DMEM containing 10% FBS, 100 U/mL of penicillin G at 37°C in

Table I. *Small interfering RNA oligonucleotides used in the study*

Genes	Sense (5'-3')	Antisense (5'-3')
siRNA-RHEB	GACGAUUCAAUUUGUUGAATT	UUCAACAAAUUGAAUCGUCTT
siRNA-RICTOR	GCCUGCAGACUCUAUGCAATT	UUGCAUAGAGUCUGCAGGCTT
Negative control	UUCUCCGAACGUGUCACGUTT	ACGUGACACGUUCGGAGAATT

a 5% CO_2 atmosphere. Cells were cultured to 50%–60% confluence and transiently transfected with 50.0 nM NC miRNA (miR-NC), miRNA mimics (miR-185) or siRNA-NC (si-NC), siRNA-RHEB/RICTOR.

MiRNA oligonucleotides and siRNA oligonucleotides

The chemically synthesized miR-185 mimics and negative mimic control were purchased from RiboBio Co., Ltd (Guangzhou, China). siRNAs were purchased from GenePharma (Shanghai, China) (Table I).

RNA isolation and quantitative RT-PCR

Total RNA from various transfected cells was prepared as described in our previous study. Total RNA was reverse transcribed into single-stranded complementary DNA (cDNA). The cDNAs were subjected to qPCR (4367659, ABI, USA) amplification using specific primers. The optimized primers used for qPCR are listed in Table II.

Western blot analysis

Protein was evaluated by 12% Bis-Tris Gel/MOPS (Invitrogen) in MOPS SDS running buffer (Thermo Fisher) for 2 hours; and transferred to a PVDF membrane (ISEQ00010, Milipore, Billerica, MA) by electroblotting. After blocking with 5% nonfat dry milk (2321000, BD) for 1.5 hours, the primary antibodies (Table III) were added and maintained at 4°C overnight, followed by the addition of secondary antibodies (Zhongshan Jinqiao).

Determination of total intracellular TG

Intracellular TG content was measured using an Adipogenesis Assay Kit (MAK040, SIGMA, USA) according to the manufacturer's instructions and normalized to total protein concentrations. Intracellular TG levels were expressed in nmol/lg protein.

Autophagy assays

Cell autophagy was visualized in HepG2 cells by co-transfection with pCMV6-AN-RFP-LC3 (pRFP-LC3) (RC100053; Origene, Rockville, MD, USA) and miR-185 mimics or mimics control. The nuclei were stained with 4′,6-diamidino-2-phenylindole (DAPI) (D9542; Sigma, St. Louis, MO, USA), followed by fluorescence microscope or confocal microscopy analysis (LSM510Meta; Zeiss, Bergisch Gladbach, Germany). Directly assess the number of bright red spots under a fluorescence microscope. Furthermore, pRFP-LC3 punctate staining was assessed from at least 6 random high-power fields under a confocal microscope for most experiments. A single random Z-section was used for each field, and a minimum of 30 cells per sample were counted with triplicate samples per condition per experiment. An LC3 punctate was considered a totally isolated RFP-positive structure >1 lm in diameter.

Oil red O staining

Before transfection, cells were plated in 12-well culture dishes in Dulbecco's modified Eagle's medium (DMEM) containing 10% foetal bovine serum (FBS). Forty-eight hours after transfection, cells were washed with PBS and fixed with 3.7% formaldehyde solution for 30-60 min. Cells were then stained with 60% filtered Oil Red O solution (O0625; Sigma-Aldrich, Missouri, Saint Louis,

Table II. *Primers Used for Real-Time Polymerase Chain Reaction (PCR)*

Genes	Sense (5'-3')	Antisense (5'-3')
RHEB	AGTGATGAAATTGTGTGCTTCCAC	ATTTGAGGGTGGAAGCACACAAT
RICTOR	CCAAAACAACTTCCTTGTGTGCTT	TCAAAAGGCTCAACAAAGCACA
SREBP2	CCCTTCAGTGCAACGGTCATTCAC	TGCCATTGGCCGTTTGTGTC
HMGCR	CTTGTGTGTCCTTGGTATTAGAGC	ATCATCTTGACCCTCTGAGTTAC
SERBP-1C	GGAGGGGTAGGGCCAACGGCCT	CATGTCTTCGAAAGTGCAATCC
FASN	AGCTGCCAGAGTCGGAGAAC	GGGTCTGCACAGACTGCAT

USA) for 30 min at room temperature after three washes with distilled water. After a brief washing step with 60% isopropanol. Cells were then washed twice with water and visualized under the microscope. Oil red staining is lipid droplets, and the lipid droplet contents were quantified using the ImageJ software.

Statistical analysis

Each experiment was performed in triplicate. Statistic differences were determined using the paired Student's t-test or Chisquare test. All data are presented as the mean ± standard error (SEM). Statistical significance was defined as $P < 0.05$.

RESULTS

MiR-185 regulated the levels of TG and total cholesterol (TC)

To assess the function of miR-185 in lipid metabolism in the liver cells, we first used staining and quantification assays to determine changes in the levels of intracellular TG and TC caused by miR-185. HepG2 and L02 cells were transfected with miR-185 or miRNA-negative control (miR-NC) for 48 h. Oil Red O staining revealed that miR-185 led to significantly lower levels of intracellular lipids in HepG2 (Fig. 1A) and L02 cells (Fig. 1E). Consistently, miR-185 could reduce the levels of TG and TC in HepG2 (Fig. 1B) and L02 cells (Fig. 1F) compared with the control group. To further study the role of miR-185 in lipid metabolism, the expression levels of genes involved in TG and TC were detected. As shown in Fig. 1, the mRNA (Fig. 1C, G) and protein (Fig. 1D, H) levels of both SREBP-1c and SREBP-2 and their downstream effectors FASN and HMGCR, were all reduced by miR-185 in both HepG2 and L02 cells. Collectively, these results strongly suggested that miR-185 could inhibit lipid accumulation.

Table III. *Primary antibody*

Primary antibody	Information
anti-SREBP1C	SC-8984; Santa Cruz Biotechnology, USA
anti-SREBP2	ab30682; Abcam, Cambridge, USA
anti-HMGCR	ab74830; Abcam, Cambridge, USA
anti-FASN	ab128870; Abcam, Cambridge, USA
anti-GAPDH	5174; Cell Signaling Technology, USA
Anti-LC3B	3868; Cell Signaling Technology, USA
anti-Beclin 1	3495; Cell Signaling Technology, USA
anti-RHEB	ab92313, Abcam, Cambridge, USA
antiRICTOR	53A2, Cell Signaling Technology, USA
anti-β-actin	sc-47778, Santa Cruz Biotechnology, USA

Exogenous overexpression of miR-185 downregulated the expression levels of RHEB and RICTOR and induced autophagy

Our previous research showed that miR-185 could induce autophagy by directly interacting with 3′-UTRs of RHEB and RICTOR in HepG2 cells (23). In the current study, we re-verified this result. As lipidation of LC3 and its association with autophagosomes could be a significant sign of autophagy, we detected LC3 by immunoblotting and fluorescence microscopy. Consistent with our previous study, RFP-LC3 punctate formation was detected by fluorescence microscopy (Fig. 2A) and confocal microscopy (Fig. 2B). In addition, LC3-II punctuation was more clearly visible in the miR-185 group than in the control group. Importantly, a significant increase in LC3-II/LC3-I ratio was detected in the miR-185 group compared with that in the control group. Moreover, we detected the protein levels of RHEB and RICTOR, which were downregulated when the liver cells were transfected with miR-185 mimics. Taken together, miR-185 plays a major role in autophagy and regulating the expression levels of RHEB and RICTOR.

Starvation upregulated miR-185 expression, induced autophagy, and reduced TG levels in HepG2 cells

The intracellular storage and utilization of lipids are noteworthy to maintain cellular energy homeostasis. The hypothesis that autophagy is associated with lipid metabolism is not new. Firstly, nutrient deprivation was conducted to detect whether miR-185-mediated cell autophagy has a relationship with lipid metabolism. Cells were treated with different levels of fetal bovine serum (FBS) for 48 h or treated with Earle's balanced salt solution (EBSS) at different time points, and then the levels of miR-185, cell autophagy, and intracellular TG and TC were determined. The results showed that when

the cells were treated with insufficient energy, the expression level of miR-185 significantly increased (Fig. 3A), whereas the TG level decreased (Fig. 3B), although the TC level did not significantly change (Fig. 3C). Therefore, in subsequent experiments, we concentrated on TG synthesis. Sterol regulatory element-binding protein 1c (SREBP1C) and fatty acid synthase (FASN) are involved in TG synthesis. The downregulated expression levels of SREBP1C and FASN confirmed that nutrient deprivation could decrease TG accumulation. The upregulated expression levels of LC3 II/LC3-I, RHEB, and RICTOR suggested that autophagy plays a role in lipid accumulation (Fig. 3D). Consistent with the decreased

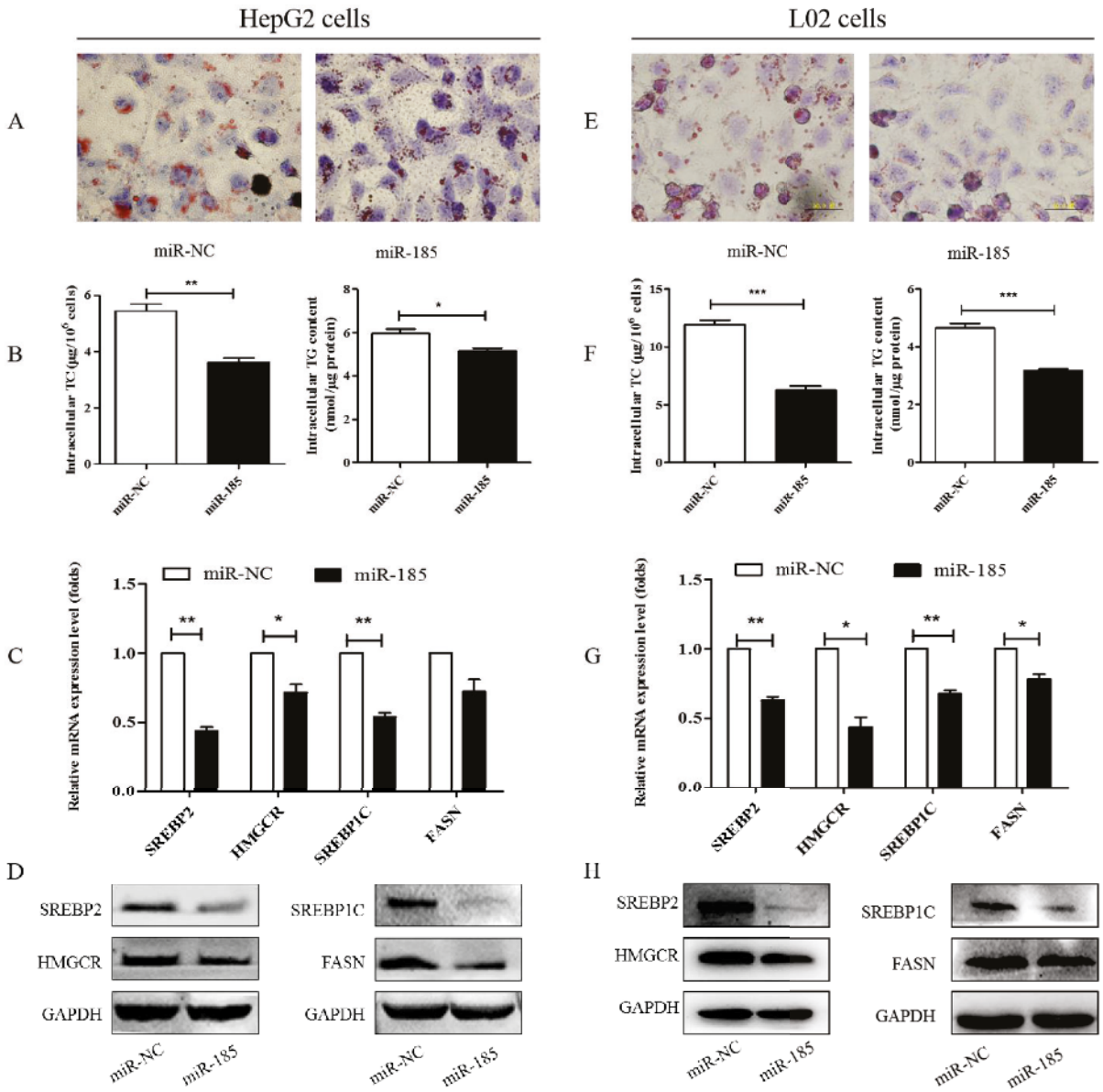

Fig. 1. *MiR-185 regulated the levels of TG and total cholesterol (TC). HepG2 and L02 cells were transfected transiently with miR-185 mimics (miR-185) or negative mimic controls (miR-NC), after transfection for 48 h, fatty acid levels were determined by Oil red O staining. Lipid droplets in HepG2 cells and L02 cells are shown (**A**, **E**). MiR-185 reduces total cholesterol (TC) and triglyceride (TG) levels in HepG2 and L02 cells (**B**, **F**). The mRNA and protein levels of both SREBP-2 and SREBP1C, as well as their downstream effectors HMGCR and FASN, were all decreased by miR-185 in both HepG2 (C, D) and L02 cells (**G**, **H**). Data are mean ± SEM from triplicate experiments. *P < 0.05, **P < 0.005, ***P < 0.0001.*

TG level, the staining of lipid droplets (LDs) with Oil Red O revealed fewer LDs in hepatocytes with EBSS (Fig. 3E). An increase in the number and size of RPF-LC3 in starvation cells was further confirmed by electron microscopy (Fig. 3F). Thus, we hypothesized that miR-185 might regulate liver lipid metabolism via promoting autophagy.

A high expression level of RHEB or RICTOR could mediate autophagy of HepG2 cells

Nutrient deprivation-induced cell autophagy and decreased the expression levels of RHEB and RICTOR. To further evaluate the roles of RHEB and RICTOR in cell autophagy, a small interfering RNA (siRNA), reducing RHEB and RICTOR mRNA (Fig. 4A) and protein (Fig. 4B) levels, was used in HepG2 cells. When cells down-expressing RHEB or RICTOR, the formation of punctate RFP-LC3 indicated that the level of autophagy increased (Figs. 4E, F). Several autophagy-related genes (ATG3, ATG4B, ATG5, ATG7, ATG12, and Beclin 1) were identified by quantitative reverse transcription-polymerase chain reaction (RT-qPCR) (Fig. 4C). The mRNA level was upregulated with si-RHEB or si-RICTOR, which was consistent with the conversion of LC3-I to LC3-II (Fig. 4D), an important autophagy marker. These

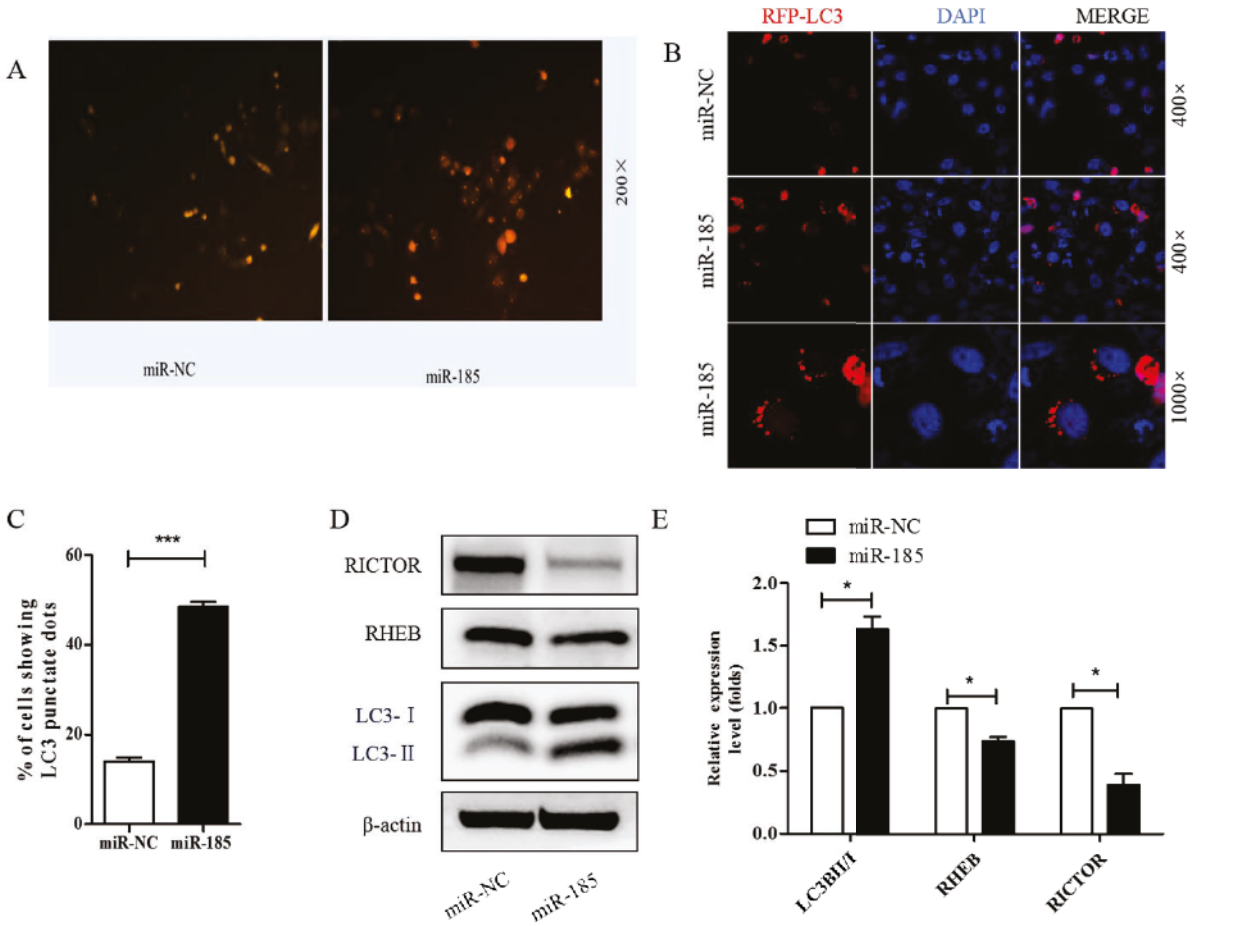

Fig. 2. *Exogenous overexpression of miR-185 downregulated the expression levels of RHEB and RICTOR and induced autophagy. HepG2 cells were transfected with miR-185 and the control for 24 h, and then transfected with pRFP-LC3 for 48 h; RFP-LC3 punctate dots were detected by fluorescence microscope (A) and confocal microscopy (B). The percentage of cells with punctate distribution of RFP-LC3, characteristic of autophagosome-bound LC3, was determined by fluorescence microscopy. The data represent the average of the duplicates plus the SD (C). HepG2 cells were transfected with miR-185 or a control vector for 48 h; cell lysates were then analyzed for RHEB, RICTOR, and LC3 expressions by western blot (D). The results are representative of 3 independent experiments and are presented as mean ± SEM values. Western blot data were quantified using the Bio1D software (E).*

results were consistent with the RFP-LC3 punctate formation detected by confocal microscopy (Figs. 4E, F). The abovementioned results demonstrated that RHEB and RICTOR play an important role in autophagy.

Knockdown of RHEB and RICTOR could decrease TG accumulation

In order to examine the potential roles of RHEB and RICTOR in TG accumulation, TG levels were measured using a TG Assay kit. Intracellular TG

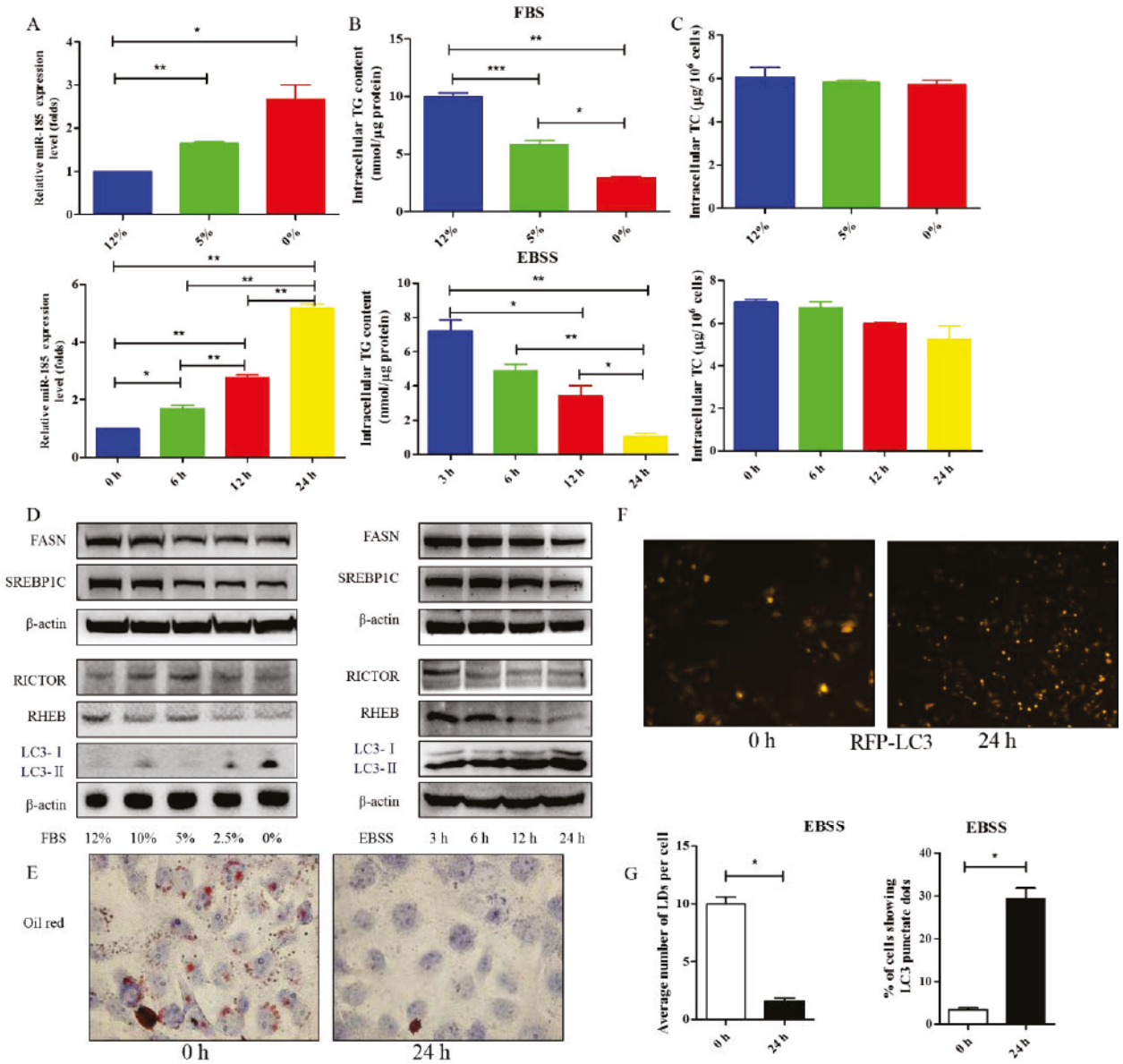

Fig. 3. *Starvation upregulated miR-185 expression, induced autophagy, and reduced TG level in HepG2 cells. HepG2 cells were treated with different density fetal bovine serum (FBS) for 48 h, or treated with Earle's Balanced Salt Solution (EBSS) at different time points (3-6-12-24 h). The levels of miR-185 (A), and intracellular TG (B) and TC (C) were determined respectively. The SERBP1C, FASN, RHEB, RICTOR, and LC3B protein levels were analyzed by western blot (D). Fatty acid levels were determined by Oil red O staining (E). HepG2 cells were transfected with pRFP-LC3 for 24 h, and then treated with Earle's Balanced Salt Solution (EBSS) for 24 h; RFP-LC3 punctate dots were detected by fluorescence microscopy (F). The percentage of cells showing LC3 punctate dots. Data are mean ± SEM from triplicate experiments. *P < 0.05, **P < 0.005, ***P < 0.0001.*

levels significantly decreased regardless of the knockdown of RHEB or RICTOR (Fig. 5A, B). Next, we investigated the potential regulatory mechanisms of RHEB and RICTOR during TG accumulation. The SRBEP1C and FASN mRNA expressions (Fig. 5C, D) and their protein expressions (Fig. 5E) were dramatically reduced after knockdown of RHEB and RICTOR. These results indicated that RHEB and RICTOR could directly regulate lipid metabolism, at least in lipid synthesis, by promoting the expression levels of SREBP1C and FASN.

RHEB/RICTOR mediated the effects of miR-185 on autophagy of HepG2 cells

In order to determine whether miR-185 could

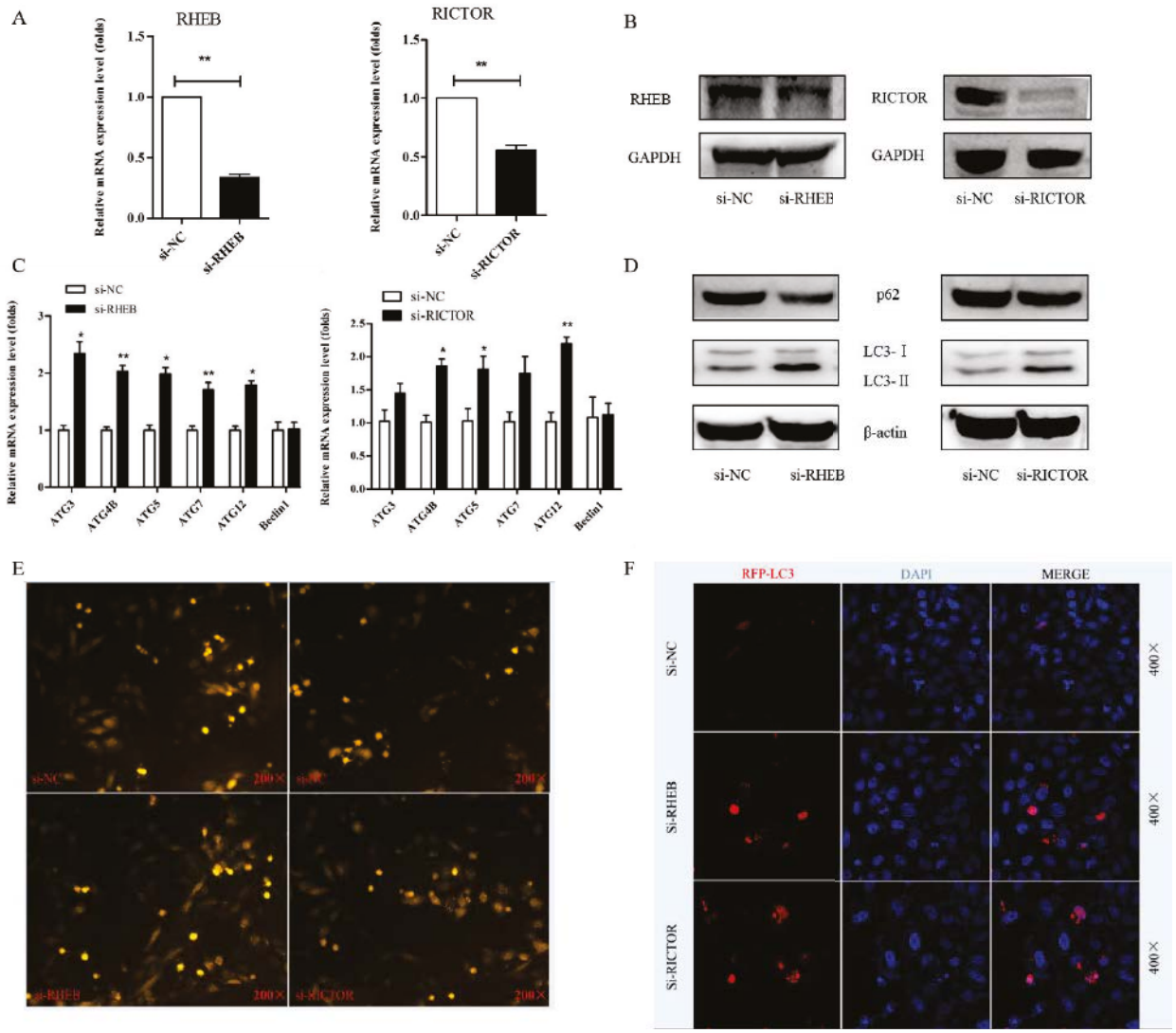

Fig. 4. *High expression level of RHEB or RICTOR could mediate autophagy of HepG2 cells. Successful silencing of RHEB / RICTOR in HepG2 cell lines. HepG2 cells were transiently transfected with siRNA control (siNC), or siRNA-RHEB / RICTOR. After 48 h, total RNA (A) and protein (B) were extracted and analyzed for RHEB / RICTOR expression quantitation. HepG2 cells were transfected with siRNA-RHEB / RICTOR or a control siRNA for 24 h, and were then transfected with pRFP-LC3 for 48 h, RFP-LC3 punctate dots were detected by fluorescence microscope (C) and confocal microscopy (D). Quantitative real-time PCR determined ATG3, ATG4B, ATG5, ATG7, ATG12, Beclin1 mRNA expression in HepG2 cells transfected with si-RHEB / RICTOR (E). Autophagy -related gene protein levels were measured after transfection with si-RHEB and si-RICTOR (F). Data shown represent the means ± SEM of independent experiments. *P < 0.05, **P < 0.005.*

promote autophagy via directly targeting RHEB and RICTOR, cells co-transfected with siRNA and miR-185 mimics were used. As illustrated in Fig. 6A, silencing of RHEB could increase LC3-II/LC3-I ratio, Beclin-1 expression, and miR-185-induced autophagy. Similar results could be obtained by cells co-transfected with si-RICTOR and miR-185 mimics (Fig. 6B). Therefore, RHEB/RICTOR could mediate the effects of miR-185 on the autophagy of HepG2 cells. These data indicated that inhibition of the expression levels of RHEB and RICTOR could be associated with miR-185-induced autophagy.

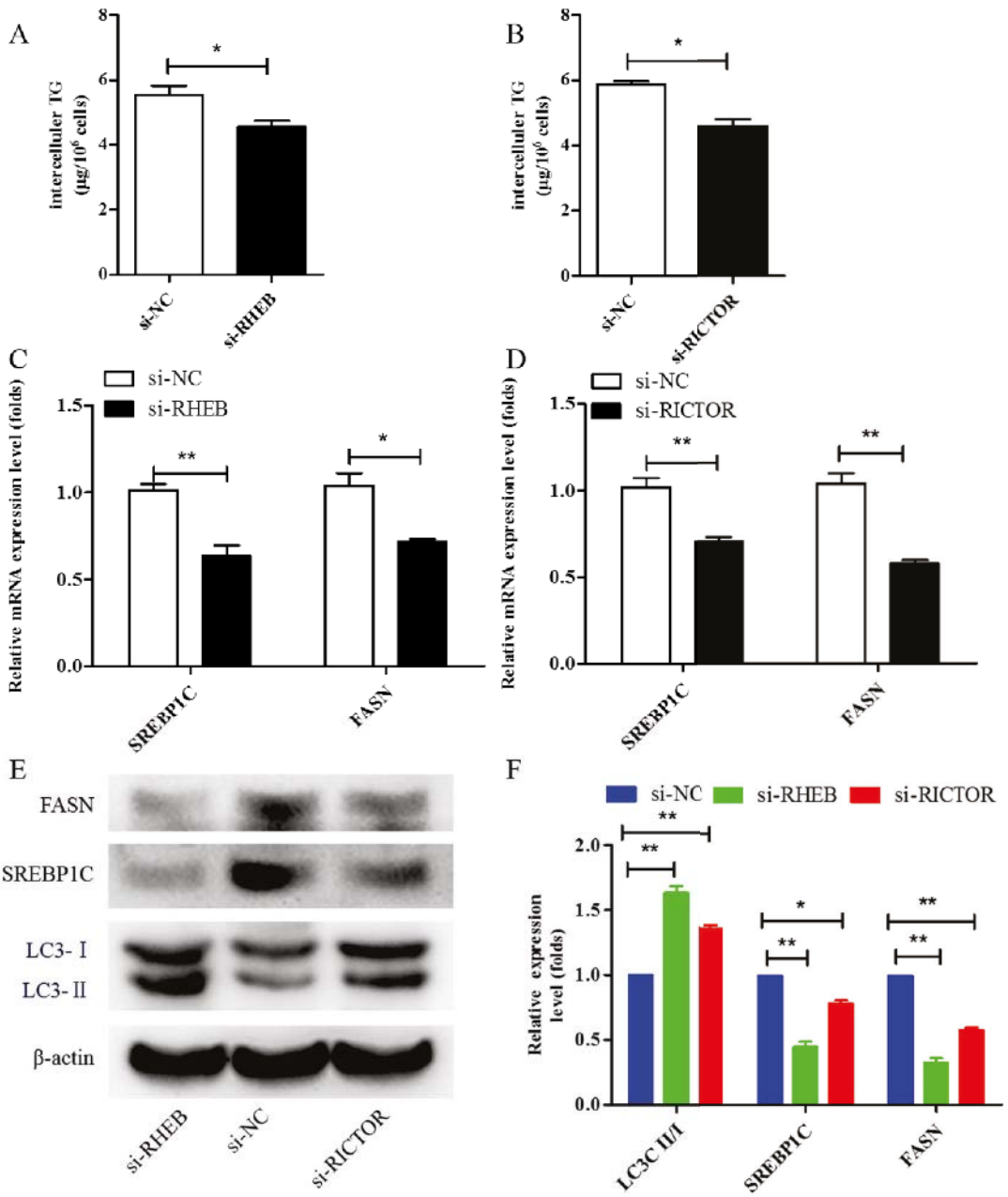

Fig. 5. *Knockdown of RHEB and RICTOR could decrease TG accumulation. After successfully knocking down RHEB or RICTOR gene expression by siRNA, intracellular TG levels were significantly decreased in HepG2 cell lines (A, B). SREBP1C and FASN mRNA (C, D) and protein (E) expression were significantly down-regulated after RHEB /RICTOR siRNA treatment. Protein ratios were calculated following Image J densitometric analysis. Similar results were obtained in three independent experiments.*

RHEB/RICTOR could be involved in the regulation of lipid metabolism mediated by miR-185

Autophagy and miRNA are important regulators of lipid metabolism. Therefore, we speculated that miR-185-mediated autophagy may play an essential role in lipid metabolism. The cells co-transfected with siRNA and miR-185 mimics showed more autophagosomes. We then detected the level of TG accumulation in co-transfected cells; as displayed in Fig. 7, RHEB-siRNA could play a significant role in the miR-185-induced downregulation of SREBP1C and FASN in both mRNA (Fig. 7C) and protein levels (Fig. 7E), which is consistent with the intracellular TG level (Fig. 7A). Similar results could be achieved when cells were co-treated with si-RICTOR and miR-185 mimics. In brief, knockdown of RHEB or RICTOR could enhance miR-185-induced downregulation of SREBP1C and FASN and decrease TG accumulation. These results demonstrated that miR-185 could be a critical impresser of hepatic lipid accumulation by interacting with RHEB/RICTOR via inducing cell autophagy.

Schematic illustration

MiR-185 or si-RHEB/RICTOR could downregulate the expression levels of RHEB and RICTOR, increase the number of autophagosomes, inhibit the expression levels of SREBP1C and FASN, and suppress the accumulation of LDs, resulting in the amelioration of NAFLD (Fig. 8).

DISCUSSION

NAFLD has become the most common chronic liver disease worldwide, and it is known as a major public health concern as well. However, no single therapy has been approved for NAFLD yet, relying solely on lifestyle modifications. Thus, the treatment of NAFLD is a serious challenge (1, 4). The pro-survival function of autophagy suggests modulation of autophagy as a potential therapeutic strategy for protecting cells against lipotoxicity and lipid-related metabolic disorders (20, 22, 28). Therefore, the function of miR-185 in cell autophagy is worthy of study. Several previous

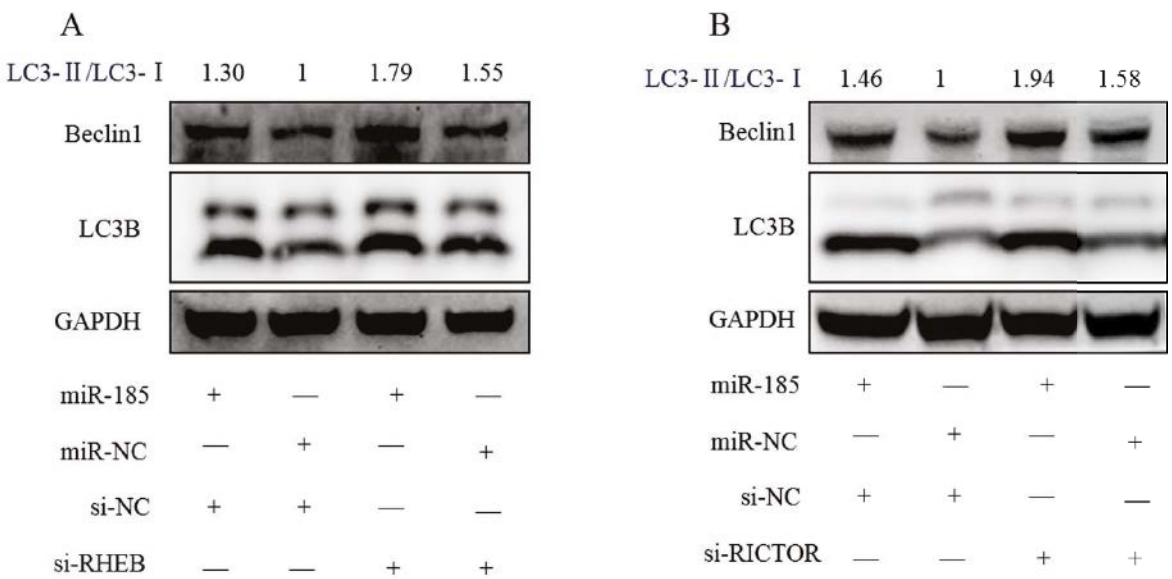

Fig. 6. *RHEB/RICTOR mediated the effects of miR-185 on autophagy of HepG2 cells. Knock-down of RHEB or RICTOR increases miR-185-induced autophagy. HepG2 was transfected with miR-185 and the control for 24 h, and then transfected with si-RHEB (A) /si-RICTOR (B) or the control for 48 h. Beclin 1, and LC3 protein levels were analyzed by western blot and quantified as described previously.*

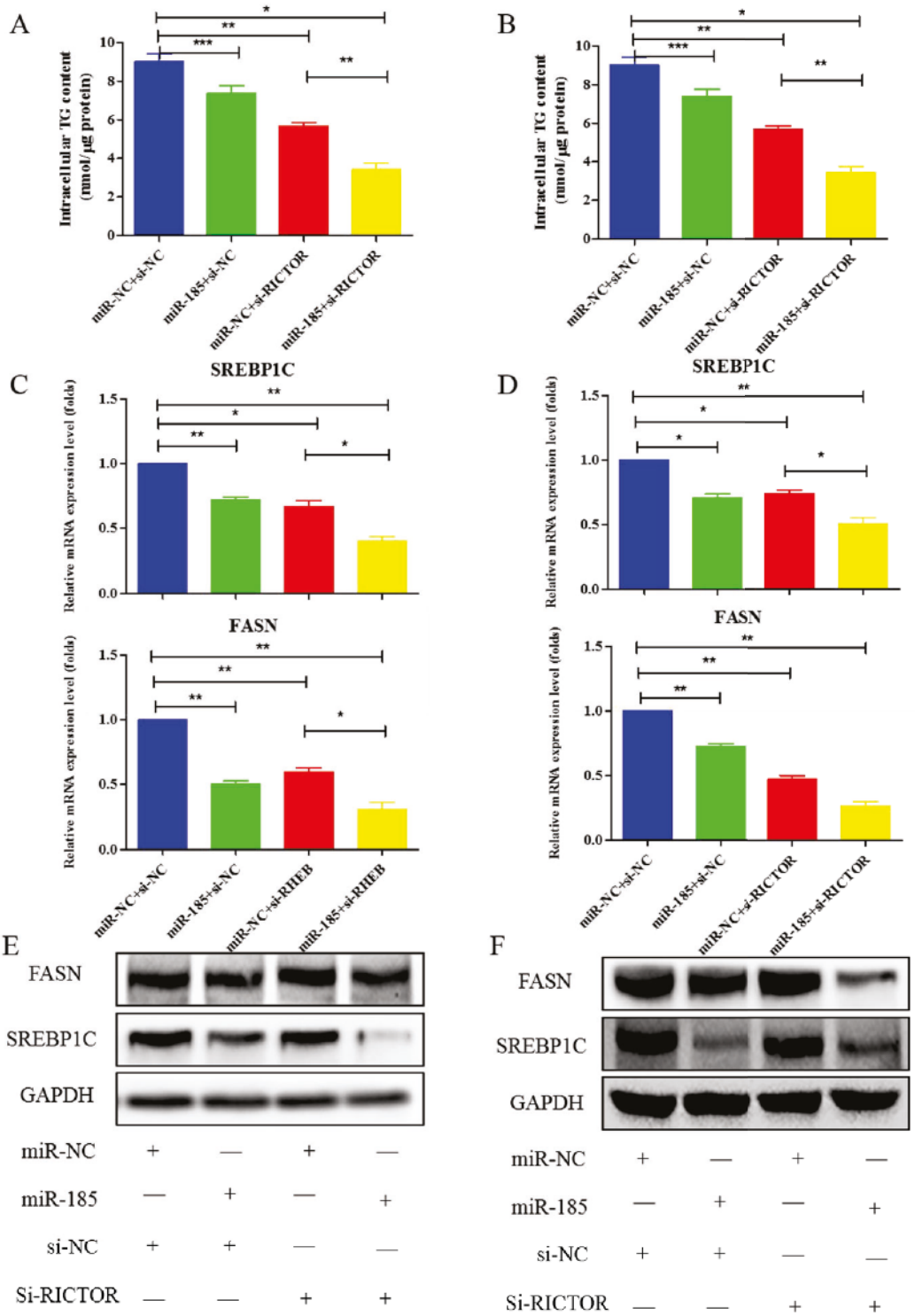

Fig. 7. *RHEB/RICTOR could be involved in the regulation of lipid metabolism mediated by miR-185. Knock-down of RHEB or RICTOR promoted miR-185 downregulated TG accumulation. HepG2 was transfected with miR-185 and the control for 24 h, and then transfected with si-RHEB (A, C, E) /si-RICTOR (B, D, F) and the control for 48 h. Cellular TG were assessed using a TG estimation kit (A, B). The mRNA (C, D) and protein (E, F) levels of SREBP1C, and FASN were measured by RT-PCR and Western blot analysis, respectively. Data shown are means ± SEM of three independent experiments (n = 3, *P < 0.05, **P < 0.005, ***P < 0.0001).*

studies showed that miR-185 could regulate lipid metabolism (16-18), and autophagy might play a vital role in lipid metabolism (20, 22, 28). Our previous research showed that miR-185 could promote cell autophagy for the first time (23); this indicated a possible role for miR-185 in regulating lipid metabolism via promoting cell autophagy.

Hepatocytes are the major cells that control lipid metabolism and the primary site of lipid accumulation in NAFLD. To verify this possibility, we first confirmed the function of miR-185 in HepG2 and L02 cells (Fig. 1). It has been extensively validated that the prevalence of NAFLD may be influenced by miR-185 (17-19). Cells transfected with miR-185 mimics for 48 h showed significant downregulation of the expression levels of SREBP1C/FASN and SREBP2/HMGCR (Fig. 1). These results revealed that miR-185 could reduce the levels of TG and TC in HepG2 and L02 cells. Alterations to the SREBP1C-FASN pathway may result in liver steatosis and type 2 diabetes (29). The present research results demonstrated that miR-185 was involved in liver steatosis. However, Yang et al.'s results were different from ours. In their research, miR-185 was upregulated via SREBP-1C. They also showed that the miR-185 level was upregulated in mice fed a high-fat diet and in human serum from patients with high TC levels (19). There could be a possible responsive feedback loop between lipid metabolism and miR-185, or at least there is a connection.

Stressful conditions always induce autophagy, controlling intracellular homeostasis. Thus, autophagy is more prevalent in tumor cells than in normal cells. The HepG2 cell line is a hepatoblastoma cell line, and the L02 cell line is a normal liver cell line; therefore, we chose the HepG2 cell line in the follow-up stage.

Under certain circumstances, autophagy constitutes a stress adaptation. Untreated HepG2 cells showed a low rate of autophagy. RFP-LC3 punctate formation was detected by fluorescence microscopy and confocal microscopy. LC3-II punctate was more clearly visible in the miR-185 group than in the control group (Fig. 2), suggesting that miR-185 is a type of miRNA that promotes autophagy.

In order to better highlight the effects of miR-185 on cell autophagy and lipid metabolism, we observed changes in stressful conditions. We found that

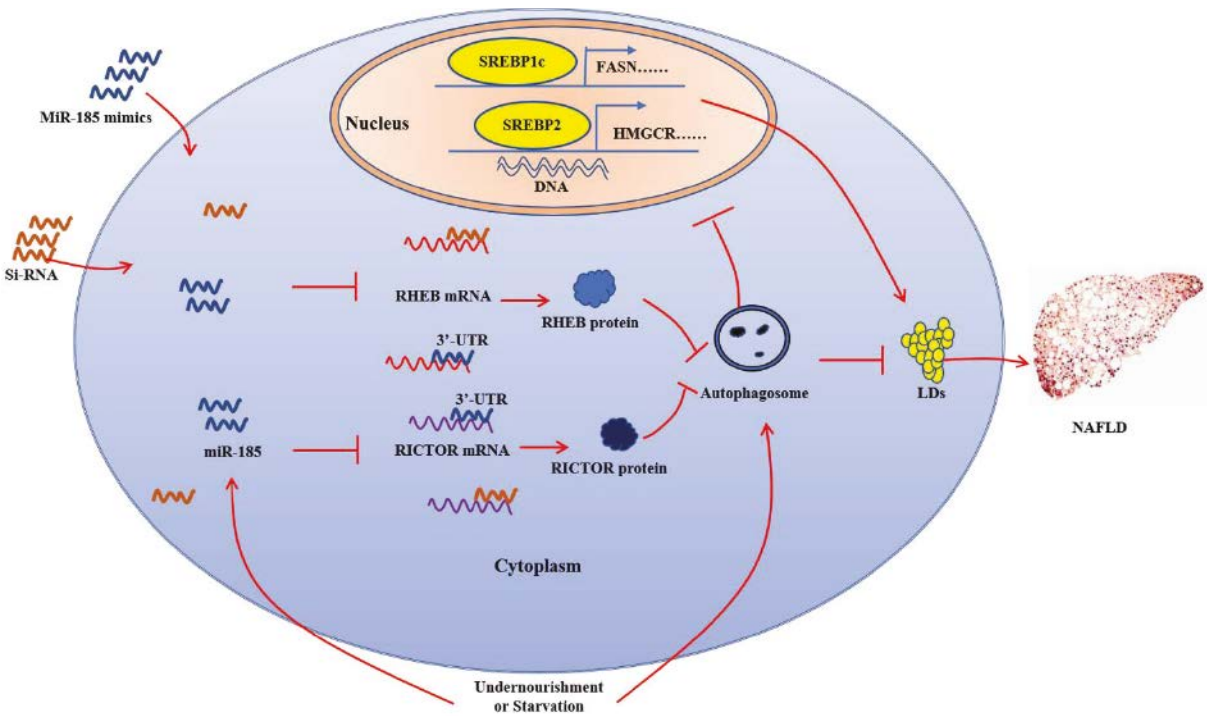

Fig. 8. *Schematic illustration*

nutrient deprivation upregulated the miR-185 level in HepG2 cells (Fig. 3A) with undernourishment or starvation pressure, associated with a remarkable downregulation of SREBP1C and FASN, as the main genes of TG synthesis, and also RHEB and RICTOR (Fig. 3D), which could upregulate mTORC1 and mTORC2 and play an important role in cell autophagy. However, we detected no change in the TC levels in these stressful conditions (Fig. 3C), demonstrating that TG is the primary energy source in stressful conditions. Furthermore, our previous research demonstrated that RHEB and RICTOR are the target gens of miR-185. As a result, there is a certain relationship between miR-185-induced autophagy and miR-185-inhibited lipid synthesis.

RHEB, a GTP-binding protein, controls the activity of mTORC1. Partha et al. demonstrated that mTORC1 could promote lipid accumulation in mammalian cells by suppressing lipolysis and stimulating *de novo* lipogenesis (26). Guo et al. pointed out that the inactivation of mTORC1 could downregulate 4EBP1 phosphorylation and the expressions of peroxisome proliferator-activated receptor-gamma (PPAR-γ) and lipogenic genes, which is critical for insulin-induced lipid synthesis and secretion in peripheral blood mononuclear cells (PBMCs) (30). RICTOR is a scaffold protein that regulates the assembly and substrate binding of MTORC2 (31). Asami et al. reported that mTORC2 could regulate hepatic glucose and lipid metabolism via insulin-induced Akt signaling to control whole-body metabolic homeostasis (32). The abovementioned studies suggested that the two mTOR complexes contribute to whole-body metabolic homeostasis. We previously reported that miR-185 could directly interact with the 3'- UTRs of RHEB and RICTOR and play a predominant suppressive role in HCC (23) and liver fibrosis (33). To determine whether RHEB or RICTOR has a relationship with autophagy and TG accumulation, si-RHEB/RICTOR were used. When cells were transfected with si-RHEB/RICTOR, the results were similar to cells transfected with miR-185 mimics. These results indicated that the downregulated expression levels of RHEB and RICTOR had autophagy-promoting effects (Fig. 4) and potential protective effects on TG accumulation in the liver cells (Fig. 5). These findings may provide a novel insight into the development of potential therapeutic targets. Previous studies suggested that resveratrol has been identified as a potential agent to suppress scar formation by activating autophagy via downregulating RHEB expression (34). RICTOR silencing increased apoptosis, concomitantly enhancing rasfonin-induced autophagy (35).

Although autophagy in metabolic disorders has been investigated extensively, few studies have addressed the role of autophagy induced by miR-185 in the molecular mechanism of fatty liver diseases. The present study revealed that miR-185-induced autophagy, through targeting RHEB and RICTOR, plays an important role. A co-transfection assay was then carried out, no matter whether silencing of RHEB or RICTOR promoted autophagy in the HepG2 cells, and the expression levels of SREBP1C and FASN were reduced (Figs. 6-7). Furthermore, our data showed that miR-185 might potentiate the regulating effect of autophagy on lipid metabolism, possibly through the regulation of RHEB and RICTOR protein levels (Fig. 8). Thus, miR-185 could inhibit the activities of mTORC1 and mTORC2 by directly acting on RHEB and RICTOR, and then, the expression levels of SREBP1C and FASN were downregulated to realize the inhibition of lipid aggregation. However, further research is required to confirm the above-mentioned findings.

In summary, this study provided novel evidence, suggesting that miR-185 plays a predominant suppressive role in TG accumulation, and it induces cell autophagy by targeting RHEB and RICTOR. It is essential to fully elucidate the diverse roles of miR-185 in different types of tissues and multiple diseases before acting as a potential therapeutic strategy. Further studies are required to explore the contribution of miR-185 to sensitivity to chemotherapy.

ACKNOWLEDGEMENTS

This study was supported by grants from the National Natural Science Foundation of China (nos.81670547) and the Beijing Municipal

Administration of Hospitals (No. ZYLX201402). Support was also provided by China-Japan Friendship Hospital Youth Fund (2019-1-QN-46).

Conflict of interest

There are no conflicts of interest.

REFERENCES

1. Huang DQ, El-Serag HB, Loomba R. Global epidemiology of NAFLD-related HCC: trends, predictions, risk factors and prevention. Nat Rev Gastroenterol Hepatol 2021; 18(4):223-38.
2. Liu Z, Suo C, Zhao R, et al. Genetic predisposition, lifestyle risk, and obesity associate with the progression of non-alcoholic fatty liver disease. Dig Liver Dis 2021; 53(11):1435-42.
3. Guirguis E, Grace Y, Bolson A, et al. Emerging therapies for the treatment of non-alcoholic steatohepatitis: A systematic review. Pharmacotherapy 2021; 41(3):315-28.
4. Schattenberg JM. Emerging Pharmacological Treatment in Nonalcoholic Steatohepatitis. Visc Med 2020; 36(5):411-16.
5. Shah RA, Alkhouri N, Kowdley KV. Emerging drugs for the treatment of non-alcoholic steatohepatitis: a focused review of farnesoid X receptor agonists. Expert Opin Emerg Drugs 2020; 25(3):251-60.
6. Zhang ZC, Liu Y, Xiao LL, et al. Upregulation of miR-125b by estrogen protects against non-alcoholic fatty liver in female mice. J Hepatol 2015; 63(6):1466-75.
7. Rayner KJ, Esau CC, Hussain FN, et al. Inhibition of miR-33a/b in non-human primates raises plasma HDL and lowers VLDL triglycerides. Nature 2011; 478(7369):404-07.
8. Citrin KM, Fernández-Hernando C, Suárez Y. MicroRNA regulation of cholesterol metabolism. Ann N Y Acad Sci 2021; 1495(1):55-77.
9. Liu M, Lang N, Chen X, et al. miR-185 targets RhoA and Cdc42 expression and inhibits the proliferation potential of human colorectal cells. Cancer Lett 2011; 301(2):151-60.
10. Xu J, Ai Q, Cao H, et al. MiR-185-3p and miR-324-3p Predict Radiosensitivity of Nasopharyngeal Carcinoma and Modulate Cancer Cell Growth and Apoptosis by Targeting SMAD7. Med Sci Monit 2015; 21:2828-36.
11. Dong-Xu W, Jia L, Su-Juan Z. MicroRNA-185 is a novel tumor suppressor by negatively modulating the Wnt/β-catenin pathway in human colorectal cancer. Indian J Cancer 2015; 52 Suppl 3:E182-5.
12. Lange NF, Radu P, Dufour JF. Prevention of NAFLD-associated HCC: role of lifestyle and chemoprevention. J Hepatol 2021; 75(5):1217-27.
13. Gabbia D, Cannella L, De Martin S. The Role of Oxidative Stress in NAFLD-NASH-HCC Transition-Focus on NADPH Oxidases. Biomedicines 2021; 9(6):687.
14. Hsu SJ, Huang HC. Non-alcoholic fatty liver disease and hepatocellular carcinoma: Distinct links. J Chin Med Assoc 2021; 84(8):737-8.
15. Paternostro R, Sieghart W, Trauner M, et al. Cancer and hepatic steatosis. ESMO Open 2021; 6(4): 100185.
16. Jiang H, Zhang J, Du Y, et al. microRNA-185 modulates low density lipoprotein receptor expression as a key posttranscriptional regulator. Atherosclerosis 2015; 243(2):523-32.
17. Wang XC, Zhan XR, Li XY, et al. MicroRNA-185 regulates expression of lipid metabolism genes and improves insulin sensitivity in mice with non-alcoholic fatty liver disease. World J Gastroenterol 2014; 20(47):17914-23.
18. Li M, Wang Q, Liu SA, et al. MicroRNA-185-5p mediates regulation of SREBP2 expression by hepatitis C virus core protein. World J Gastroenterol 2015; 21(15):4517-25.
19. Yang M, Liu W, Pellicane C, et al. Identification of miR-185 as a regulator of de novo cholesterol biosynthesis and low density lipoprotein uptake. J Lipid Res 2014; 55(2):226-38.
20. Singh R, Kaushik S, Wang Y, et al. Autophagy regulates lipid metabolism. Nature 2009; 458(7242):1131-35.
21. Rottiers V, Näär AM. MicroRNAs in metabolism and metabolic disorders. Nat Rev Mol Cell Biol 2012; 13(4):239-50.
22. Hernández-Gea V, Ghiassi-Nejad Z, Rozenfeld R, et al. Autophagy releases lipid that promotes fibrogenesis by activated hepatic stellate cells in mice and in human tissues. Gastroenterology 2012; 142(4):938-46.
23. Zhou L, Liu S, Han M, et al. MicroRNA-185 induces potent autophagy via AKT signaling in hepatocellular carcinoma. Tumour Biol 2017; 39(2):1010428317694313.

24. Foster KG, Fingar DC. Mammalian target of rapamycin (mTOR): conducting the cellular signaling symphony. J Biol Chem 2010; 285(19):14071-77.
25. Uno K, Yamada T, Ishigaki Y, et al. A hepatic amino acid/mTOR/S6K-dependent signalling pathway modulates systemic lipid metabolism via neuronal signals. Nat Commun 2015; 6:7940.
26. Chakrabarti P, English T, Shi J, et al. Mammalian target of rapamycin complex 1 suppresses lipolysis, stimulates lipogenesis, and promotes fat storage. Diabetes 2010; 59(4):775-81.
27. Li S, Oh YT, Yue P, et al. Inhibition of mTOR complex 2 induces GSK3/FBXW7-dependent degradation of sterol regulatory element-binding protein 1 (SREBP1) and suppresses lipogenesis in cancer cells. Oncogene 2016; 35(5):642-50.
28. Ding WX, Li M, Chen X, et al. Autophagy reduces acute ethanol-induced hepatotoxicity and steatosis in mice. Gastroenterology 2010; 139(5):1740-52.
29. Dal S, Van der Werf R, Walter C, et al. Treatment of NASH with Antioxidant Therapy: Beneficial Effect of Red Cabbage on Type 2 Diabetic Rats. Oxid Med Cell Longev 2018; 2018:7019573.
30. Guo Z, Cheng X, Feng X, et al. The mTORC1/4EBP1/PPARγ Axis Mediates Insulin-Induced Lipogenesis by Regulating Lipogenic Gene Expression in Bovine Mammary Epithelial Cells. J Agric Food Chem 2019; 67(21):6007-18.
31. Gkountakos A, Pilotto S, Mafficini A, et al. Unmasking the impact of Rictor in cancer: novel insights of mTORC2 complex. Carcinogenesis 2018; 39(8):971-80.
32. Hagiwara A, Cornu M, Cybulski N, et al. Hepatic mTORC2 activates glycolysis and lipogenesis through Akt, glucokinase, and SREBP1c. Cell Metab 2012; 15(5):725-38.
33. Zhou L, Liu S, Han M, et al. miR-185 Inhibits Fibrogenic Activation of Hepatic Stellate Cells and Prevents Liver Fibrosis. Mol Ther Nucleic Acids 2018; 10:91-102.
34. Pang K, Li B, Tang Z, et al. Resveratrol inhibits hypertrophic scars formation by activating autophagy via the miR-4654/Rheb axis. Mol Med Rep 2020; 22(4):3440-52.
35. Hou B, Liu S, Li E, et al. Different Role of Raptor and Rictor in Regulating Rasfonin-Induced Autophagy and Apoptosis in Renal Carcinoma Cells. Chem Biodivers 2020; 17(12):e2000743.

The relationship between the L-type amino acid transporter 1 expression and clinical features in resectable pancreatic cancer

WG. Zhao[1,2], X. Fang[2], Y. Li[2] and DM. Kang[2]*

[1]Cheeloo College of Medicine, Shandong University, Jinan, Shandong, China; [2]Department of Geriatrics, Anhui Provincial Hospital, Hefei, Anhui, China

Objective: To explore the relationship between the expression of L-type amino acid transporter 1 (LAT1) and pancreatic cancer's clinical features and prognosis.

Methods: The expression of LAT1 in pancreatic cancer and paracancerous tissue was detected in 32 patients with pancreatic cancer postoperatively. The patients' general condition and expression of Carcinoembryonic antigen (CEA), Carbohydrate Antigen 19-9 (CA19-9), and Ki67 were recorded. In addition, the patients' clinical course was inquired about via telephone calls.

Results: The expression of LAT1 in pancreatic carcinomas was positive significantly higher than that in paracancerous tissues (13/32 vs 0/32, $P<0.001$). The expression of LAT1 was positively correlated with Ki67 expression ($r=0.632$, $P=0.001$) and the degree of differentiation significantly ($r=0.390$, $P=0.027$), but negatively correlated with the number of lymph nodes ($r=-0.378$, $P=0.033$). Multivariate analysis confirmed that the expressions of CEA and LAT1 were independent prognostic factors for disease-free survival (DFS) ($P_{CEA}=0.015$, $P_{LAT1}=0.042$). Meanwhile, CEA and CA199 could predict poor overall survival (OS) ($P_{CEA}=0.024$, $P_{CA19-9}=0.040$).

Conclusion: Overall, LAT1 is related to the degree of proliferation and differentiation of pancreatic cancer. Moreover, while LAT1 and CEA are markers for predicting DFS in pancreatic cancer, LAT1 is not good at predicting OS.

Tumors are the main cause of human death. Pancreatic cancer is considered a solid tumor with a high degree of malignancy. It is generally found later and, thus, too late to be operated on, leads to a poor effect of comprehensive treatment and has low long-term survival. In the United States and Europe, pancreatic cancer mortality has increased by about 3%, accounting for about 7% of all cancer deaths (1).

Several potential pancreatic cancer biomarkers are being investigated, including CECAM, Span-1, DUPAN-2, Alpha4GnT, PAM4 and combined biomarkers with CEA, CA19-9 and CA242. CA19-9 is the most widely used tumor marker in diagnosing pancreatic cancer (2, 3). However, it may be falsely positive in biliary tract infection or obstruction cases, therefore, it performs poorly as a screening tool, with a low positive predictive value of 0.5% to 0.9% (4). However, CA19-9 predicts prognosis and detects recurrence after resection (5). Therefore, there is an urgent need to find a new tumor marker, which can have a good performance in the screening, diagnosis and prognosis of pancreatic cancer.

The L-type amino acid transporter (LAT) is located on the surface of the cell membrane and is a Na+-

Keywords: LAT1, pancreatic cancer, prognostic factor, immunohistochemistry

*Corresponding author
Dr Dong-Mei Kang
Department of Geriatrics, Anhui Provincial Hospital,
NO.17 of Lujiang Road, Luyang District, Hefei,
Anhui, 230001, China
Tel.: +86 13705697807
e-mail:ekangdongmei@126.com

0393-974X (2022)

independent transport system; it is mainly responsible for transporting amino acids into cells. At present, 4 subtypes of LATs have been found, i.e. LAT1, LAT2, LAT3, and LAT4. Of these, LAT1 has attracted much attention because of its close relationship with tumors. It can transport a variety of essential amino acids, including leucine, isoleucine, arginine, tyrosine, phenylalanine, tryptophan, methionine, and histidine (6). It consists of 512 amino acids encoded by *SLC7A5* and covalently bound with CD98 by disulfide bonds to perform its amino acid transport functions (7).

It is believed that LAT1 plays an important role in tumors. It is highly expressed in a variety of human tumor cells, including lung cancer (8), gastric cancer (9), esophageal cancer (10), colorectal cancer (11), pancreatic cancer (12), laryngeal carcinoma (13), breast cancer (14), thymic carcinomas (15), prostate cancer (16), renal clear cell carcinoma (17), neuroendocrine tumor (18), lymphoid tumor, and leukemia (19).

In normal human tissues, the expression of LAT1 mRNA is limited to the brain, spleen, placenta, and testis (20). It has been suggested that LAT1 is related to tumor cell proliferation, angiogenesis, invasion, metastasis, and metabolism (21). The growth of tumor cells requires a large and sufficient supply of proteins and amino acids, and LAT1 controls and regulates this process. In most tumors, LAT1 is associated with the degree of malignancy and poor prognosis, but inconsistent results have been found in some tumors (11).

Currently, LAT1 is considered a new target for tumor treatment. There are a variety of LAT1 inhibitors, including 2-aminobicyclo-(2,2,1)-heptane-2-carboxylic acid (BCH), JPH203, and KYT-0353. In vivo experiments have shown that LAT1 inhibitors could inhibit the growth of many kinds of tumor cells and induce apoptosis (22, 23). For instance, KYT-0353 has displayed an obvious inhibitory effect on the growth of HT-29 cells in vitro (24). Moreover, to the best of our knowledge, JHP203, a selective inhibitor of LAT1, is the only compound currently included in the Phase I clinical trial (25).

In the present study, we retrospectively analyze 32 patients with surgically resected primary pancreatic cancer and conduct immunohistological examinations for LAT1. The Ki67 labelling index and CEA and CA19-9 serum levels are detected to clarify the relationship between the expression of LAT1 and the clinical features and prognosis of pancreatic cancer.

Yanagisiwa et al. has evaluated LAT1 in pancreatic cancer using similar methods (26). However, few studies on the relationship between pancreatic cancer and LAT1 expression in China are present. The novelty of this study is that it focuses on the data of China.

MATERIALS AND METHODS

Patients

This study evaluated 32 patients from September 2019 to February 2020, twenty-two males and 10 females, ranging from 34- to 83- years-old, in Anhui Provincial Hospital, China. Patients presented pancreatic cancer and underwent radical pancreatectomy but did not receive adjuvant treatment. The average age at the time of operation was 63. All clinical specimens were gathered from surgical resection, containing cancerous tissues and adjacent no tumor cell tissues. The clinical-stage was defined according to the 2009 guidelines of the American Joint Commission on Cancer.

The patients' related clinical data were extracted by consulting their electronic medical records, including their general condition, pathological type, and serum CEA, CA19-9, and Ki67 expression. In addition, the postoperative clinical course was evaluated via telephone inquiry from the patients' hospitalization records. This study was approved by the Clinical Research Ethics Committee of Anhui Provincial Hospital.

Immunohistochemical staining

The expressions of LAT1 were detected by immunohistochemistry. The tissue slices were dewaxed with xylene, and endogenous peroxidase was blocked with 3% H2O2 in methanol for 20 minutes. For the LAT1 immunostaining, slides were placed in a citrate buffer and heated for antigen retrieval using a microwave oven for two minutes. After the antigen reactivity was restored, the slides were incubated with the primary antibody (antibody

dilution ratio 1:100, Abcam) for 60 minutes at 37°C. After being washed thoroughly with phosphate buffer saline (PBS), the slices were incubated with secondary antibodies (diluted ratio 1:400, Zsbio) for 20 minutes at 37°C. Diaminobenzidine was applied as the chromogen. The nuclei were counterstained with Mayer's hematoxylin.

LAT1 expressions were considered positive only when distinct membrane staining was present. Staining intensity was scored as follows: score 1,

Table I. *The patient demographics according to the expression status of LAT1.*

Parameter	LAT1-positive	LAT1-negative	P-value
Total	13	19	
Age ≤60/>60	5/8	6/13	0.721
Gender Male/Female	9/4	13/6	1.000
Disease stage IIorIIIorIV T factor	6/7	6/13	0.473
T1-2/T3-4	6/7	9/10	1.000
N factor N0/N1-2	12/1	11/8	0.050
Vascular invasion Positive/negative	3/10	6/13	0.704
Nerve invasion Positive/negative	8/5	10/9	0.725
Degree of differentiation	2.5(2,2.75)	2(2,2.5)	**0.042**
Tumor volume	28.85(11.20,128.85)	43.27(20.19,75.72)	0.908

Degree of differentiation: score 1, high differentiation, score 2, middle-high differentiation and middle differentiation, score 3, Poor differentiated and poor-middle differentiation. Tumor volume= (Length×width×height×π/6) cm3.

up to 10% of tumor area stained; score 2, 11%-25% stained; score 3, 26-50% stained; and score 4, at least 51% stained. The tumors whose stained tumor cells were scored as 1 were defined as negative, whereas those whose tumours were scored as 2, 3, or 4 were defined as positive (27).

Statistical analysis

A P-value <0.05 indicated that there was a statistical difference. Fisher's exact test was used to test the difference between the two classification variables. Non-normally distributed data were analyzed using the Mann-Whitney U test and Wilcoxon rank-sum test and expressed as median (P_{25}, P_{75}). The non-parametric Spearman's rank test analysed the correlations between different variables. The survival was estimated by the Kaplan-Meier method, and the long-rank test estimated the survival difference. The overall survival (OS) was determined as the time from tumor resection to death from any cause. Disease-free survival (DFS) was defined as the time between tumor resection and the first instance of disease progression or death. Thirty-two patients were followed up by phone calls from the hospital medical records. The stepwise Cox proportional hazard model was used to determine independent prognostic factors for the multivariate analysis. The SPSS 19.0 software was used for the statistical analysis.

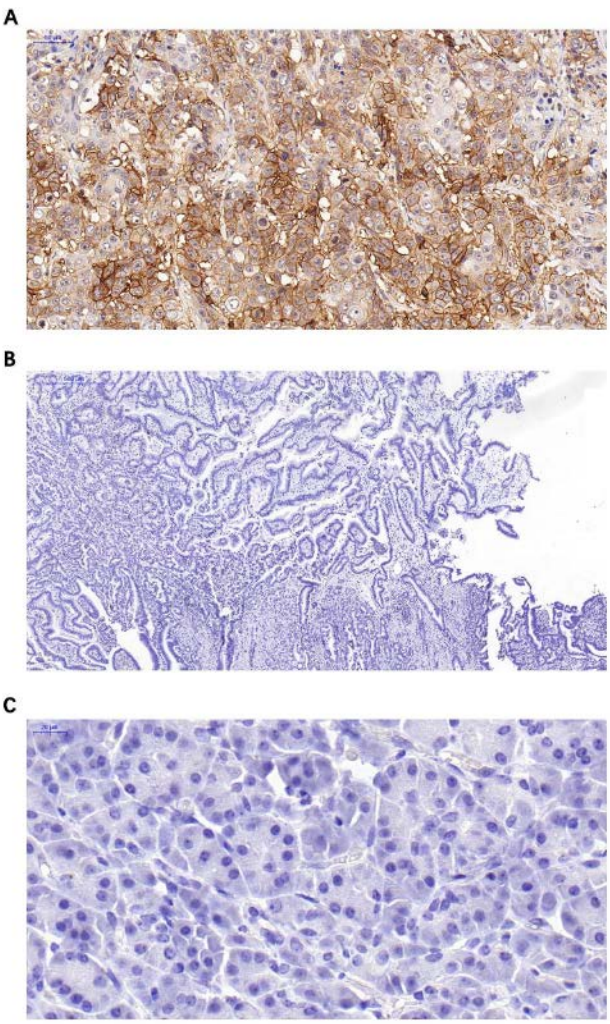

Fig. 1. *Immunohistochemical findings of LAT1 in pancreatic carcinomas and paracancerous tissues. The LAT1 expression was considered positive only when the cell membrane of pancreatic cancer tissue (**A**) showed obvious immunoreactivity; The LAT1 expression was considered negative when the cell membrane of pancreatic cancer tissue (**B**) and adjacent tissue (**C**) did not show obvious immunoreactivity.*

RESULTS

Immunohistochemical analysis

The primary lesions and paracancerous tissues of 32 patients with pancreatic cancer were analyzed by immunohistochemistry. Fig. 1 shows the results of the immunohistochemical LAT1 staining. This immunostaining can be detected in pancreatic cancer tissues, mainly located in the cell membrane. All positive cells showed strong membrane immunostaining (Fig. 1), while cytoplasmic staining was rare. The expression rate of LAT1 in the pancreatic cancer tissues was 40.6% (13/32), and that in the adjacent tissues was 0% (0/32). The difference was statistically significant (P < 0.001).. The patient demographics according to LAT1 expression status are summarized in Table I.

Correlations between the LAT1 expression and the different variables

Spearman's rank test showed that the expression of LAT1 was positively correlated with Ki67 expression (r=0.632, P=0.001) and the degree of differentiation significantly (r=0.390, P=0.027), but negatively correlated with the number of lymph nodes (r=-0.378, P=0.033) (Table II).

According to the LAT1 expression, the DFS and OS rates were analyzed by the Kaplan-Meier test. The results showed a significant difference between the expression of LAT1 and DFS(P=0.043) but no significant difference between the expression of LAT1 and OS (Fig. 2).

Of the 32 patients studied, 15 died, and 20 relapsed postoperatively. Tab. 3 and 4 show the results of the univariate and multivariate analyses of all patients (n=32). The univariate analysis showed that the CA19-9, CEA, and LAT1 expression levels were important variables affecting the DFS. The multivariate analysis confirmed that the CEA and LAT1 expressions were independent prognostic factors for DFS (P_{CEA}=0.015. P_{LAT1} =0.042). The univariate analysis confirmed that CA19-9 and CEA were important variables affecting the OS, and the multivariate analysis confirmed that CEA and CA19-9 were independent prognostic factors for poor OS (P_{CEA}=0.024, $P_{CA19\text{-}9}$=0.040) (Table II, III).

DISCUSSION

Many previous studies have reported that LAT1 is highly expressed at different tumor tissues, with low

Table II. *Correlation with LAT1 expression.*

Variables	Spearman's r	P-value
Ki-67	0.632	**0.001**
CEA	0.051	0.801
CA19-9	-0.003	0.985
Tumor volume	0.080	0.663
Degree of differentiation	0.390	**0.027**
N factor	-0.378	**0.033**

Bold values indicate a statistically significant difference. Degree of differentiation: score 1; high differentiation: score 2; middle-high differentiation and middle differentiation: score 3; Poor differentiated and poor-middle differentiation. Tumor volume= (Length×width×height×π/6)cm3.

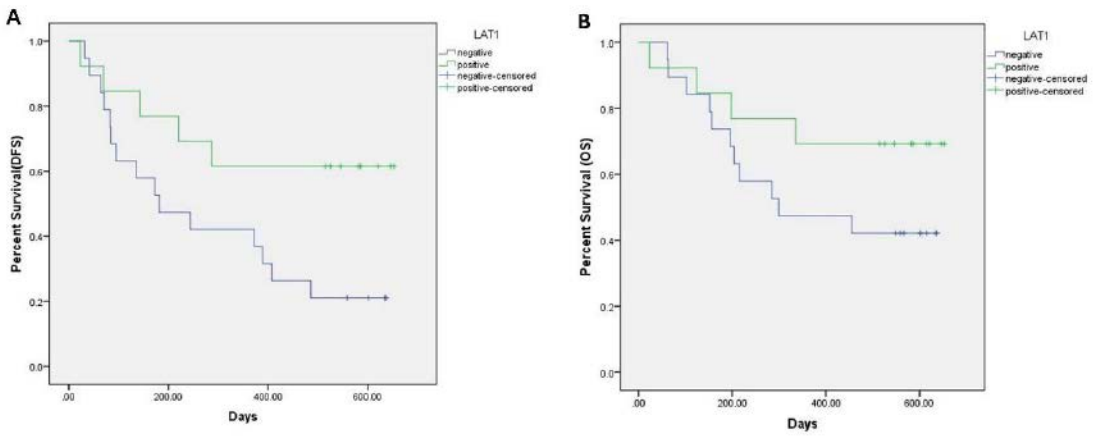

Fig. 2. *Postoperative DFS and OS of patients with completely resected pancreatic cancer. The postoperative DFS and OS were compared according to the LAT1 expression. The LAT1 expression was significantly different from the DFS (A) but not different from the OS (B).*

Table III. *Univariate and multivariate analysis in disease-free survival.*

		Univariate analysis			Multivariate analysis		
Variables	group	HR	95%CI	P value	HR	95%CI	P value
Age		1.033	0.988-1.081	0.148	1.021	0.977-1.066	0.359
Gender	Male *	1.215	0.484-3.049	0.679	-	-	-
	Female						
Degree of differentiation		1.120	0.516-2.431	0.774	1.869	0.769-4.543	0.167
T factor	T1-2 *	0.964	0.398-2.334	0.934	-	-	-
	T3-4						
N factor	N0 *	1.326	0.527-3.337	0.549	-	-	-
	N1-2						
TNM(disease stage)	I*	0.753	0.306-1.855	0.538	-	-	-
	II/III/IV						
Vascular invasion	negative *	1.297	0.497-3.380	0.595	-	-	-
	positive						
Nerve invasion	negative *	1.531	0.623-3.760	0.353	-	-	-
	positive						
Ki67		1.292	0.051-32.881	0.877	-	-	-
CA19-9		1.002	1.000-1.003	**0.015**	-	-	-
CEA		1.122	1.031-1.221	**0.008**	1.113	1.021-1.214	**0.015**
LAT1	negative *	0.364	0.131-1.007	**0.052**	0.306	0.098-0.961	**0.042**
	positive						

**Control group. Bold values indicate a statistically significant difference. CI: 95%; HR: LAT1,L-type amino acid transporter 1.*

or no expression in normal tissues (20, 27). Extensive research has been conducted on the expression of LAT in lung cancer. For instance, the Kaira et al. research team has studied the expression and role of LAT1 in lung cancer. At present, there is considered to be high LAT1 expression in lung cancer cells, but the expression rate differs in different histological types. The high expression of LAT1 is significantly related to the biological characteristics of lung cancer, such as lymph node metastasis, distant metastasis, and vascular invasion (8, 28). The expression of LAT1 in the pathological tissues of patients with advanced tumors is higher than that of patients in the early stage. Eventually, LAT1 could even predict the long-term survival of patients with lung cancer. The survival time of patients with negative LAT1 is significantly higher than that of patients with positive LAT1, and the patients with both positive CD98 and LAT1 had the least long-term survival (8). In addition, LAT1 expression has been studied in gastric cancer(9), breast cancer(14), prostate cancer (16), renal cell carcinoma(17), neuroendocrine tumor (18), laryngeal carcinoma (13), lymphoma, and leukemia (19).

There have been few studies on the expression of LAT1 in pancreatic cancer and paracancerous tissue. Thus, in this study, we detected its expression in postoperative specimens of pancreatic cancer and paracancerous tissue and analyzed the relationship between the LAT1 expression and patients' clinical features, the relationship between the LAT1 expression and DFS and OS, and the effects of the LAT1 expression and other variables on the DFS and OS. In addition, the relationship between the LAT1 expression and the patients' clinical features and prognoses was preliminarily analyzed.

This study showed that the expression of LAT1 was positively correlated with the Ki67 expression and the degree of tumor differentiation. Ki67 is considered an indicator of tumor cell proliferation (29), and the degree of tumor differentiation is related to poor prognosis. Moreover, LAT1 can transport and regulate a variety of amino acids in cells. Therefore, it is considered able to regulate the metabolism of tumor cells. The growth of tumor cells requires a large and sufficient supply of proteins and amino acids; this may explain why the higher the expression of LAT1 in patients with pancreatic cancer, the worse the tumor differentiation. The faster the proliferation of tumor cells, the worse the degree of differentiation and the more amino acids and proteins the tumor cells need—leading to the higher LAT1 expression. It has been suggested that the high expression of LAT1 indicates a potentially poor prognosis.

Here, we analyzed the effects of univariate and multivariate factors on the DFS and OS via Cox regression. The univariate analysis showed that the expressions of CA19-9, CEA, and LAT1 were statistically significant for the DFS, while the multivariate analysis showed that the expressions of CEA and LAT1 had a statistically significant effect on the DFS. However, we found that positive LAT1 expression could promote prolonged DFS, contrary to most similar literature reports. The reasons for this analysis result may be as follows: 1) the fact that positive LAT1 expression promotes the prolongation of DFS is indeed the embodiment of the real world; 2) our sample size was small, and there may have been sampling errors; 3) Positive LAT1 expression represents a rapid proliferation of tumor cells and a high degree of malignancy, but in clinical practice, the long-term prognosis of tumor patients with the above two characteristics is not necessarily poor. In addition, the CEA level had a statistically significant effect on the DFS in the multivariate analysis, differing from the results of Kaira et al. and other researchers, who found no independent prognostic factors in their multivariate analyses (12). Our univariate and multivariate Cox analyses showed that the effects of CA19-9 and CEA on the OS were statistically significant but that the effect of LAT1 on the OS was not statistically significant, this also differed from the results of Kaira et al., who believed that LAT1, Ki67, and the disease stage are independent prognostic factors for poor OS (12). Since the sample sizes of our and Kaira et al.'s studies were relatively small, the conclusion may need to be verified by a larger research sample or a meta-analysis to answer this question.

Currently, it is related to the degree of differentiation and Ki67 level in pancreatic cancer. The higher the expression of LAT1, the worse the differentiation of tumor cells and the higher the proliferation process, leading to a potentially poor prognosis. By interfering

Table IV. *Univariate and multivariate analysis in overall survival.*

		Univariate analysis			Multivariate analysis		
Variables	group	HR	95%CI	P value	HR	95%CI	P value
Age		1.045	0.933-1.100	0.089	-	-	-
Gender	Male *	1.046	0.357-3.067	0.934	-	-	-
	Female						
Degree of differentiation		1.415	0.602-3.326	0.427	-	-	-
T factor	T1-2 *	0.686	0.248-1.898	0.468	-	-	-
	T3-4						
N factor	N0 *	0.886	0.282-2.785	0.836	-	-	-
	N1-2						
TNM(disease stage)	I*	0609	0.220-1.688	0.341	-	-	-
	II/III/IV						
Vascular invasion	negative *	1.535	0.523-4.507	0.436	-	-	-
	positive						
Nerve invasion	negative *	1.929	0.658-5.675	0.231	-	-	-
	positive						
Ki67		2.668	0.058-123.211	0.616	-	-	-
CA19-9		1.002	1.000-1.003	**0.010**	1.001	1.000-1.003	**0.040**
CEA		1.098	1.020-1.183	**0.013**	1.098	1.013-1.191	**0.024**
LAT1	negative *	0.454	0.144-1.429	0.177	0.746	0.208-2.677	0.653
	positive						

**Control group. Bold values indicate a statistically significant difference. CI 95%: HR: hazard ratio; LAT1, L-type amino acid transporter 1.*

with the amino acid metabolism of tumor cells, LAT1 inhibitors can "starve" to death. There are many kinds of LAT1 inhibitors, among which JPH203 is a selective inhibitor of LAT1 and the only compound in Phase I clinical trial (25). In general, LAT1 inhibitors are expected to lead to a breakthrough in the clinical treatment of pancreatic cancer.

Although LAT1 might participate in pancreatic cancer's pathogenesis and clinical features, the mechanism was not further clarified, which will be the focus of our future work and a larger sample size is needed for further validation and research. However, our experiments can be used for theoretically and clinically reference future studies.

CONCLUSION

Taken together, LAT1, as a potential tumor facilitator, may play important roles in pancreatic cancer, especially being related to the degree of proliferation and differentiation, but not well in evaluating the OS. Moreover, LAT1 combined with CEA could effectively predict the DFS in pancreatic cancer as a biological marker. Besides, the discovery could also provide a perspective to increase our understanding of pancreatic cancer and the utmost importance for developing new therapies for pancreatic cancer. LAT1 inhibitors or amino acid restriction may be a promising strategy for treating pancreatic cancer.

ACKNOWLEDGEMENTS

We would like to acknowledge the hard and dedicated work of all the staff that implemented the intervention and evaluation components of the study.

Funding

None

Competing interests

The authors declare that they have no competing interests.

REFERENCES

1. Xu YP, Yang M.Advancement in treatment and diagnosis of pancreatic cancer with radiopharmaceuticals.World J Gastrointest Oncol. 2016 Feb 15;8(2):165-72.
2. Ni XG, Bai XF, Mao YL,e tal. The clinical value of serum CEA, CA19-9, and CA242 in the diagnosis and prognosis of pancreatic cancer. Eur J Surg Oncol 2005; 31: 164-169
3. O'Brien DP, Sandanayake NS, Jenkinson C,e tal. Serum CA19-9 is significantly upregulated up to 2 years before diagnosis with pancreatic cancer: implications for early disease detection. Clin Cancer Res 2015; 21: 622-631
4. Marrelli D, Caruso S, Pedrazzani C,e tal.CA19-9 serum levels in obstructive jaundice: clinical value in benign and malignant conditions. Am J Surg 2009; 198: 333-339
5. National Comprehensive Cancer Network. 2017 (cited March 1, 2018). In: NCCN guidelines version 3.2017: pancreatic adenocarcinoma (Internet).
6. Yanagida O, Kanai Y, Chairoungdua A, et al. Human L-type amino acid transporter 1 (LAT1): characterization of function and expression in tumor cell lines. Biochim Biophys Acta. 2001; 1514:291-302.
7. Kanai Y, Segawa H, Miyamoto Ki, Uchino H, Takeda E and Endou H: Expression cloning and characterization of a transporter for large neutral amino acids activated by the heavy chain of 4F2 antigen (CD98). J Biol Chem 273: 23629-23632, 1998.
8. Kaira K, Oriuchi N, Imai H, *et al*. Prognostic significance of L-type amino acid transporter 1 (LAT1) and 4F2 heavy chain (CD98) expression in surgically resectable stage III non-small cell lung cancer. Exp Ther Med. 2010; 1:799-808
9. Ichinoe M1, Yanagisawa N2, Mikami T3. L-Type amino acid transporter 1 (LAT1) expression in lymph node metastasis of gastric carcinoma: Its correlation with size of metastatic lesion and Ki-67 labeling. Pathol Res Pract. 2015 Jul;211(7):533-8.
10. Kobayashi H, Ishii Y, Takayama T. Expression of L-type amino acid transporter 1 (LAT1) in esophageal carcinoma. J Surg Oncol. 2005 Jun 15;90(4):233-8
11. Hayase S, Kumamoto K, Saito K,etal. L-type amino acid transporter 1 expression is upregulated and associated with cellular proliferation in colorectal cancer. Oncol Lett. 2017 Dec;14(6):7410-7416.
12. Kaira K1, Sunose Y, Arakawa K, etal. Prognostic significance of L-type amino-acid transporter 1 expression in surgically resected pancreatic cancer. Br

J Cancer. 2012 Aug 7;107(4):632-8.
13. Nikkuni O, Kaira K, Toyoda M, etal. etal.Expression of Amino Acid Transporters (LAT1 and ASCT2) in Patients with Stage III/IV Laryngeal Squamous Cell Carcinoma.Pathol Oncol Res. 2015 Sep;21(4):1175-81
14. Furuya M1, Horiguchi J, Nakajima H, etal. Correlation of L-type amino acid transporter 1 and CD98 expression with triple negative breast cancer prognosis.Cancer Sci. 2012 Feb;103(2):382-9.
15. Kaira K1, Oriuchi N, Imai H, etal. L-type amino acid transporter 1 (LAT1) is frequently expressed in thymic carcinomas but is absent in thymomas.J Surg Oncol. 2009 Jun 1;99(7):433-8
16. Yanagisawa N1, Satoh T, Hana K. etal. L-amino acid transporter 1 may be a prognostic marker for local progression of prostatic cancer under expectant management. Cancer Biomark. 2015;15(4):365-74.
17. Betsunoh H, Fukuda T, Anzai N,etal. Increased expression of system large amino acid transporter (LAT)-1 mRNA is associated with invasive potential and unfavorable prognosis of human clear cell renal cell carcinoma..BMC Cancer. 2013 Oct 30;13:509.
18. Feral CC, Tissot FS, Tosello L,etal. 18F-fluorodihydroxyphenylalanine PET/CT in pheochromocytoma and paraganglioma: relation to genotype and amino acid transport system L. Eur J Nucl Med Mol Imaging. 2017 May;44(5):812-821
19. Rosilio C, Nebout M, Imbert V, etal. L-type amino-acid transporter 1 (LAT1): a therapeutic target supportinggrowth and survival of T-cell lymphoblastic lymphoma/T-cell acutelymphoblastic leukemia Leukemia. 2015 Jun;29(6):1253-66
20. Prasad PD1, Wang H, Huang W,etal. Human LAT1, a subunit of system L amino acid transporter: molecular cloning and transport function.Biochem Biophys Res Commun. 1999 Feb 16;255(2):283-8.
21. Janpipatkul K1, Suksen K2,etal. Borwornpinyo S3,Downregulation of LAT1 expression suppresses cholangiocarcinoma cell invasion and migration. Cell Signal. 2014 Aug;26(8):1668-79.
22. Yun DW1, Lee SA, Park MG,etal. JPH203, an L-type amino acid transporter 1-selective compound, induces apoptosis of YD-38 human oral cancer cells.J Pharmacol Sci. 2014;124(2):208-17.
23. Kim CS1, Cho SH, Chun HS. etal. BCH, an inhibitor of system L amino acid transporters, induces apoptosis in cancer cells.Biol Pharm Bull. 2008 Jun;31(6):1096-100.
24. Oda K, Hosoda N, Endo H. etal. L-type amino acid transporter 1 inhibitors inhibit tumor cell growth. Cancer Sci. 2010 Jan;101(1):173-9.
25. Okano, N.; Naruge, D.; Kawai, K.; Kobayashi, T.; Nagashima, F.; Endou, H.; Furuse, J. First-in-human phase I study of JPH203, an L-type amino acid transporter 1 inhibitor, in patients with advanced solid tumors. Investig. New Drugs 2020.
26. Nobuyuki Yanagisawa , Masaaki Ichinoe, Tetuo Mikami,etal. High expression of L-type amino acid transporter 1 (LAT1) predicts poor prognosis in pancreatic ductal adenocarcinomas. J Clin Pathol. 2012;65(11):1019-1023
27. Akira Shimizua, Kyoichi Kairab, Madoka Kato,etal. Prognostic significance of L-type amino acid transporter 1(LAT1) expression in cutaneous melanoma. Melanoma Res. 2015,25(5):399-405.
28. Miroslava Juríková , Ľudovít Danihel, Štefan Polák,etal. Ki67, PCNA, and MCM proteins: Markers of proliferation in the diagnosis of breast cancer. Acta Histochem. 2016 Jun;118(5):544-552
29. Kaira, K, Oriuchi N, Imai H.et al. Prognostic significance of L-type amino acid transporter 1 expression in resectable stage I-III nonsmall cell lung cancer. British Journal of Cancer, 2008, 98(4): 742-748.

LETTER TO THE EDITOR

Type VI Osteogenesis imperfecta: effect of plasma transfusion on bone metabolism

F. Antoniazzi[1,2*], A. Pietrobelli[1,2,3], A. Gandini[2], P. Cavarzere[1], D-A. Ramaroli[1,4], M. Mottes[5], A. Guzzo[6], M. De Gironcoli[7], S. Genesini[7], M. Zaffanello[1,2], R. Gaudino[1,2], L. Dalle Carbonare[8], M-T. Valenti[8], D. Gatti[8], A. Fassio[8], F. Bertoldo[8], S. Tardivo[4] and G. Piacentini[1,2]

[1]Pediatric Clinic C, Azienda Ospedaliera Universitaria Integrata, Verona, Italy; [2]Department of Surgical Sciences, Dentistry, Gynecology and Pediatrics, Pediatric Clinic, University of Verona School of Medicine, Verona, Italy; [3]Pennington Biomedical Research Center, Baton Rouge, LA, USA; [4]Department of Diagnostic and Public Health, University of Verona School of Medicine, Verona, Italy; [5]Department of Neurosciences, Biomedicine and Movement Sciences, University of Verona School of Medicine, Verona, Italy; [6]Department of Pathology and Diagnostics, University of Verona School of Medicine, Verona, Italy; [7]Transfusion Center, Azienda Ospedaliera Universitaria Integrata, Verona, Italy; [8]Department of Medicine, University of Verona School of Medicine, Verona, Italy

Received October 6, 2021 – Accepted March 23, 2022

To the Editor,

Osteogenesis imperfecta (OI) is a phenotypically and genetically heterogeneous group of inherited bone dysplasias characterized mainly by bone fragility and deformity (1). Of the various OI types, autosomal recessive-type VI OI (OMIM 613982) (2) has peculiar clinical and histological features. Neonates appear normal at birth, but they start fractures within 6 to 12 months of age, followed by severe, progressive deforming bone dysplasia, vertebral compressions and scoliosis, losing the ability to walk autonomously. Type VI OI is caused by homozygous or compounds heterozygous null mutations in the SERPINF1 gene (OMIM 172860), coding for pigment-epithelium derived factor (PEDF), a 418-amino acid secreted glycoprotein expressed in several tissues including osteoblasts (3, 4), well-known for its neurotrophic and antiangiogenic properties.

Patients with type VI OI have undetectable levels of serum PEDF (5) and show a weaker response to "standard" treatment with bisphosphonates (6). For this reason, it would be helpful to search for more effective treatment modalities, but replacement therapy using recombinant PEDF and/or mesenchymal stem cell therapy is currently not possible.

The observation that all null SERPINF1 mutant patients appear healthy at birth and do not have fractures until after 6 months of age may suggest a protective effect of circulating maternal PEDF during fetal development due to hypothetical placental passage which would persist in the first months of life. Moreover, unaffected heterozygotes parents, clinically asymptomatic, have PEDF circulating levels of about 1 μg/mL (4), which is lower than normal concentrations of about 5-10 μg/mL but enough for normal bone metabolism/development and a healthy status (7).

Keywords: osteogenesis imperfecta; PEDF; bone metabolism; bisphosphonates; plasma transfusion

*Corresponding Author:
Dr Franco Antoniazzi,
Department of Surgical Sciences, Dentistry, Gynecology and Pediatrics,
Pediatric Clinic C, University of Verona,
Ospedale Donna e Bambino,
Piazza A. Stefani 1, 37126 Verona, Italy
e-mail: franco.antoniazzi@univr.it

0393-974X (2022)

DISCLOSURE: ALL AUTHORS REPORT NO CONFLICTS OF INTEREST RELEVANT TO THIS ARTICLE.

The aim of this study on patients with type VI OI was to evaluate the efficacy and safety of PEDF administration using pharmaceutical grade plasma to provide a minimum amount of PEDF similar to the levels found in heterozygotes.

MATERIALS AND METHODS

The study was carried out at Pediatric Clinic C, University of Verona Medical School, a third level Paediatric Center for the Study of Rare Skeletal Diseases, partner of the European Reference Network for Rare Bone Disorders (ERN-BOND). The study protocol was approved by the local Ethics Committee (PEDFOI: Prog. n. 633CESC).

Inclusion criteria were children between 1- and 18-years-of-age with genetically and biochemically confirmed type VI OI. Exclusion criteria were previous transfusion adverse events. Informed written consent to participate in the study was obtained from each patient's family or guardians.

Ten patients aged 1-18 years were eligible to participate in the study. Clinical history was recorded with particular attention to the number of fractures, height or length in cm, weight in kg and body mass index (BMI = kg/m2). Height and weight SD values were calculated according to Italian growth charts. All subjects had already undergone several treatment periods using bisphosphonates (neridronate), with results lower than expected. All 10 patients were given vitamin D and calcium supplements for almost one year before participating in the study.

After being selected for inclusion, one patient (OI 63 - bedridden) declined to participate in the study protocol due to the clinical impossibility to be moved (to avoid fractures) because the family lived approximately 700 km from the hospital. Two other patients (OI 122 and OI 123 – 2 brothers) declined because of family financial difficulties (despite the possibility of financial support from the *Associazione Italiana Osteogenesis Imperfecta* - AsItOI). Three patients (OI 93, OI 94 and OI 162 – 3 sisters) did not continue

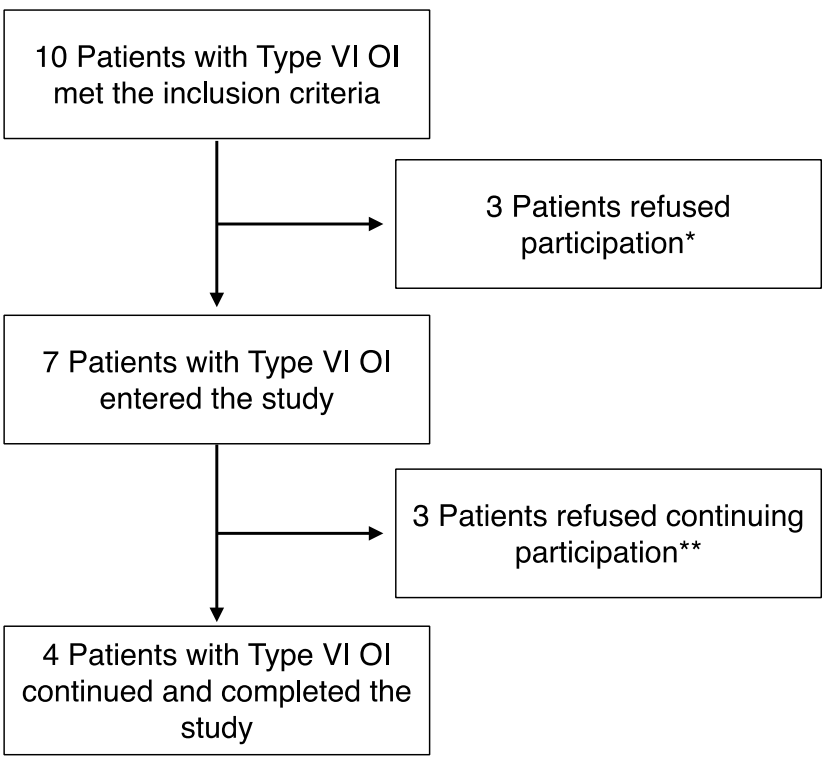

Fig.1. *Trial profile.*
**Patients refused participation: OI 63 for the clinical impossibility to be transported; OI 122 and OI 123 for the impossibility of parents to participate in the study due to work problems and economic difficulties (even if there was the possibility of financial support).*
*** Patients did not continue treatment after the first plasma transfusion due to problems with non-acceptance of transfusions and their frequency: OI 93, OI 94 and OI 162.*

their treatment after the first plasma transfusion because of family ethical problems in accepting transfusions and their frequency. Of the initial 10 patients, only four completed the study. Fig. 1 shows the study profile.

Once included in the study, pharmaceutical-grade plasma (Plasmasafe) (12-15 mL/Kg) was administered e.v. over 3 hours. Plasma used for the treatment came from the same production batch, and the PEDF content was measured before each transfusion (9.95 ± 2.2 μg/mL). The quantity per kg was empirically calculated to reach the theoretical concentration of about 1 μg/mL of PEDF in plasma patients. Plasma transfusions were repeated every month for 6 months with the same procedure giving the same plasma dose. The timetable of the study protocol is shown in Fig. 2.

Any plasma transfusion adverse events, such as hemodynamic overload, allergic-type transfusion reactions or non-haemolytic febrile reactions, were carefully evaluated. Vital signs before, during, and at the end of each transfusion session and in the first three hours immediately following were recorded. In addition, before the first plasma infusion and six months after the last plasma infusion, we determined antibody title, ran a nucleic acid test for hepatitis B virus (HBV), hepatitis C virus (HCV), tested for human immunodeficiency virus (HIV) and antibody title for syphilis in order to exclude potential transmission of infectious disease.

Biochemical and instrumental determinations

At baseline (T0), before each plasma transfusion (T4, before second plasma infusion, T5 - 3rd, T6 - 4th, T7 - 5th, T8 - 6th and T9 - 7th), and 6 months after the last plasma transfusion (T10), PEDF, bone metabolic markers [Ca, P, 25-OH VitaminD, PTH, bone alkaline phosphatase (bone ALP), osteocalcin (Oc), procollagen type 1 N-terminal propeptide (P1NP), dickkopf-1 (DKK1), sclerostin, C-terminal telopeptides of type I collagen (β CTX)], iron and ferritin were determined in serum or plasma; Ca and creatinine were measured in urine. PEDF determination was also repeated after 1 (T1), 2 (T2) and 7 days (T3) of first plasma administration to see the effective increase in the patients' bloodstream establish half-lives and record-level changes over time. At those same times, we also assayed DKK1, sclerostin and P1NP to evaluate the short-term response to PEDF, if present.

All samples were frozen immediately after collection and stored at -30°C until analysis. At baseline and after 12 months, bone mineral density was measured, and fracture rate was checked. In addition, serum Ca and P, iron and ferritin values and urinary Ca and creatinine values were determined using standard techniques.

Serum 25OH Vitamin D, intact 1–84 PTH, bone ALP and Oc were determined using a LIAISON analyzer and commercial methods (DiaSorin Inc, Stillwater, MN, USA): 25 OH Vitamin D total assay (intra- and interassay CV 5.1% and 5.8%, respectively; analytical sensitivity 10 nmol/L), 1-84 PTH assay (3.6% and 4.7%; 0.5 pg/mL), BAP OSTASE assay (4.6% and 6.1%, 1.5 μg/L), osteocalcin assay (5.0 and 6.0%; 0.5 ng/mL).

Serum intact N-propeptide of type I collagen (P1NP)

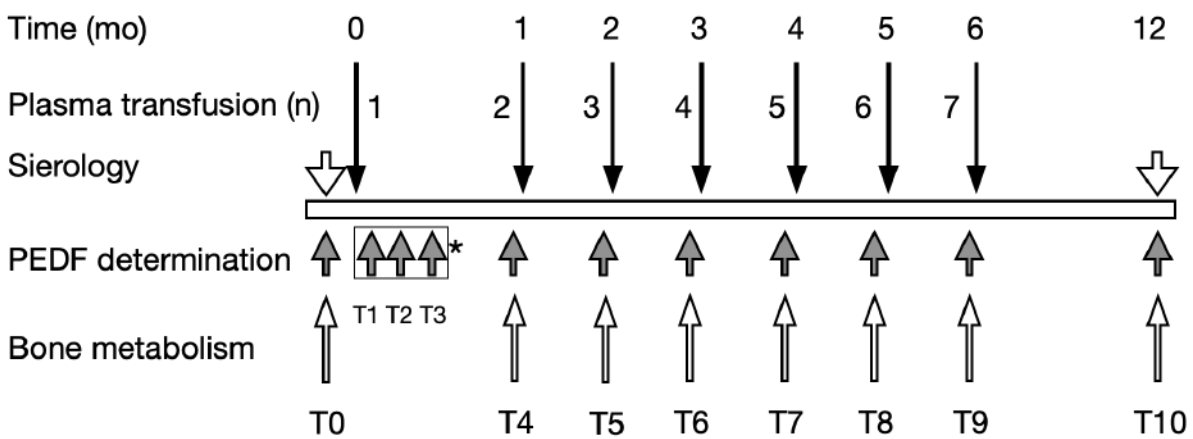

Fig. 2. *Study protocol timetable and flow chart. PEDF determination: 1, 2 and 7 days after first plasma transfusion.*

was measured using the IDS-ISYS Multi-Discipline automated analyzer (Immunodiagnostic System, Boldon, UK) based on chemiluminescence immunoassay (CLIA): intra- and interassay CVs were 4% and 5%, respectively, and analytical sensitivity was 2 ng/mL.

Serum DKK1 and sclerostin were measured by ELISA (Biomedica Medizinprodukte, Vienna, Austria); for DKK1 intra- and interassay CV were 7% and 8.2% respectively, analytical sensitivity was 0.38 pmol/L; for sclerostin, intra- and interassay CV were 5% and 6.9%, respectively, analytical sensitivity was 2.6 pmol/L.

Serum β-CTx was determined using electrochemiluminescence immunoassay (ECLIA): β-CrossLaps/serum (Roche Diagnostics GmbH, Mannheim, Germany). The intrassay and interassay coefficients of variation were 2.1% and 3.2 %, respectively; the analytical sensitivity of the assay was 0.07 ng/mL.

Circulating PEDF levels were measured with the *Human* PEDF ELISA Kit (BioVendor-Laboratornì medicìna a.s, Czech Republic) following the manufacturer's instructions. The intra- and interassay CVs were 4.0% and 6.6%, respectively; analytical sensitivity was 0.045 µg/mL.

Dual-energy x-ray absorptiometry (DXA)

Lumbar spine bone mineral density (BMD) (g/cm^2) was evaluated using Dual Energy X-ray Absorptiometry (DXA) (Hologic Discovery A, Hologic Inc., Waltham, MA, USA). The quality scan was assessed according to a strict quality control procedure. Instruments were calibrated daily with local spine phantom and periodically with a cross-calibration phantom. The values were expressed in g/cm^2 and Z-score (number of standard deviations compared to normal subjects of the same age and gender).

Statistical analysis

The data are expressed as mean ± standard deviation (SD). Due to the low number of type VI OI study patients, data are expressed as differences in SDs. T-tests were conducted to establish differences in plasma and biochemical markers. Statistical significance was set at $p<0.05$. The data were analyzed using the SAS program (SAS Institute Inc., Cary, NC, USA).

RESULTS

Anthropometric and clinical findings at baseline in all the type VI OI patients studied are presented in Table I. Parental consanguinity and homozygosity were found in 7 of 10 patients. Only in one homozygosity patient (OI63), there was no information on parental consanguinity. There was compound heterozygosity and non-consanguinity in 2 patients.

Anthropometric and clinical findings showed that the disease varies in severity, growth impairment,

Table I. *Genetic, Anthropometric and Clinical findings in patients affected by type VI OI at the beginning of the study (n = 10)*

Patient Id	OI 389	OI 60	OI 298	OI 343	OI 93	OI 94	OI 162	OI 122	OI 123	OI 63
Origin (Country)	Italy	Italy	Pakistan	Pakistan	Switzerland	Switzerland	Switzerland	Morocco	Morocco	Italy
Consanguinity between parents	no	no	yes	yes	yes	yes	yes	yes	yes	no
Mode of inheritance:	Compound hetero-zygosity	Compound hetero-zygosity	Homo-zygosity	Homo-zygosity	Homo-zygosity	Homo-zygosity	Homo-zygosity	Homo-zygosity	Homo-zygosity	Homo-zygosity
Gender	M	M	F	F	F	F	F	F	M	M
age (yrs)	14.8	13.2	12.4	5.4	16.3	11.6	8.5	14.4	12.4	17.5
Weight kg (SDS)	42.0 (-2.0)	35.0 (-1.9)	34.0 (-4.7)	15.6 (-1.8)	61.0 (-0.5)	25.0 (-2.7)	18.8 (-2.6)	32.1 (-3.4)	30.0 (-2.2)	39.2 (-5.2)
Length cm (SDS)	152.0 (-2.1)	132.0 (-3.4)	116.0 (-5.4)	105.0 (-1.5)	143.0 (-4.1)	118.0 (-4.5)	119.5 (-1.8)	136.0 (-3.7)	132.0 (-2.9)	140.0 (-5.8)
BMI kg/m^2 (SDS)	18.2 (-1.1)	20.1 (-0.1)	25.3 (1.3)	14.2 (-1.1)	29.8 (1.9)	17.9 (-0.5)	13.2 (-2.4)	17.3 (-1.5)	17.2 (-0.9)	19.9 (-0.9)
Age of first fracture (yrs)	6.1	1.2	1.1	0.9	0.8	0.5	1.0	1.2	0.8	0.5
Total n. of fractures	15	>30	24	6	>30	16	26	23	18	>30
Lumbar spine BMD (SDS)	-2.2	-4.1	-1.1	-3.5	-0.5	-1.9	-3.2	ND°	-3.0	-3.5
Walking capacity	Yes crutches	No wheelchair	No wheelchair	Yes crutches	No wheelchair	No wheelchair	Yes crutches	Yes crutches	Yes crutches	No bedridden

Patients OI 298 and OI 343 were two sisters; Patients OI 93, OI 94 and V4 were three sisters; Patients OI 122 and OI 123 were brothers. Gender: M = male; F = Female; SDS: Standard deviation score; Weight and length SDS values were calculated with respect to Italian growth charts (see text). Lumbar Spine BMD: Lumbar Spine Bone Mineral Density °ND: not detectable for vertebral arthrodesis

number of fractures and BMD. Fractures started a few months after birth, with a clear correlation between earlier age of presentation and clinical severity.

Only patient OI 389 (compound heterozygosity) showed a milder phenotype with fractures starting at 6 years. However, walking capacity was reduced in all patients and five were confined to a wheelchair (in 1 of them bedridden).

BMD varied according to vertebrae meshing and degree of scoliosis. Kyphoscoliosis was present in all patients, particularly in patient OI 122, where the lumbar spine BMD could not be evaluated due to vertebral arthrodesis. All patients had white sclerae, with no characteristic facies of typical OI.

Table II shows biochemical findings at baseline in our type VI OI patients. Bone metabolic markers showed high bone ALP, P1NP and β CTx with normal levels of osteocalcin, sclerostin and DKK1.

All patients had taken vitamin D and calcium supplements before the study and had normal levels of 25 OH vitamin D (>75 nmol/L). They continued calcium and vitamin D supplementation during the study (almost 1000 UI per day) and showed normal levels of 25 OH vitamin D, Ca, P and Ca/creatinine ratio in urine during the entire study period. In addition, all patients had an age-appropriate calcium intake in agreement with recommended daily allowances.

Interestingly, all patients showed low ferritin levels before and during the study, despite iron supplementation. In every case, faecal occult blood was negative, Giardia lamblia infestation and celiac disease were excluded. In a few cases, we found microcytic anaemia (OI 298, OI 343, OI 122, OI 123 and OI 63).

Plasma infusion

PEDF determinations before (T0), and at 1 (T1), 2 (T2) and 7 days (T3) after the first plasma infusion (in 5 out of 7 patients that received the first infusion), showed an increase from <0.045 μg/mL before the infusion to 1.36 ± 0.27 μg/mL at day 1, returning to <0.045 from day 2 onwards. In addition, we found a significant decrease in DKK1 ($p=0.05$) and a non-significant increase in P1NP levels the day after the first transfusion (T1), with a rapid return to previous levels in the following days. PEDF, P1NP, DKK1 and sclerostin levels at these times are shown in Fig. 3.

Table III shows the biochemical findings in the 4 type VI OI patients that completed the study. Bone metabolic markers persistently showed high bone ALP, P1NP and β CTx with normal levels of osteocalcin, sclerostin and DKK1. Biochemical markers of bone turnover, BMD and fracture rate did not significantly change during the study.

Adverse events

Only one patient (OI 298) had an urticarial reaction after the first transfusion, which resolved with an antihistamine. For subsequent transfusions, this patient required prior antihistamine medication. In all patients, there was a moderate improvement in asthenia.

DISCUSSION

Our hypothesis that a small increase in circulating

Table II. *Biochemical findings in patients with type VI OI at baseline (n = 10)*

Patient Id	OI 389	OI 60	OI 298	OI 343	OI 93	OI 94	OI 162	OI 122	OI 123	OI 63	M ± SD
PTH pg/mL	11.2	5.8	13.9	5.2	14.2	6.4	8.6	9.3	10.7	7.6	9.3 ± 3.2
Bone ALP μg/L	87.3	102.8	84.1	144.5	17.2	38.0	52.9	81.3	76.3	97.3	78.1 ± 35.6
Oc nmol/L	8.3	5.9	7.7	9.1	7.1	7.6	8.5	7.8	8.8	6.9	7.8 ± 0.9
P1NP ng/mL	238	482	217	631	137	221	260				312 ± 176*
DKK1 pmol/L	23.5	19.7	22.0	26.2	16.3	34.8	23.8				23.7 ± 5.8*
Sclerostin pmol/L	28.0	24.9	40.3	14.5	25.4	25.6	16.1				25.0 ± 9.3*
β CTx ng/mL	0.62	0.66	0.65	1.12	0.38	0.95	0.79	0.88	0.98	0.45	0.75 ± 0.24
Iron μmol/L	16.0	9.2	7.1	6.4	17.9	8.9	12.9	8.7	11.5	9.4	10.7 ± 3.8
Ferritin pmol/L	65.2	44.9	33.7	11.2	112.3	67.4	78.6	47.2	38.2	22.5	52.1 ± 23.6

**7 patients*

PEDF levels might correct the bone phenotype in OI type VI proved incorrect, at least in the ways we supposed. PEDF levels did increase as desired but returned immediately to undetectable values and consequently, bone metabolism markers and BMD did not change during the treatment period.

We could speculate that more frequent infusions over time with greater quantities of plasma or daily administration of PEDF could achieve better results. However, the only effect found was a significant decrease in DKK1 and a non-significant increase in P1NP levels the day after the first transfusion. This DKK1 behaviour could clarify the relationship between PEDF and the Wnt/β-catenin signalling pathway (8). However, besides the lack of persistence over time of circulating levels of PEDF, the action time in the early differentiation phase of osteoblast and skeletal development may be important. We can hypothesize that small quantities may be sufficient to get an action in the early stages of life (i.e., in the fetal/neonatal period), but not in later stages (9). Finally, bioavailability could be another essential factor and the action rather than endocrine could be paracrine or autocrine. The PEDF action mode is still unclear. In vitro, the addition to the culture medium does not always result in the desired effects, and in animal models, exogenous PEDF given to Serpinf1 $^{-/-}$ mice gave rise to different outcomes (10, 11).

The main limitation of our study is the small number of patients that completed it; this was because type VI OI is an extremely rare disease and the number of patients, which was sufficient at the time

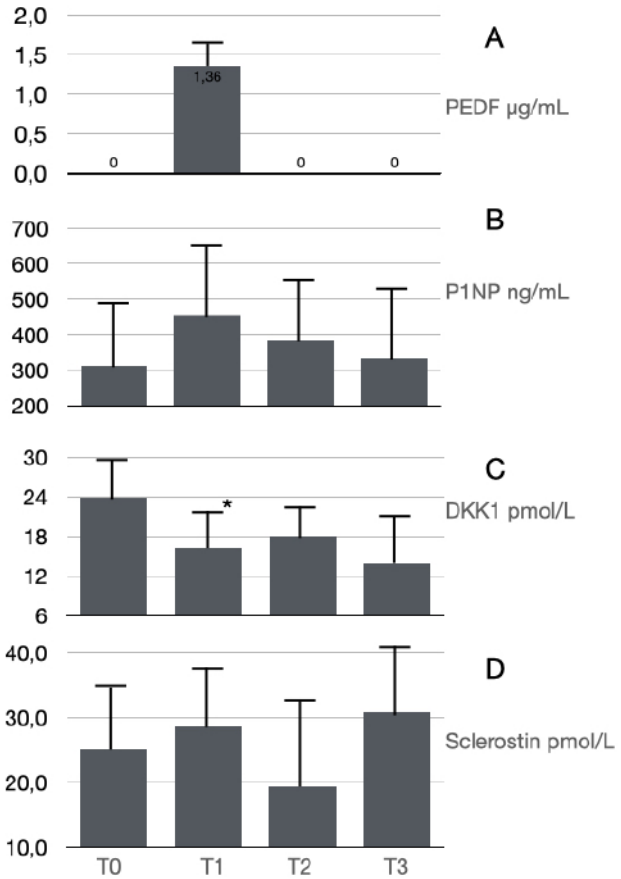

Fig. 3. *Biochemical determinations before, 1, 2 and 7 days after the first plasma infusion in 5 patients. **A)** PEDF µg/mL; **B)** P1NP ng/mL; **C)** DKK1 pmol/L; **D)** Sclerostin pmol/L. T0: before the 1st plasma infusion; T1: 1 day after the 1st plasma infusion; T2: 2 days after the 1st plasma infusion; T3: 7 days after the 1st plasma infusion.*
**Significantly decreased (p = 0.05) respect to T0.*

Table III. *Biochemical findings in the 4 Patients with type VI OI who completed the study (M ± SD)*

	T0	T4	T5	T6	T7	T8	T9	T10
PTH pg/mL	9.0 ± 4.2	11.1 ± 6.6	12.3 ± 4.8	11.7 ± 4.7	11.5 ± 6.0	13.4 ± 6.1	13.6 ± 6.7	13.8 ± 4.5
Bone ALP µg/L	104.5 ± 27.6	95.7 ± 13.8	106.7 ± 33.4	103.0 ± 32.4	104.7 ± 34.1	100.7 ± 36.0	125.0 ± 46.8	107.7 ± 51.8
Oc nmol/L	7.75 ± 1.36	9.83 ± 4.93	10.20 ± 3.65	10.55 ± 3.24	8.73 ± 3.27	8.90 ± 3.00	8.23 ± 3.58	10.50 ± 2.84
P1NP ng/mL	392 ± 199	374 ± 115	444 ± 177	378 ± 107	447 ± 164	357 ± 100	385 ± 126	406 ± 266
DKK1 pmol/L	22.9 ± 2.7	24.7 ± 1.9	19.3 ± 4.1	25.3 ± 10.5	22.6 ± 6.5	24.3 ± 9.7	25.8 ± 3.2	22.1 ± 4.2
Sclerostin pmol/L	27.6 ± 12.9	24.8 ± 12.9	23.9 ± 5.0	39.4 ± 19.4	22.7 ± 10.0	25.1 ± 10.7	21.5 ± 10.3	23.0 ± 16.6
β CTx ng/mL	0.76 ± 0.24	0.72 ± 0.15	0.87 ± 0.33	0.85 ± 0.28	0.84 ± 0.39	0.82 ± 0.34	0.72 ± 0.20	0.67 ± 0.19
Iron µmol/L	9.5 ± 4.5	11.2 ± 8.5	8.0 ± 2.9	9.5 ± 4.8	6.5 ± 3.9	5.7 ± 1.5	5.0 ± 1.8	9.5 ± 5.7
Ferritin pmol/L	38.8 ± 22.5	43.2 ± 35.2	38.8 ± 32.9	37.6 ± 20.7	41.0 ± 35.8	39.9 ± 28.1	29.2 ± 21.8	42.1 ± 35.7

T0: before the 1st plasma infusion; T4, before 2nd plasma infusion, T5 - 3rd, T6 - 4th, T7 - 5th, T8 - 6th, T9 - 7th; T10: 6 months after the last plasma transfusion.

of inclusion, subsequently declined due to various problems. In this regard, our small sample size limits the conclusions drawn from our results.

In conclusion, plasma infusion at the doses and intervals used in our study does not help modify bone metabolic markers and BMD in type VI OI patients. Replication of our study protocol in a multicenter with a larger number of subjects could be an option; however, further studies with other replacement therapy approaches or totipotent mesenchymal cell therapies are needed.

Conflict of interests:

The authors have no conflicts of interest to declare.

ACKNOWLEDGEMENTS

The authors are grateful to the *Associazione Italiana Osteogenesis Imperfetta* (As.It.O.I.) for their continued interest and support. We also thank the children and parents who took part in the study. Finally, the authors thank the LURM (Laboratorio Universitario di Ricerca Medica) Research Center, University of Verona, and especially Dr Eliana Amato for performing some biochemical analyses.

REFERENCES

1. Marini JC, Forlino A, Bächinger HP, et al. Osteogenesis imperfecta. Nat Rev Dis Primers 2017; 3:17052.
2. Glorieux FH, Ward LM, Rauch F, Lalic L, Roughley PJ, Travers R. Osteogenesis imperfecta type VI: a form of brittle bone disease with a mineralization defect. J Bone Miner Res 2002;17(1):30-8.
3. Becker J, Semler O, Gilissen C, et al. Exome sequencing identifies truncating mutations in human SERPINF1 in autosomal-recessive osteogenesis imperfecta. Am J Hum Genet 2011; 88(3):362-71.
4. Venturi G, Gandini A, Monti E, et al. Lack of expression of SERPINF1, the gene coding for pigment epithelium-derived factor, causes progressively deforming osteogenesis imperfecta with normal type I collagen. J Bone Miner Res 2012; 27(3):723-8.
5. Rauch F, Husseini A, Roughley P, Glorieux FH, Moffatt P. Lack of circulating pigment epithelium-derived factor is a marker of osteogenesis imperfecta type VI. J Clin Endocrinol Metab 2012; 97(8):E1550-6.
6. Trejo P, Palomo T, Montpetit K, et al. Long-term follow-up in osteogenesis imperfecta type VI. Osteoporos Int 2017; 28(10):2975-2983.
7. Al-Jallad H, Palomo T, Moffatt P, Roughley P, Glorieux FH, Rauch F. Normal bone density and fat mass in heterozygous SERPINF1 mutation carriers. J Clin Endocrinol Metab 2014; 99(11):E2446-50.
8. Li F, Cain JD, Tombran-Tink J, Niyibizi C. Pigment epithelium derived factor regulates human Sost/Sclerostin and other osteocyte gene expression via the receptor and induction of Erk/GSK-3beta/beta-catenin signaling. Biochim Biophys Acta Mol Basis Dis 2018; 1864(10):3449-3458.
9. Li F, Song N, Tombran-Tink J, Niyibizi C. Pigment epithelium derived factor suppresses expression of Sost/Sclerostin by osteocytes: implication for its role in bone matrix mineralization. J Cell Physiol 2015; 230(6):1243-9.
10. Rajagopal A, Homan EP, Joeng KS, Suzuki M, Bertin T, Cela R, et al. Restoration of the serum level of SERPINF1 does not correct the bone phenotype in Serpinf1 null mice. Mol Genet Metab 2016; 117(3):378-82.
11. Belinsky GS, Sreekumar B, Andrejecsk JW, et al. Pigment epithelium-derived factor restoration increases bone mass and improves bone plasticity in a model of osteogenesis imperfecta type VI via Wnt3a blockade. FASEB J 2016; 30(8):2837-48.

LETTER TO THE EDITOR

Banded and bonded rapid maxillary expansion: a cephalometric evaluation

L. Giannini[1], G. Galbiati[1], E. Del Rosso[1,2], FMR. Parisi[1*], L. Esposito[1,2] and C. Maspero[1,2]

[1]Department of Biomedical, Surgical and Dental Sciences, School of Dentistry, University of Milan, Milan, Italy; [2]Fondazione IRCCS Cà Granda, Ospedale Maggiore Policlinico, Milan, Italy

Received November 5, 2021 – Accepted April 1, 2022

To the Editor,

The medium palatal suture is still in a state of synfibroses up to the age of 16, after which a slow ossification process begins that completes around the twenty-fifth year of age. This last information has based on the possibility of palatal expansion in young adult patients (1). In the etiology of the transverse superior maxillary deficit, the hereditary factory has a primary role. It is necessary to add extrinsic etiological factors, like oral health and oral habits (suction, oral breathing, atypical swallowing) (2-4). The complexity of these factors makes typical malocclusions clinically manifested as mono or bilateral crossbite and constriction or high-arched palate (2). In addition, a nasal septum deviation is frequently present (5).

Orthopaedic expansion of the palatal suture is the gold-standard therapy in cases of maxillary transverse constriction (6). Among the most used expanders are those with bands and those with bite-block. The Hyrax expander has two or four anchor bands at the level of the teeth abutment and a median 9 mm screw. It consists of a central double guide screw, without mucoid support, with two or four arms to which the orthodontic bands for the anchor teeth are welded. Unloading the force on the anchor teeth does not irritate the palate. It can be anchored on the first permanent molars or deciduous second molars. The expander with bite blocks has been proposed in cases of transverse hypoplasia of the maxilla associated with skeletal openbite. The bite blocks are cemented on the teeth and act as a bite block so that the posterior teeth undergo intrusive pressure due to the elastic return of the soft tissues. The tendency to open the bite is therefore checked (7). Different effects have been described on the three planes of space following the use of these two types of appliances.

This study aimed to evaluate cephalometric parameters on latero-lateral teleradiographs before and after treatment with the rapid expander of the palate and with bite blocks (Fig. 1, 2). In addition, the significant differences in the three planes of space were evaluated after the activation of the two devices to verify in which clinical situations one is more suitable than the other.

MATERIALS AND METHODS

This prospective study involved 60 patients (30 males and 30 females) between the ages of 6 and 15 who presented lateral-posterior crossbite due to hypoplasia of the upper jaw. The research was approved by the research project of Fondazione IRCCS Cà Granda, O.U 420/425. N. 3 2018. Informed consent was obtained from all patients (Table I).

Keywords: Maxillary transverse deficiency; Bite-block maxillary expander; Rapid Maxillary expansion; Hyrax expander

*Corresponding Author:
Dr Francesca Maria Rita Parisi
Department of Biomedical, Surgical and Dental Sciences,
School of Dentistry, University of Milan,
Via dell'Unione 8,
20122 Milan, Italy
e-mail: francescamr.parisi@gmail.com

0393-974X (2022)

The transverse deficit was determined by calculating the difference in distance between the mesial and distal cusps of the right and lower left molars and the distance between the central pits between the right and upper left molars.

The patients were randomly divided into two groups (15 males and 15 females each). The two groups were homogeneous by age: I group = 9.4 average years, II group = 9.4 average years. The initial cephalometric values are described in Table 2. The amount of the cross discrepancy was similar in the two groups. The first group was treated with a Hyrax rapid palatal expander cemented on the first upper molars. The second group was cemented with a rapid palate expander with bite blocks.

Both devices were left in situ for 6 months and activated with a standardized expansion protocol consisting of two screw turns per day (1 revolution = 0.25 mm) until crossbite correction was obtained. The average expansion amounted to 7.5 mm at the end of the 15 days. Two cranial teleradiographies were performed in latero-lateral projection by the same radiology technician and with the same radiological equipment, one before starting the therapy and one after removing the appliance. Cephalometric measurements were then made according to the Milan School of Orthodontics analysis, a validated analysis (Fig. 3) (4).

Cephalograms were taken by the same technician

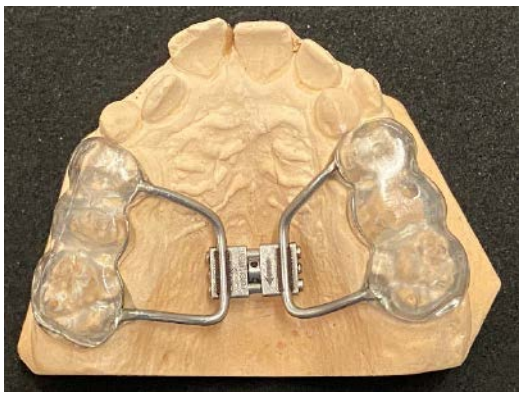

Fig. 1. *Expander with bite blocks*

Fig. 2. *Expander with bands*

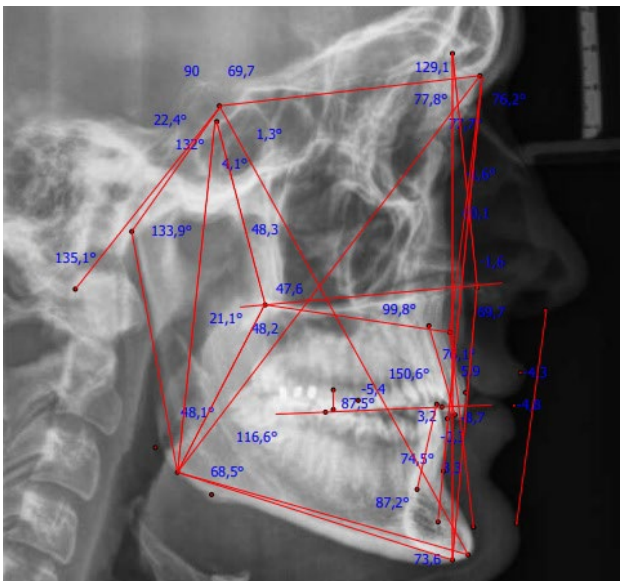

Fig. 3. *Cephalometric measurements according to the Milan School of Orthodontics*

Table I. *Partecipant inclusion and exclusion criteria*

Inclusion Criteria	Exclusion Criteria
absence of previous orthodontic treatments	congenital dental or skeletal anomalies
deciduous or mixed dentition	previous orthodontic treatments
dynamic phase of growth	patients at the end of growth
absence of skeletal or dental abnormalities	patients who frequently missed appointments
presence of crossbite associated with maxillary hypoplasia	

with the same machine and manually traced by one operator, and verified for landmark location and anatomic contours by a second operator. The measurements of the first operator [L.G.] were controlled by a second operator [G.G.] to reduce intra- and inter-operator variability. Any disagreements were solved by retracing the landmark or structure to the mutual satisfaction of both operators. In order to exclude intra-operator error, each measurement was repeated by the same operator after 7 days.

Lateral cephalograms were traced by using acetate papers. A lateral cephalogram was taken before treatment (T0), and a second one was taken after retention (T1). The mean values between the first and second measurements were considered. The cephalometric parameters considered are the following: SNA = sagittal position of the upper jaw; SNB = sagittal position of the jaw; ANB = skeletal class; SN-SNP.SNA = upper jaw inclination; SN-GoGn = inclination of the lower maxilla.

A statistical analysis of the values was then conducted by identifying the mean and standard deviations and conducting the t-test for the paired samples ($p < 0.05$). The error percentage (PE) was calculated with the Dahlberg formula ($ME=\sqrt{\Sigma d^2/2n}$), where n = number of subjects and d = difference between two measurements). Errors for linear measurements are between 0.3 and 0.6.

All subjects gave informed, signed consent to participate in the study or informed the family or guardian gave written consent in the case of children or deceased.

RESULTS

There was a statistically significant difference between the values detected before the expansion and those after the removal of the appliance (Table III and Table IV). In the group of patients treated with Hyrax RME, there were no statistically significant changes in the sagittal position of the maxilla, mandible, and skeletal class, as described by Farronato et al. (6). In

Table II. *Cephalometric values of the two groups at the beginning.*

	SNA	SNB	ANB	SN-SNP.SNA	SN-GoGn
RME bonded	79,73	77,26	2,46	9,41	36,05
RME	79,20	77,59	1,61	9,10	37,5
Difference	0,52	-0,33	0,85	0,31	-1,45

Table III. *Cephalometric values pre and post-expansion with RME appliance.*

	SNA	**SNB**	**ANB**	**SN-SNP.SNA**	**SN-GoGn**
PRE-EXPANSION					
Mean	79,20	77,59	1,61	9,10	37,5
SD	2,97	2,05	0,68	2,10	1,00
t-test	NS	NS	NS	S	NS
POST-EXPANSION					
Mean	80,60	78,30	2,30	11,30	38,45
SD	2,98	2,93	0,76	2,50	2,99
t-test					

Table IV. *Cephalometric values pre and post-expansion with RME bonded appliance.*

	SNA	**SNB**	**ANB**	**SN-SNP.SNA**	**SN-GoGn**
PRE-EXPANSION					
Mean	79,73	77,26	2,46	9,41	36,05
SD	1,79	1,61	0,73	2,39	4,61
t-test	NS	S	NS	NS	S
POST-EXPANSION					
Mean	79,79	77,53	2,26	9,39	33,41
SD	1,94	1,86	0,82	2,41	4,61
t-test					

addition, no significant changes were found in the values of SNA, ANB and SN-SNP. In the group of patients treated with RME bonded appliance, there was a statistically significant increase in SNB angle and a reduction of the inclination of the lower maxilla.

DISCUSSION

In this study, the different effects on the space planes were highlighted using the expander with bite-bands or blocks. Both appliances have been similarly effective in obtaining the transverse disjunction of the upper jaw. Regarding the vertical and sagittal dimensions, the two devices showed different effects: in patients of the RME Hyrax group, there were no significant changes in the sagittal position of the maxilla, according to the studies performed by Da Silva et al.

By contrast, there was a statistically significant increase in the cranial-spinal angle and a non-statistically significant increase in the mandibular cranial angle due to a post-rotation of the bi-spinal plane in agreement with the studies published (7-9). In addition, there was also an increase in the cranio-mandibular angle in this group of patients.

This effect, generally due to the vestibular inclination of the lateral-posterior dental elements, is particularly negative in patients with increased anterior vertical dimension. In this skeletal pattern, the use of an expander with bite blocks may be indicated for greater control at the level of the anterior vertical dimension. The results obtained in patients treated with a bonded expander, according to McNamara, show an increase in the SNB angle due to mandibular advancement. This effect is explained because the jaw was forced due to maxillary hypoplasia before expansion. In fact, according to McNamara, following the rapid expansion of the upper jaw, there is a mandibular advancement and improvement of occlusal relationships.

The same dental elements play an important role in determining this postural improvement of the jaw and a change in the relationship between the two jaws. All this is evident during the six / twelve months after removing the RPE (10-12).

There was also a statistically significant decrease in the SN-GoGn angle in the group of patients treated with a bonded expander. These results agree with the McNamara studies, which state that the expander acts as a bite-block at the posterior level and therefore allows the control of the vertical anterior dimension due to the stimulation effect on the soft tissues.

It is possible to obtain the transverse disjunction of the palatal suture with both devices. In patients with increased anterior vertical dimension, it was observed that the palatal expander bonded with bite blocks allows better control in the vertical plane.

Palatal expansion can be obtained in all patients regardless of their skeletal class and vertical dimension. Furthermore, the early treatment of the

transverse hypoplasia of the upper jaw allows the restoration of the correct stomatognathic evolutionary parabola. Therefore, palatal expansion is a valid technique effective at restoring the correct transversal dimension of the upper jaw and correcting anomalies at both dental and respiratory levels.

Conflicts of Interest

The authors declare no conflict of interest.

Author Contributions

All authors actively participated in all phases of the manuscript. All authors have read and agreed to the published version of the manuscript.

REFERENCES

1. Farronato G, Carletti V, Giannini L, Farronato D, Maspero C. Juvenile idiopathic arthritis with temporomandibular joint involvement: Functional treatment Eur J Paediatr Dent 2011; 12(2):131-134.
2. Rosa M, Lucchi P, Mariani L, Caprioglio A. Spontaneous correction of anterior crossbite by RPE anchored on deciduous teeth in the early mixed dentition. Eur J Paediatr Dent 2012; 13(3):176-80.
3. Contaldo M, Lucchese A, Lajolo C, et al. The Oral Microbiota Changes in Orthodontic Patients and Effects on Oral Health: An Overview. J Clin Med 2021; 10(4):780.
4. Maspero C, Cavagnetto D, Abate A, Cressoni P, Farronato M. Effects on the Facial Growth of Rapid Palatal Expansion in Growing Patients Affected by Juvenile Idiopathic Arthritis with Monolateral Involvement of the Temporomandibular Joints: A Case-Control Study on Posteroanterior and Lateral Cephalograms. J Clin Med 2020; 9(4):1159.
5. Abate A, Cavagnetto D, Fama A, Maspero C, Farronato G. Relationship between Breastfeeding and Malocclusion: A Systematic Review of the Literature. Nutrients 2020; 12(12):3688.
6. Farronato G, Giannini L, Galbiati G, Sesso G, Maspero C. Orthodontic-surgical treatment: Neuromuscular evaluation in skeletal Class II and Class III patients. Progress in Orthodontics 2021; 13(3):226-236.
7. Haas AJ. Rapid expansion of the maxillary dental arch and nasal cavity by opening the midpalatal suture. Angle Orthodontist 1961; 31:73-90.
8. Haas AJ. Palatal expansion: just the beginning of dentofacial orthopaedics. Am J Orthod 1970; 57:219-55.
9. Maspero C, Giannini L, Riva R, Tavecchia MG, Farronato G. Nasal cycle evaluation in 10 young patients: Rhynomanometric analysis [Valutazione del ciclo nasale di died giovani soggetti: Indagine rinomanometrica] (2009) Mondo Ortodontico 2009; 34(5):263-8.
10. Lanteri V, Farronato M, Ugolini A, et al. Volumetric Changes in the Upper Airways after Rapid and Slow Maxillary Expansion in Growing Patients: A Case-Control Study. Materials 2020; 13:2239.
11. Fastuca R, Perinetti G, Zecca PA, Nucera R, Caprioglio A. Airway compartments volume and oxygen saturation changes after rapid maxillary expansion: a longitudinal correlation study. Angle Orthod 2015; 85(6):955-61.
12. Maspero C, Abate A, Cavagnetto D, et al. Operculectomy and spontaneous eruption of impacted second molars: a retrospective study. J Biol Regul Homeost Agents 2019; 33(6):1909-12.

LETTER TO THE EDITOR

Etomidate alleviates lung injury in sepsis rats through NF-κB signaling pathway

S-F. Sun[#], X-Q. Shao[#*], X-S. Xu, Y-Y. Wang, Y. Lin and F-Y. Liu

Department of Anesthesiology, Weifang Maternal and Child Health Hospital, Weifang, China

[#]These Authors contributed equally to this work

To the Editor,

Sepsis is the first cause of diseases in the intensive care unit, and its morbidity rate and mortality rate (about 50%) are increasing year by year. Sepsis mainly refers to the systemic inflammatory responses caused by pathogenic bacteria or toxins released after invasion into the body. The main target organ of sepsis is the lungs, and acute lung injury (ALI) is a severe respiratory disease that usually occurs in the early stage of sepsis (1). According to epidemiological studies, ALI is a significant public health problem worldwide, bringing considerable challenges to clinicians (2-4). In addition, lipopolysaccharide (LPS) is a component of the gram-negative bacterial membrane, which can cause an inflammatory response, immune dysfunction, shock and even death (5, 6).

Moreover, LPS can activate signal transduction pathways mediated by inflammatory mediators. The animal model of ALI is usually established *via* intraperitoneal injection of LPS. Etomidate is an imidazole derivative and an important short-acting non-barbiturate intravenous general anaesthetic used in the clinic, which is characterized by the ability to keep the stability of the cardiovascular system, short infusion half-life and elimination half-life, and ability to quickly pass through the blood-brain barrier to exert a hypnotic affect. In addition to its anaesthetic effect, etomidate possesses various biological effects, reducing the body's oxygen consumption, dilating cerebral blood vessels, reducing intracranial pressure, and protecting against ischemic-hypoxic brain damage (7-9). Furthermore, it reduces the damage of ischemia-reperfusion to the body by improving microcirculation disorders, protecting vascular endothelial cells, keeping cell membrane stability, reducing the production of free radicals, inhibiting free radical-induced lipid peroxidation, and stimulating the antioxidant ability of cells. In the present study, the protective effect of etomidate against lung injury in sepsis rats and its mechanism were explored with the NF-κB signalling pathway as an entry point to provide a theoretical basis for the prevention and treatment of sepsis-induced ALI.

MATERIALS AND METHODS

Laboratory animals

A total of 30 male Sprague Dawley (SD) rats (8-10 weeks old, 200-250 g on average) were fed at 23-25°C under 40-50% humidity. This study was approved by the Animal Ethics Committee of Weifang Medical University Animal Center.

Animal grouping and drug administration

After adaptive feeding for 1 week, 30 SD rats were divided into 3 groups using a random number table. All SD

Keywords: etomidate, sepsis, lung injury, NF-κB signalling pathway

**Corresponding Author:*
Dr Xiaoqing Shao,
Department of Anesthesiology,
Weifang Maternal and Child Health Hospital, Weifang, China
407 Qingnian Road, Weicheng District,
Weifang, Shandong 261021, China
e-mail: shaoxiaoqing@hdu.edu.cn

0393-974X (2022)

rats were deprived of food but had access to water for 12 h before the experiment. In the control group (n=10), 200 μL of normal saline was intraperitoneally injected. The rats were weighed in the model group (n=10), and LPS was intraperitoneally injected (50 mg/kg) to establish the rat model of sepsis-induced lung injury. In the etomidate group (n=10), etomidate was intraperitoneally injected (40 μg/kg) at 15 min before modelling.

Preparation of bronchoalveolar lavage fluid (BALF)

After anaesthesia, the rats were dissected in each group, and 2 mL of blood was drawn from the abdominal artery, of which 1 mL was anticoagulated with heparin sodium, and the serum was separated from the remaining 1 mL of blood for later use. The thoracic cavity was cut open, bilateral lung hili were clamped, and bilateral main bronchi were ligated. Then the needle was inserted from the proximal end of the left main bronchus, and the needle guard was indwelled. Next, 15 mL of pre-cooled sterile heparin sodium saline was infused into the left lung 3 times (3-5 times per time), and BALF was recycled. The two lungs were cut off at the ligation site in each group for subsequent detection of indexes.

Pathological changes in lung tissues

The inferior lobe of the right lung was fixed in 4% paraformaldehyde for 24 h in each group, decalcified at room temperature, dehydrated, embedded, deparaffinized, stained, transparentized and sealed. Then the sections were observed under an upright biological microscope to observe the pathological changes in lung tissues, and the observation results were recorded.

Detection of lung function indexes

The arterial blood gas indexes pH, partial pressure of oxygen (PaO_2) and base excess (BE) value of 1 mL of blood anticoagulated with heparin sodium were detected using an animal electrolyte and blood gas analyzer. The superior lobe of the right lung was taken in each group, the tissue fluid and blood on the surface of lung tissues were sucked dry using filter paper, and the wet weight (W) of lung tissues was measured using an analytical balance. After the samples were dried in an incubator at 65°C for 48-72 h and cooled to room temperature in a dryer, the dry weight (D) of lung tissues was measured 3 times. Then the W/D ratio of lung tissues was calculated, and the degree of pulmonary oedema was evaluated based on the lung water content.

Detection of protein content and neutrophil count in BALF

BALF was centrifuged in each group, and the supernatant was used to detect the protein content and cytokines, while the sediment was used to detect the neutrophil count. The protein content in BALF was determined using BCA: 20 μL of BALF was added into each well of a 96-well plate, with 3 replicates for each sample, and 200 μL of BCA working solution was also added into each well, followed by incubation at 37°C for 20-30 min. After equilibration to room temperature, the absorbance value was measured at 560 nm using a microplate reader, and the standard curves were plotted, based on which the protein content in BALF was detected. The neutrophil count in BALF was detected using a haematology analyzer.

Detection of the content of inflammatory cytokines in BALF and serum

The levels of inflammatory cytokines TNF-α, IL-1β and IL-6 in BALF and serum were determined *via* ELISA in each group: The blank wells, control wells and sample wells were set on an ELISA plate, and 100 μL of diluent, standards and samples were added into the corresponding wells, followed by incubation in a wet box at 37°C for 2 h. After the liquid in each well was discarded, 100 μL of biotin-labelled antibody working solution was added to each well, followed by incubation in the wet box at 37°C for 1 h. After the liquid in each well was discarded, the plate was washed 5 times (3 min per time), and 100 μL of horseradish peroxidase (HRP)-labelled secondary antibody working solution was added to each well, followed by incubation in the wet box at 37°C for 1 h. After that, the liquid in each well was discarded, the plate was washed again 5 times (3 min per time), and 90 μL of substrate solution was added to each well, followed by colour development at room temperature for 10-15 min in the dark. Then the reaction was terminated using 50 μL of stop buffer added to each well, and the optical density value of each well was measured at a wavelength of 450 nm using the multifunctional microplate reader, based on which the levels of inflammatory factors TNF-α, IL-1β and IL-6 in BALF and serum were analyzed.

Detection of MPO and SOD activity and MDA level in lung tissues

According to the instructions, the grinding solution of lung tissues was added with o-dianisidine, xanthine oxidase and thiobarbituric acid reagents, and the blank group and control group were set up. The absorbance values of lung tissue samples, negative control and standards were measured using an ultraviolet spectrophotometer, and the MPO and SOD activity and MDA level in lung tissues were determined according to the formula.

Detection of mRNA expressions of IRAK1, TRAF6, NF-κB and IκB

The lung tissues in each group were cut into pieces and fully ground with liquid nitrogen. The total RNA was extracted from lung tissues and reversely transcribed into cDNA. The RT system consisted of 2 μL of 5×PrimeScript RT Master Mix (Perfect Real Time), 5 μL of total RNA and 3 μL of RNase-free dH_2O. The primers were shown in Table I with GAPDH as an internal reference. According to the Ct value of each gene, the relative mRNA expression levels of IRAK1, TRAF6, MyD88, NF-κB and IκB in lung tissues were analyzed using the $2^{-\Delta\Delta Ct}$ method in each group.

Expressions of NF-κB signalling pathway-related proteins in lung tissues

The lung tissues were fully ground with liquid nitrogen and lysed with RIPA lysis buffer, from which the protein was extracted, and its content was determined using the BCA method. After sodium dodecyl sulphate-polyacrylamide gel electrophoresis (SDS-PAGE) in each group, 40 μg of total proteins were transferred onto an activated polyvinylidene fluoride (PVDF) membrane (Millipore, Billerica, MA, USA) *via* wet transfer process, and the membrane was sealed with blocking buffer [Tris-buffered saline with Tween®20 (TBST) containing 5% skim milk powder] at room temperature (18-22°C) for 1-2 h and washed with TBST for 3 times (5 min per time). Then the proteins were incubated with a diluted primary

Table I. *Primer sequences in fluorescence quantitative PCR.*

Gene	Primer sequence	GenBank ID
GAPDH	F: 5'-AAG GTC GGT GTG AAC GGA TTT-3' R: 5'-AGA TGA TGA CCC TTT TGG CTA-3'	NM_017008.4
IRAK1	F: 5'-TTC CAC TCC CTG TTT CCC TC-3' R: 5'-AAC CAC CCT CTC CAA TCC TG-3'	NM_001127555.1
TRAF6	F: 5'-ATG CTG GTC ATT CAT C-3' R: 5'-GTA GGA GAT TGG GAA-3'	NM_001107754.2
NF-κB p65	F: 5'-GAT TGA AGA GAA GCG CAA AA-3' R: 5'-CAG AAG TTG AGT TTC GGG TA-3'	NM_007393.5
IκB	F: 5'-TGA AGG ACG AGG AGT ACG AGC-3' R: 5'-TGC AGG AAC GAG TCT CCG T-3'	NM_053355.2

antibody solution of IRAK1 (1:2000), TRAF6 (1:2000), NF-κB p65 (1:1000), p-p65 (1:5000) and IκB (1:10000) at 4°C overnight, and the membrane was washed with TBST for 3 times (5 min per time). The proteins were incubated again with diluted secondary antibody solution (1:5000) at room temperature for 1 h, and the membrane was washed with TBST 3 times (5 min per time), followed by colour development using ECL solution for 1 min. The experimental results were recorded using a multifunctional imager. Finally, the ratio of the grey value of IRAK1, TRAF6, NF-κB, p-p65 and IκB protein bands to that of GAPDH was analyzed using ImageJ, and the changes in expressions of NF-κB signalling pathway-related proteins in lung tissues were detected in each group.

Statistical analysis

Statistical Product and Service Solutions (SPSS) 22.0 software (IBM, Armonk, NY, USA) was used for statistical analysis of experimental data, and the analysis results were expressed as mean ± standard error. Differences between the two groups were analyzed by using the Student's t-test. Comparison between multiple groups was made using a one-way ANOVA test followed by Post Hoc Test (Least Significant Difference). $P<0.05$ was considered to be statistically significant, and $P<0.01$ indicated great statistical significance.

RESULTS

Behavioural observation in the model group

The rat model of sepsis-induced lung injury was established *via* intraperitoneal injection of LPS, after which the behaviours of rats were observed. It was found that the rats in the model group had mental depression, shivering, upright hair, anorexia, and significantly increased respiratory frequency and nasal secretions, indicating the successful establishment of the rat model of sepsis-induced lung injury.

Effects of etomidate on lung function of rats with sepsis-induced lung injury

The lung tissues in each group were fixed, sliced into sections and stained with HE, and the pathological changes in lung tissues were compared among the three groups. Compared with the control group, the rats in the model group had a thickening of the alveolar wall, disappearance of partial alveolar spaces and inflammatory cell infiltration among tissues. Compared with those in the model group, the degree of lung tissue injury was reduced, the inflammatory cell infiltration gradually disappeared, and the alveolar wall thickness became smaller in the etomidate group. It can be seen that etomidate reduces the degree of LPS-induced lung injury. The lung function of rats was evaluated in each group by comparing the W/D ratio of lung tissues, pH, PaO_2 and BE value. As shown in Table II, the W/D ratio of lung tissues and BE value obviously rose ($P<0.05$), while pH and PaO_2 obviously declined in the model group compared with those in the control group ($P<0.05$). Compared with those in the model group, the W/D ratio of lung tissues and BE value obviously declined ($P<0.05$), while pH and PaO_2 obviously rose in the etomidate group, with statistically significant differences ($P<0.05$). It can be seen that etomidate can reduce the degree of oedema and improve the lung function of rats with LPS-induced lung injury.

Table II. *Comparison of lung function indexes in each group (χ±s, n=10).*

Group	W/D	pH	PaO_2 (mmHg)	BE (mmol/L)
Control group	4.633±0.078	7.389±0.030	109.641±4.618	-8.160±0.871
Model group	7.879±0.094*	7.188±0.305*	84.969±1.073*	-3.256±0.123*
Etomidate group	5.562±0.141*#	7.306±0.065*#	97.429±4.605*#	-5.64±0.076*#

*Note: * a significant difference vs. control group, # a significant difference vs. model group*

Effects of etomidate on protein content and neutrophil count in BALF

The protein content and neutrophil count in BALF were determined using the BCA method and haematology analyzer, respectively. As shown in Table III, the protein content and neutrophil count in BALF evidently rose in the model group compared with those in the control group (P<0.5). Compared with those in the model group, the protein content and neutrophil count in BALF evidently declined in the etomidate group, with statistically significant differences (P<0.5).

Effects of etomidate on levels of inflammatory cytokines in BALF and serum

The levels of inflammatory cytokines TNF-α, IL-1β and IL-6 in BALF and serum were determined through ELISA. The results showed that the levels of TNF-α, IL-1β and IL-6 in BALF and serum were markedly higher in the model group than those in the control group (P<0.5), while they were markedly lower in the etomidate group than those in the model group, with statistically significant differences (P<0.5) (Table IV). It can be inferred that etomidate inhibits the production and release of inflammatory cytokines in BALF and serum in sepsis-induced lung injury.

Effects of etomidate on oxidative stress indexes MPO and SOD activity and MDA level

The changes in MPO and SOD activity and MDA level in serum were detected in each group using o-dianisidine, xanthine oxidase and thiobarbituric

Table III. *Comparison of protein content and neutrophil count in BALF ($\bar{\chi}$±s, n=10)*

Group	Protein content (μg/mL)	Neutrophil count ($\times10^8$/L)
Control group	278.415±6.914	2.620±0.410
Model group	644.555±14.874*	14.477±3.779*
Etomidate group	444.943±9.228*#	7.323±8.724*#

*Note: * a significant difference vs. control group, # a significant difference vs. model group*

Table IV. *Content of inflammatory cytokines in BALF and serum ($\bar{\chi}$±s, n=10).*

Group	TNF-α (pg/mL)		IL -1β (pg/mL)		IL-6 (pg/mL)	
	BALF	Serum	BALF	Serum	BALF	Serum
Control group	55.318±2.692	55.143±2.161	4.550±0.256	3.621±0.200	41.263±2.113	49.245±1.779
Model group	139.460±1.863*	152.276±14.042*	21.548±1.526*	22.394±3.187*	136.413±3.385*	140.172±2.087*
Etomidate group	103.091±1.149*#	109.961±18.877*#	9.654±1.090*#	10.564±1.635*#	76.891±2.143*#	85.189±2.122*#

*Note: * a significant difference vs. control group, # a significant difference vs. model group*

acid reagents, respectively. The results revealed that the model group had lower SOD activity and higher MPO activity and MDA levels than the control group, and there were statistically significant differences (P<0.5). The Etomidate group had higher SOD activity and lower MPO activity and MDA level than the model group, and there were statistically significant differences (P<0.5) (Table V). The above findings indicate that etomidate reduces the oxidative stress response in lung injury rats.

Effects of etomidate on mRNA expressions of IRAK1, TRAF6, NF-κB and IκB in lung tissues

The total RNA was extracted from lung tissues and reversely transcribed into cDNA, followed by real-time PCR amplification so as to detect the changes in the relative mRNA expressions of IRAK1, TRAF6, NF-κB and IκB in lung tissues. As shown in Fig. 1, the mRNA expressions of IRAK1, TRAF6, NF-κB and IκB were remarkably increased in the model group compared with those in the control group (P<0.05), while they were remarkably decreased in the etomidate group compared with those in model group (P<0.05). The above results demonstrate that etomidate suppresses the mRNA expressions of IRAK1, TRAF6, NF-κB and IκB in rats with LPS-induced lung injury.

Effects of etomidate on expressions of NF-κB signalling pathway-related proteins in lung tissues

The expressions of NF-κB signalling pathway-related proteins IRAK1, TRAF6, NF-κB p65, p-p65 and IκB in lung tissues were determined *via* Western blotting. The results manifested that the protein expressions of IRAK1, TRAF6, NF-κB p65, p-p65 and IκB in lung tissues distinctly rose in the model group compared with those in control group (P<0.05), while they distinctly declined in etomidate group compared with those in model group (P<0.05) (Fig. 2). To sum up, etomidate suppresses the protein expressions of IRAK1, TRAF6, NF-κB p65, p-p65 and IκB in rats with LPS-induced lung injury.

DISCUSSION

The current study manifested that etomidate significantly lowered the MPO activity and enhanced the SOD activity in rats with lung injury so as to resist oxidative damage to lung tissues. Etomidate reduced the MDA level by effectively reducing the oxidative stress of respiratory epithelial cells. The level of

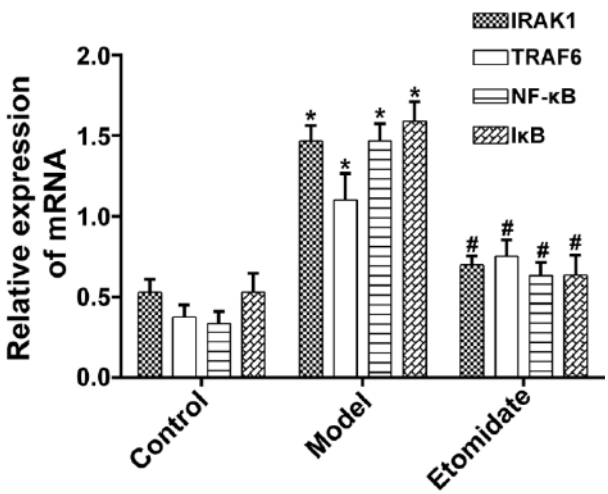

Fig. 1. *MRNA expressions of IRAK1, TRAF6, NF-κB and IκB in lung tissues. *P<0.05: model group vs. control group, #P<0.05: etomidate group vs. model group.*

Table V. *MPO and SOD activity and MDA level in serum ($\bar{\chi}$±s, n=10).*

Group	MPO (U/mg)	SOD (U/mL)	MDA (mmol/mg)
Control group	1.109±0.923	31.478±12.841	19.518±4.327
Model group	2.384±0.794*	8.697±9.437*	68.581±8.346*
Etomidate group	1.617±1.595*#	18.981±13.261*#	24.475±9.648*#

MDA, one of the important indexes of oxidative stress, usually reflects the degree of the cell damage caused by reactive oxygen metabolites (10). The endogenous antioxidant molecule SOD plays an important role in resisting ROS-induced oxidative stress injury (11). Neutrophils and macrophages recruited resist infection by pathogenic microorganisms and release inflammatory mediator enzymes to kill pathogenic microorganisms (12). In this study, it was found that etomidate could effectively inhibit neutrophil infiltration, suppress inflammatory response and lower the W/D ratio of lung tissues in rats with lung injury, indicating that etomidate reduces alveolar cell permeability and relieves pulmonary oedema induced by tissue fluid accumulation, thereby improving the lung function. The levels of inflammatory cytokines such as TNF-α, IL-1β and IL-6 released by respiratory epithelial cells and alveolar macrophages are key indexes measuring the degree of the inflammatory response (12). In this study, the results manifested that etomidate greatly improved LPS-induced oxidative stress response and lowered the levels of inflammatory cytokines, suggesting that the protective effect of etomidate against LPS-induced lung injury is achieved by adjusting the oxidative stress indexes and inflammatory cytokines in the body. NF-κB exists as heterodimers composed of p50 and p65 subunits, which binds to its inhibitory protein IκB to form complexes in the cytoplasm in a resting state. In the present study, the results showed that the protein expressions of NF-κB and IκB remarkably declined in the etomidate group compared with those in the model group. However, limitations still existed in the present study. All the above findings were based on animal experiments. These conclusions should be further validated via in vitro assays in cell lines. Additionally, the potential underlying molecular mechanism should also be further explored by future studies. In conclusion, etomidate exerts a significant protective effect against lung injury in sepsis rats by alleviating the inflammatory response and oxidative stress response, which may be related to the NF-κB signalling pathway. This study provides a theoretical basis for the application of etomidate as a potentially effective drug for ALI.

Conflict of interest

The authors declared no conflict of interest.

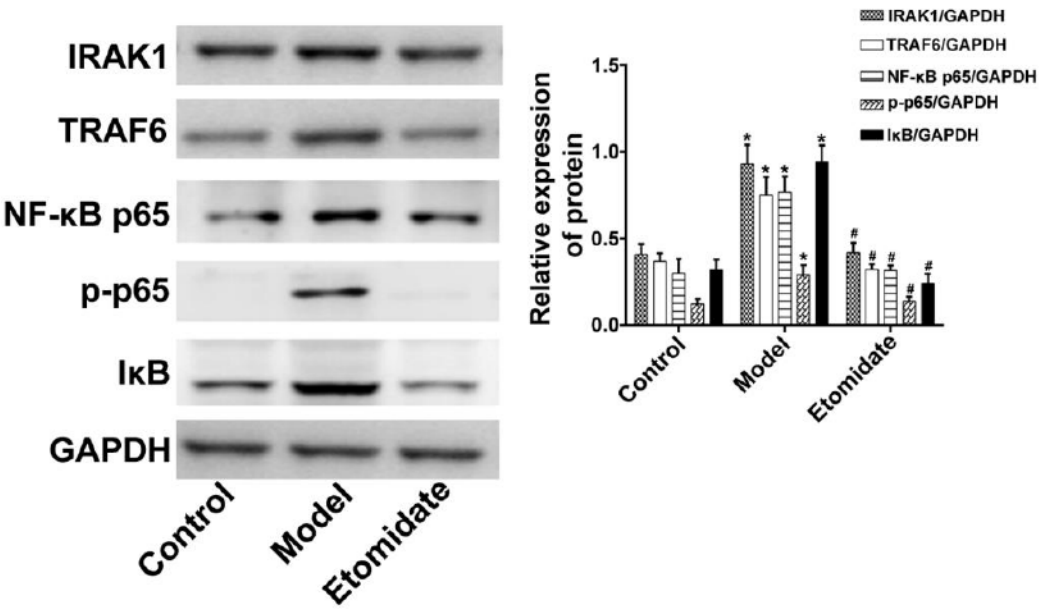

Fig. 2. *Expressions of NF-κB signaling pathway-related proteins in lung tissues. *P<0.05: model group vs. control group, #P<0.05: etomidate group vs. model group.*

REFERENCES

1. Li Y, Feng L, Zhao Y, Cong Y, Tang WL. AATF knockdown reduces cell proliferation and promotes cell apoptosis in LPS-induced sepsis. J Biol Reg Homeos Ag 2021; 35:1817-25.
2. Yu YL, Yu G, Ding ZY, Li SJ, Fang QZ. Overexpression of miR-145-5p alleviated LPS-induced acute lung injury. J Biol Reg Homeos Ag 2019; 33:1063-72.
3. Xin Y, Peng J, Hong YY, Chao QC, Na S, Pan S, Zhao LF. Advances in research on the effects of platelet activation in acute lung injury (Review). Biomedical reports 2022; 16:17.
4. Zhang Y, Zhang J, Fu Z. Molecular hydrogen is a potential protective agent in the management of acute lung injury. Mol Med 2022; 28:27.
5. Cui X, Lin P, Yu J, Liu L, Wang Z, Tang X. Dimethyl fumarate attenuates lipopolysaccharide-induced acute lung injury by inhibiting inflammation and oxidative stress. J Biol Reg Homeos Ag 2021; 35:1389-95.
6. Omercioglu G, Akat F, Ficicilar H, et al. Effects of aerobic exercise on lipopolysaccharide-induced experimental acute lung injury in the animal model of type 1 diabetes mellitus. Exp Physiol 2022; 107:42-57.
7. Gao JD, Song H, Fu P, Guo YX, Zhang HY, Qiu M. Effects of etomidate on cell apoptosis during myocardial ischemia-reperfusion. J Biol Reg Homeos Ag 2021; 35:67-72.
8. Klaric M, Diers A, Klingler H, Bantel C, Weyland A. Haemodynamic effects of anaesthesia induction with etomidate/remifentanil followed by sevoflurane/remifentanil balanced anaesthesia. Anasth Intensivmed 2021; 62:474-85.
9. Dmello D, Taylor S, O'Brien J, Matuschak GM. Outcomes of etomidate in severe sepsis and septic shock. Chest 2010; 138:1327-32.
10. Ahmed MA. Amelioration of nandrolone decanoate-induced testicular and sperm toxicity in rats by taurine: effects on steroidogenesis, redox and inflammatory cascades, and intrinsic apoptotic pathway. Toxicol Appl Pharmacol 2015; 282:285-96.
11. Jing W, Chunhua M, Shumin W. Effects of acteoside on lipopolysaccharide-induced inflammation in acute lung injury via regulation of NF-kappaB pathway in vivo and in vitro. Toxicol Appl Pharmacol 2015; 285:128-35.
12. Antus B. Oxidative Stress Markers in Sputum. Oxid Med Cell Longev 2016; 2016:2930434.

LETTER TO THE EDITOR

Evaluation of the therapeutic efficacy of vulvovaginal radiofrequency in the treatment of genitourinary syndrome

A. Lusi, G. Pasquali, L. Cavalieri, I. Simonelli, E. Bartoletti

Aesthetic Medicine Center, Ospedale San Giovanni Calibita fatebenefratelli, Rome, Italy

Menopause, with the lack of estrogen that accompanies it, causes physiological changes at the anatomical level of the vulva and vagina that can lead to a condition of vulvovaginal atrophy (1). The vaginal epithelium thins, and the production of collagen and hyaluronic acid decrease in the lamina propria, and the levels of elastin are reduced. The vaginal epithelium in this condition becomes very thin and flammable and often undergoes ulceration with bleeding sites (2, 3).

Symptoms related to vulvovaginal atrophy are vaginal dryness, itching, and dyspareunia (2). These symptoms can be accompanied by urinary disorders (stress urinary incontinence, recurrent cystitis) and alterations in the sexual sphere, configuring what is currently called Genitourinary syndrome of menopause (7, 8, 12). These symptoms can worsen the quality of sexual life and the quality of life in general of women who suffer from it (1, 9).

The first-choice therapy in these patients is systemic hormone replacement therapy which has proven effective in resolving the symptoms of vulvovaginal atrophy but is also unfortunately associated with an increased risk of thromboembolism and stroke as well as being contraindicated in patients with previous cancer of the breast (2, 4, 16). In addition, the use of non-ablative radiofrequency as a local regenerative/rehabilitation therapy in various gynaecological areas with various indications has recently been introduced (10, 11).

The radiofrequency generates electromagnetic waves, which determine high frequency alternating electric energy production. The resistances that electromagnetic waves encounter through the tissues stimulate the production of endogenous thermal energy, which induces a stimulus to activate the dermal fibroblasts (10); this determines the production of new collagen fibres in the tissues s as well as a stoichiometric rearrangement in the fibres already present. Furthermore, an improvement in tissue vascularization and oxygenation is determined through neoangiogenesis (14).

The objective of the study

The aim of this study was to evaluate the effects produced by non-ablative radiofrequency in the treatment of the signs and symptoms of Genitourinary Syndrome. Therefore, it was decided to evaluate therapy from an objective qualitative point of view of the vulvar and vaginal epithelium through instrumental evaluations and at a subjective level of the symptomatology reported by the patients by investigating the response to the therapy with a specific questionnaire.

MATERIALS AND METHODS

We considered 10 female patients, aged between 51 and 63 years, all in spontaneous menopause for at least three years. All patients had signs and symptoms of vulvovaginal atrophy, determined by Vaginal Health Index <15.

Exclusion criteria were:

• Presence of pacemakers or other implantable electronic

Corresponding Author:
Alessandra Lusi;
Aesthetic Medicine Center,
Ospedale San Giovanni Calibita fatebenefratelli,
viale dell'Umanesimo 307, 00144, Rome, Italy
Tel.: +39 3339148930
e-mail: lusialessandra@gmail.com

0393-974X (2022)

DISCLOSURE: ALL AUTHORS REPORT NO CONFLICTS OF INTEREST RELEVANT TO THIS ARTICLE.

devices or metal implants inside the body;

• Skin diseases or lesions in the treatment area;

• Other treatments on the region carried out in the last 30 days;

• Presence of oncological pathologies;

• Use of systemic hormone replacement therapy not suspended for at least six months;

• Use of other endovaginal hormonal therapies or other topical local therapies that have not

been suspended for at least a month;

• Vaginal infections or other local pathologies in place.

The patients were all treated with a class IIB electromedical device, of the latest generation, with multi-frequency radiofrequency that combines thermal technologies to develop heat inside the tissues at different depths. The operation of the device is based on heating the deep dermis and subcutaneous tissue through electromagnetic waves, which, by improving the activity of the sodium-potassium pump of the fibroblastic membrane, stimulate the production of new collagen, elastin and hyaluronic acid naturally. In addition, the device includes automatic feedback on the energy supply control, including:

1) temperature sensor inside the handpiece. Through this sensor, it is possible to control the temperature reached by the fabric to increase the safety and effectiveness of the treatment, making the heating implemented by the operator objective.

2) skin recognition: the correct power is delivered only when the skin is recognized in contact with the applied part.

At the beginning of the study, the treatment protocol was established to carry out bipolar radiofrequency treatment on each patient with a single wave intravaginal handpiece and an external double controlled wave chained handpiece. It was decided to carry out 1 weekly session for 8 consecutive weeks. During each session, the patients were treated with an endovaginal handpiece set in bipolar mode (power 2.5-3.5 J/cmq/sec) for 15 m applied in the vagina after affixing gel. The session was completed with the application of the external handpiece in the vulvar region using the bipolar mode at a power of 2.5-3.5 J/cmq/sec for 10 m. The power of the device was set at each session in order to develop a temperature measured by the sensor of 41-43°C. Overall, each session lasted about 25 m.

To evaluate and quantify the effects of the therapy, we used the following assessments:

1. Evaluation of the Vaginal Health Index (VHI);
2. Measurement of vaginal PH;
3. Cytological evaluation on vaginal smear.

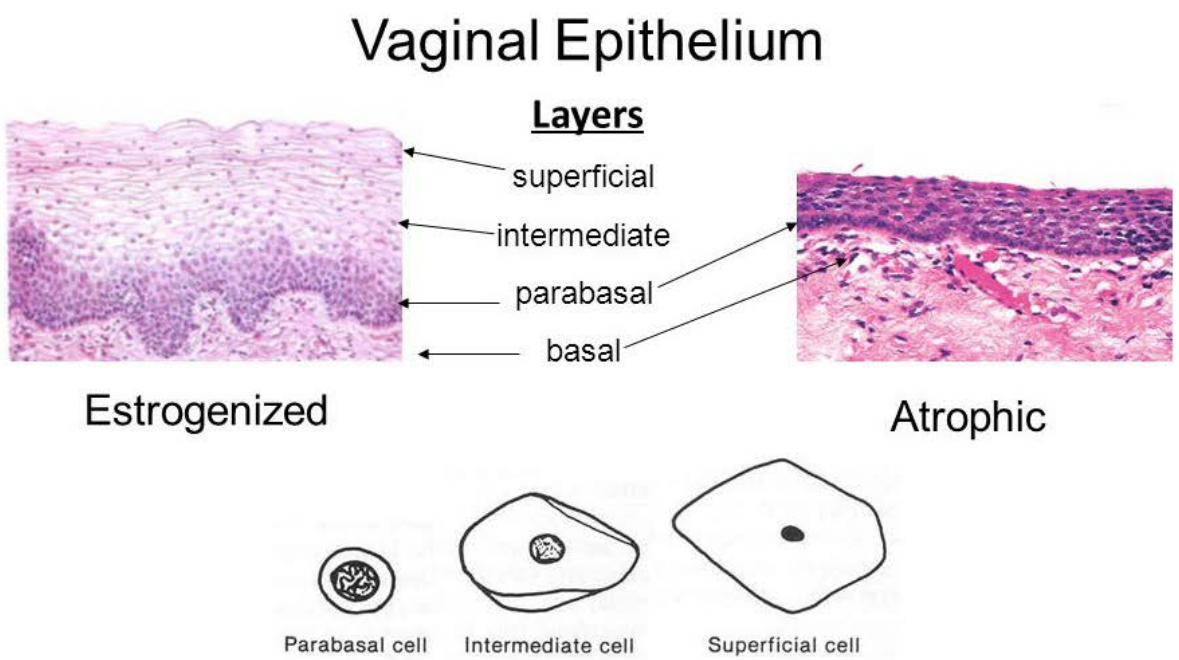

Fig. 1. *Three types (or stages) of Vaginal Epithelial Cells all scored to quantify estrogenization in the Vaginal Maturation Index. The Vaginal Maturation Index quantifies the relative proportion of the vaginal parabasal (P), intermediate (I), and superficial (S) cells presented as % P, % I, and % S.*
Source: Mills, Histology for Pathologists. 3rd Edition; LWW, 2006. Wheater, Functional Histology, 2nd Edition; Bibbo, 1997.

4. Questionnaire on Female Sexual Dysfunctions- FSFI.

The Vaginal Health Index (VHI) is a tool that the doctor uses to evaluate and quantify the degree of vulvovaginal atrophy. Five parameters are considered (vaginal elasticity, vaginal secretions, PH, epithelial mucosa, hydration of the vagina). A single score is assigned, from the sum of which derives a "score" which defines the presence and severity of vulvovaginal atrophy. The total score can vary between 5 and 25. Low scores correspond to greater atrophy. If the score is <15, the vagina is considered atrophic (15).

Vaginal PH is a very sensitive indicator of vaginal health and is subject to obvious variations in case of mucosal atrophy. Its increase lies in the reduced production of lactic acid by the vaginal lactobacilli, whose populations are considerably reduced due to the lack of estrogen (17).

The cytological examination of vaginal smear aims to assess the cell maturation index by quantifying the type of cells of the vaginal epithelium (basal, parabasal, intermediate and superficial) expressed as a percentage. Generally, the atrophic epithelium has a reduction until the disappearance of the superficial cells with a reduction of the intermediate and parabasal cells (15). Therefore, the sampling was performed on a vaginal smear with Ayre's spatula on the anterior, posterior and lateral walls of the vagina (Fig. 1).

The Female Sexual Function Index (FSFI), a self-report of 19 items, is the gold standard for the screening of female sexual dysfunctions, and for this reason, it is one of the most widely used validated questionnaires in the gynaecological and sexological field (6). Analyze female sexual functioning across 5 areas: sexual activity, sexual intercourse, sexual stimulation, sexual desire or interest, and sexual arousal. Its reading allows for investigation of the individual areas of reference, and the "cut-off" of the total score is established for values <26.55.

All assessments were carried out before the start of treatment (T0) and one week after the end of the treatment (T1).

RESULTS

In all the patients assessed, there was good compliance with the treatment, so it was possible to carry out the entire cycle of sessions in all cases. In no case were adverse events or undesirable effects detected.

VHI

Concerning the evaluation of the VHI, all parameters improved their score, which translated into an overall increase of 43% (Table I, Fig. 2).

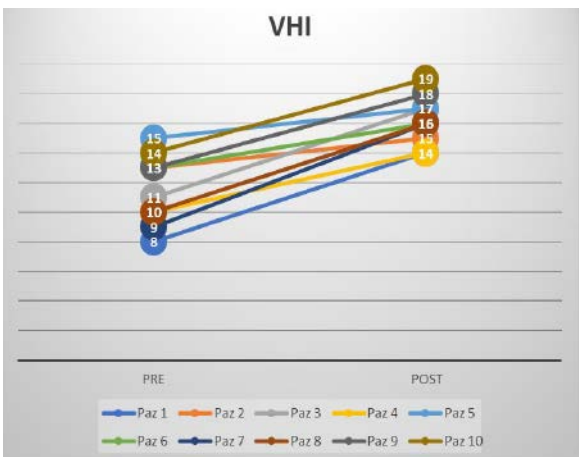

Fig. 2. *VHI variation - 43% increase in average score.*

Table I. *VH variations - overall variation and individual items.*

N=10	*Mean Score pre treatment (SD)*	*Mean Score post treatment*
VHI parameters	*Score +/- SD*	*Score +/- SD*
Elasticity	1.9 (0.7)	3.1 (0.8)
fluid volume	1.9 (0.6)	2.8 (0.7)
PH	2.5 (0.9)	3.4 (0.9)
epithelial integrity	2.9 (1.1)	3.6 (1.1)
Moisture	2.4 (0.6)	3.3 (0.6)
Total Score	**11.6 (1.9)**	**16.2 (1.8)**

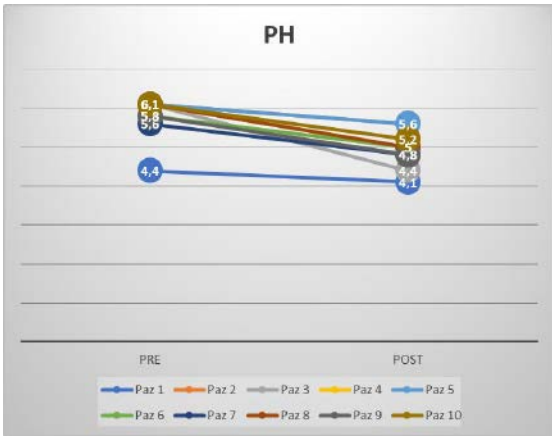

Fig. 3. *Vaginal PH variation - average overall reduction of 15%.*

Vaginal PH

Vaginal PH showed a slight reduction in almost all cases which overall was 15%. This reduction could be due to increased vaginal secretions that have returned acidity to the vaginal environment (Fig. 3).

FSFI questionnaire

The following data emerged from the evaluation of the FSFI questionnaire: a noticeable increase in vaginal lubrication (97%) with a significant reduction in pain during intercourse was reported. Consequently, a 57% increase in sexual desire and 32% in pleasure during intercourse emerged, just as the ability to achieve orgasm and 55% sexual satisfaction

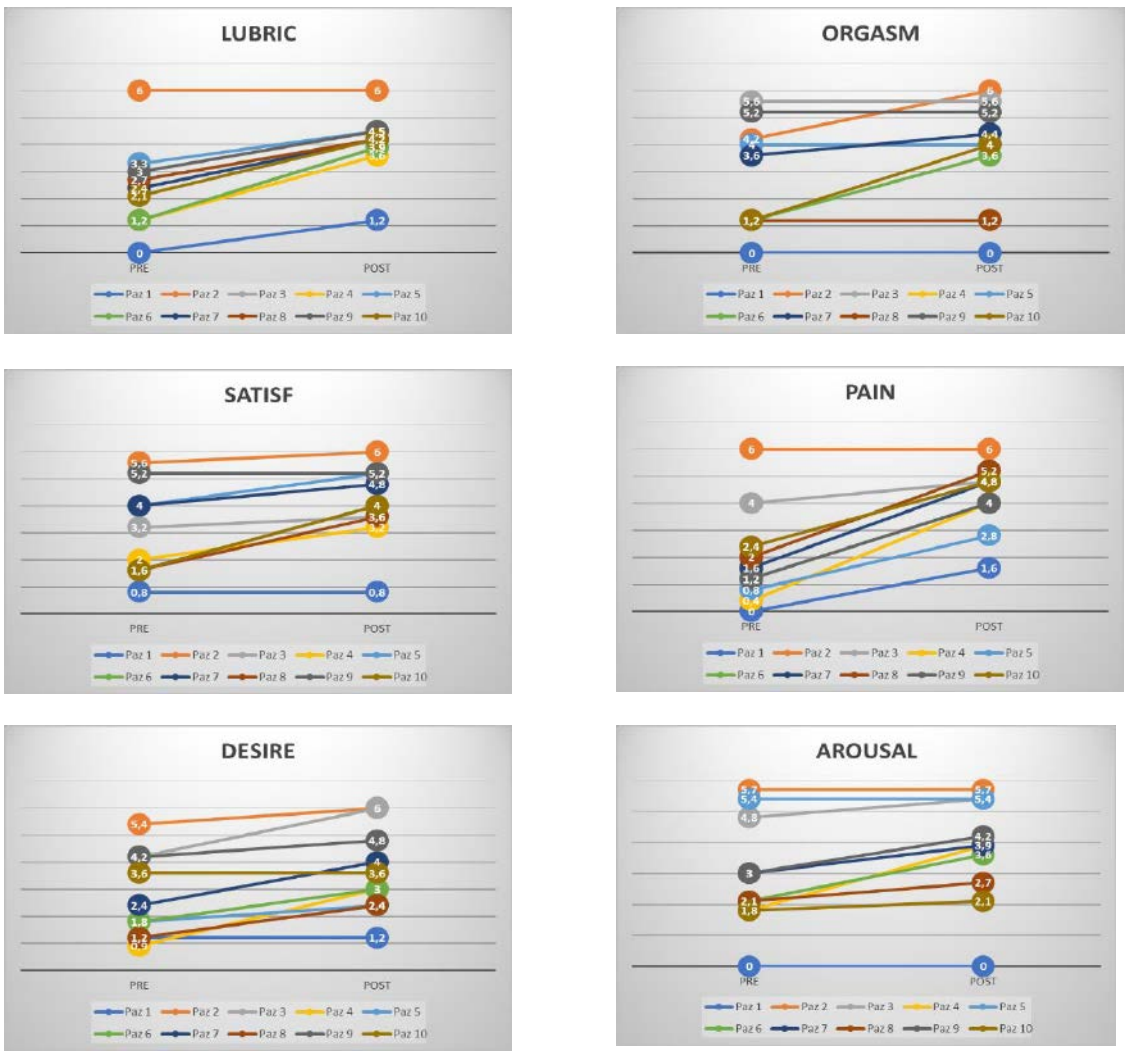

Fig. 4. *FSFI changes - overall and individual item changes.*

increased. Overall, the FSFI questionnaire recorded a 74% improvement in the score from an average score of 15.61 to 23.11. (Fig. 4, Table II).

From the analysis of the overall relative variations, the most significant figure turns out to be the reduction of dyspareunia and the increase in lubrication, with an improvement of all the other parameters analyzed (Fig. 5)

Cytological evaluation

There was a significant variation in the cell populations detected on a cytological examination performed on a vaginal smear in all the analysed cases. In particular, an increase in the surface and intermediate cells with a reduction in parabasal cells was detected (Table III). On the other hand, there was no statistically significant variation in basal cell populations.

CONCLUSIONS

Treatment of vulvovaginal atrophy with bipolar

Table II. *The FSFI questionnaire scores.*

N=10	*Mean Score pre treatment (SD)*	*Mean Score post treatment*
FSFI items	*Score +/- SD*	*Score +/- SD*
Desire	2.67 (1.5)	3.64 (1.5)
Arousal	2.97 (1.8)	3.69 (1.7)
Lubrication	2.31 (1.6)	4.02 (1.2)
Orgasm	2.74 (1.9)	3.52 (2.0)
Satisfaction	2.96 (1.6)	4.04 (1.4)
Dyspareunia	1.96 (1.8)	4.20 (1.2)
Total FSFI score	**15.61 (9.02)**	**23.11 (8.15)**

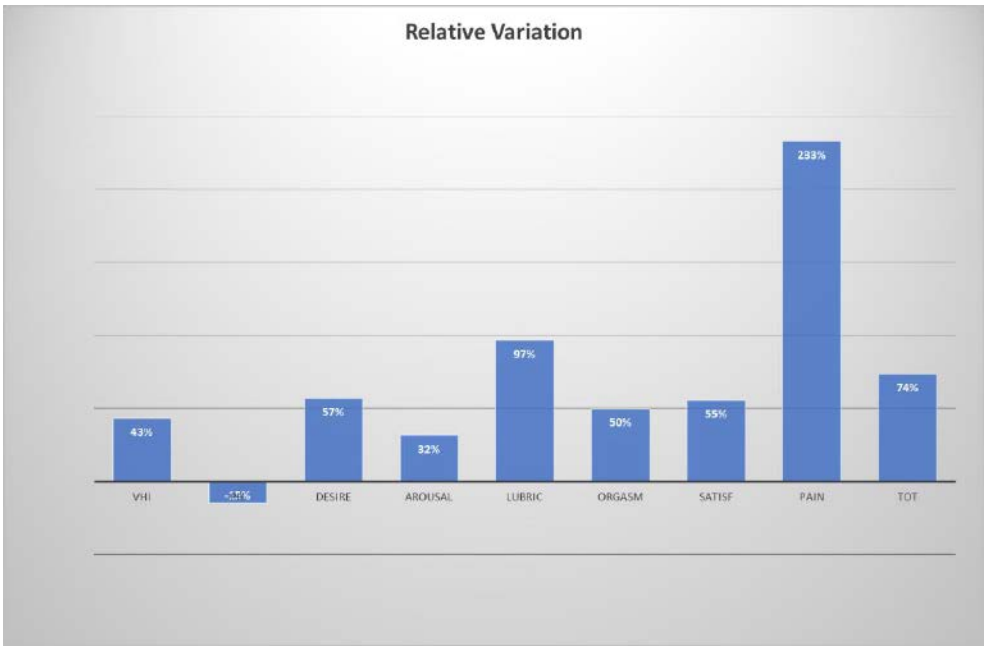

Fig. 5. *Relative changes expressed as a percentage of all investigations carried out.*

non-ablative radiofrequency has shown excellent compliance by patients and good efficacy in countering the signs and symptoms of Genitourinary Syndrome. The treatment was pleasant and well tolerated by all patients, resolving in many cases the resistance of some patients to approach less comfortable local physical regenerative therapies. The most significant aspect was the increase in hydration and elasticity of the vulvar and vaginal tissues, probably produced by the increase of collagen and the improvement of vascularization and oxygenation of the tissues (Fig. 7). Furthermore, the relatively short treatment times

Table III. *Percentage variations of vaginal cell populations*

N=10	***Mean Score pre-treatment***	***Mean Score post-treatment***
cellule superficiali	*26.6%*	*36.6%*
cellule intermedie	33.3%	36.6%
cellule parabasali	36.6%	23.3%
cellule basali	3.33%	3.33%

Fig. 1. *Cytological evaluation before and after treatment on vaginal smear stained with hematoxylin, OG6, EA50. Pre-treatment cytology on the left, post-treatment cytology on the right.*

and the absence of side effects make this method easy and safe in expert hands.

It was established to carry out follow-up assessments in the period following the treatment's end, monitor the effects of long-term therapy, and thus also evaluate the duration of these effects over time.

The preliminary data that our study obtained encourage us to look confidently towards these innovative, minimally invasive technologies that allow us to bypass the use of drugs and offer patients valid alternatives in cases where previous local pharmacological or topical therapies were not conclusive, or in cases where these therapies are not usable. In particular, vaginal radiofrequency can represent an excellent opportunity to treat Genitourinary Syndrome in all cases where there is a resistance to approaching other local regenerative methods (laser, PRP, biostimulation). In addition, it may represent an option as maintenance therapy for those who have already carried out treatment with other devices.

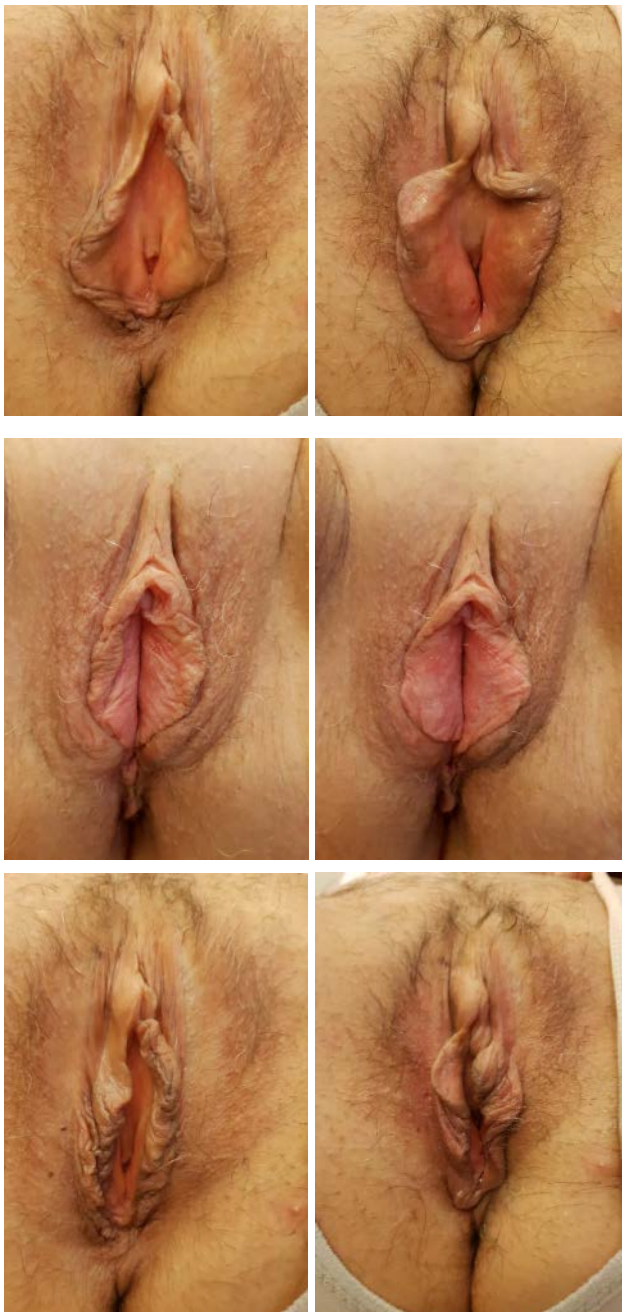

Fig. 7. *Left side: aspect of the vulva pretreatment; right side: after therapy with vulvar bipolar radiofrequency.*

REFERENCES

1. Palacios S, et al. treatment of the genitourinary syndrome of menopause. Climacteric 2015; 18(Suppl 1):23-9.
2. Palacios S, Castelo-Branco C, Currie H, et al. Update on management of genitourinary syndrome of menopause: A practical guide. Maturitas 2015; 82:308-13.
3. Palacios S - Managing urogenital atrophy. Maturitas 2009; 63:315-1.
4. Anderson GL et al. Effects of conjugated equine estrogen in postmenopausal women with hysterectomy: the Women's Health Initiative randomized controlled trial – JAMA 2004; 291(14):1701-12.
5. Bachmann GA et al. Long-term nonhormonal treatment of vaginal dryness - Clin Pract Sex 1992; 8:8.
6. Rosen R et al. The Female Sexual Function Index (FSFI): A Multidimensional Self-Report Instrument for the Assessment of Female Sexual Function. J Sex Marital Ther. 2000; 26(2):191-208.
7. Palacios S et al. Vulvar and vaginal atrophy as viewed by the Spanish REVIVE participants: Symptoms, management and treatment perceptions. Climacteric 2017; 20:55-61.
8. Portman DJ, Gass ML. Vulvovaginal Atrophy Terminology Consensus Conference Panel. Genitourinary syndrome of menopause: new terminology for vulvovaginal atrophy from the International Society for the Study of Women's Sexual Health and the North American Menopause Society. J

Sex Med 2014; 11:2865.
9. Nappi RE, Palacios S. Impact of vulvovaginal atrophy on sexual health and quality of life at postmenopause. Climacteric 2014; 17:3-9.
10. Tadir Y, Gaspar A, Lev-Sagie A, Alexiades M, Alinsod R, Bader A, Calligaro et al. Light and energy based therapeutics for genitourinary syndrome of menopause: Consensus and controversies. Lasers Surg Med. 2017; 49(2):137-159.
11. Qureshi AA, Tenenbaum MM, Myckatyn TM. Nonsurgical Vulvovaginal Rejuvenation With Radiofrequency and Laser Devices: A Literature Review and Comprehensive Update for Aesthetic Surgeons. Aesthet Surg J. 2018; 38(3):302-311.
12. Simon JA, Lukas VA. Distressing sexual function at midlife: unmet needs, practical diagnoses, and available treatments. Obstet Gynecol 2017; 130:889-905.
13. Wańczyk-Baszak J, Woźniak S, Milejski B, Paszkowski T. Genitourinary syndrome of menopause treatment using lasers and temperature-controlled radiofrequency. Prz Menopauzalny. 2018;17(4):180-184.
14. Hantash BM, Bedi VP, Kapadia B, Rahman Z, Jiang K, Tanner H, Chan KF, Zachary CB.2007 Feb. In vivo Histological Evaluation of a Novel Ablative Fractional Resurfacing Device. Lasers Surg Med; 39(2):96-107.
15. Gandhi J, Chen A, Dagur G, et al. Genitourinary syndrome of menopause: an overview of clinical manifestations, pathophysiology, etiology, evaluation, and management. Am J Obstet Gynecol 2016; 215:704.
16. NAMS.2013. Management of symptomatic vulvovaginal atrophy: 2013 position statement of the North American Menopause Society. Menopause; 20:888-902.
17. Palacios S, Gonzalez SP, Cancelo MJ. Is the PH a vaginal health marker? Phemale Study. Minerva Ginecol. 2018; 70(2):138-143.

LETTER TO THE EDITOR

LncRNA FLVCR1-AS1 facilitated cell viability and restrained cell apoptosis via sponging miR-381-3p in papillary thyroid carcinoma

M-J. Chen[1,#], X-J. Wang[1,#], D-X. Li[1] and J.-P. Han[1,2,*]

[1]Department of Thyroid Surgery, Yantai Yuhuangding Hospital, Affiliated Hospital of Qingdao University, Yantai, China; [2]Department of Gastrointestinal and Thyroid Surgery Ward I, Affiliated Hospital of Qingdao University, Yantai Yuhuangding Hospital, Yantai, China

Received November 5, 2021 – Accepted March 24, 2022

[#]These authors contributed equally to this work

To the Editor,

Thyroid cancer is the most common endocrine malignant tumor. In the past decades, the incidence of rapid rise. Papillary thyroid carcinoma (PTC) accounted for more than 80% of thyroid cancers. PTC has a relatively good prognosis; however, there are still 10%-30% cases with rapid malignant progression and poor prognosis (1). Therefore, it is of great clinical significance and value to deeply explore the mechanism of the occurrence and development of PTC for the diagnosis and treatment of PTC.

Long non-coding RNA (LncRNA) is a class of RNA molecules with a length of over 200nt. LncRNAs do not encode proteins but regulate gene expression through epigenetic, transcriptional, and post-transcriptional (2). It is believed that lncRNA is involved in various cellular functions, including X chromosome silencing, genomic imprinting, transcriptional regulation and intranuclear transport regulation. Although the mechanism related to LncRNA and tumorigenesis has not been clarified, current studies have shown the important significance of LncRNA in tumors (3). LncRNA is associated with the development of various tumors (lung, liver, bowel, prostate and bladder) (4, 5), including PTC. However, the mechanism of a large number of lncRNAs in PTC remains unclear.

The present study aimed to investigate the role of lncRNA FLVCR1-AS1 in PTC progression and further explore the potential underlying molecular mechanism.

MATERIALS AND METHODS

Clinical specimen and cell lines

A total of 30 PTC specimens were obtained from the patients who received surgery in our hospital. Furthermore, written informed consent was obtained from each participant before the study. This study was approved by the Ethics Committee of Yantai Yuhuangding Hospital.

Human normal thyroid cells (HT-ori3) were purchased from Cell Bioscience Inc (Shanghai, China). PTC cell lines (K1, BCPAP, TPC-1) were obtained from the Chinese Academy of Science cell bank (Shanghai, China). Cells were cultured with penicillin, Roswell Park Memorial Institute 1640 (RPMI 1640) medium (Thermo Fisher Scientific, Waltham, MA, USA) and 10% fetal bovine serum (FBS; Life Technologies, Gaithersburg, MD, USA)

Keywords: lncRNA; FLVCR1-AS1; miR-381-3p; PTC

**Corresponding Author:*
Dr Junping Han, BM.
Dept. of Gastrointestinal and Thyroid Surgery Ward I,
Yantai Yuhuangding Hospital,
Affiliated Hospital of Qingdao University,
20 Yuhuangding East Road, Zhifu District,
Yantai, Shandong 264000, China
e-mail: hanjunping@hdu.edu.cn

0393-974X (2022)

DISCLOSURE: ALL AUTHORS REPORT NO CONFLICTS OF INTEREST RELEVANT TO THIS ARTICLE.

in a humidified incubator containing 5% CO_2 at 37°C.

Cell transfection

For knocking-down FLVCR1-AS1, cells were transfected with constructed lentiviral vectors following the standard protocol (Genepharma, Shanghai, China). In addition, cells were transfected using miRNA mimics or inhibitors purchased from Genepharma (Shanghai, China).

RNA extraction and qRT-PCR

Total RNA was extracted using TRIzol reagent (Invitrogen, Carlsbad, CA, USA) and was then reverse-transcribed to complementary deoxyribose nucleic acids (cDNAs) by Transcription Kit (TaKaRa Biotechnology, Dalian, China). The primers were as follows:

FLVCR1-AS1-forward:
5'-GTGGCTCTCTCGTTCCC-3',
FLVCR1-AS1-reverse:
5'-CCGTCCTTCGGTAGTGTC-3'.
glyceraldheyde 3-phosphate dehydrogenase (GAPDH)
GAPDH-forward:
5'-CGCTCTCTGCTCCTCCTGTTC-3',
GAPDH-reverse:
5'-ATCCGTTGACTCCGACCTTCAC-3'.

Cell counting kit-8 assay (CCK-8)

Cell Counting Kit-8 assay was performed to examine the cell proliferation of PTC. Transfected cells were planted into 96-wells plates (6.0×10^3/well) and were then treated with CCK-8 solution (Beyotime, Shanghai, China) (10 μL/well) for 2 hours at 37°C. The OD value (450 nm) was then measured.

Colony formation

Cells (1.0×10^3) were planted into the culture plates (60 mm) and cultured for 2 weeks. Cells on the plates were then washed by phosphate buffer saline (PBS) (Gibco, China) twice and fixed in 70% ice-cold methanol for 15 min. Subsequently, Crystal Violet Staining Solution (Beyotime, Shanghai, China) was used to stain the cell colonies.

Transwell assay and Matrigel assay

Diluted Matrigel gel (200 μL) was added to the upper chamber with 1×10^5 cells (200 μL) inoculated. In addition, 300 μL of RPMI-1640 medium containing 10% fetal bovine serum was added as the chemokine in the lower chamber. The transmembrane cells in the Transwell upper chamber were fixed in 95% ethanol, washed twice with phosphate-buffered saline (PBS), and stained with freshly prepared hematoxylin solution.

Luciferase assay

The pGL3 vector (Promega, Madison, WI, USA) was used for transfection of the 3′-untranslated region (3′-UTR) of lncRNA FLVCR1-AS1 and WT 3′-UTR. In addition, quick-change site-directed mutagenesis kit (Stratagene, La Jolla, CA, USA) was used for site-directed mutagenesis of the miR-381-3p binding site in lncRNA FLVCR1-AS1 3′-UTR and MUT 3′-UTR.

Xenograft model

The present study was approved by the Animal Ethics Committee of Yantai Yuhuangding Hospital Animal Center. Transfected cells were injected subcutaneously into the nude mice (6 weeks old). Tumor growth was monitored and recorded every week. Tumors were extracted after 4 weeks for further analysis.

Statistical analysis

The data were presented as mean ± SD (standard deviation). Statistical Product and Service Solutions (SPSS) 17.0 (SPSS, Chicago, IL, USA) was used for statistically assessing. Chi-square test, analysis of variance (ANOVA) test and Kaplan-Meier were performed. *$P<0.05$ was considered statistically significant.

RESULTS

FLVCR1-AS1 was over-expressed in PTC tissues and cell lines

The qRT-PCR assay was recruited to determine the expression level of FLVCR1-AS1. FLVCR1-AS1 was significantly over-expressed in tumor specimens (Fig. 1A). Additionally, results also showed that PTC cell lines had a relatively higher expression level of FLVCR1-AS1 compared to the human normal thyroid cell (Fig. 1B).

Down-regulated FLVCR-AS1 suppressed cell proliferation, migration and invasion in vitro

We examined the transfection efficiency in selected cell lines, including BCPAP and TPC-1 (Fig.

2A). As shown in Fig. 2B, the FLVCR1-AS1 down-regulated group exhibited a significantly lower OD value than the control group. As well as in the results of colony formation assay, down-regulated FLVCR1-AS1 inhibited cell colony formation *in vitro* (Fig. 2C). In addition, the FLVCR1-AS1 down-regulated group had markedly lower migration cells and invasion cells than the control group (Fig. 2D), suggesting that FLVCR1-AS1 down-expression led to suppression in cell proliferation, migration and invasion *in vitro*.

LncRNA FLVCR1-AS1 interacted with miR-381-3p

By online public available databases, we found that FLVCR1-AS1 may have underlying interaction with miR-381-3p (Fig. 3A). The luciferase reporter assay showed the reduction activity of cells transfecting

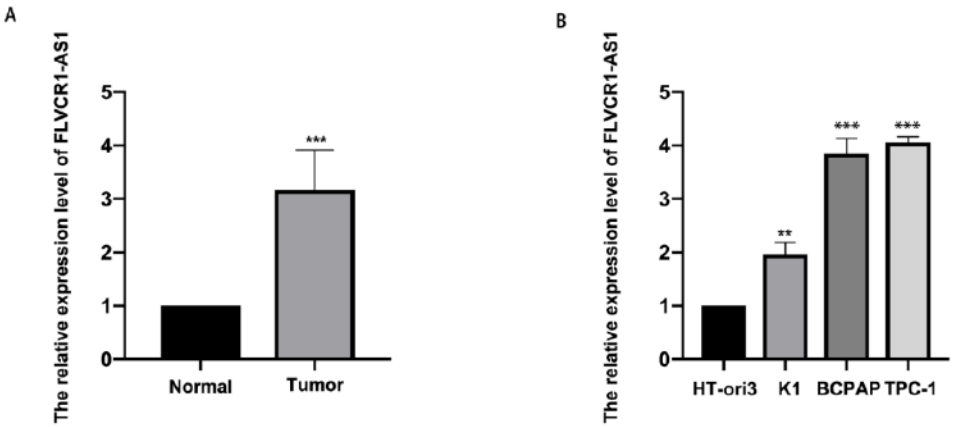

Fig. 1. *LncRNA FLVCR1-AS1 was over-expressed in PTC tissues and cell lines. (**A**) qRT-PCR analysis of lncRNA FLVCR1-AS1 expression in PTC tissues and normal tissues. (**B**) qRT-PCR analysis of lncRNA FLVCR1-AS1 expression in PTC cell lines. ** P<0.01, *** P<0.001.*

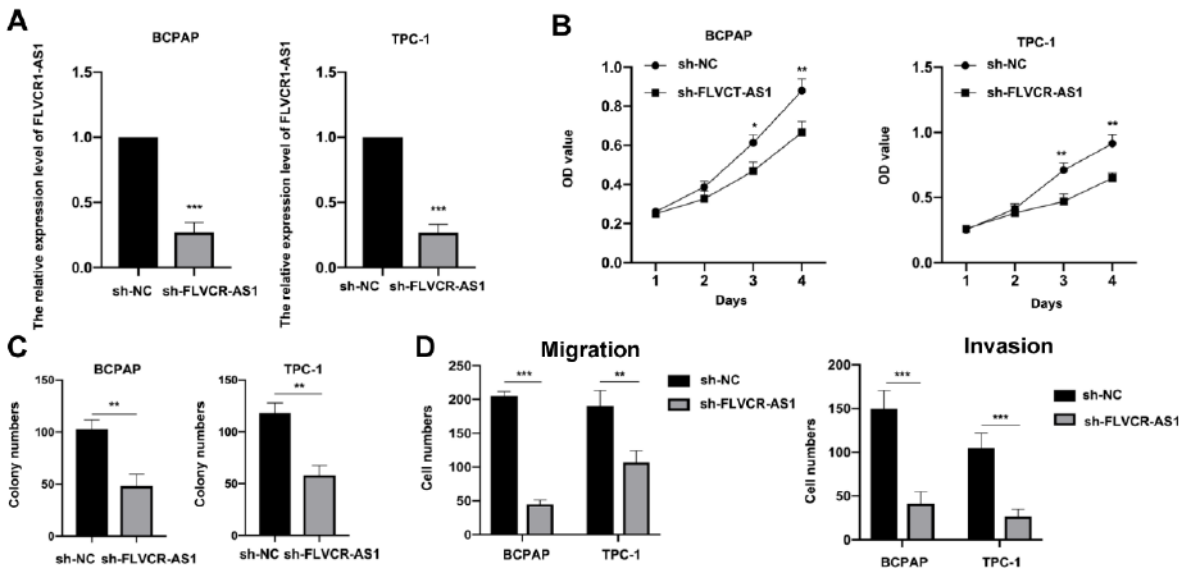

Fig. 2. *LncRNA FLVCR1-AS1 down-expression inhibited cell proliferation, migration and invasion in vitro. (**A**) Transfection efficiency was evaluated by qRT-PCR. (**B**) The cell proliferation ability was determined by CCK-8 assay. (**C**) Colony formation assay was recruited for detecting cell proliferation. (magnification: 40×) (**D**) Transwell assay and matrigel assay were involved to investigate the ability of cell migration and cell invasion. Magnification (magnification: 200×). Data are presented as the mean ± SD of three independent experiments. * P<0.05, ** P<0.01, *** P<0.001.*

with FLVCR1-AS1-wild type with miR-381-3p mimics (Fig. 3B). In transfected cell lines, we found that the expression level of miR-381-3p was increased in the FLVCR1-AS1 down-regulated group (Fig. 3C). Besides, qRT-PCR indicated that miR-381-3p was down-regulated in PTC (Fig. 3D). Furthermore, we conducted the Pearson correlation analysis and showed that the expression level of FLVCR1-AS1 was negatively correlated with miR-381-3p (Fig. 3E).

FLVCR1-AS1 accelerated tumor formation in vivo

Subsequently, we used the tumor formation assay *in vivo* to examine the ability of FLVCR1-AS1 on tumorigenesis. As shown in Fig. 4A-B, down-regulation of FLVCR1-AS1 inhibited tumor formation *in vivo*. The qRT-PCR assay was used to determine the expression of FLVCR1-AS1, and it turned out that the FLVCR1-AS1 down-expression group had a relatively lower expression level FLVCR1-AS1 (Fig. 4C). The expression level of miR-381-3p in the FLVCR1-AS1 down-regulated group was increased (Fig. 4D). Our data elucidated that FLVCR1-AS1 may exert its oncogenic function in PTC progression by sponging miR-381-3p.

DISCUSSION

Recent studies have shown that various LncRNAs are transcriptional dysregulation in cancer and play a role in promoting or inhibiting cancer (6). For example, LncRNA BANCR, MEG3 and PTCSC3 play the role of tumor inhibition by down-regulating transcription in PTC (7-9). In the studies related to LncRNAs and PTC, other LncRNAs also participated in the occurrence and process of PTC by combining with miRNAs (10). For example, LncRNA CNALPTC1

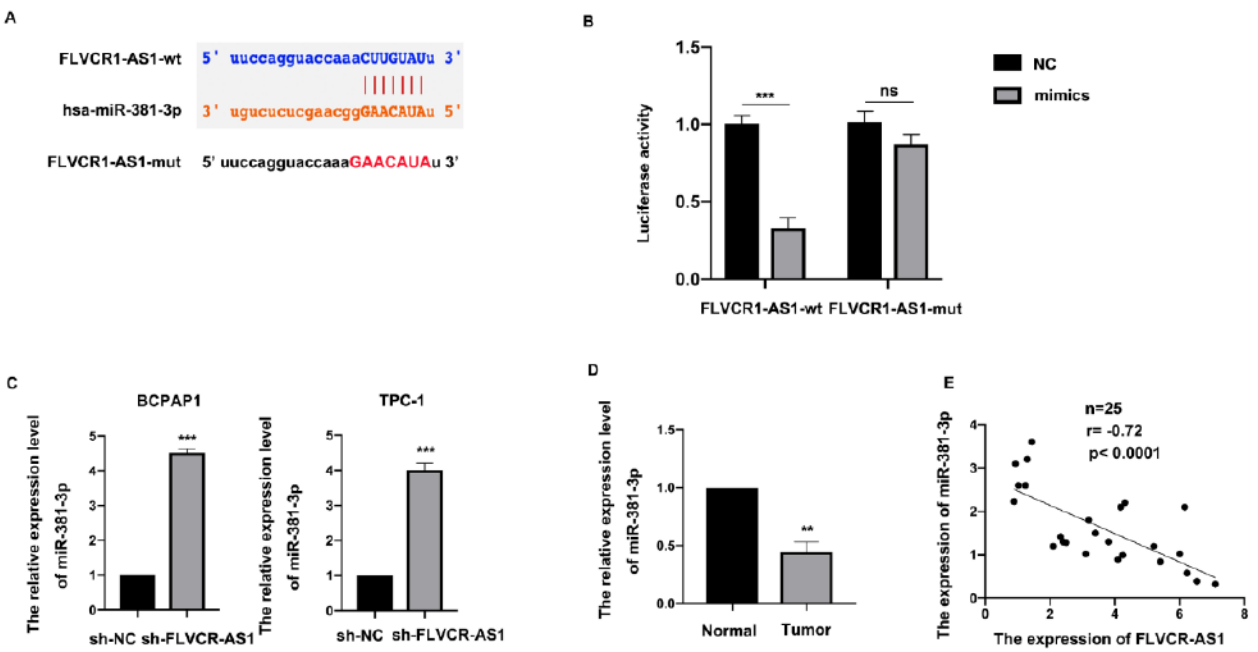

Fig. 3. *LncRNA FLVCR1-AS1 was interacted with miR-381-3p. (**A**) By using online databases, we found that there was a potential functional relationship between miR-381-3p and lncRNA FLVCR1-AS1. (**B**) The luciferase reporter showed the reduction activity of cells transfecting with lncRNA FLVCR1-AS1-wild type with miR-381-3p mimics. (**C**) Increased miR-381-3p was exhibited in lncRNA FLVCR1-AS1 down-regulation group. (**D**) miR-381-3p was down-regulated in PTC. (**E**) The expression level of FLVCR1-AS1 was negatively correlated with miR-381-3p. ** P<0.01, *** P<0.001.*

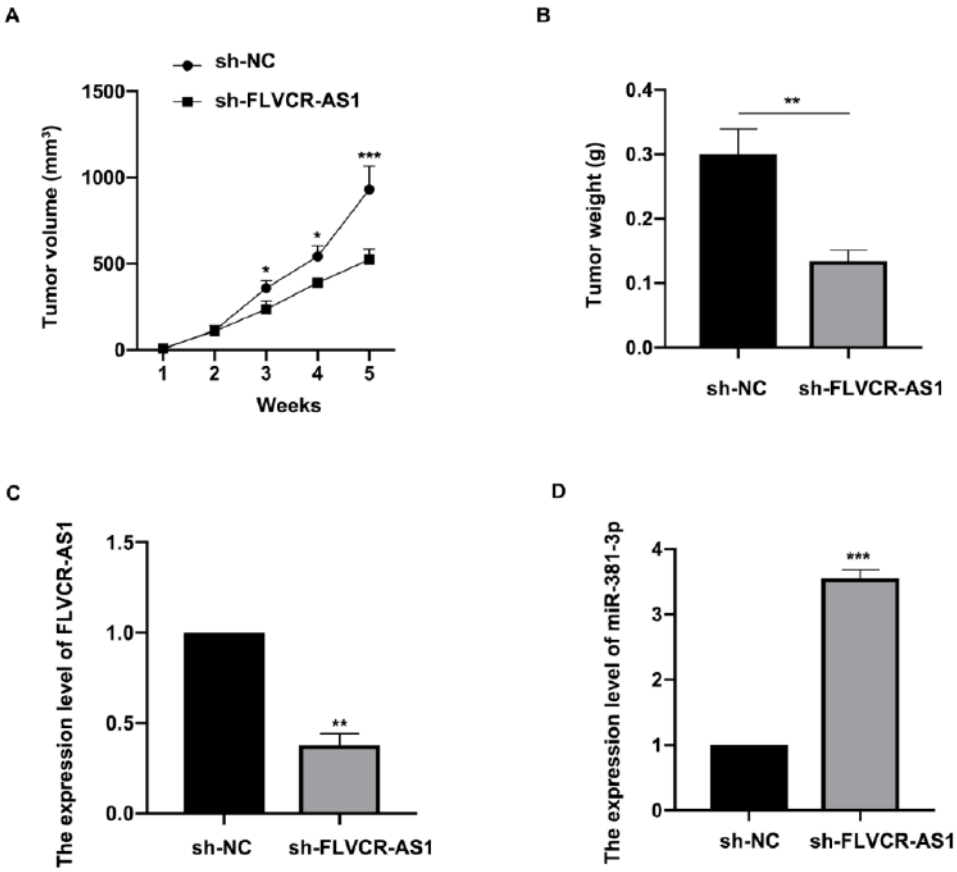

Fig. 4. *Over-expressed FLVCR1-AS1 promoted tumor formation in vivo. (**A**) After tumor extraction, tumor volume was calculated respectively and made into a graph; (**B**) Tumor weight were recorded; (**C**) The relative expression of FLVCR1-AS1 in tumors were examined by qRT-PCR; (**D**) The relative expression of miR-381-3p in tumors were examined by qRT-PCR Data are presented as the mean ± SD of three independent experiments. * P<0.05, ** P<0.01, *** P<0.001.*

can act as a molecular bait, competing to bind to the miR-30 family (miR-30a/miR-30b/miR-30c) and promote the process and development of PTC (11). LncRNA PTCSC3 can promote the proliferation and invasion, and metastasis of PTC by regulating miR-574-SCAI-Wnt/catenin (12).

The current study found that FLVCR1-AS1 was up-regulated in PTC, and down-regulated FLVCR1-AS1 suppressed cell proliferation, migration, and invasion *in vitro*. Furthermore, through luciferase reporter assay and Pearson correlation analysis, we revealed that FLVCR1-AS1 may exert its function in PTC by sponging miR-381-3p. Besides, the tumor formation assay demonstrated that the down-expression of FLVCR1-AS1 inhibited tumor formation *in vivo*.

In conclusion, downregulation of lncRNA FLVCR1-AS1 inhibited PTC cell proliferation, migration, and invasion by sponging miR-381-3p. LncRNA FLVCR1-AS1 functioned as an oncogenic role in PTC progression.

Conflict of Interest

The authors declared no conflict of interest.

REFERENCES

1. Roman BR, Morris LG, Davies L. The thyroid cancer epidemic, 2017 perspective. Curr Opin Endocrinol Diabetes Obes 2017; 24:332-336.
2. Chen L, Zhang YH, Pan X, et al. Tissue Expression

Difference between mRNAs and lncRNAs. Int J Mol Sci 2018; 19(11):3416.
3. Hou CJ, Wei R, Tang JL, Hu QH, He HF, Fan XM. Diagnostic value of ultrasound features and sex of fetuses in female patients with papillary thyroid microcarcinoma. Sci Rep 2018; 8:13374.
4. Sacks D, Baxter B, Campbell B, et al. Multisociety Consensus Quality Improvement Revised Consensus Statement for Endovascular Therapy of Acute Ischemic Stroke. Int J Stroke 2018; 13:612-632.
5. Chen J, Dai X, Yu H, Pe F, Chen L. SiRNA-mediated lncRNA ANRIL knockdown enhances the sensitivity of gastric cancer cells to doxorubicin. Iran Red Crescent Med J 2020; 22:e120.
6. Guo Z, Lin X, Guo X. LncRNA TUG1 facilitates the development of endometrial cancer via interaction with FXR1. Trop J Pharm Res 2021; 20(9):1839-1844.
7. Jendrzejewski J, Thomas A, Liyanarachchi S, et al. PTCSC3 Is Involved in Papillary Thyroid Carcinoma Development by Modulating S100A4 Gene Expression. J Clin Endocrinol Metab 2015; 100:E1370-E1377.
8. Wang C, Yan G, Zhang Y, Jia X, Bu P. Long non-coding RNA MEG3 suppresses migration and invasion of thyroid carcinoma by targeting of Rac1. Neoplasma 2015; 62:541-549.
9. Wang Y, Gu J, Lin X, Yan W, Yang W, Wu G. lncRNA BANCR promotes EMT in PTC via the Raf/MEK/ERK signaling pathway. Oncol Lett 2018; 15:5865-5870.
10. Jeong S, Lee J, Kim D, et al. Relationship of Focally Amplified Long Noncoding on Chromosome 1 (FAL1) lncRNA with E2F Transcription Factors in Thyroid Cancer. Medicine (Baltimore) 2016; 95:e2592.
11. Chen C, Zhou L, Wang H, et al. Long non-coding RNA CNALPTC1 promotes cell proliferation and migration of papillary thyroid cancer via sponging miR-30 family. Am J Cancer Res 2018; 8:192-206.
12. Wang X, Lu X, Geng Z, Yang G, Shi Y. LncRNA PTCSC3/miR-574-5p Governs Cell Proliferation and Migration of Papillary Thyroid Carcinoma via Wnt/beta-Catenin Signaling. J Cell Biochem 2017; 118:4745-4752.

LETTER TO THE EDITOR

Down-regulation of CXXC5 inhibits proliferation and extracellular matrix accumulation in uterine leiomyoma cells via the TGF-β/Smad pathway

L. He[1], L. Shen[2], Z. Wang[3], Y. Shen[2], Y. Gao[4], J. Qu[5] and J. Sun[1*]

[1]Department of Reproductive Surgery, Shanghai First Maternity and Infant Hospital, School of Medicine, Tongji University, Shanghai, China; [2]Department of Gynaecology and Obstetrics, Shanghai First Maternity and Infant Hospital, School of Medicine, Tongji University, Shanghai, China; [3]Department of Gynecology, Shanghai First Maternity and Infant Hospital, School of Medicine, Tongji University, Shanghai, China; [4]Department of Uterine Neck, Shanghai First Maternity and Infant Hospital, School of Medicine, Tongji University, Shanghai, China; [5]Department of Assisted Reproduction, Shanghai First Maternity and Infant Hospital, School of Medicine, Tongji University, Shanghai, China

Received August 24, 2021 – Accepted March 31, 2022

Uterine leiomyoma is a benign tumor of the smooth muscle in the uterus, with an incidence of 70% in all women. Numerous studies have shown that CXXC-type zinc finger protein 5 (CXXC5) is involved in the development of various diseases. However, whether CXXC5 plays a role in the progression of uterine leiomyoma is unknown. The expression of CXXC5 was evaluated by immunofluorescence (IF), immunohistochemistry (IHC) and western blot analysis, and CXXC5 was shown to be overexpressed in uterine leiomyoma tissues. The elevated expression levels of transforming growth factor-beta (TGF-β)/Smad pathway-related proteins (TGF-β1, p-Smad2 and p-Smad2) and extracellular matrix (ECM) key markers (MMP-2, MMP-9, ADAM10 and ADAM15) were measured through western blot analysis. The proliferation of uterine leiomyoma cells was tested using 3-(4,5-dimethylthiazol-2-yl)-2,5-diphenyltetrazolium bromide (MTT) assays, IHC staining detected the expression of proliferation marker Ki-67. Results showed that TGF-β1 promoted the proliferation of uterine leiomyoma cells while silencing RNA and TGF-β1 inhibitor SB431542 suppressed this effect. The expression of ECM accumulation-related proteins collagen IV and fibronectin was examined via western blot analysis and IF staining. CXXC5 attenuation by silencing RNA and TGF-β1 inhibitor SB431542 suppressed TGF-β1-induced ECM accumulation in primary uterine leiomyoma cells. Silencing of CXXC5 and treatment with SB431542 restrained the TGF-β/Smad pathway in TGF-β1-treated primary uterine leiomyoma cells. CXXC5 inhibition suppressed uterine leiomyoma cell proliferation and ECM accumulation by modulating the TGF-β/Smad pathway.

Uterine leiomyoma is considered to be a type of uterine fibroid, which is a benign tumor of the smooth muscle in the uterus (1). It has been reported that the incidence of uterine leiomyoma is 70% in all women and approximately 25% of the present clinical lesions (2,3). Although the pathogenesis of uterine leiomyoma is not yet fully understood, one of the most commonly accepted hypotheses is that

Keywords: CXXC5; TGF-β/Smad pathway; uterine leiomyoma

**Corresponding Author:*
Dr Jing Sun
Department of Reproductive Surgery,
Shanghai First Maternity and Infant Hospital,
School of Medicine, Tongji University,
No. 2699 Gaoke West Road, Pudong New District,
Shanghai 201204, China
e-mail: sunjingdr@163.com

0393-974X (2022)

it is related to the accumulation of extracellular matrix (ECM) (4). The proliferation of leiomyoma cells along with the deposition of excessive ECM are characteristics of uterine leiomyoma development and growth (5). Patients with uterine leiomyoma usually have heavy or prolonged menstrual bleeding, influencing fertility and quality of life (6). Currently, the main treatments for uterine leiomyoma patients are surgeries and pharmacotherapies, including myomectomy or hysterectomy by hysteroscopy or laparoscopy and oral progestins, contraceptives and GnRH analogues (7). However, the overall prognosis of patients is still poor. A previous study indicated that about 30% of uterine leiomyoma patients might die as a result of abnormal uterine bleeding and pelvic pressure (8). Therefore, it is imperative that we identify novel biomarkers to effectively improve therapeutic methods for uterine leiomyoma patients.

As a retinoid-responsive gene, CXXC-type zinc finger protein 5 (CXXC5), located in the 5q31.3 chromosomal region, encodes a retinoid-inducible nuclear factor (RINF) (9). There is evidence indicating that CXXC5 is widely found in various types of cells, including fibroblasts, nerve cells, bone cells, stem cells, hepatocytes, cardiomyocytes, and others (10). In addition, CXXC5 has been found to play a significant role in different diseases. For instance, in a bleomycin-triggered mouse model, CXXC5 suppresses pulmonary fibrosis by regulating the CD40/CD40L pathway (11). As an unmethylated CpG binder, CXXC5 can modulate estradiol-mediated gene expression and contribute to the growth of breast cancer cells, which further aggravates the progression of estrogen receptor-positive breast cancer (12). Moreover, CXXC5 leads to the differentiation of hematopoietic stem and progenitor cells into monocytes to regulate hematopoiesis (13). CXXC5 promotes autophagy and inflammation caused by *P. gingivalis* and affects the growth of cells through regulation of the Stat3/Erk/Akt signalling pathway (14). Nevertheless, the function of CXXC5 in uterine leiomyoma is still ambiguous.

Transforming growth factor β (TGF-β) is a polypeptide that consists of the three isoforms TGF-β1, TGF-β2, and TGF-β3, and is considered to be one of the key factors in the pathophysiology of uterine leiomyoma (15). TGF-β isoforms function in conjunction with activins to stimulate signals within the cells through Smad2/3 transcribing factors (16). Smad2/3 activation affects the expression of various profibrotic genes, including collagens (17). In cardiac and renal tissue, TGF-β1 can cause phosphorylation of its downstream mediators, Smad2/Smad3, and directly activate the accumulation of fibronectin and collagen and EMT progression (17,18). The TGF-β pathway includes Smads that play a role in the regulation of cellular proliferation and ECM formation at the transcriptional level in uterine leiomyoma (19). CXXC5 is capable of regulating TGF-β signal transduction processes (20); for example, CXXC5 suppresses hepatocellular carcinoma by promoting TGF-b-induced cell cycle arrest and apoptosis (21). CXXC5 can inhibit the proliferation and apoptosis of fibroblasts induced by TGF-β1 in mouse lung fibroblast models (11). However, the relationship between CXXC5 and the TGF-β/Smad pathway in uterine leiomyomas is not fully understood.

This work was designed to explore the role and function of CXXC5 in regulating the progression of uterine leiomyoma. The findings of our study may suggest a novel biomarker for effectively treating uterine leiomyoma.

MATERIALS AND METHODS

Tissue samples

In total, 20 pairs of uterine leiomyoma samples and adjacent normal tissues were harvested from uterine leiomyoma patients in our hospital. Some of the collected tissue specimens were frozen in liquid nitrogen and stored at −80°C for further use. Written informed consent was collected from all patients, and the work was approved by the Ethics Committee of our hospital (protocol number: 009).

Cell culture and identification

The collected uterine leiomyoma tissue specimens were sliced, and then collagenase A was used to digest the tissues to obtain a single-cell suspension. Dulbecco's modified Eagle's medium (DMEM; SK10092, Hyclone, USA) with 10% fetal bovine serum (FBS; 16140063, Gibco, USA)

was employed to incubate the primary cells under 5% CO_2 at 37°C. The smooth muscle characteristics of the myoma cells were identified by immunohistochemistry (IHC) staining using an α-actin monoclonal antibody (ab8226, Abcam, China). Formaldehyde was used to fix cells, followed by phosphate-buffered saline (PBS) washing. Then, H_2O_2 was added to the cells to quench the activity of endogenous peroxidase before washing with PBS. The cells were blocked in 1% bovine serum albumin (BSA; A8010, Solarbio, China) for 1 h and rinsed with PBS for 3 min, then were incubated with anti-α-actin at 4°C overnight. Thereafter, an HRP-labeled secondary antibody (Abcam) was added at room temperature for 30 min. Finally, the cells were stained by 3,3'-diaminobenzidine (DAB; D8001, Sigma, USA) and counterstained by hematoxylin (H8070, Solarbio) to observe immunoreactivity. A Nikon Eclipse Ni microscope (Nikon, USA) was used to capture images.

MTT assay

Uterine leiomyoma cells were seeded at 1x10(5) cells/well in a 96-well plate and cultured for 24 h. Thereafter, 10 µl of 3-(4,5-dimethylthiazol-2-yl)-2,5-diphenyltetrazolium bromide (MTT) reagent (2240130, Bio-Rad, USA) was added to the wells and incubated at 37˚C for 4 h. The medium was then removed, and 150 µl of dimethyl sulfoxide (D8418, Sigma) was added. After shaking on a micro vibrator for 10 min, the optical density at 570 nm was evaluated with a microplate reader (1681130, Bio-Rad).

Western blot analysis

Uterine leiomyoma cells and tissues were lysed, and protein concentrations were measured by a bicinchoninic acid (BCA) protein assay kit (ab102536, Abcam). Samples were resolved by 10% SDS-PAGE followed by transfer to polyvinylidene difluoride (PVDF; V515816, Millipore, USA) membranes. The blots were blocked in 5% non-fat milk for 2 h, then incubated overnight at 4°C with primary antibodies purchased from Abcam, including anti-CXXC5 (ab106533), anti-TGF-β1 (ab215715), anti-Smad2 (ab40855), anti-p-Smad2 (ab216482), anti-Smad3 (ab126761), anti-p-Smad3 (ab226821), anti-collagen IV (ab227616), anti-fibronectin (ab2413), anti-GAPDH (ab9485), anti-MMP2 (ab92536), anti-MMP9 (ab76003), anti-ADAM10 (ab1997) and anti-ADAM15 (ab124698), followed by incubation with the corresponding HRP-conjugated secondary antibodies (Abcam). An enhanced chemiluminescence detection kit (EK1001, Millipore) was utilized to visualize the proteins.

Immunofluorescence (IF) and IHC staining

The uterine leiomyoma tissues were subjected to IF staining to investigate CXXC5, collagen IV and fibronectin expression. The tissues were fixed in formalin and embedded in paraffin, followed by the preparation of 3- to 4-µm sections. Then, the sections were dewaxed, rehydrated, and submerged in 3% hydrogen peroxide to quench endogenous peroxidase activity. Afterwards, 1% BSA was used to block non-specific binding sites. Following incubation with primary antibodies against CXXC5 (ab106533), collagen IV (ab235296) or fibronectin (ab268020; all from Abcam) for 12 h at 4°C, anti-mouse secondary antibodies conjugated to fluorescein isothiocyanate (FITC) fluorophore (Sigma-Aldrich) were added to the sections. Finally, mounting media with DAPI was used to mount the sections on glass, and the sections were visualized with a confocal microscope (Nikon).

For IHC staining, uterine leiomyoma tissue sections were incubated with Abcam antibodies anti-CXXC5 (ab133191) and anti-Ki-67 (ab15580), followed by incubation with anti-mouse secondary antibodies. Finally, DAB was used to visualize the uterine leiomyoma tissue sections with a light microscope.

Hematoxylin & eosin (H&E) staining

Uterine leiomyoma samples were collected and fixed in 4% paraformaldehyde in 0.01 M PBS overnight, then dehydrated, embedded in paraffin, and sectioned into 4-µm-thick slices. The sections were deparaffinized using xylene, followed by rehydration via decreasing gradient alcohol. Thereafter, the tissues were subjected to hematoxylin and eosin (H&E) staining (Jiancheng, Nanjing, China). A light microscope was used to observe the stained sections.

Statistical Analysis

Statistical analyses were performed with SPSS 22.0 software (IBM, USA). All experiments were repeated at least three times and are represented as means ± standard deviation. Comparisons between the two groups were performed using Student's *t*-tests. One-way ANOVA followed by Turkey's post-hoc test was used to compare differences among three or more groups. $P < 0.05$ was considered statistically significant.

RESULTS

CXXC5 was overexpressed in uterine leiomyoma tissue

In Fig. 1A, H&E staining showed that uterine leiomyomas mainly consisted of smooth muscle cells and fibrous tissue compared to normal uterine tissues. In order to identify the role of CXXC5 in uterine leiomyoma, the expression of CXXC5 was evaluated in uterine leiomyoma tissues. The results of IF staining manifested that CXXC5 expression was

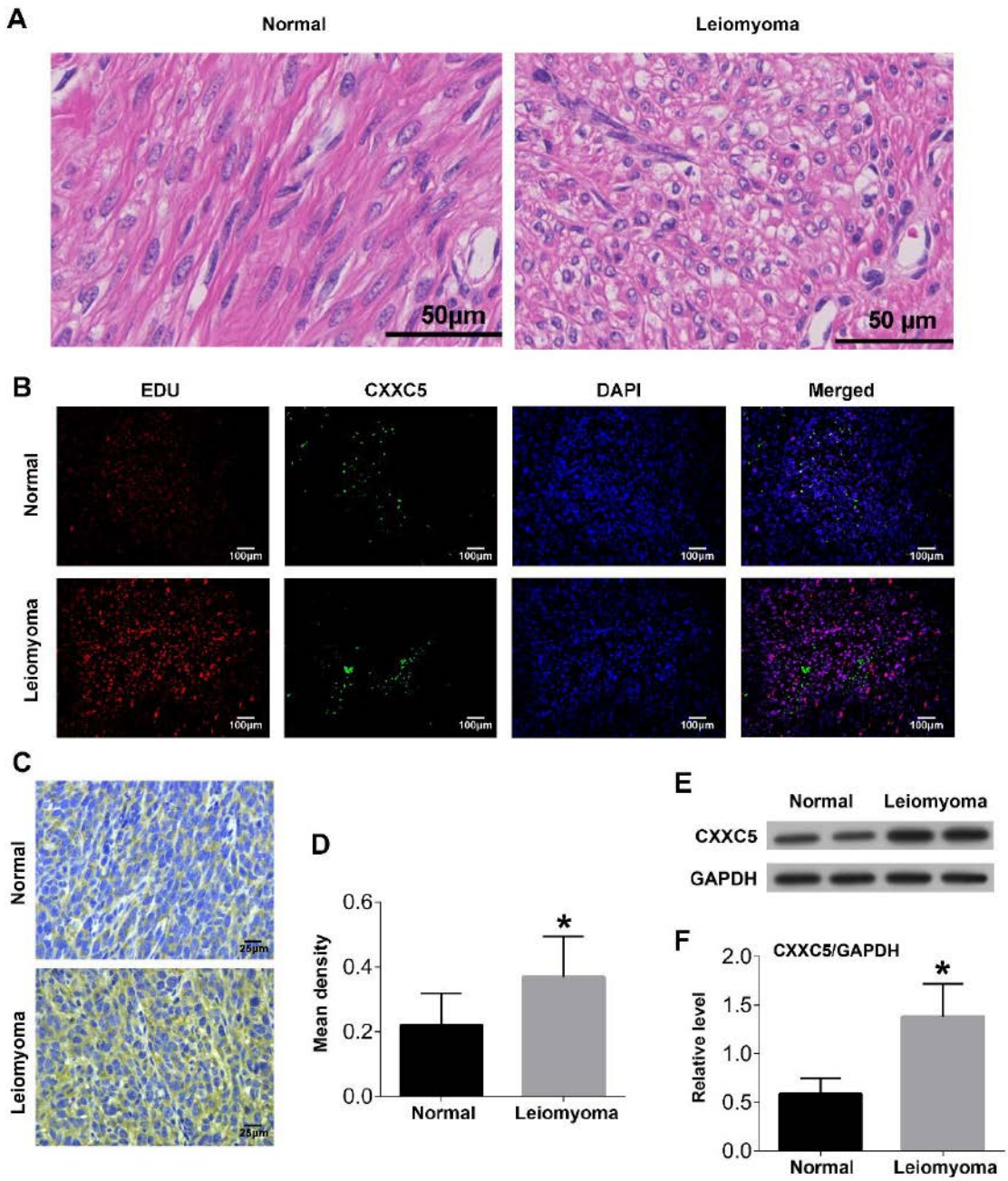

Fig. 1. *CXXC5 is overexpressed in uterine leiomyoma tissue.* ***A)*** *H&E staining showed that uterine leiomyomas mainly consisted of smooth muscle cells and fibrous tissue.* ***B)*** *IF staining was applied to detect CXXC5 levels in uterine leiomyoma tissues.* ***C-D)*** *IHC staining was performed to evaluate the level of CXXC5 in uterine leiomyoma tissues.* ***E-F)*** *Western blot analysis demonstrated increased CXXC5 protein levels in uterine leiomyoma tissues.* $^{*}p < 0.05$ *compared to the control group.*

dramatically up-regulated in leiomyoma tissues in comparison with normal tissues (Fig. 1B). Moreover, the elevated CXXC5 expression was also observed by IHC staining (Fig. 1C-D). In addition, western blot analysis was applied to measure CXXC5 protein expression in leiomyoma tissues and showed that the protein level of CXXC5 was obviously increased in leiomyoma tissues relative to normal tissues (Fig. 1E-F). In summary, CXXC5 was overexpressed in uterine leiomyoma tissues.

Expression of TGF-β/Smad pathway and ECM marker proteins in uterine leiomyoma tissue

The expression status of TGF-β/Smad pathway proteins (TGF-β1, p-Smad2 and p-Smad3) and ECM deposition in uterine leiomyoma tissues were tested

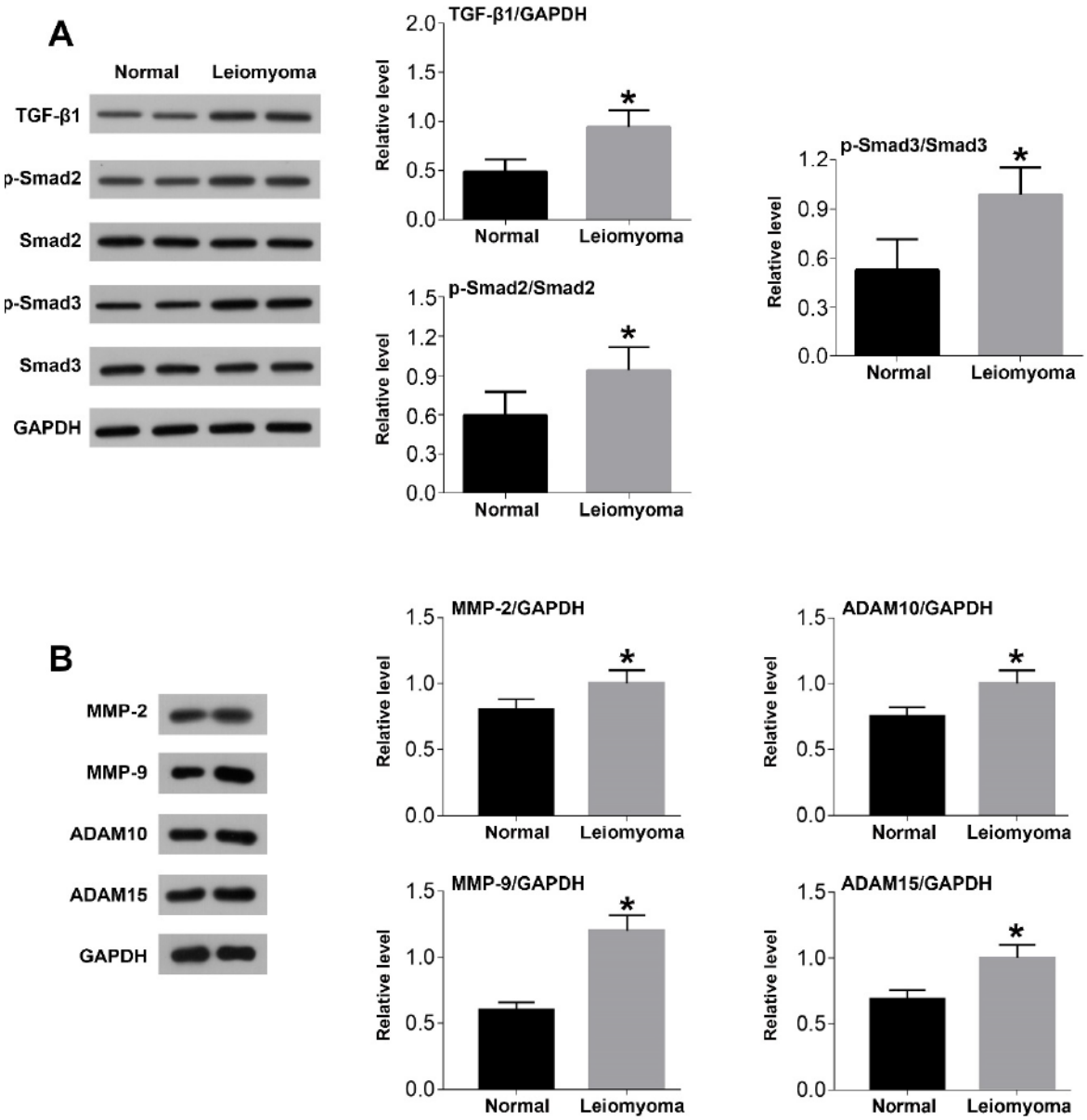

Fig. 2. *Expression of TGF-β/Smad pathway and ECM marker proteins in uterine leiomyoma tissue.* ***A)*** *Western blot analysis was used to measure TGF-β1, p-Smad2 and p-Smad3 protein levels in uterine leiomyoma tissues.* ***B)*** *Western blot analysis was used to measure MMP-2, MMP-9, ADAM10 and ADAM15 protein levels in uterine leiomyoma tissues.* $^{*}p < 0.05$ *vs control.*

through western blot analysis. The data indicated that TGF-β1, p-Smad2 and p-Smad3 protein levels were dramatically elevated in uterine leiomyoma tissues relative to normal tissues (Fig. 2A). Similarly, as shown in Fig. 2B, the expression levels of ECM representative enzyme markers (22, 23)(MMP-2, MMP-9, ADAM10 and ADAM15) were enhanced in uterine leiomyoma tissues compared to normal tissues.

Both si-CXXC5 and TGF-β1 inhibitor SB431542 suppressed TGF-β1-induced proliferation in primary uterine leiomyoma cells

Next, the functions of CXXC5 and the TGF-β/Smad pathway in uterine leiomyoma were analyzed. First, primary uterine leiomyoma cells and smooth muscle cells isolated from uterine leiomyoma tissues were identified by IHC staining with α-actin (Fig. 3A). CXXC5 was down-regulated in uterine leiomyoma cells after transfection with silencing RNA for CXXC5 (si-CXXC5), and western blot analysis revealed that CXXC5 protein level was overtly decreased by si-CXXC5 transfection of uterine leiomyoma cells (Fig. 3B-C). In addition, TGF-β1 inhibitor SB431542 also effectively suppressed TGF-β1 protein expression in uterine leiomyoma cells (Fig. 3D-E). Uterine leiomyoma cell proliferation was then tested by MTT assay, which revealed that proliferation was increased by

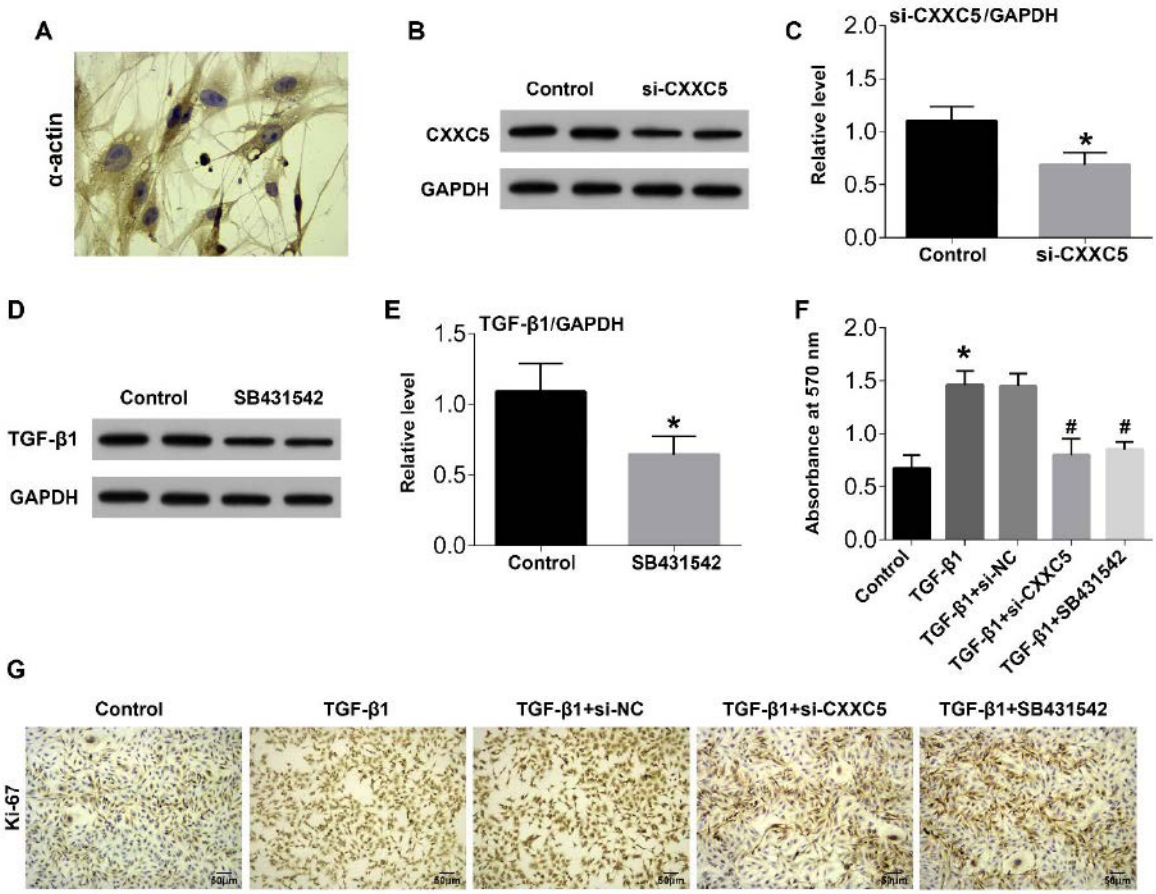

Fig. 3. *Both si-CXXC5 and TGF-β1 inhibitor SB431542 inhibit TGF-β1-induced proliferation in primary uterine leiomyoma cells.* ***A****) IHC staining was used to identify uterine leiomyoma cells.* ***B-C****) Western blot analysis was utilized to quantify CXXC5 protein levels.* ***D-E****) Western blot analysis measured the protein expression of TGF-β1.* ***F****) The proliferation of uterine leiomyoma cells was examined by MTT assay.* ***G****) IHC staining was applied to measure the expression of Ki-67.* $^{*}p < 0.05$ *relative to control;* $^{\#}p < 0.05$ *relative to TGF-β1 + vehicle.*

TGF-β1 but decreased by si-CXXC5 transfection or SB431542 treatment (Fig. 3F). To evaluate uterine leiomyoma cell proliferation, we assessed the expression of the proliferation marker Ki-67 (24). Similarly, IHC staining showed that expression of Ki-67 positive cells was up-regulated in the TGF-β1 group but was reversed by si-CXXC5 or SB431542 transfection (Fig. 3G).

Both si-CXXC5 and TGF-β1 inhibitor SB431542 inhibited TGF-β1-induced extracellular matrix accumulation in primary uterine leiomyoma cells

Thereafter, we investigated whether CXXC5 and the TGF-β/Smad pathway could affect extracellular matrix accumulation in primary uterine leiomyoma cells. Western blot analysis indicated that collagen IV and fibronectin protein levels were up-regulated by TGF-β1 induction but were down-regulated by transfection with si-CXXC5 or treatment with SB431542 (Fig. 4A-C). Additionally, IF staining demonstrated that the elevated levels of collagen IV and fibronectin induced by TGF-β1 were decreased by si-CXXC5 transfection or SB431542 treatment (Fig. 4D).

Both si-CXXC5 and SB431542 inhibited the protein expression of the TGF-β/Smad pathway and ECM markers in TGF-β1-treated primary uterine leiomyoma cells

Subsequently, western blot analysis was employed to detect TGF-β1, p-Smad2 and p-Smad3 and ECM marker protein levels in TGF-β1-treated primary uterine leiomyoma cells. The data demonstrated that TGF-β1, p-Smad2 and p-Smad3 protein levels were significantly increased due to the induction of TGF-β1, which was counteracted by treatment with si-CXXC5 or SB431542 (Fig. 5A). We also found that expression levels of the ECM markers were up-regulated after treatment

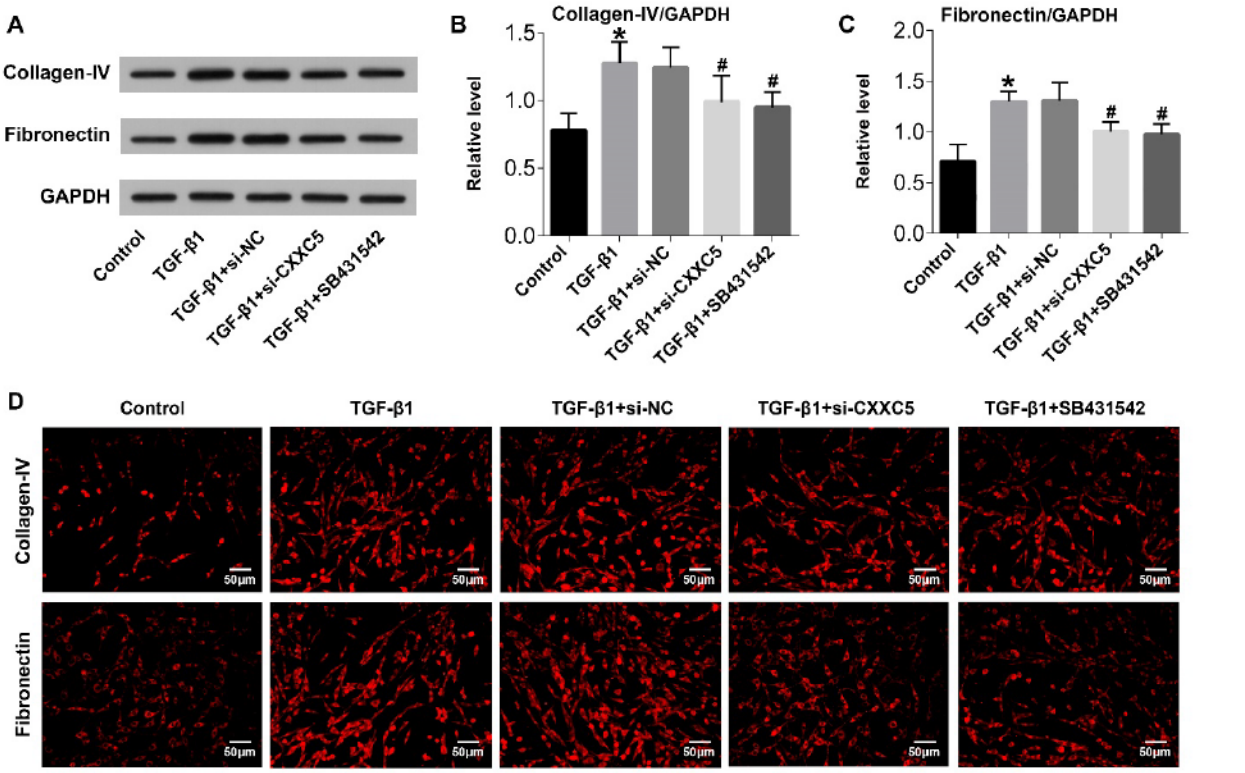

Fig. 4. *Both si-CXXC5 and TGF-β1 inhibitor SB431542 inhibit TGF-β1-induced extracellular matrix accumulation in primary uterine leiomyoma cells.* ***A-C****) Collagen IV and fibronectin protein expression were investigated via western blot analysis.* ***D****) IF staining was applied to show collagen IV and fibronectin expression.* $^{*}p < 0.05$ *relative to control;* $^{\#}p < 0.05$ *relative to TGF-β1 + vehicle.*

of TGF-β1, but treatment with si-CXXC5 or SB431542 reversed these effects (Fig. 5B). As a whole, these results indicate that both si-CXXC5 and SB431542 inhibited the TGF-β/Smad pathway and the deposition of ECM in TGF-β1-treated primary uterine leiomyoma cells.

DISCUSSION

Uterine leiomyoma, occurring with high prevalence, is frequently subjected to hysterectomy, which causes substantial expense to both patients and society (1). Although the etiology remains unclear, the excessive production of ECM has been reported to play a pivotal role in the development of uterine leiomyoma (25).

Previous studies have identified numerous mRNAs, which play significant roles in the development of uterine leiomyoma (26). For example, TRIM9 is associated with the growth of uterine leiomyoma cells through modulation of the NF-κB signalling pathway (27). CCND1, a target of miR-93, mediates uterine leiomyoma by altering the cell cycle and increasing the apoptosis of

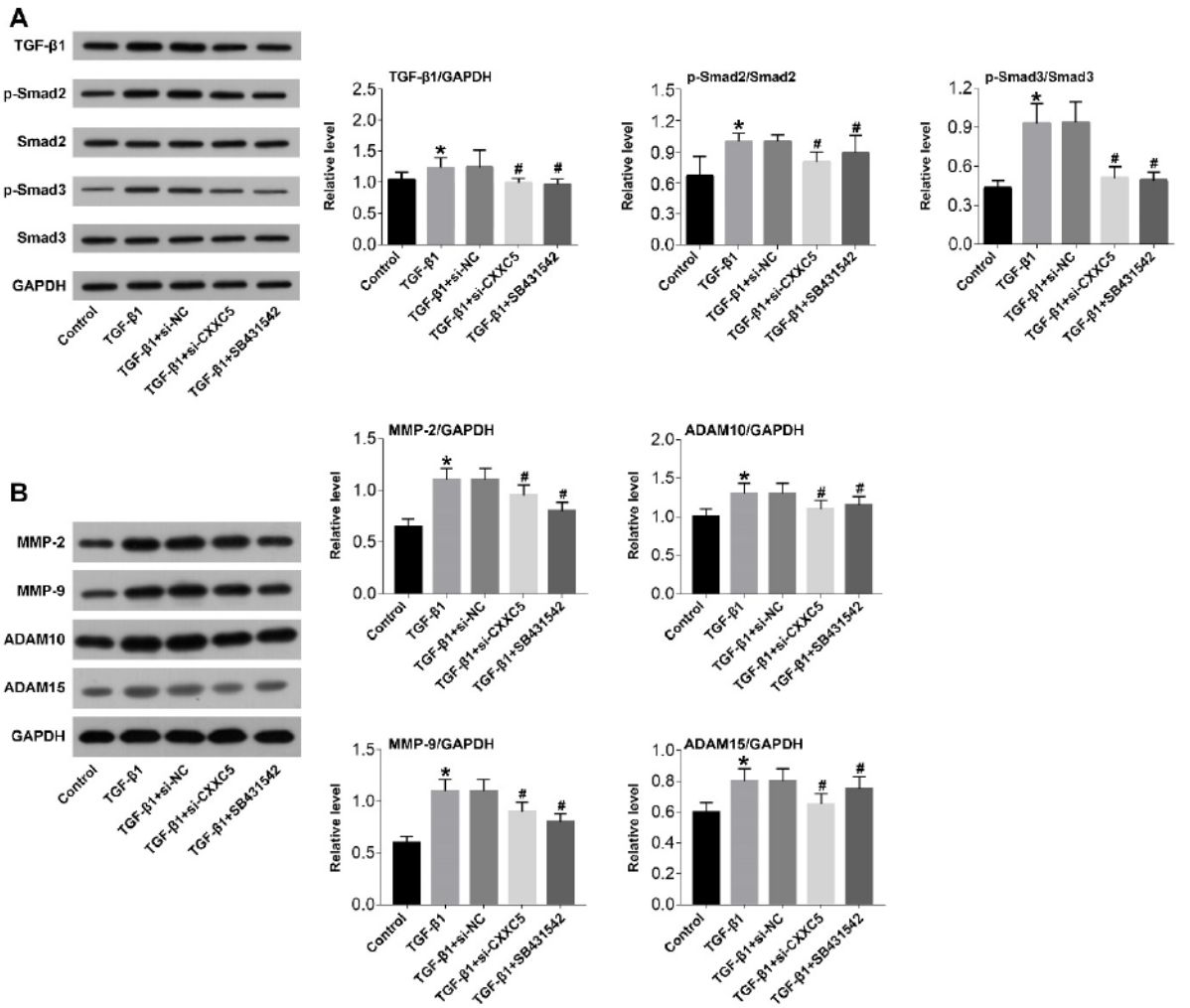

Fig. 5. *Both si-CXXC5 and SB431542 inhibit protein expression of the TGF-β/Smad pathway and expression of ECM markers in TGF-β1-treated primary uterine leiomyoma cells.* ***A)*** *Western blot analysis was used to detect TGF-β1, p-Smad2 and p-Smad3 protein expression in uterine leiomyoma cells.* ***B)*** *Western blot analysis was used to detect MMP-2, MMP-9, ADAM10 and ADAM15 protein expression in uterine leiomyoma cells.* $^{*}p < 0.05$ *relative to control;* $^{\#}p < 0.05$ *relative to TGF-β1 + vehicle.*

uterine leiomyoma cells (28). TET1 participates in the progression of uterine leiomyoma by promoting the growth and inhibiting the apoptosis of uterine leiomyoma cells (29). Although increasing evidence has shown that CXXC5 is implicated in the pathogenesis of a variety of diseases (11-14), the detailed role of CXXC5 in uterine leiomyoma has not been elucidated until now. In our work, the role of CXXC5 in the development of uterine leiomyoma was explored. The data revealed that CXXC5 was obviously up-regulated in uterine leiomyoma tissues, indicating that CXXC5 may play a vital role in the progression of this disease.

TGF-β is an important cytokine implicated in various cell processes, especially the proliferation of different kinds of cells (30,31). Smad proteins are the major intracellular signal transducers in the TGF-β1 signalling pathway, and multiple studies have demonstrated that Smad proteins are phosphorylated by TGF-β signalling (32). The TGF-β/Smad signalling pathway was previously corroborated to play a vital role in the progression of diseases. This was evidenced by a study by Wang et al. (33), indicating that the TGF-β/Smad signalling pathway regulates proliferation, invasion, apoptosis and collagen synthesis in keloid fibroblast cells to modulate the progression of keloid. Another study also revealed that epithelial cell viability influenced the development of oral submucous fibrosis via regulation of the TGF-β/Smad signalling pathway (34). In addition, the TGF-β/Smad signalling pathway promotes renal interstitial fibrosis (35). However, the participation of the TGF-β/Smad signalling pathway in uterine leiomyoma has not been fully explored. In this study, we found the levels of proteins associated with the TGF-β/Smad pathway (TGF-β1, p-Smad2 and p-Smad3) were evidently elevated in uterine leiomyoma tissues. Previous studies have shown that TGF-β expression in the uterine smooth muscle that directly contacts the fibroid is significantly increased, as has been demonstrated in the laboratory (36) and clinical studies (37).

In addition, compared to the myometrium, Smad2 and Smad3 are over-phosphorylated in the leiomyoma (38). TGF-β was able to increase the synthesis of ECM components through the activation of Smad signalling pathways (39).

Furthermore, we assessed ECM deposition in uterine leiomyoma. Several matrix metalloproteinases (MMPs) and ADAM (a disintegrin and metalloproteinase) family members are marker enzymes of ECM (40,41), which contribute to ECM degradation. Our results are consistent with those of previous studies showing that MMP-2 and MMP-9 expression are significantly higher in fibroids compared to normal myometrium (42). ADAM10 and ADAM15 exert their action by degrading the ECM proteins collagen IV and fibronectin and thus are involved in disease development (41).

Subsequently, we found that TGF-β1enhanced the proportion of Ki-67 positive cells and protein expression levels of fibronectin and collagen-IV. Our results are consistent with those previously reported indicating that TGF-β1 is known to activate several ECM components, including collagen type IV and fibronectin (43). ECM can enhance excessive proliferation (44) while silencing CXXC5 or inhibiting the TGF-β/Smad pathway with the TGF-β1 inhibitor SB431542 attenuated proliferation and ECM accumulation in primary uterine leiomyoma cells. Subsequently, rescue assays demonstrated that both CXXC5 down-regulation and SB431542 restrained the TGF-β/Smad pathway in TGF-β1-treated primary uterine leiomyoma cells. The down-regulation of CXXC5 depressed proliferation and extracellular matrix accumulation in uterine leiomyoma cells and was mediated by the TGF-β/Smad pathway.

In summary, this study is the first to our knowledge to find that CXXC5 inhibition suppressed uterine leiomyoma cell proliferation and extracellular matrix accumulation via modulation of the TGF-β/Smad pathway. Results of this work may provide new insights to help improve the treatment of uterine leiomyoma and the prognosis of uterine leiomyoma patients.

Conflicts of interest

The authors declare that there is no conflict of interest.

REFERENCES

1. Islam MS, Protic O, Stortoni P, et al. Complex networks of multiple factors in the pathogenesis of uterine leiomyoma. Fertil Steril 2013; 100(1):178-193.
2. Styer AK, Rueda BR. The Epidemiology and Genetics of Uterine Leiomyoma. Best Pract Res Clin Obstet Gynaecol 2016; 34:3-12.
3. Cramer SF, Patel A. The frequency of uterine leiomyomas. Am J Clin Pathol 1990; 94(4):435-438.
4. Islam MS, Ciavattini A, Petraglia F, Castellucci M, Ciarmela P. Extracellular matrix in uterine leiomyoma pathogenesis: a potential target for future therapeutics. Hum Reprod Update 2018; 24(1):59-85.
5. Borahay MA, Al-Hendy A, Kilic GS, Boehning D. Signaling Pathways in Leiomyoma: Understanding Pathobiology and Implications for Therapy. Mol Med 2015; 21:242-56.
6. Stewart EA, Laughlin-Tommaso SK, Catherino WH, Lalitkumar S, Gupta D, Vollenhoven B. Uterine fibroids. Nat Rev Dis Primers 2016; 2:16043.
7. Donnez J, Arriagada P, Donnez O, Dolmans MM. Emerging treatment options for uterine fibroids. Expert Opin Emerg Drugs; 23(1):17-23.
8. Donnez J, Donnez O, Dolmans MM. With the advent of selective progesterone receptor modulators, what is the place of myoma surgery in current practice? Fertil Steril 2014; 102(3):640-48.
9. Kim HY, Yoon JY, Yun JH, et al. CXXC5 is a negative-feedback regulator of the Wnt/β-catenin pathway involved in osteoblast differentiation. Cell Death Differ 2015; 22(6):912-20.
10. Tsuchiya Y, Naito T, Tenno M, et al. ThPOK represses CXXC5, which induces methylation of histone H3 lysine 9 in Cd40lg promoter by association with SUV39H1: implications in repression of CD40L expression in CD8+ cytotoxic T cells. J Leukoc Biol 2016; 100(2):327-38.
11. Cheng W, Wang F, Feng A, Li X, Yu W. CXXC5 Attenuates Pulmonary Fibrosis in a Bleomycin-Induced Mouse Model and MLFs by Suppression of the CD40/CD40L Pathway. Biomed Res Int 2020; 2020:7840652.
12. Ayaz G, Razizadeh N, Yaşar P, et al. CXXC5 as an unmethylated CpG dinucleotide binding protein contributes to estrogen-mediated cellular proliferation. Sci Rep 2020; 10(1):5971.
13. Capitano ML. CXXC5: A novel regulator of myelopoiesis. J Leukoc Biol 2020; 108(2):451-53.
14. Ma L, Liu H, Wang X, et al. CXXC5 orchestrates Stat3/Erk/Akt signaling networks to modulate P. gingivalis-elicited autophagy in cementoblasts. Biochim Biophys Acta Mol Cell Res 2021; 1868(3):118923.
15. Ciebiera M, Wlodarczyk M, Wrzosek M, et al. Role of Transforming Growth Factor beta in Uterine Fibroid Biology. Int J Mol Sci 2017; 18(11):2435.
16. Hata A, Chen YG. TGF-beta Signaling from Receptors to Smads. Cold Spring Harb Perspect Biol 2016; 8(9):a022061.
17. Saadat S, Noureddini M, Mahjoubin-Tehran M, et al. Pivotal Role of TGF-beta/Smad Signaling in Cardiac Fibrosis: Non-coding RNAs as Effectual Players. Front Cardiovasc Med 2020; 7:588347.
18. Geng XQ, Ma A, He JZ, et al. Ganoderic acid hinders renal fibrosis via suppressing the TGF-beta/Smad and MAPK signaling pathways. Acta Pharmacol Sin 2020; 41(5):670-77.
19. Cetin E, Al-Hendy A, Ciebiera M. Non-hormonal mediators of uterine fibroid growth. Curr Opin Obstet Gynecol 2020; 32(5):361-70.
20. Xiong X, Tu S, Wang J, Luo S, Yan X. CXXC5: A novel regulator and coordinator of TGF-beta, BMP and Wnt signaling. J Cell Mol Med 2019; 23(2):740-49.
21. Yan X, Wu J, Jiang Q, Cheng H, Han JJ, Chen YG. CXXC5 suppresses hepatocellular carcinoma by promoting TGF-beta-induced cell cycle arrest and apoptosis. J Mol Cell Biol 2018; 10(1):48-59.
22. Fujisawa C, Castellot JJ, Jr. Matrix production and remodeling as therapeutic targets for uterine leiomyoma. J Cell Commun Signal 2014; 8(3):179-94.
23. Bonnans C, Chou J, Werb Z. Remodelling the extracellular matrix in development and disease. Nat Rev Mol Cell Biol 2014; 15(12):786-801.
24. Zhang Q, Kanis MJ, Ubago J, et al. The selected biomarker analysis in 5 types of uterine smooth muscle tumors. Human pathology 2018; 76:17-27.
25. Chen HY, Lin PH, Shih YH, et al. Natural Antioxidant Resveratrol Suppresses Uterine Fibroid Cell Growth and Extracellular Matrix Formation In Vitro and In Vivo. Antioxidants (Basel) 2019; 8(4):99.
26. Anjum S, Sahar T, Nigam A, Wajid S. Transcriptome Analysis of mRNA in Uterine Leiomyoma Using

Next-generation RNA Sequencing. Anticancer Agents Med Chem 2019; 19(14):1703-18.
27. Yang F, Liu H, Yu Y, Xu L. TRIM9 overexpression promotes uterine leiomyoma cell proliferation and inhibits cell apoptosis via NF-κB signaling pathway. Life Sci 2020; 257:118101.
28. Zhang D, Liu E, Tian W, Zhang Z, Wang L, Li J. MiR-93 blocks cell cycle progression and promotes apoptosis in uterine leiomyoma cells by targeting CCND1. Anat Rec (Hoboken) 2020; 303(9):2372-2381.
29. Lu JL, Zhao L, Han SC, et al. MiR-129 is involved in the occurrence of uterine fibroid through inhibiting TET1. Eur Rev Med Pharmacol Sci 2018; 22(14):4419-26.
30. Massagué J. TGFbeta in Cancer. Cell 2008; 134(2):215-230.
31. Zhao H, Gao Y, Chen Q, et al. RAD51AP1 promotes progression of ovarian cancer via TGF-β/Smad signalling pathway. J Cell Mol Med 2021; 25(4):1927-38.
32. Massagué J, Chen YG. Controlling TGF-beta signaling. Genes Dev 2000;14(6):627-44.
33. Wang XM, Liu XM, Wang Y, Chen ZY. Activating transcription factor 3 (ATF3) regulates cell growth, apoptosis, invasion and collagen synthesis in keloid fibroblast through transforming growth factor beta (TGF-beta)/SMAD signaling pathway. Bioengineered 2021; 12(1):117-26.
34. Li L, Gu L, Yao Z, Wang Y, Tang Z, Wu X. Arecoline suppresses epithelial cell viability by up-regulating tropomyosin-1 through the transforming growth factor-β/Smad pathway. Pharm Biol 2020;58(1):1244-51.
35. Wang R, Wu G, Dai T, et al. Naringin attenuates renal interstitial fibrosis by regulating the TGF-β/Smad signaling pathway and inflammation. Exp Ther Med 2021; 21(1):66.
36. Halder SK, Osteen KG, Al-Hendy A. 1,25-dihydroxyvitamin d3 reduces extracellular matrix-associated protein expression in human uterine fibroid cells. Biol Reprod 2013; 89(6):150.
37. Shen T, Shi H, Xu Q, Song Q, Xu Y, Huang Y. Effects of TGF-beta on uterine fibroids of women of childbearing age and uterine artery embolization. Minim Invasive Ther Allied Technol 2017; 26(5):292-99.
38. Chegini N, Luo X, Ding L, Ripley D. The expression of Smads and transforming growth factor beta receptors in leiomyoma and myometrium and the effect of gonadotropin releasing hormone analogue therapy. Mol Cell Endocrinol 2003; 209(1-2):9-16.
39. Ciebiera M, Wlodarczyk M, Zgliczynska M, et al. The Role of Tumor Necrosis Factor alpha in the Biology of Uterine Fibroids and the Related Symptoms. Int J Mol Sci 2018; 19(12):3869.
40. Ramachandran RK, Sorensen MD, Aaberg-Jessen C, Hermansen SK, Kristensen BW. Expression and prognostic impact of matrix metalloproteinase-2 (MMP-2) in astrocytomas. PLoS One 2017; 12(2):e0172234.
41. Paolillo M, Schinelli S. Extracellular Matrix Alterations in Metastatic Processes. Int J Mol Sci 2019; 20(19):4947.
42. Bogusiewicz M, Stryjecka-Zimmer M, Postawski K, Jakimiuk AJ, Rechberger T. Activity of matrix metalloproteinase-2 and -9 and contents of their tissue inhibitors in uterine leiomyoma and corresponding myometrium. Gynecol Endocrinol 2007; 23(9):541-46.
43. Leask A, Abraham DJ. TGF-beta signaling and the fibrotic response. FASEB J 2004; 18(7):816-27.
44. Bulun SE. Uterine fibroids. N Engl J Med 2013; 369(14):1344-55.